HYDRATE-BEARING SEDIMENTS: FORMATION and GEOPHYSICAL PROPERTIES

A Thesis

Presented to

The Academic Faculty

By

Joo-yong Lee

In Partial Fulfillment

of the Requirements of the Degree

Doctor of Philosophy in Civil and Environmental Engineering

Georgia Institute of Technology

August 2007

HYDRATE-BEARING SEDIMENTS:
FORMATION and GEOPHYSICAL PROPERTIES

Approved by

J. Carlos Santamarina, Chairman
School of Civil and Environmental Engineering
Georgia Institute of Technology

J. David Frost
School of Civil and Environmental Engineering
Georgia Institute of Technology

Glenn J. Rix
School of Civil and Environmental Engineering
Georgia Institute of Technology

Carolyn D. Ruppel
School of Earth and Atmospheric Science
Georgia Institute of Technology

Costas Tsouris
School of Civil and Environmental Engineering
Georgia Institute of Technology

Date Approved: June 29th 2007

ACKNOWLEDGEMENTS

First, I thank to God for His speechlessly great love that He has given to me.

I would like to thank to my advisor Dr. Carlos Santamarina for his guidance, support, and generosity not only as an advisor, but also as a sincere friend. It was a great pleasure to work with him at Georgia Tech. I am deeply impressed by his deep knowledge, brilliant ideas, and philosophy while I was working with him.

I would like to express my appreciation to my committee members for their insightful comments and suggestions: Dr. Carolyn Ruppel, Dr. David Frost, Dr. Glenn Rix and Dr. Costas Tsouris. Especially, I appreciate Dr. Carolyn Ruppel for her supports and advices in many occasions.

I also thank my family for all the supports and love they've given to me. I would like to thank past and current members of the Particulate Media Laboratory for their assistance, encouragement, and discussion: Jong-Sub Lee, Angelica Palomino, Franco Francisca, Jose Alvarellos, Guillermo Narsilio, Hyunki Kim, Tae Sup Yun, Veronica R. Landa, Ahmed M. Bayoumi, Maria Cristina, Hosung Shin, Jongwon Jung, Jaewon Jang, Douglas D. Cortes, D. Nicolas Espinoza, and Taehyuk Kwon. I also would like to thank the Korean Civil Engineering Society for their support.

I would like to acknowledge the Georgia Institute of Technology, Joint Industry Project, and Goizueta foundation for providing funding for this research.

TABLE OF CONTENTS

LIST OF TABLES

LIST OF FIGURES

SUMMARY

Hydrate-bearing sediments may contribute to the availability of energy resources, affect climate change, or cause seafloor instability. The comprehensive study of hydrate-bearing sediments documented in this manuscript includes physicochemical aspects of hydrate nucleation near mineral surfaces, the validity of THF as a substitute guest molecule for the study of hydrate-bearing sediments, and the effects of hydrate formation on the electromagnetic and the mechanical properties of various soils with a wide range of specific surface. Natural marine sediments are included as part of this investigation to explore the effects of inherent fabric, salts, organic matter, and stress history on the geophysical properties of hydrate-bearing sediments. Experiments are designed to reproduce the state of effective stress in the field at the time of hydrate formation. A comprehensive set of instruments is deployed in this study, and the unprecedented development of electrical resistivity tomography for the study of hydrate formation and dissociation is also documented in detail. Results from this research have important implications for geophysical field characterization and monitoring processes such as production.

CHAPTER I

INTRODUCTION

1.1 INTRODUCTION

Clathrate hydrates consist of guest gas molecules inside hydrogen bonded water lattices. Gas hydrates were first reported by H. Davy in 1811 (Davy, 1811). E. G. Hammerschmidt detected hydrates clogging oil and gas pipelines in 1934 (Hammerschmidt, 1934); this discovery stimulated research interest in the identification of hydrate-forming gas molecules and the thermodynamic properties of hydrates. Y. F. Makogon found gas hydrates in the Siberian permafrost region in 1965, and C. Bily and J.W.L. Dick reported the presence of hydrates in a core extracted from the MacKenzie Delta in 1974 (Bily and Dick, 1974 and Sloan, 1998). The discovery of bottom simulating reflectors (BSR) as potential indicators of the existence of gas hydrates lead to active geophysical research to identify the locations and amounts of gas hydrates in sediments.

Natural gas hydrates are found in offshore and permafrost regions. The reported global estimation of gas hydrates ranges from 10^{13} m^3 to $10^{18}m^3$ (Trofimuk et al, 1977, McIver, 1981, Dobrynin et al, 1981, Meyer, 1981, MacDonald, 1990, and Ginsburg and Soloviev, 1995). These large amounts of reserves suggest the potential of gas hydrates as an energy resource if economically viable production methods are developed. Furthermore, the proper understanding of hydrate formation/dissociation is important to

drilling and oil production applications (Sloan, 1998). In addition, the dissociation of hydrates within sediments due to natural changes in seawater temperature or human activities may cause massive seafloor instabilities (Sultan 2004 and Vogt and Jung, 2002). More recent research explores utilization of gas hydrate to dispose of “green house” gases (Brewer et al., 1999 and Masuda, 1998).

1.2 THESIS ORGANIZATION

The mechanisms of hydrate formation and dissociation in sediments and the associated changes in properties of hydrate-bearing sediments are the central themes of this research. Chapter two documents a molecular-level study of the interaction between guest molecules, water molecules and mineral surfaces during hydrate formation. The purpose of this study is to confirm the potential similarities and differences between THF and methane hydrates in the context of hydrate-bearing sediments.

Chapter three is focused on theoretical analyses and experimental studies of hydrate nucleation and growth in marine sediments. The effects of salt-water interaction and mineral surface-water-hydrate interaction on nucleation and growth are emphasized.

Chapter four is an investigation of the elastic and electromagnetic properties of hydrate-bearing sediments. The comprehensive experimental study covers various types of sediments, effective confining stress levels, and hydrate fractions. The analyses of results are oriented towards field applications, including sediment assessment and process monitoring during destabilization.

Chapter five parallels the study in Chapter four but involves natural marine sediments from the Gulf of Mexico. The goal of the complementary study is to identify effects related to fabric and salt concentration. Pore scale analyses reveal the importance of the pore size and the pore fluid composition in equilibrium conditions.

Chapters six and seven document the development of an Electrical Resistivity Tomography (ERT) system as a new tool for the study of gas hydrate-bearing sediments. Emphasis is placed on the design of optimal electrode configurations to maximize signal to noise ratio, resolution of ERT, and the sensitivity of electrodes to conductivity changes in the specimen. Electrical resistivity monitoring of CO_2 hydrate formation and dissociation in sediments confirm that the ERT system can detect macro-scale hydrate nucleation and growth patterns.

Salient conclusions and recommendations for further studies are summarized in chapter eight.

CHAPTER II

OBSERVATIONS RELATED TO TETRAHYDROFURAN AND METHANE HYDRATE FOR LABORATORY STUDIES OF HYDRATE-BEARING SEDIMENTS

2.1 INTRODUCTION

Gas hydrate is a crystalline compound consisting of guest gas molecules encaged in water molecules. In nature, gas hydrates occur in the sediments of permafrost regions and continental margins, and methane is the most common guest molecule. The stability of gas hydrate depends on temperature, pressure, salinity, and other factors (e.g., soil characteristics). The difficulty of maintaining recovered natural samples at in situ temperatures (usually 0 to ~25ºC) and fluid pressures (typically 5 to 25 MPa) has been one of the key challenges in studying natural gas hydrate-bearing sediments. At the same time, the analysis of measurements obtained in hydrate-bearing provinces during borehole logging or exploration geophysical surveys (e.g., seismic prospecting) has been limited by the lack of high-quality calibrations of physical properties on synthetic laboratory samples with well-characterized lithology, hydrate saturation, and confining pressures.

Numerous laboratory studies have used sediments containing synthetic gas hydrates to investigate mechanical, thermal, and electromagnetic properties of both pure crystals and hydrate-bearing sediments (Cameron et al., 1990; Waite et al., 2002; Ebinuma et al., 2005; Priest et al., 2005; Santamarina et al., 2005; Winters et al., 2005; Yun et al., 2005, 2007). Unfortunately, the controlled synthesis of methane hydrate in

sediments is challenging owing to methane's low solubility in water and the prolonged time required to form hydrate from aqueous phase methane, which is the way that gas hydrate probably forms in deep sediments that are within (not at the boundaries of) the gas hydrate stability zone (e.g., Buffett and Zatsepina, 2000; Spangenberg et al., 2005). Forming methane hydrate in this way requires a source of methane within the sediment (e.g., microbes) and/or transport of methane via diffusional or advective processes.

Several alternative methods have been proposed to produce methane hydrate-bearing sediments, including flushing methane gas through partially saturated sediments, exploiting pre-existing ice cages, and using surfactants to increase the availability of the methane gas in water (Handa and Stupin, 1992; Stern et al., 1996; Zhong and Rogers, 2000; Waite et al., 2002; Lin et al., 2004; Waite et al., 2004). Each of these procedures produces different pore scale growth patterns (Zhong and Rogers, 2000; Ebinuma et al., 2005; Spangenberg and Kulenkampff, 2005) and differences in the macroscale behavior of sediments containing these hydrates (e.g., Yun et al., 2007). Detailed description on these synthesis methods is tabulated in Appendix A.

Tetrahydrofuran (C_4H_8O, hereafter THF) has long been used as a substitute for methane in laboratory studies (e.g., *Leaist et al*., 1982; *Handa*, 1984; *Rueff and Sloan*, 1985). The main advantage of THF relative to methane is THF's complete miscibility in water, which enables relatively rapid, homogeneous synthesis of THF hydrate in sediments and close control of the hydrate volume fraction. THF hydrate, unlike methane hydrate, also has the advantage of being stable at atmospheric pressure and easily achieved temperatures, making possible the use of standard soil cells and loading frames for laboratory experiments (Bondarev et al., 1996; Santamarina et al., 2005; Yun

et al., 2005, 2007). Finally, because THF hydrate does not dissociate to a gaseous phase, poroelastic complications associated with the formation of highly mobile, compressible gas can be avoided.

In recent years, the use of THF as a proxy for methane in studies of hydrate-bearing sediment properties has also been a source of controversy (Doyle et al., 2004), particularly owing to the polar nature of the THF molecule compared to the nonpolar nature of the methane molecule. This section of the thesis examines the differences and similarities between the interactions of methane and THF with water, salt, and mineral grains, the major components of natural sedimentary systems in which gas hydrate occurs.

2.2 COMPARISON OF KNOWN PROPERTIES

The properties of THF and methane molecules, their hydrates, and water ice are compiled in Table 2.1. The properties of methane and THF, the hydrate guest molecules are first compared. Methane, an alkane, consists of a carbon atom with four attached hydrogens that form a tetrahedral structure. As a cyclic ether, THF has ether oxygen as part of the ring. The THF molecule is ~1.5 times larger than the methane molecule and is completely miscible in water. Methane is a nonpolar molecule (dipole moment of zero), but the dipole moment of THF is as high as that of water. Yet the permittivity of THF is very low relative to water and approaches a value comparable to that for nonpolar fluids.

Table 2.1 Properties of methane and THF, their hydrates, and water ice.

Property	Methane	Tetrahydrofuran (THF)	Water ice
	Properties of guest molecule		
Molecular formula	CH_4	C_4H_8O	H_2O
Chemical structure	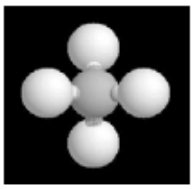	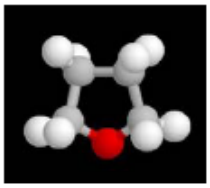	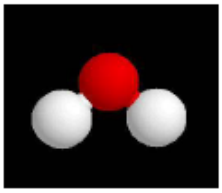
Molecular Size [Å]	4.36[1]	6.3[2]	~ 1.8[1]
Dipole moment [D]	0[3]	1.63[4]	1.85[3]
Molecular Polarizability [Å^3]	2.6[5]	7.9[6]	1.5[5]
Permittivity	1.7[7]	7.5[4]	80[3]
Density [kg m^{-3}] at 293.5K	N/A	888 [4]	1000[3]
Viscosity [cP] at 298.5K	N/A	0.46[4]	0.89[3]
Surface tension [N m^{-1}] at 293.5K	0.00676 at 140K[8]	0.028[4]	0.0728[3]
Solubility in water at 293.5K	0.04×10^{-3} [mole fraction][9]	Miscible[7]	N/A
	General Characteristics		
Hydrate structure	I	II	n/a
Hydrate cavity diameter [Å]	7.9, 8.66[1]	7.82, 9.46[1]	n/a
Ideal hydrate stoichiometric ratio	$CH_4.6H_2O$	$C_4H_8O.17H_2O$	n/a
Slope of phase transformation boundary at 10 MPa [K MPa^{-1}]	+0.96[1]	-0.08[10]	-0.01 [11]
	Thermal properties of the frozen state		
Heat capacity [kJ kg^{-1}K^{-1}] at 270K	2.07[12]	2.07[13]	2.10 [13]
Heat of dissociation [kJ kg^{-1}] at 273K	338.7[12]	262.9[13]	333.5[14]
Thermal conductivity [W m^{-1}K^{-1}]	0.5 @ 270 K[15]	0.5 @ 270 K[16]	2.2 @ 263 K[1]
Thermal diffusivity [m^2 s^{-1}]	3×10^{-7} @ 270 K[15]	2.8×10^{-7} @ 270 K[17]	8.43×10^{-7} @ 273 K[18]
Thermal linear expansivity [K^{-1}] at 200K	77×10^{-6} [1]	52×10^{-6} [1]	56×10^{-6} [1]
	Mechanical properties of the frozen state		
Density [kg m^{-3}] at 273 K	910[1]	~ 910[1]	917[1]
Interfacial Tension [J m^{-2}]	0.017[19]-0.032[20]	0.016-0.031[21]	0.029[19]-0.032[20]
Adiabatic Bulk Compressibility [Pa] at 273K	$\sim14\times10^{-11}$ [1]	$\sim14\times10^{-11}$ [1]	12×10^{-11}[1]
Isothermal Young's Modulus [Pa] at 268K	$\sim8.4\times10^9$ [1]	$\sim8.2\times10^9$ [1]	9.5×10^9[1]
Shear wavespeed V_s [m s^{-1}]	1950[22]	1890[23]	1950[24]~1990[25]
Compressional wavespeed V_p [m s^{-1}]	3370[23] ~ 3800[22]	3670[23]	3890[24]~3910[25]
Strength [MPa]	2 to 10[26]	0.9 to 44[27]	0.6 to 1[26]
	Electrical properties of frozen state		
Electrical conductivity [S/m]	~0.01[28]	0.01	0.01[29]
Dielectric constant at 273K	~2.5[28]	4.3	2.8[29]

[1]*Sloan* [1998]; [2]*Dyadin et al.* [1999]; [3]*Lide* [2003]; [4]*Smallwood* [1996]; [5]*Atkins* [1978]; [6]*Davidson et al.* [1986]; [7]*Carey* [1987]; [8]*Upstill and Evans* [1977]; [9] At 0.1 MPa and 278.15K from *Handa* [1990]; [10]*Circone et al.* [2003]; [11]*Florusse et al.* [2004]; [12] *Handa* [1986]; [13]*Handa et al.* [1984]; [14]*Petrenko and Whitworth* [1999]; [15]*deMartin* [2001]; [16]*Ross et al.* [1981]; [17] Thermal diffusivity of tetrahydrofuran hydrate is estimated from published thermal conductivity and heat capacity values; [18]*Hobbs* [1974]; [19]*Uchida et al.* [2002]; [20]*Anderson et al.* [2003]; [21] Estimated from data in *Zakrzewski and Handa* [1993] assuming cylindrical and spherical geometry; [22]*Helgerud et al.* [2003b]; [23]*Kiefte et al.* [1985]; [24]*Helgerud et al.* [2003a] ; [25]*Gagnon et al.* [1987]; [26]At 50 MPa confining pressure and 270 K for methane hydrate and the same confining pressure and 260K for ice, from *Durham et al.* [2005]; [27]Measured with no confinement and at 276K by *Ohmura et al.* [2002]; [28]*Galashev et al.* [2006]; [29]*Shi et al.* [2005].

In terms of hydrate properties, THF hydrate forms as Structure II, with THF filling only large cavities. In contrast, methane hydrate most commonly occurs as Structure I with methane filling both large and small cavities. Despite these structural differences, a comparison of the macroscale mechanical and electrical properties and some thermal properties (e.g., heat capacity, thermal conductivity) of the two hydrates reveals gross similarities (Table 2.I), particularly when each property is considered within the range of values attained in marine or permafrost sediments. On the other hand, there are important differences in thermal expansivity, the heat of dissociation, and the degree to which equilibrium temperature depends on pressure for the two hydrates.

2.3 DIPOLE MOMENT EFFECTS

The polar nature of the THF molecule (relatively large dipole moment) compared to the nonpolar methane molecule has led to concerns about the potential interaction of THF with water and THF hydrate with sediments. Each of these issues is discussed next in detail.

2.3.1 THF-Water Interaction

As mentioned above, the dipole moment of the THF molecule is similar to that of water, but its permittivity is much smaller. The molecular dipole moment μ [Debye = C·m] is determined by the geometric arrangement of charges in a molecule while the permittivity is a measure of macroscale polarizability per unit volume (Santamarina et al., 2001). The orientational polarization P [Debye = C·m] reflects μ and the number of

molecules per unit volume N, as well as the competing effects between the externally imposed electric field E and the randomizing thermal motion at temperature T [K]. The relationship among these parameters is captured in Atkins (1978):

$$P = \frac{N\mu^2}{3kT} E = \varepsilon_o \left(\kappa' - 1\right) E, \tag{2.1}$$

where k is Boltzmann's constant [1.38×10^{-23} J/K], ε_o is the elementary charge [1.602×10^{-19} C], and κ' is the relative permittivity. The permittivities of water and THF are related as:

$$\frac{\kappa'_{water} - 1}{\kappa'_{THF} - 1} = \frac{P_{water}}{P_{THF}} = \frac{N_{water} \mu_{water}^{\ 2}}{N_{THF} \mu_{THF}^{\ 2}}. \tag{2.2}$$

Using values from Table 2.1, the polarization ratio is $P_{water}/P_{THF} \cong 11$, which is similar to the ratio of measured permittivities $\left(\kappa'_{water} - 1\right)/\left(\kappa'_{THF} - 1\right) = 12$, as shown for microwave complex permittivity spectra in Figure 2.1. Therefore, molecular size, which is captured by N in (2.1), must be considered in conjunction with the molecular dipole moment for the analysis of the macroscale behavior of THF.

Hydrogen bonds between water molecules are responsible for the interaction between water and other fluids (e.g., THF) and for the activity of water, which is closely related to phase equilibrium conditions (Luck, 1973). Among organic compounds, alcohol and ether form hydrogen bonds with water, which explains the high miscibility of these fluids. As a cyclic ether, the oxygen of a THF molecule uses one of its unshared electron pairs to accept a proton from a water molecule to form a hydrogen bond (Carey, 1987). However, the interaction between THF and water molecules is relatively weak compared to water-water interaction, and water clusters formed by the hydrogen-bonded water network are preserved around THF molecules (Fukasawa et al., 2004; Ohtake et al.,

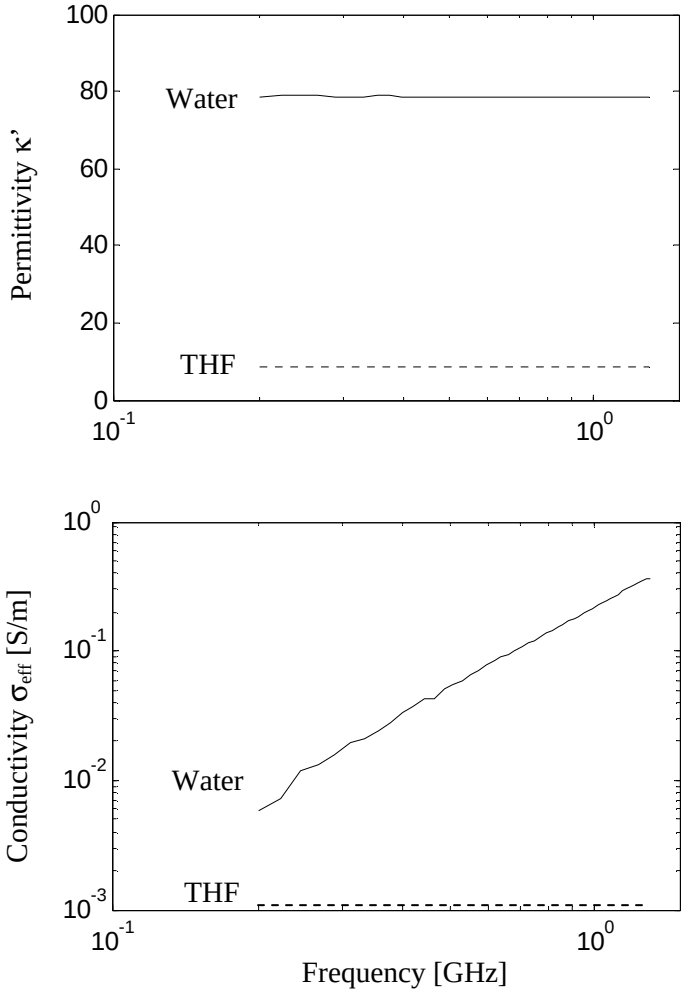

Figure 2.1 Frequency-dependent electrical properties of liquid water and liquid THF: (a) Permittivity and (b) Electrical conductivity. The conductivity of THF is below the detection limit for the instruments.

2005; Takamuku, 2003). Thus, THF's capacity to form hydrogen bonds does not play a crucial role in hydrate formation, and THF molecules essentially behave as nonpolar molecules.

2.3.2 Fluid-Salt Interaction

Salts are often present in natural systems as precipitates in sediments or in a dissolved phase in pore fluids. Polar solvents like water can dissolve ionic compounds through thermal agitation and ion-dipole interactions, even though the ion-dipole interaction is weaker than ion-ion interaction. The dissolution of salts by water starts with the alignment of the polar water molecules near ions, with H-ends toward anions and O-ends toward cations. The small water molecules gradually position themselves between surface anions and cations, weaken the ion-ion attraction forces, and eventually pull ions away from the crystal. This sequence of events shows the relevance of polarity and molecular size for the ability of a fluid to dissolve salt. For reference, Figure 2.2 illustrates the relative sizes of the sodium chloride, tetrahydrofuran, and water molecules.

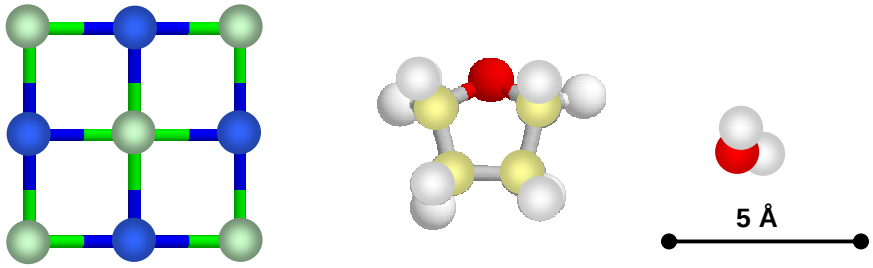

(a) (b) (c)

Figure 2.2 Ball-and-stick representation showing the relative sizes of the (a) sodium chloride; (b) tetrahydrofuran; and (c) water molecules

A key question is whether fluids that contain large polar molecules (e.g., THF) can also dissolve salt. We devised a simple, yet robust, experiment to evaluate the effect of molecular polarity and size on the ability of a fluid to dissolve salt. Three fluids were considered for the study of salt-fluid interactions: water (small polar molecule, high permittivity), THF (large polar molecule, low permittivity), and benzene (nonpolar molecule, low permittivity). The relevant properties of benzene are molecular size of 5.36 Å, zero dipole moment, molecular polarizability of 10.32 $Å^3$, permittivity of 2.28, density of 879 kg m^{-3} at 293.5K, viscosity of 0.65 cp at 298.5K, surface tension of 0.0289 N m^{-1} at 293.5K, and solubility of 0.18 kg kg^{-1} of water at 293.5K (Atkins, 1978; Smallwood, 1996; Yoshida et al., 2005).

Table salt (7g of NaCl) was thoroughly mixed in 50 ml of each liquid. The mixture was then filtered through P5 (5-10 μm) filter paper, and the retained salt was oven-dried and weighed. Within the precision of these measurements, the results show that THF (κ'=7.52) and benzene (κ'=2.28) do not dissolve NaCl (> 99% of the salt retained in solid form) while water (κ'=80) dissolves NaCl completely (no salt retained)

Under the microscope, the salt crystals that had been mixed with benzene had intact crystal surfaces (Figure 2.3b), indicating that the benzene did not react with the salt. The crystal surfaces of the salt mixed with THF showed flakes of precipitated butylated hydroxytoluene (BHT, $C_{15}H_{24}O$), which is added to THF at 0.2g/L to prevent peroxide formation during storage (Figure 2.3c), but revealed no indication of dissolution. To confirm whether the observed flakes were BHT, the same experiment was repeated with excess BHT (250 g/L) added to the THF, producing extensive BHT precipitation on salt grains (Figure 2.3d).

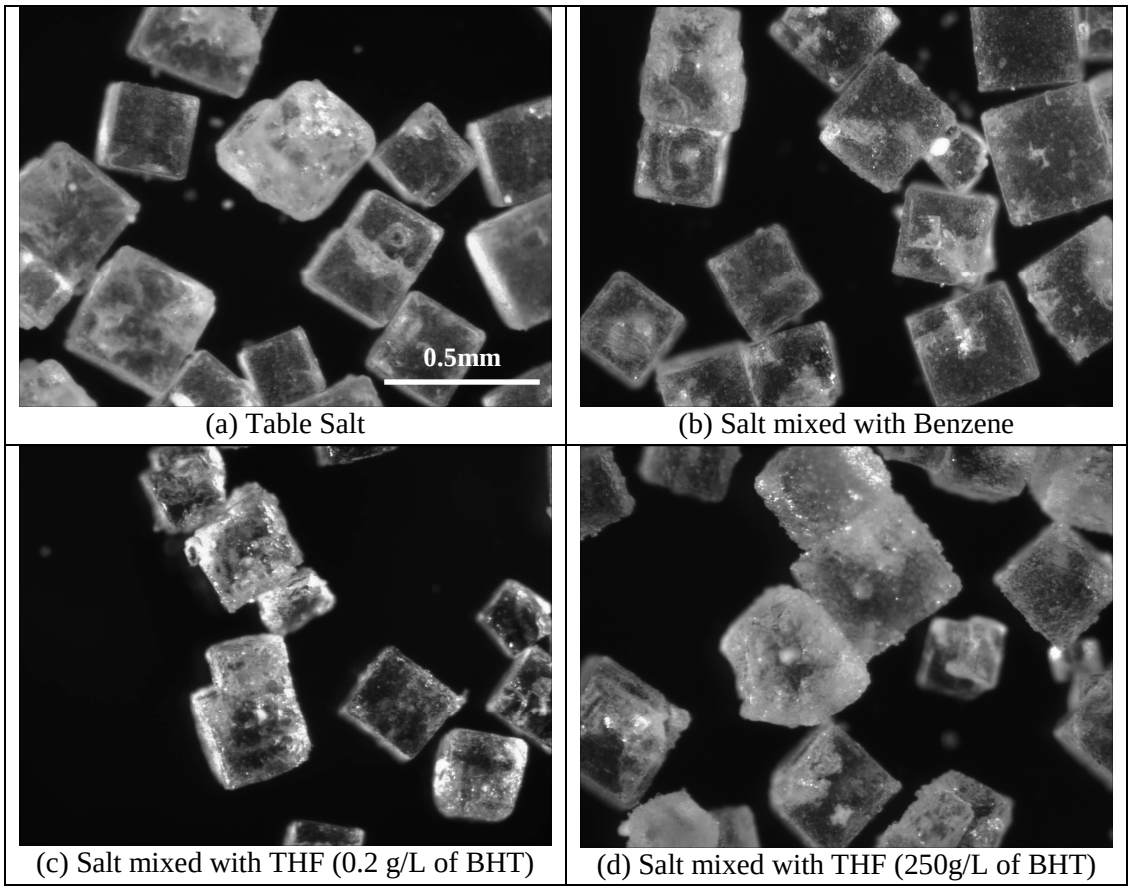

(a) Table Salt

(b) Salt mixed with Benzene

(c) Salt mixed with THF (0.2 g/L of BHT)

(d) Salt mixed with THF (250g/L of BHT)

Figure 2.3 Optical microphotographs of NaCl salt: (a) oven-dried, (b) mixed with benzene and oven-dried; (c) mixed with THF and oven-dried; and (d) mixed with THF with excess BHT and oven-dried.

These results suggest that the case of dispersed ions surrounded by oriented THF molecules is not entropically favored over a salt crystal surrounded by randomly oriented THF molecules. Yet, while THF cannot dissolve ionic crystalline compounds like salt, there is evidence that THF can solvate pre-existing free ions (Nishinaga et al., 2003). This implies ion-dipole interaction that is much weaker than the ion-ion interaction in the salt crystal, yet possibly stronger than the Debye interaction of ion to polarized molecule in the case of free ions and methane.

2.3.3 Fluid-Mineral Interaction

Understanding the interaction of fluids with mineral surfaces is critical for the study of hydrate-bearing sediments. Hence, we extended the previous experiments to examine the solvation of ions on dry minerals by the three selected fluids.

Charged mineral particles and absorbed ions near mineral surfaces lower the activity of water (Hobbs, 1974). The formation of electrical double layers on mineral surfaces reflects the balance between the thermal activity and the electrical forces that develop among fluids, ions, and charged mineral surfaces. The characteristic scale of the double layer is determined by the ionic concentration of pore fluids c_o [mol m^{-3}], ionic valence z, temperature T [K], and permittivity κ' (Mitchell and Soga, 2005). The thickness of a double layer is

$$\theta = \sqrt{\frac{\varepsilon_0 k}{2e_0^{\,2} N_{av}} \frac{\kappa' T}{c_0 z^2}}, \tag{2.3}$$

where N_{av} is Avogadro's number [$6.023 \cdot 10^{23}$ mol^{-1}]. Thicker double layers imply higher interparticle repulsion forces for a given interparticle distance and lower probability of particle aggregation by van der Waals attraction (Santamarina et al., 2001).

We investigated the interaction between each of the three fluids and mineral surfaces using two indirect experimental methods. The first was a sedimentation test, a low solid-fraction experiment that provides insight into incipient fabric formation. The second is the standardized liquid limit test, which is a high solid-fraction experiment frequently used in geotechnical testing to elucidate the effect of the pore fluid character on the interaction among mineral particles in sediments. Both tests were run with bentonite because of its high specific surface (226 m^2 g^{-1}). Particle-to-particle interactions in high specific surface substances are controlled by electrical forces, which in turn reflect fluid-mineral interaction.

2.3.3.1 Sedimentation

Particle-fluid interaction can be inferred from the settling behavior of sediment suspensions. While Stokes sedimentation of single particles is controlled by particle size and fluid viscosity, the sedimentation of suspensions composed of submicron-sized particles such as bentonite is governed by electrical interparticle forces.

Bentonite (2.5 g) was thoroughly mixed with each fluid (50 ml) in graduated cylinders, and then left to sediment. The height of the suspension-water interface and sedimentation characteristics were monitored with time, as shown in Figure 2.4. Sedimentation ended within 10^2 s in benzene and in THF, with only a few fine particles remaining in suspension for longer time in THF. In contrast, bentonite remained suspended in water even after 10^6 s.

Using the evaluation criteria in Palomino and Santamarina (2005), the observed sedimentation behavior clearly contrasts dispersed sedimentation in water with

aggregated sedimentation in THF and benzene. In water, the suspended particles are dispersed due to the large double layer repulsive forces between particles. In THF and benzene, unsolvated, adsorbed ions shield the clay charge, van der Waals attraction prevails, and particle aggregation occurs followed by fast sedimentation. These results indicate that, despite the polar nature of the THF molecule, its interaction with minerals and its ability to solvate ions on mineral surfaces resemble that of nonpolar molecules such as benzene.

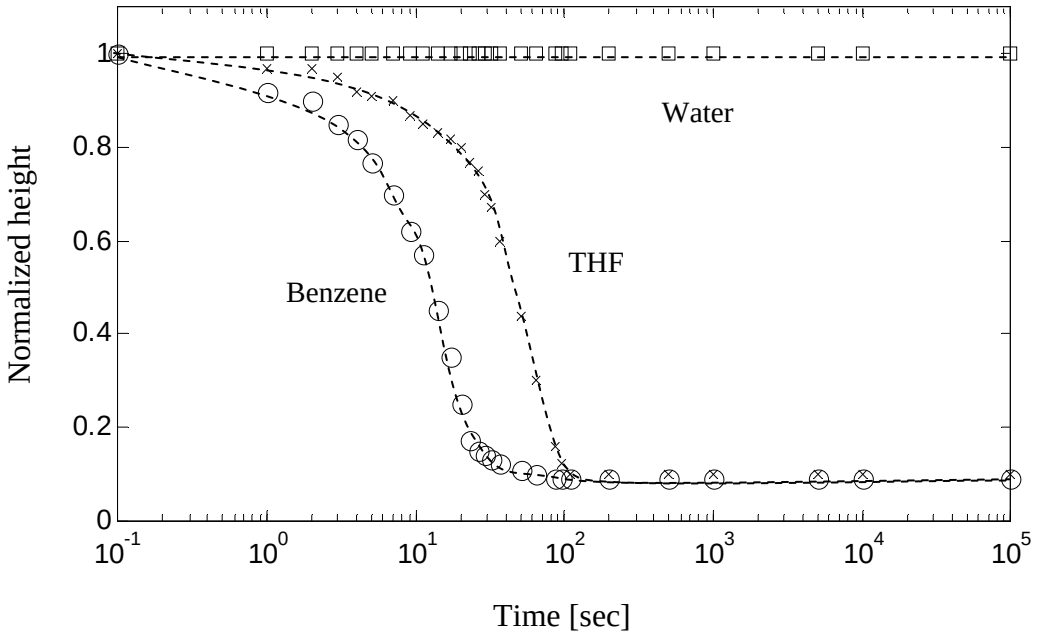

Figure 2.4 Sedimentation curves for water-bentonite, THF-bentonite, and benzene-bentonite mixtures.

2.3.3.2 Liquid Limit

The liquid limit test is used to determine the water content associated with changes in the rheological behavior of a paste from that of a viscous liquid to a plastic solid. The liquid limit is affected by the specific surface of particles, fluid-mineral interaction, and the resulting soil fabric. High specific surface, thick double layers, and flocculated fabrics lead to higher liquid limits.

The liquid limit of bentonite mixed with each of the three liquids was determined using the standardized fall cone test, which consists of a free-falling stainless steel 80 g cone with a 30^{o} apex into the specimen (British Standards Institute, 1990). The cone is released at the soil surface and penetrates the soil paste until it comes to rest. The test is repeated for different fluid mass fractions. The liquid limit is the fluid content at which the cone penetrates 20 mm.

As shown in Figure 2.5, small changes in fluid content produced large variations in cone penetration depth when mixtures were prepared with either THF or benzene. The results for water, THF, and benzene were 302%, 69%, and 57%, respectively. This confirms the nonpolar, benzene-like interaction between THF and bentonite.

The soil-fluid pastes were oven-dried after the liquid limit tests, and the cohesiveness of the dried specimens was assessed by indenting them with a blade. The dried water-bentonite mixture was strong and behaved like stiff cemented soil, whereas the dried THF-bentonite mixture maintained its shape but readily crumbled into powder when disturbed. The dried benzene-bentonite mixture had changed back to powder. The cohesiveness of the oven-dried water-bentonite paste suggests that ionic bonding had developed between particles by sharing of dissolved ions while in wet conditions. On the

other hand, the slight bonding that remains in the dried THF-bentonite paste might reflect minor interaction among THF, ions, and mineral surfaces, or more likely, the contribution of the precipitated BHT.

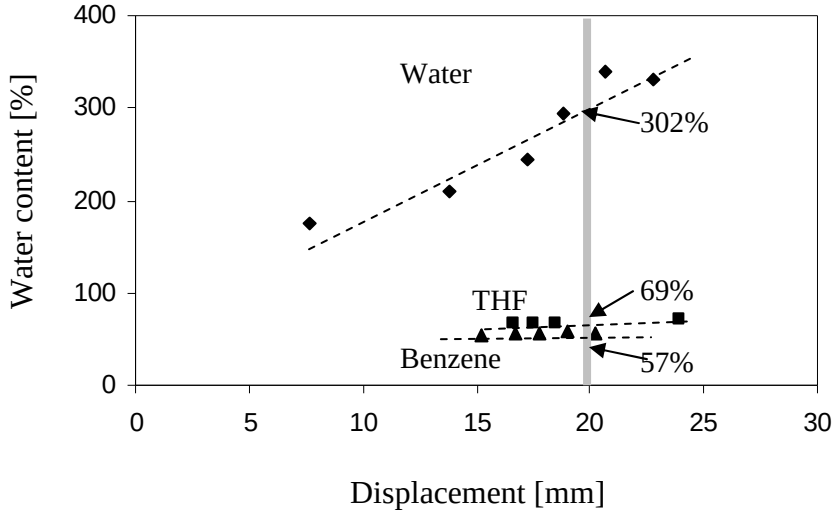

Figure 2.5 Fall cone penetration lines for water-bentonite, water-THF, and water-benzene mixtures. The vertical line indicates the displacement (20 mm) at which liquid limit is assessed.

Overall, the evaluation of sedimentation characteristics, liquid limits, and dry paste strengths for the bentonite-liquid mixtures confirms that the interaction of THF with fine particles much more closely resembles that of benzene (nonpolar) than that of water (polar). These observations support the contention that THF behaves like methane (nonpolar) in the presence of sediment particles.

2.4 HYDRATE FORMATION IN SEDIMENTS

After nucleation, the evolution of gas hydrate in porous media is prescribed by the Young-Laplace and the Gibbs-Thompson equations (Clennell et al., 1999). Within experimental variability, the interfacial tension between hydrate and water is similar for both THF and methane hydrate (Table 2.1), implying that similar growth patterns should be expected in water-saturated sediments. Beyond these similarities, guest molecules and cavity types can affect mechanical properties of hydrate-bearing sediments (Durham et al., 2005). In practice, though, factors such as transport parameters (e.g., cooling rate, diffusion rate for heat of transformation and excluded ions, and, for methane hydrate, the rate of guest molecule diffusion) and the spatial distribution of hydrate in the pore space have a greater impact on measured mechanical properties.

The distribution of hydrates in pore space depends strongly on the hydrate formation history. For example, water in partially saturated sediments tends to accumulate near contacts (pendular regime); therefore, flooding with gas to trigger hydrate formation (e.g., Handa and Stupin, 1992) in such a system leads to preferential hydrate formation at contacts (Waite et al., 2004; Winters et al., 2004; Ebinuma et al., 2005; Masui et al., 2005). The version of the ice seed method used by Priest et al. (2005) involves the introduction of ice and melt prior to pressurizing, making it close to the unsaturated method, and produces a similar effect. On the other hand, the Stern et al. (1996) ice-seeding method causes hydrate to preferentially replace ice (Ebinuma et al., 2005) in pore space, even though water from melting ice may also migrate to grain contacts if hydrate formation takes place at a rate lower than ice melting (Valiullin and

Furo, 2002; Priest et al., 2005). In contrast, THF hydrate forms from the combination of dissolved THF molecules and water molecules, much as methane hydrate probably forms in deep sediments under natural conditions (Buffett and Zatsepina, 2000). Previous studies with THF hydrate in water-saturated porous media suggest that nucleation occurs at particle surfaces and that hydrate crystals then grow into the pore space (Yun et al., 2005).

The differences in the spatial distribution of hydrates induced by different formation histories affect the stiffness and strength of sediments as well as the bulk conduction properties. For example, the small-strain stiffness and shear strength increase dramatically even with small hydrate saturations in sediments in which hydrate is synthesized by gas flooding sediments with initially low water saturation (Waite et al., 2004; Winters et al., 2004). From the discussion above, the ice-seeding method produces different results depending on its implementation (Ebinuma et al., 2005; Masui et al., 2005; Priest et al., 2005). The small-strain stiffness does not increase significantly at low hydrate concentration in sediments when hydrate is synthesized by flushing water containing aqueous phase methane (Spangenberg and Kulenkampff, 2005) through initially saturated sediments or by forming hydrate from dissolved THF (Yun et al., 2005, 2007). Thus, it appears that the hydrate formation method is likely more important than the hydrate former in controlling some of the properties of the hydrate-bearing sediment.

2.5 CONCLUSIONS

Despite a dipole moment close to that of water, THF has permittivity as low as

that of nonpolar molecules owing primarily to the large size of the molecule. In turn, molecular size hinders THF from hydrating salts or mineral surfaces; therefore, the overall behavior of THF in sediments resembles that of a nonpolar fluid. The fact that THF is a polar molecule while methane is not appears to have little relevance for assessing the differences between sediments containing THF hydrate versus those containing methane hydrate.

Despite its polar nature, THF forms weaker hydrogen bonds with water than the water molecules form with each other, meaning that THF has only limited impact on the hydrogen-bonded water network. The available data also indicate that the interfacial tension, a factor important in hydrate growth in pore space between water and either THF or methane hydrate is similar.

Laboratory formation history and ensuing pore-scale spatial distribution likely have a more pronounced effect on the macroscale mechanical properties of hydrate-bearing sediments than differences between THF and methane hydrates themselves. Nevertheless, the analysis of results gathered with THF hydrate-bearing sediments as a proxy for methane hydrate-bearing sediments should still take into consideration the inherent differences between these hydrates, particularly with regard to kinetics.

CHAPTER III

HYDRATE NUCLEATION IN POROUS MEDIA

The kinetics of hydrate formation has been studied to elucidate inhibiting or promoting mechanisms in hydrate formation. Natural gas hydrates form in seafloor and permafrost sediments. The role of mineral surfaces and pore characteristics on gas hydrate formation has been investigated in previous studies (Cha et al. 1988; Clennell et al. 1999; Englezos and Hall 1994; Ouar et al. 1992; Riestenberg et al. 2003). The purpose of this chapter is to further address the understanding of hydrate formation in bulk water, on mineral surfaces, and within sediment pores through theoretical and experimental investigations.

3.1 THEORETICAL BACKGROUND

The nucleation of solid phase from bulk fluids without impurities often occurs at temperatures below the equilibrium temperature. For example, ice nucleation in pure water occurs between -36ºC and -42ºC (Pound et al. 1953). Nucleation is governed by T/P conditions, cooling rate, time, degree of disturbance, and thermal history of the liquid. Nucleation starts with lower supercooling and within a shorter induction time when impurities are present. The effect of impurities depends on the characteristics of foreign particles, and on the interfacial energy between the liquid and the solid. The nucleation temperature and the induction time exhibit stochastic behavior, therefore, their

predictability is limited (Sloan 1998) and experimental results are often reported in statistical terms.

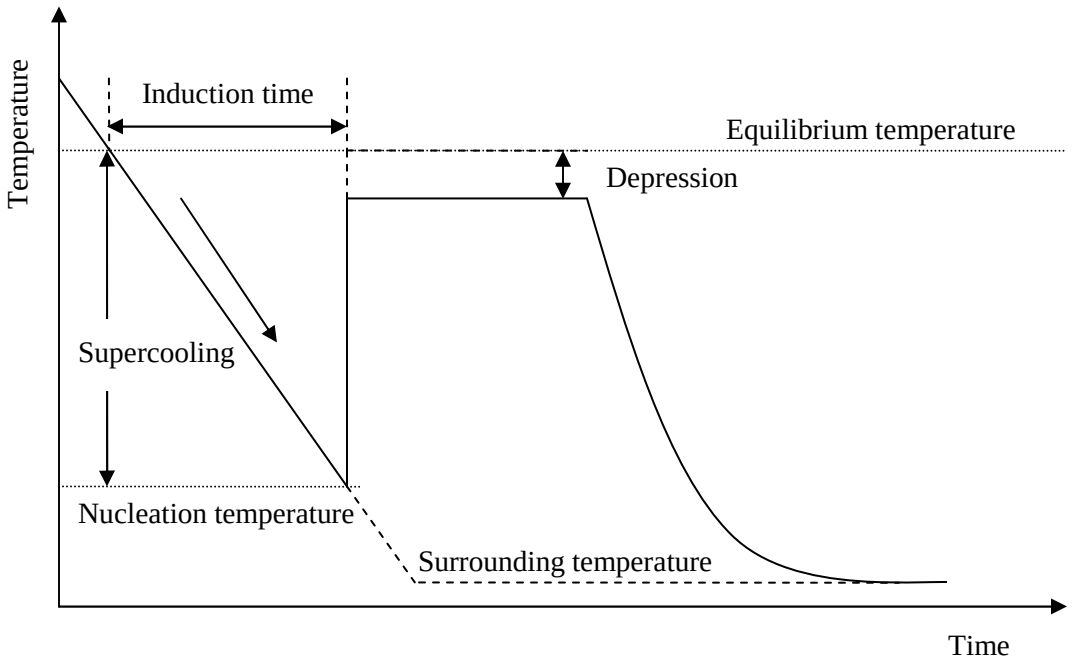

Figure3.1 Supercooling and equilibrium temperature depression

Table 3.1 Enhancing or inhibiting factors in hydrate nucleation and growth

	Description	Reference
Enhancement		
Thermodynamic	**Mixed guest molecules**	(Khokhar et al. 1998; Tsuji et al. 2005; Tsuji et al. 2004; Gnanendran et al. 2005)
	1,4-dioxine	(Gnanendran et al. 2005, Jager et al. 1999)
	Bovine Serum Albumin: Lower the surface tension of water at gas-water interface (the experiments were performed at one T/P condition and shorter induction time observed. But the mechanism should be regarded as a thermodynamic enhancer)	(Dick and Servio 2005)
Kinetic	**Particles**: Provide preferable nucleation sites - **Inorganic** AgI, $AgNO_3$, Ag_2S, PbI_2 : Crystal properties are similar to that of ice	(Hobbs 1974)
	Bentonite, momorillonite, kaolinite: The layer of water adsorbed on the particle surface resembles 2-D layer of ice	(Edwards et al. 1970; Hobbs 1974; Riestenberg et al. 2003; Roberts and Hallett 1968)
	-**Organic** Snow Max (Commercial product name) α-phenazine, phloroglucinol dehydrate, tetra-chloro-phthalic anhydrate, and etc.	(Evans 1967; Hobbs 1974)
	Memory Effect: Dissociated water has memory of previous cluster structure, and induction time is reduced during refreezing	(Bishnoi and Natarajan 1996; Moon et al. 2003; Vysniauskas and Bishnoi 1983)
	Mechanical Impact: Agitation, mechanical shock, and friction often induce nucleation.	(Mullin 2001; Skovborg et al. 1993; Young 1911; Young and Cross 1911; Young and Van Sicklen 1913)
	Degree of supercooling: higher the degree of supercooling, smaller induction time	(Natarajan et al. 1994; Skovborg et al. 1993)
	Stirring Effect: Stirring makes larger gas-water interfaces	(Tajima et al. 2005)
	Surfactants: Enhance gas solubility in water by lowering interfacial tension	(Lin et al. 2004; Zhong and Rogers 2000)
Inhibition		
Thermodynamic	**Salts**: lowers activity of water by ionic and Van der Waals interaction	(Berecz and Balla-Achs 1983; Dickens and Quinby-Hunt 1997; Englezos and Hall 1994; Sloan 1998)
	Methanol, Ethanol, Ethylene glycol, and etc.	(Gnanendran et al. 2005)
	Capillary effect: due to the presence of curved hydrate-water interfaces	(Clennell et al. 1999; Everett 1961; Handa et al. 1992)
	Polymer-based chemicals	(Lee and Englezos 2005)

3.1.1 Supercooling and Equilibrium Temperature Depression

A liquid can be cooled below its equilibrium temperature without phase transformation; this phenomena is called 'supercooling' (Figure 3.1). When a phase changes from liquid to solid, the atoms become arranged in the characteristic configuration of the solid. Supercooling takes place while molecules rearrange prior to phase transformation. In this metastable state, nucleation occurs preferentially on surfaces. With time, the number of nuclei increases rapidly and phase transformation in a supercooled liquid may appear to be "spontaneous" (Mires and Issac 1906).

The equilibrium temperature T_{eq} during phase transformation can be altered by the ionic concentration of the pore fluid, charged particles, and capillary effects. Factors that affect supercooling and the equilibrium temperature in hydrate formation/dissociation are summarized in Table 3.1.

3.1.2 Hydrate Formation in Bulk Water

A discussion on the effect that various factors exert on hydrate formation in bulk water follows.

Salt Effect: Salts depress the equilibrium temperature of hydrate formation by competing with guest gas molecules for available water molecules. Salts ionized in water lower the activity of water through strong coulombic attraction rather than hydrogen or Van der Vaals bonds. In other words, water-ion attraction is stronger than water-water attraction in hydrate structures, thus hydrate formation is inhibited. Furthermore, salts decrease the solubility of guest gas molecules in water. This is known as 'salting out' effect. Strong

inhibition due to salting out have been found in several experiments (Englezos and Hall 1994).

Memory Effect: Reduced induction time is observed when previously frozen and melted water is used for phase transformation experiments (Bishnoi and Natarajan 1996; Vysniauskas and Bishnoi 1983). This phenomenon is called "memory effect" and suggests that the structure of water molecules is not completely disordered after hydrate dissociation, and the remaining water structures facilitate hydrate re-formation.

Mechanical Impact: Agitation, mechanical shock, and friction often induce nucleation. For example, vigorous agitation allows only about 0.5 ºC of supercooling before nucleation, whereas very pure and quiescent water can be supercooled to as low as -40 ºC (Mullin 2001). The nucleation rate is not proportional to the magnitude of the disturbance (Mullin 2001; Young and Cross 1911): once the impact amplitude reaches a certain threshold value, higher intensity does not make much difference on the nucleation rate.

3.1.3 Hydrate Formation on Mineral Surfaces

Mineral surfaces prompt the alignment of nearby water molecules and lower their thermal agitation so nucleation is often favored on mineral surfaces. Also, mineral surfaces alter the surface energy of embryos and offer favorable nucleation sites (Cha et al. 1988; Englezos and Hall 1994; Fisher et al. 1949; Fletcher 1958; Ouar et al. 1992; Riestenberg et al. 2003).

The Gibbs free energy difference ΔG^* due to an embryo formation in the presence of foreign particles varies according to the particle character: particle size, the chemical nature of particles, crystallography, and surface charges (Fletcher 1969); the contact

Table 3.2 Gibbs free energy difference ΔG* for embryos in bulk water, on a plane surface, and on a spherical particle

Nucleation in bulk water (Turnbull and Fisher 1949)

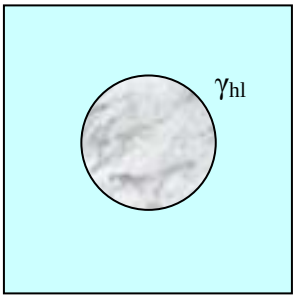

$$\Delta G^* = \frac{16\pi v_h^2 \gamma_{hl}^3}{3\Delta\mu_{hl}^2}$$

v_h [m^3]: the molar volume of hydrate, γ_{hl} [$J \cdot m^{-2}$]: the interfacial tension between hydrate and liquid, and $\Delta\mu_{hl}$ [$J \cdot mol^{-1}$]: the difference in chemical potential of water in hydrate and liquid phases.

Nucleation on a plane surface (Kashchiev and Firoozabadi 2002)

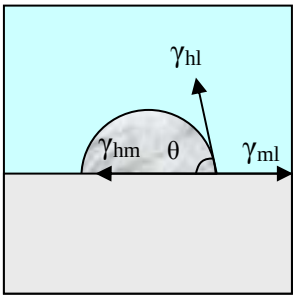

$$\Delta G^* = \frac{16\pi v_h^2 \gamma_{hl}^3}{3\Delta\mu_{hl}^2} \times \left[\frac{1}{4}(2+\cos\theta)(1-\cos\theta)^2\right]^{\frac{1}{3}}$$

$$\cos\theta = \frac{\gamma_{ml} - \gamma_{mh}}{\gamma_{hl}} \qquad \text{(Young's equation)}$$

γ_{ml} [$J \cdot m^{-2}$] is the interfacial tension between mineral surface and liquid and γ_{hm} [$J \cdot m^{-2}$] is the interfacial tension between hydrate and mineral surface

Nucleation on a spherical particle (Fletcher 1958)

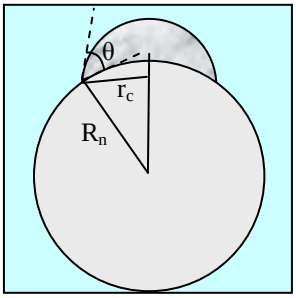

$$\Delta G^* = \frac{16\pi v_h^2 \gamma_{hl}^3}{3\Delta\mu_{hl}^2} \times f(m,x)$$

$$f(m,x) = \frac{1}{2}\left[1 + \left[\frac{1-mx}{g}\right]^3 + x^3\left[2 - 3\left(\frac{x-m}{g}\right) + \left(\frac{x-m}{g}\right)^3\right] + 3mx^2\left[\frac{x-m}{g} - 1\right]\right]$$

$$g = \left(1 + x^2 - 2mx\right)^{0.5},\ m = \cos\theta,\ x = \frac{R_n}{r_c},\ \text{and}\ r_c = \frac{2v_h\gamma_{hl}}{\Delta\mu_{hl}}$$

R_n [m]: Mineral Particle radius
r_c [m]: Radius of Critical Embryo

angle between liquid, gas hydrate, and particles captures some of these effects. Models for the variation in ΔG^* due to the presence of mineral surfaces are tabulated in Table 3.2 (Fletcher 1958; Kashchiev and Firoozabadi 2002). The first model is for nucleation in bulk solution, and ΔG^* is a function of the chemical potential $\Delta\mu_{hl}$ and the hydrate-liquid interfacial tension γ_{hl}. The second model is for nucleation on a plane mineral surface, and ΔG^* is also a function of the contact angle θ of hydrate on mineral surface as well as $\Delta\mu_{hl}$ and γ_{hl}. The third model is for nucleation on a spherical mineral surface, and ΔG^* is also governed by the spherical particle radius R_n and the embryo radius r_c as well as by θ, $\Delta\mu_{hl}$, and γ_{hl}.

Interfacial Tension: The interfacial interaction between hydrate, liquid, and minerals defines the contact angle a hydrate embryo forms on a surface (Young's equation in Table 3.2). Typically, the surface energy on an embryo due to the hydrate-liquid interfacial tension γ_{hl} [$J \cdot m^{-2}$] in bulk water is altered when the embryo is surrounded by both water and mineral surface. The increase in the hydrate-liquid interfacial tension γ_{hl} or mineral-hydrate interfacial tension γ_{mh} decreases the contact angle and thus increases the nucleation rate (See the figure in Table 3.2)

Particle Size: Particle size influences ΔG^* by affecting the contact area between mineral surface and embryo and embryo size in pores (Table 3.2). The nucleation rate increases as the particle size increases and reaches an asymptote at D_{50}= 0.01 ~ 0.1 μm (Fletcher 1958; Fletcher 1960; Hobbs 1974). Consequently, differences in nucleation rate due to particle size vanish for larger particles.

Particle Crystallography: An embryo is strained due to a crystallographic misfit between an embryo and mineral surfaces. Therefore, mineral surfaces that more closely mimic the

crystal structure favor nucleation (Blackwell 1998; Turnbull and Vonnegut 1952). Also, any substance which orients the ice dipoles parallel to one another is a poor ice nucleating agent. For example, basal planes are inadequate nucleating surfaces, but prismatic faces are better locations in ice nucleation on hexagonal materials with lattice dimensions similar to that of ice (Fletcher 1959).

Surface Roughness: Steps and corners on particle surfaces are favored nucleation sites since the number of mineral surface planes in contact with an embryo increases. The role of roughness gains relevance when particles are larger than 0.01μm (Hobbs 1974). The presence of steps or corners reduces the free energy ΔG^* as follows (Fletcher 1969):

$$\Delta G_1^* = \Delta G_0^* \left[(1-m)/2 \right] \qquad \text{Surface} \qquad (3.1)$$

$$\Delta G_2^* = \Delta G_0^* \left[(1-m)/2 \right]^2 \qquad \text{Step} \qquad (3.2)$$

$$\Delta G_3^* = \Delta G_0^* \left[(1-m)/2 \right]^3 \qquad \text{Corner} \qquad (3.3)$$

where ΔG_0^* is the Gibbs free energy difference of an embryo in bulk water, and m is $\cos\theta$. For a sphere with a conical pit, ΔG^* becomes (Fletcher 1969).

$$\Delta G^* = \Delta G_0^* f(m,x) - \alpha R^2 (1-m) \gamma_{hl} \qquad (3.4)$$

where αR^2 is the area of the conical pit on the spherical particle.

3.1.4 Hydrate Formation in Pores

Pores can affect the equilibrium and nucleation kinetics in various ways. Pores may prevent nucleation by restricting the embryo size in extremely small pores; this manifests as supercooling during hydrate formation. Capillary suction in unsaturated conditions lowers the pressure in pores and hampers nucleation (Clennell et al. 1999). In saturated conditions, the equilibrium temperature decreases due to the increased pressure

on the hydrate phase induced by the curvature of the hydrate-liquid interface (Anderson et al. 2003; Clennell et al. 1999; Handa et al. 1992; Ostergaard et al. 2002; Wilder et al. 2001).

3.2 EXPERIMENTAL STUDY

Experiments are designed to study the influence of salts, mineral surfaces, and pores on nucleation and equilibrium temperatures. Materials selected for these experiments are described first, followed by devices, specimen preparation, and test procedures.

3.2.1 Materials

THF is used as the hydrate former in this study. The equilibrium temperature during THF hydrate formation from the stoichiometric solution is ~4.5ºC at atmospheric pressure. The equilibrium temperature changes according to the solution composition as shown in Figure 3.2.

The soils selected for this study are kaolinite (RP2 and SA1), precipitated silt, crushed silt, precipitated calcium carbonate (PCC), and ground calcium carbonate (GCC) (Table 3.3). RP2, randomly-shaped kaoline, is smaller than hexagonaly shaped SA1 (Palomino 2003). Crushed silt is an angular, low specific surface silt-sized soil. Precipitated silt consists of silt-size aggregations with extensive inter-particle pore networks and high specific surface. The irregularly shaped GCC particles are bulkier than the very uniform and rice-shaped PCC particles.

Table 3.3 (a) Physical and chemical properties of selected soils

Property	RP2	SA1	GCC	PCC	Precipitated Silt	Crushed Silt
G_s	2.6	2.6	2.71	2.71	2.08	2.65
d_{50} (μm)	0.36	1.1	12	1	20	20
pH	4.66	6.5	8.76	9.87	7	7
$S_s(m^2/gm)$	22~35	36-37	1.8	9.9	5-7* , 120**	0.113
Sphericity	0.7	0.7	0.8	0.2	0.9	0.9
Roundness	0.3	0.1	0.5	0.9	0.7	0.1
Liquid Limit	78	43	28	52		
Chemical composition (%)						
SiO_2	45.6	45.6			99.5	99.5
Al_2O_3	38.4	38.4			0.2	0.2
Fe_2O_3	0.88	0.4			0.07	0.07
TiO_2	1.69	1.5				
CaO	0.05	0.06			0.03	0.03
MgO	0.02	Trace				
K_2O	0.15	0.18				
Na_2O	0.21	Trace				
LOI	13.7	13.82				
$CaCO_3$			~95	~95		
$MgCO_3$			< 3.00	< 3.00		

References: (Palomino 2003; Parks 1990; Santamarina et al. 2002; Yun 2005)

* by methylene blue method and ** by N_2 absorption method

Table 3.3 (b) SEM pictures of the six sediments (Courtesy of Dr. Palomino)

Precipitated Silt 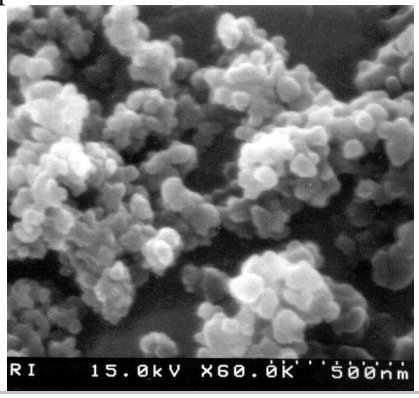	Crushed Silt 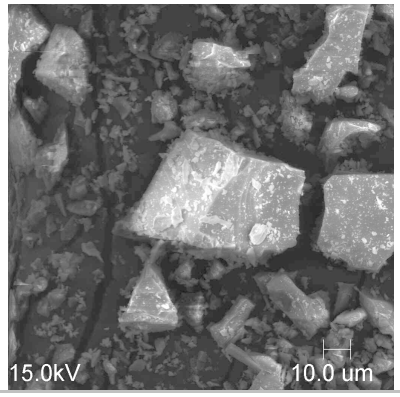
RP2 Clay 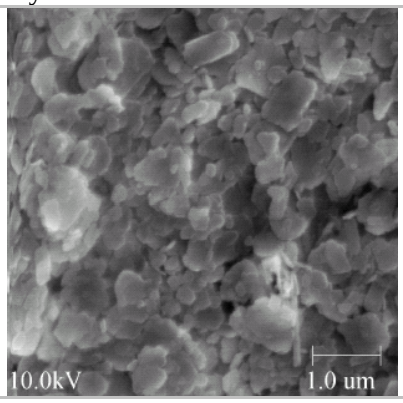	SA1 Clay 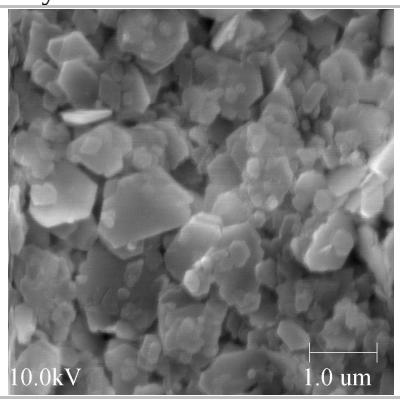
GCC 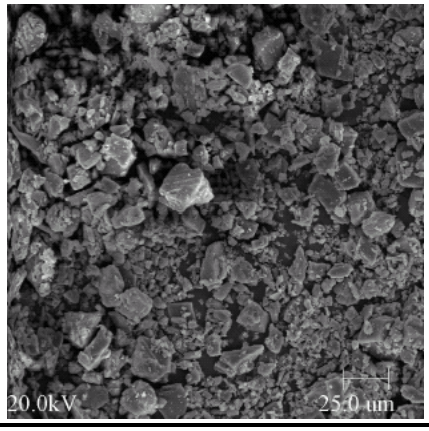	PCC 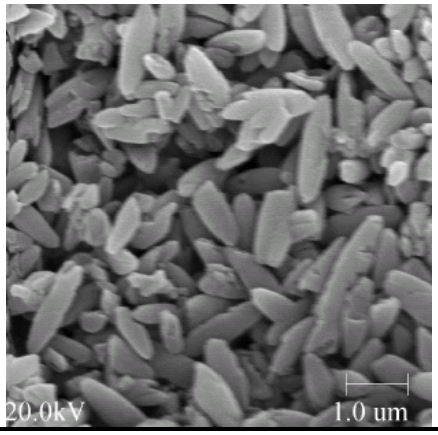

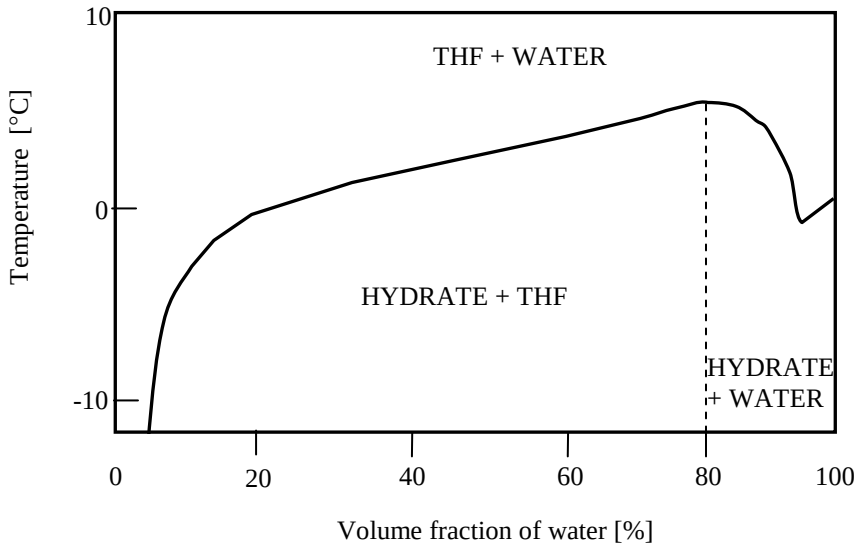

Figure3.2 Equilibrium temperature of THF Hydrate for solutions with different THF-water volume fractions (after Makino et al. 2005).

3.2.2 Specimen Preparation

The scope of the study involves different pore fluid compositions, high porosity sediments to investigate mineral surface effects, and remolded soils to study pore size effects.

Pore Fluid: THF solutions are prepared by mixing different volumes of water and THF (10, 20, and 30% of THF). Then, different weights of NaCl are added to these solutions. The resulting 9 different pore fluids are described in Table 3.4.

High Porosity Sediments: Soils (5g) are added to test cylinders filled with 20ml of the 20% THF solutions with different salt concentrations. The suspensions are shaken vigorously and left to rest for 1~2 hours for soils to sediment in the sealed cylinders.

Remolded Sediments: Mixture of SA1 and the 20% THF solution (0 molal salt) are prepared at 30%, 40%, 50%, and 60% of gravimetric liquid contents. Mixtures are left in sealed containers for 24 hours to allow for homogenization. Detailed specimen preparation for KC 151 specimen is described in Chapter 5.

Table3.4 Solution preparation for nucleation experiments (Percentage of THF is by volume)

THF%/Salt concentration	Water (ml)	THF (ml)	Mixing thoroughly with top cap colsed	Salt (g)	Mixing thoroughly with top cap closed
10% THF	17.7	2.3		0	
20% THF	15.8	4.2		0	
30% THF	13.1	6.9		0	
10% THF + 0.05 molal salt	17.7	2.3		0.06	
20% THF + 0.05 molal salt	15.8	4.2		0.06	
30% THF + 0.05 molal salt	13.1	6.9		0.06	
10% THF + 0.5 molal salt	17.7	2.3		0.6	
20% THF + 0.5 molal salt	15.8	4.2		0.6	
30% THF + 0.5 molal salt	13.1	6.9		0.6	

3.2.3 Experimental Device

The experimental device is illustrated in Figure 3.3. Thermocouples are inserted through the top cap. Then, test cylinders are submerged into the cooler. For mechanical impact experiments, cylinders are fitted in a circular acrylic plate, and a rod attached to a motor taps the plate at 1 Hz frequency throughout the duration of the experiment.

Thermocouples themselves can act as nucleation site. The effectiveness of thermocouples as promoters of nucleation was examined by forming hydrates with two

different types of thermocouples: smooth bar type and wire type. Test results show that the smooth bar type thermocouples are less effective as nucleation sites and are used for the rest of the study.

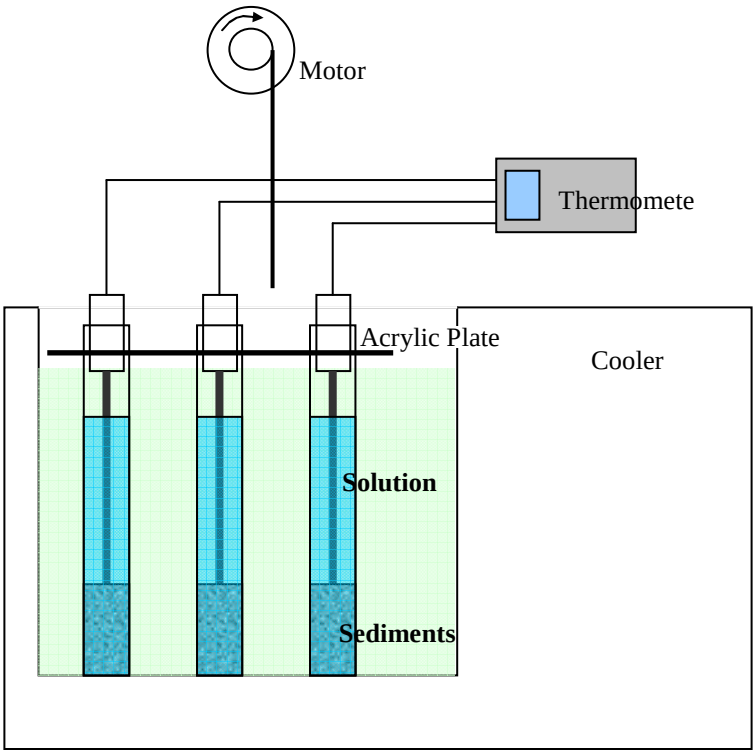

Figure 3.3 Experimental device

3.2.4 Experimental Procedure

The prepared specimens are submerged in the cooler. The system is equilibrated at 5˚C for 1~2 hours. Then, the temperature of the cooler is gradually lowered at 0.1 ˚C/min of cooling rate to the target temperature: T= -5˚C for 9˚C supercooling tests and T= -10˚C for 14˚C supercooling tests. The cooling rate has minor effect on the nucleation rate: An order of magnitude increase of cooling rate lowers the mean nucleation

temperature by 0.6 to 2˚C (Hobbs 1974). The cooler and specimen temperatures are monitored every 5 minutes. Tapping is performed only for the mechanical disturbance study. All other tests are conducted at the normal background vibration within the cooler.

3.3 RESULTS

Experimental results are presented next, starting with hydrate formation in bulk solution. Then, hydrate formation on mineral surfaces and in sediment pores are reported.

3.3.1 Hydrate Formation in Bulk Solution

A typical temperature signature during two bulk solution experiments with 20% THF solution (0 molal salt) specimen at T=-5˚C (9˚C of supercooling) and T=-10˚C (14˚C of supercooling) are shown in Figure 3.4. The temperature decreases to the target supercooled temperature and remains constant before hydrate formation. The induction period is shorter for higher degrees of supercooling. The temperature increases to the equilibrium temperature at the onset of nucleation due to the exothermic hydrate formation response. Once phase transformation is completed the temperature decreases back to the surrounding cooler temperature. The duration of the signal depends on factors such as nucleation and growth rate, cooler temperature, and the volume of fluid.

Degree of Supercooling: The effect of supercooling can be observed in experimental results with 20% THF solution (0 molal salt) at the different degree of supercooling. Two out of eight specimens formed hydrate at T=-5˚C (9˚C of supercooling, Figure 3.4a)

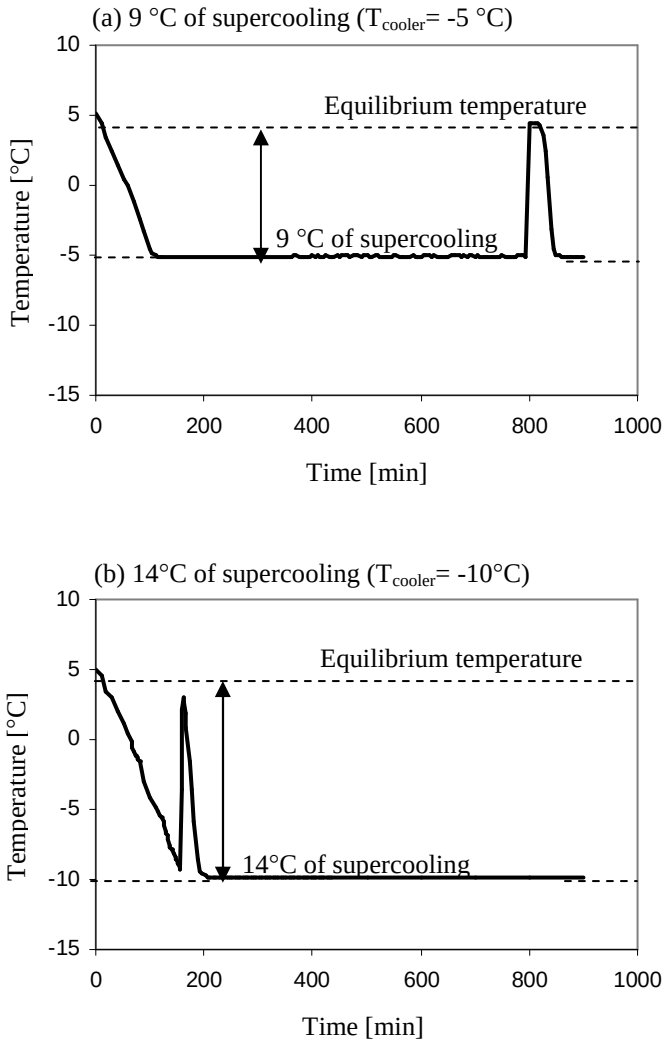

Figure 3.4 Typical signature of nucleation tests (20% THF solution+0 molal salt). (a) 9°C of supercooling (T_{cooler}= -5 °C). (b)14°C of supercooling (T_{cooler}=-10 °C).

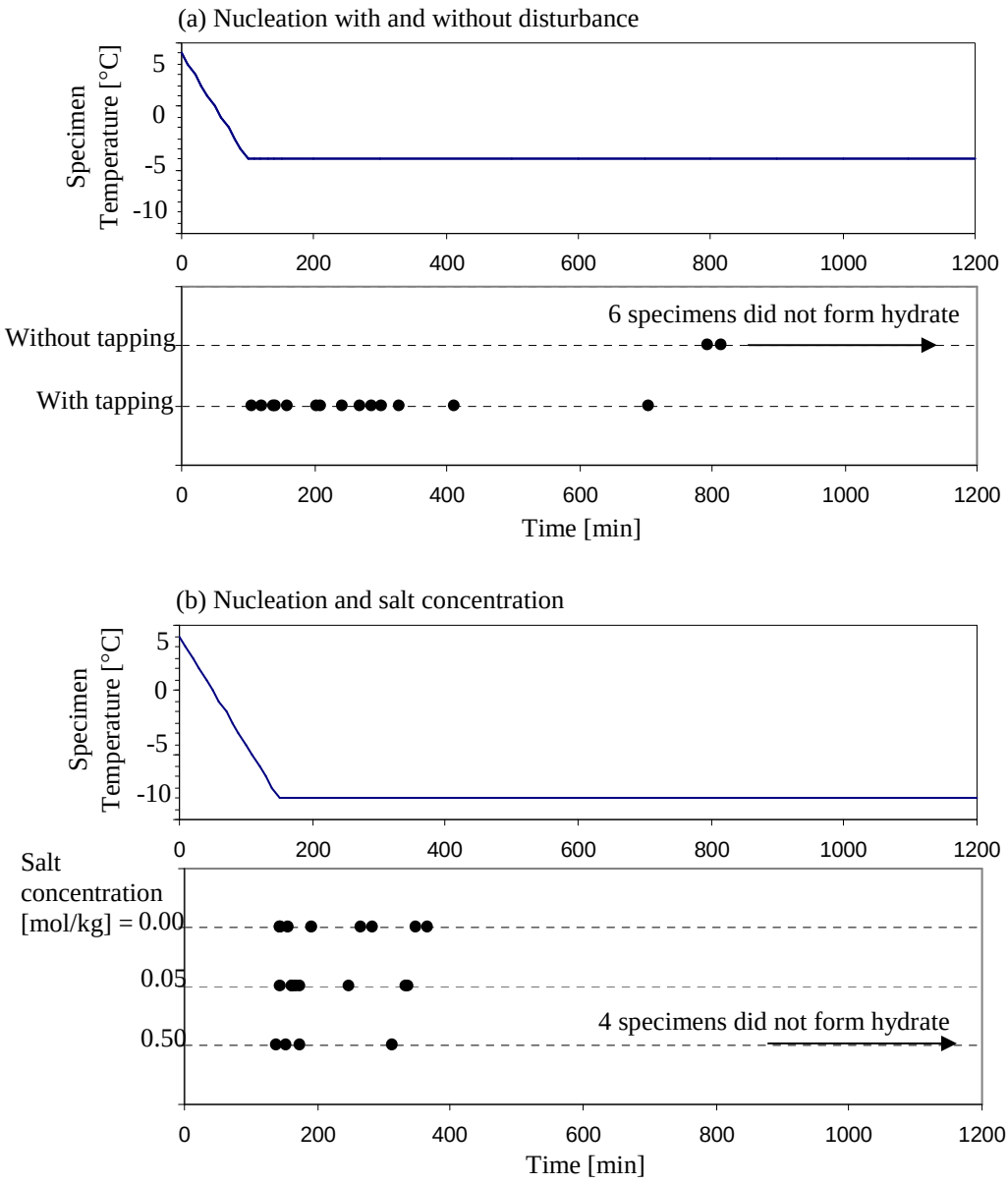

Figure 3.5 Nucleation results in bulk solution: (a) Nucleation with and without mechanical disturbance (20% THF solution+0 molal salt; T_{cooler}= -5 °C). (b) Nucleation for varying salt concentration (20% THF solution+salt; T_{cooler}= -10 °C, no tapping)

whereas eight out of eight specimens formed hydrate at T=-10˚C (14˚C of supercooling, Figure 3.4b). This confirms the importance of driving force on nucleation.

Mechanical Impact: Mechanical disturbance effects are explored by forming hydrate with 20%THF solution at T=-5˚C with and without tapping. Only two out of eight specimens formed hydrate without tapping within the 1200 minutes of test duration. Fourteen out of sixteen specimens formed hydrate within much shorter induction time when tapping was imposed (Figure 3.5a). Clearly, mechanical disturbance facilitates nucleation, but the stochastic nature of nucleation remains even in the presence of systematic disturbance.

Salt Cocentration: The 20% THF solution specimens with 0, 0.05, and 0.5 molal salt concentrations are tested at T=-10˚C (i.e. 14˚C of supercooling). Eight specimens are tested for each salt concentration. Specimens with 0 and 0.05 molal salt concentration do not show significant difference in induction time; however, hydrate formed in only four out of eight specimens with 0.5 molal salt concentration. This decrease in nucleation rate in the presence of salt is directly related to equilibrium change due to water activity.

3.3.2 Hydrate Formation in High Porosity Sediments – Mineral Surface Effects

Results in Figures 3.5 and 3.6 show that the induction time is much shorter in the presence of minerals than in the bulk solution (without tapping). Other observations follow.

Particle Size: RP2 (D_{50}=0.36μm) and SA1 (D_{50}=1.1μm) are tested to explore the effect of particle size on hydrate nucleation. Both in RP2 and SA1, hydrates nucleate between -3˚C and -5˚C, and size has no significant effect on the result (Figure 3.6a).

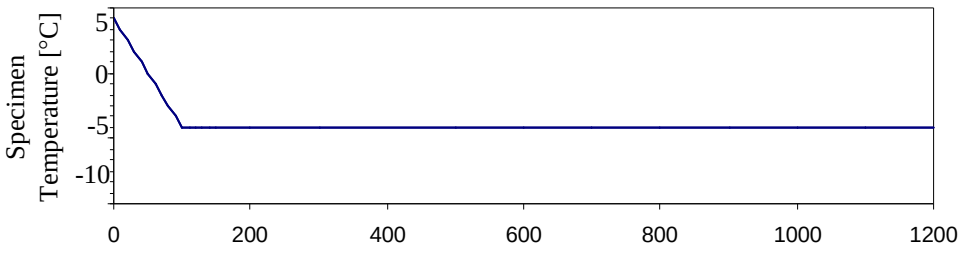

(a) Nucleation in highly porous sediment (20% THF solution)

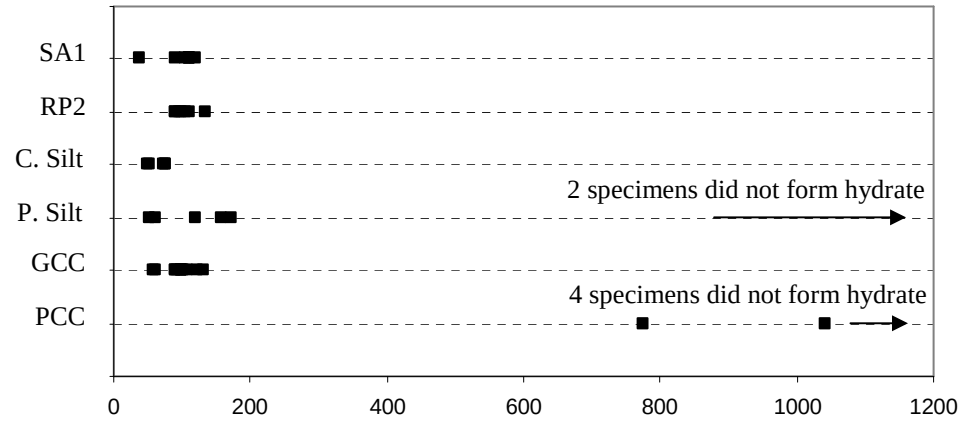

(b) Nucleation in highly porous sediment (20% THF solution +salt)

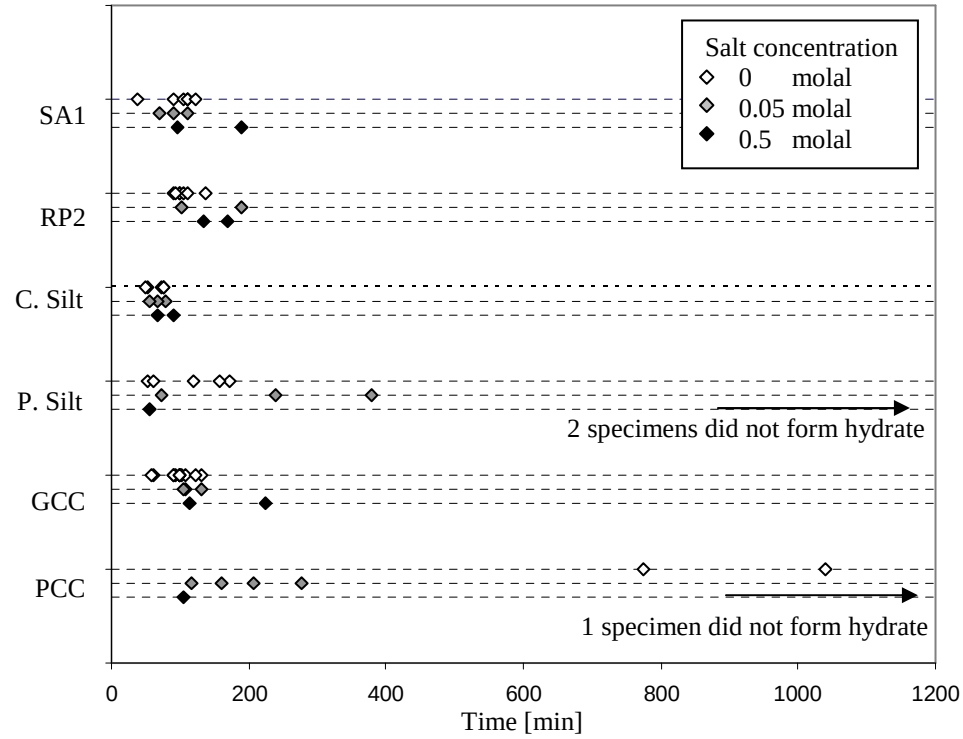

Figure 3.6 Nucleation results in suspension: (a) Nucleation in suspension (20% THF solution + 0 molal salt + soil; T_{cooler}= -5 °C, no tapping). (b) Nucleation in electrolyte suspension (20% THF solution + soil + salt; T_{cooler}= -5 °C, no tapping)

Specific Surface: The precipitated silt (S_s=120m^2g^{-1}) has much higher specific surface than the crushed silt (S_s=0.113m^2g^{-1}) yet their particle sizes are the same. Results show that crushed silt is a more effective nucleating agent, implying that specific surface is less important than surface characteristics such as angularity and roughness (Figure 3.6 a).

Particle Roughness: Both GCC (angular) and PCC (rounded) are $CaCO_3$ but exhibit very different particle shapes and roughness. Results in Figure 3.6a show that PCC is not an efficient nucleation agent, showing the induction time similar to that in bulk water.

Salts and Mineral Surfaces: Overall, the induction time is not considerably affected by salt concentration similar to cases in bulk water (Figure 3.6b). Interestingly, the presence of salt decreases the induction time in the PCC specimens.

3.3.3 Hydrate Formation in Remolded Sediments - Pore Size Effects

Remolded SA1 pastes: The results gathered for SA1 specimens with different liquid contents (20% THF solution with 0 molal salt) show that the nucleation temperature increases and the induction time decreases as the liquid content increases (Figure 3.7). However, the equilibrium temperature remain more or less constant (not shown here). Consequently, the increasing nucleation temperature with liquid content is not caused by equilibrium temperature change but caused by rather kinetic reason, which may be the available volume of water for nucleation.

Remolded Gulf of Mexico Sediment: Unique insight into pore size and salt effects in hydrate formation are gathered as a part of an extensive experimental program conducted with natural sediments (a detailed description on this experiment is presented in Chapter 5 - KC151 remolded specimen with 20% THF solution+0.91 molal salt as pore fluid).

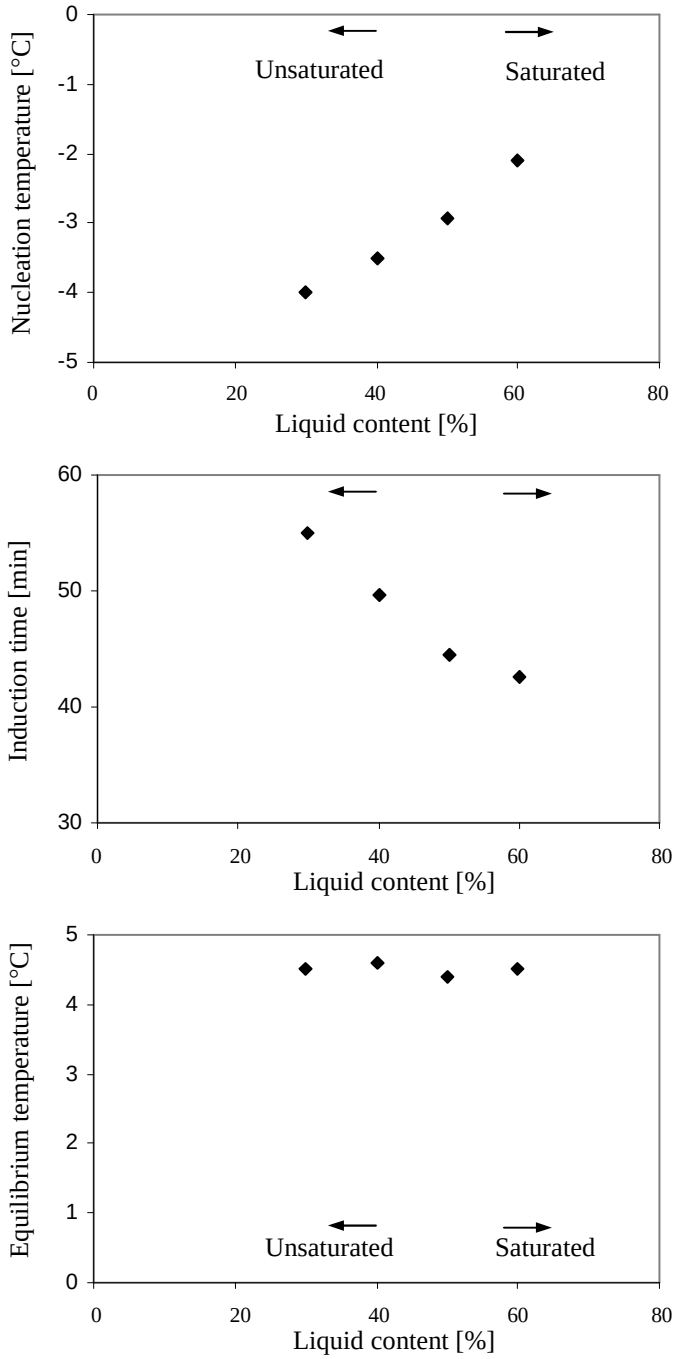

Figure 3.7 Capillary pressure effect - Nucleation temperature, induction time, and liquid content (20% THF solution +0 molal+ SA1; T_{cooler}= -5 °C, no tapping). Average of two measurements is plotted.

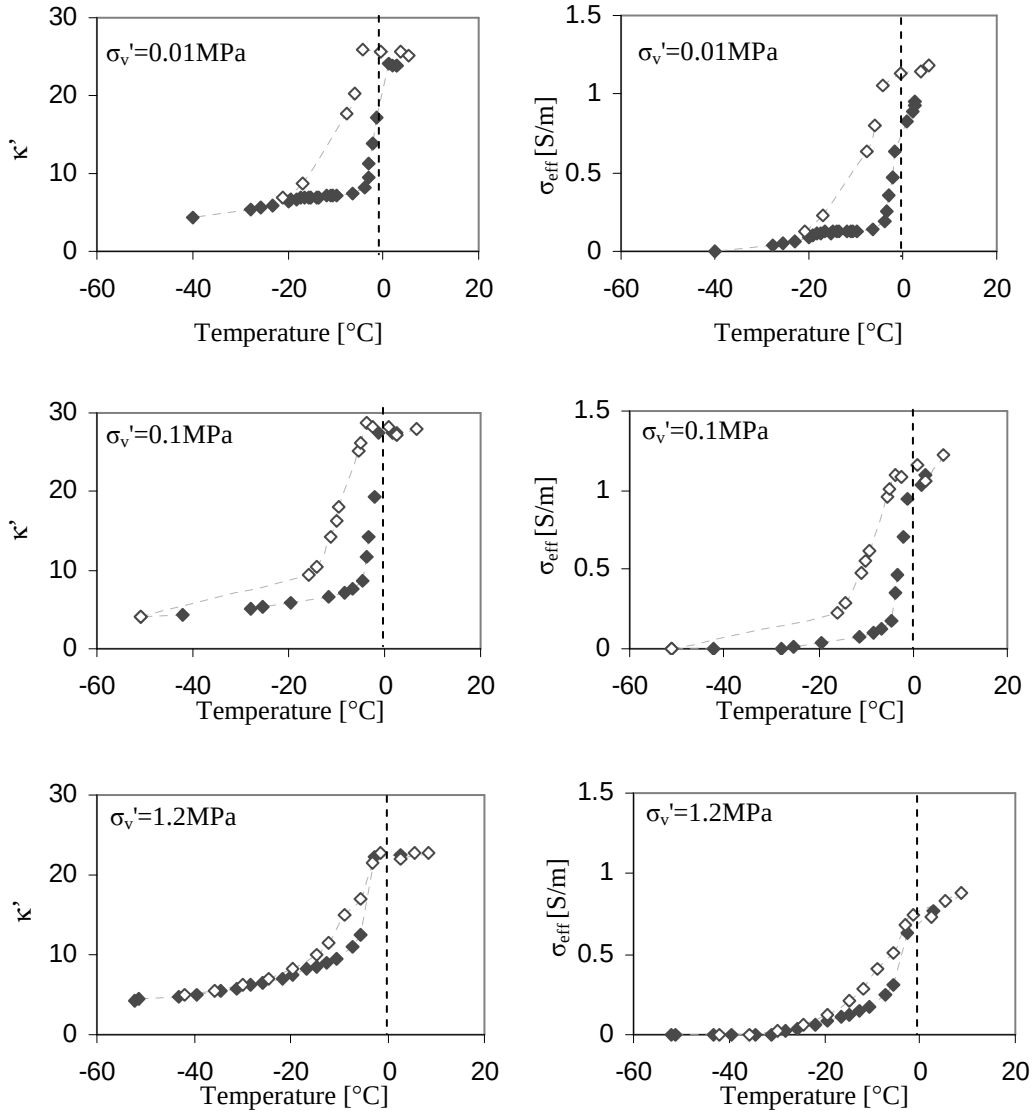

Figure 3.8 Hysteresis in real permittivity κ' and electrical conductivity σ_{eff} values during hydrate formation and dissociation in the KC151 with 20% THF solution +0.91 molal salt as pore fluid (Details in Chapter 5). Solid dots indicate formation data, and blank dots are dissociation data. The rate of cooling is 0.5°C/min.

The evolution in real permittivity and electrical conductivity against temperature during hydrate formation and dissociation under different vertical effective stresses are plotted in Figure 3.8. The trends show a gradual decrease in real permittivity κ' and electrical conductivity σ_{el} [S/m] during hydrate formation. Such gradual hydrate formation can reflect gradually decreasing pore size being invaded by hydrates and gradual increase in ionic concentration as a result of ionic exclusion during hydrate formation. Initial permittivity and conductivity values are lower as the vertical effective stress increases as a result of lower volume fraction of pore fluids. More importantly, phase transformation starts at lower temperatures for higher vertical effective stresses.

3.4 ANALYSES

3.4.1 Salt Effect

Several theoretical and empirical methods have been suggested to estimate the effect of salt on the equilibrium temperature of gas-hydrate phase transformation; these methods are based on the equilibrium temperature depression of water due to salt, which can be estimated from the Hammerschmidt equation (Berecz and Balla-Achs 1983; Dickens and Quinby-Hunt 1997; Sloan 1998). The freezing temperature of water with salts T_{fs} [K] and without salts T_f [273.15 K] is related to the activity of water as:

$$\ln a_w = \frac{\Delta H_{ice}}{R}\left[\frac{1}{T_f} - \frac{1}{T_{fs}}\right], \tag{3.5}$$

where ΔH_{ice}=6008 J mol^{-1} is the heat of fusion of ice. Likewise, the activity of water a_w is related to the equilibrium temperature of gas-hydrate phase transformation with salts T_s [K] and without salts T_w [K] by:

$$\ln a_w = \frac{\Delta H_{hydrate}}{NR}\left[\frac{1}{T_w} - \frac{1}{T_s}\right], \tag{3.6}$$

where $\Delta H_{hydrate}$ [kJ mol^{-1}] is the heat of dissociation of hydrate, N [] is the hydration number, and R=8.31 J K^{-1} mol^{-1} denotes the universal gas constant. Equations (3.5) and (3.6) can be combined to relate the equilibrium temperature depression in hydrate formation to that in ice formation:

$$\left[\frac{1}{T_w} - \frac{1}{T_s}\right] = \frac{\Delta H_{ice} N}{\Delta H_{hydrate}}\left[\frac{1}{T_f} - \frac{1}{T_{fs}}\right] \quad . \tag{3.7}$$

The equilibrium temperature depression due to salt concentration is modeled using Equation (3.7). The equilibrium temperature depression of water-to-ice transformation for different salt concentrations are extracted from Lide (2003). The heat of dissociation for THF hydrate is $\Delta H_{hydrate}$ = 98kJ/mol in case of congruent melting (Leaist et al. 1982; White et al. 2003). The experimental data and modeled equilibrium temperatures of THF hydrate are plotted in Figure 3.9.

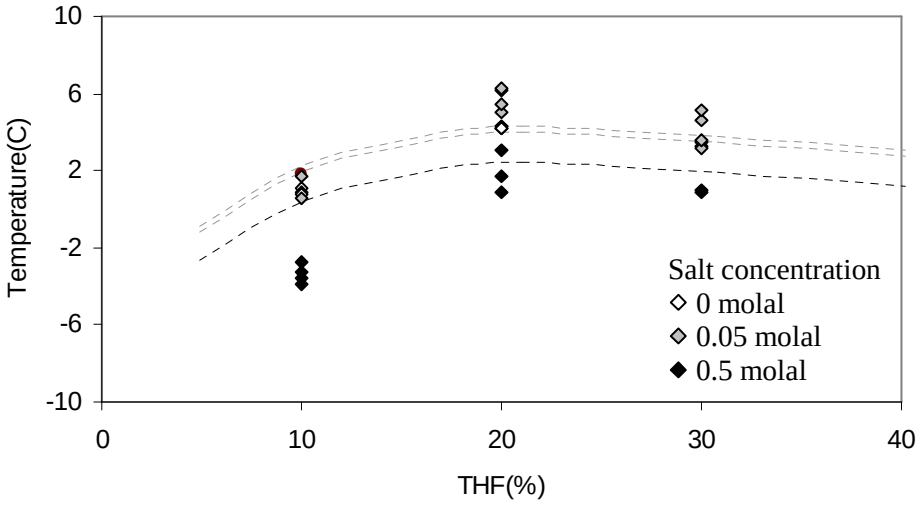

Figure 3.9 Effect of salt concentration on the equilibrium temperature (10, 20, and 30% THF solution with 0, 0.05, 0.5 molal salt concentration; T_{cooler}= -10 °C, no tapping).

The estimated equilibrium temperature of THF hydrate for the bulk salt solution using Equation (3.7) is T_{eq}=0.9°C for C=0.91 molal initial salt concentration, and it drops to -16.6°C for a salt-saturated (6 molal) pore fluid. Consequently, the equilibrium temperature in KC151 specimen can gradually decrease from 0.9°C to -16.6°C as ion exclusion takes place during hydrate formation in closed systems.

3.4.2 Mineral Surface Effect

The nucleation rate J [$m^{-3}sec^{-1}$] in bulk water is a function of temperature T [K], the activation energy for an embryo to gain more molecules and grow freely Δg [J], and the Gibbs free energy difference due to an embryo formation ΔG^* [J] which is a function of the surface energy of an embryo (Hobbs 1974),

$$J = n_w \frac{kT}{h} \exp\left(-\frac{\Delta g}{kT}\right) \exp\left(-\frac{\Delta G^*}{kT}\right) \tag{3.8}$$

where n_w [m^{-3}] is the number of water molecules in unit volume, k = 1.38×10^{-23} J·K^{-1} is Boltzmann's constant, and h = 6.626×10^{-34} J·sec is Planck's constant.

The beneficial effects of mineral surfaces on nucleation suggest that heterogeneous nucleation is favored over homogenous nucleation. Then, assuming that nucleation occurs only on mineral surfaces, the number of water molecules involved per unit volume n_w [m^{-3}] can be estimated in terms of porosity n [] and specific surface S_a [$m^2 \cdot g^{-1}$]:

$$n_w = \frac{\frac{S_a \times W_s}{(l_{water})^2}}{V_{Specimen}} = \frac{S_a (1-n) G_s \rho_w}{(l_{water})^2} \tag{3.9}$$

where W_s is specimen weight [kg], l_{water} [m] is the size of a water molecule, $V_{specimen}$ [m^3] is the specimen volume, G_s [] is specific gravity, and ρ_w [$kg \cdot m^{-3}$] is water density. Therefore, porosity and specific surface affect nucleation rates according to Equations (3.8) and (3.9).

Figure 3.10a shows nucleation rates as a function of specific surface and porosity for a contact angle θ=90° using Equations (3.8) and (3.9) and plane and spherical surface equations in Table 3.2 (Note: equations for plane and spherical surfaces in Table 3.2 produce almost identical trends - smaller contact angles increases the nucleation rate in agreement with Young's equation in Table 3.2). The regions for the different sediments (n, Sa) are superimposed on the figure. The result confirms that assessing nucleation rate only with availability of water molecule is improper when the surface characters are different. The comparison of nucleation experiment results in Figure 3.6 and Figure 3.10b suggest that the crushed materials, crushed silt and GCC appear to have the lowest contact angles, while the precipitated materials, precipitated silt and PCC have high contact angle.

3.4.3 Pore Size Effect

Capillary suction may depress the equilibrium temperature in unsaturated systems. The capillary pressure P_c [Pa] in platy particles can be estimated as follows (Cho and Santamarina 2001):

$$P_c = \gamma_{gl}\left(\frac{S_a \rho_w}{w}\right) \tag{3.10}$$

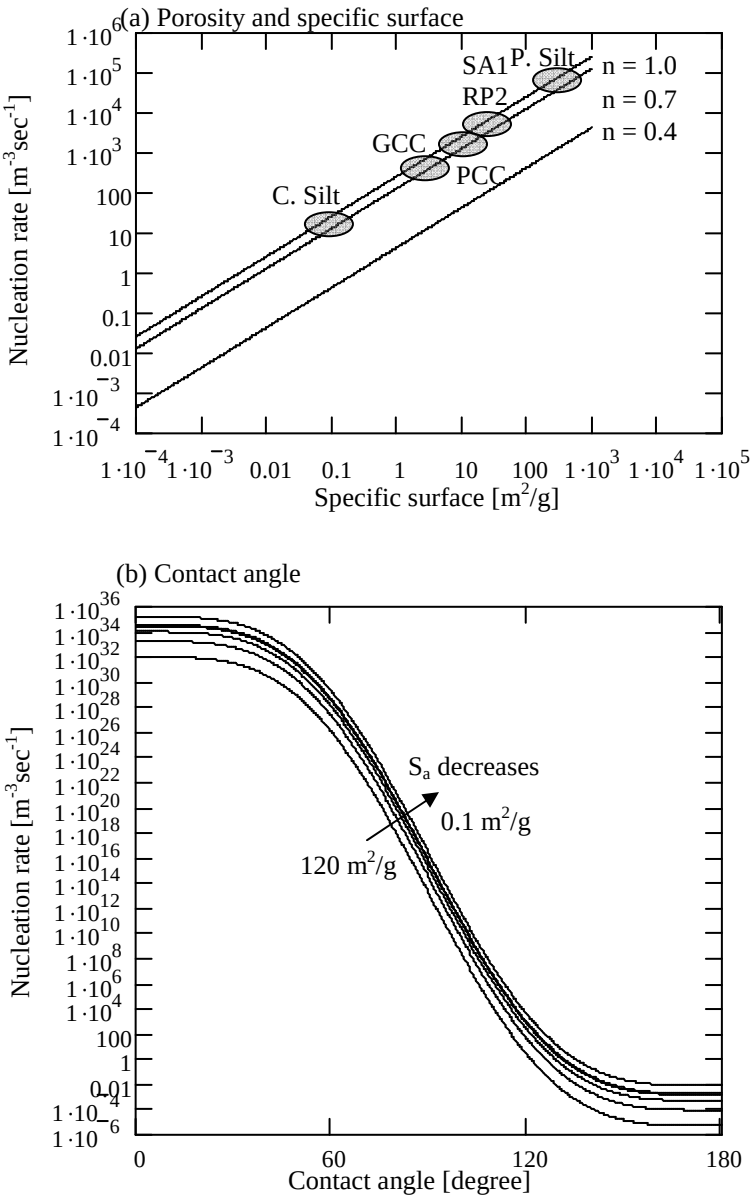

Figure 3.10 Effects of porosity, specific surface, and contact angle on nucleation rate. Lines indicate modeled values with Equation 3.4. (a) Porosity and specific surface: Both plane and spherical surface equations in Table 3.2 are used for free energy calculation. (b) Contact angle: Plane surface equation in Table 3.2 is used for free energy calculation. Thick lines indicate the range in experimental induction times for each soil.

where γ_{gl} [$J \cdot m^{-2}$] is the gas-liquid interfacial tension and w [] is the liquid content. The estimated capillary pressure for the KC151 sediment (S_a=120 [$m^2 g^{-1}$], 20% THF solution + 0.91 molal salt concentration) ranges between P_c=20 kPa and 80kPa for liquid contents between 40% and 10%. The temperature depression ΔT [°C] due to the capillary pressure P_c [Pa] according to Clausius-Clapeyron relation is

$$\Delta T = P_c \frac{T_{eq} \Delta V}{\Delta H_{hydrate}} \tag{3.11}$$

where T_{eq} = 4.5°C is the equilibrium temperature in bulk water, ΔV = 11.11×10^{-5} $m^3 \cdot kg^{-1}$ is the volume change due to hydrate phase transition. The estimated equilibritum temperature depression for the KC151 specimen is less than 6×10^{-3}°C. Consequently, the depression due to capillary pressure between gas and fluid in unsaturated condition is negligible.

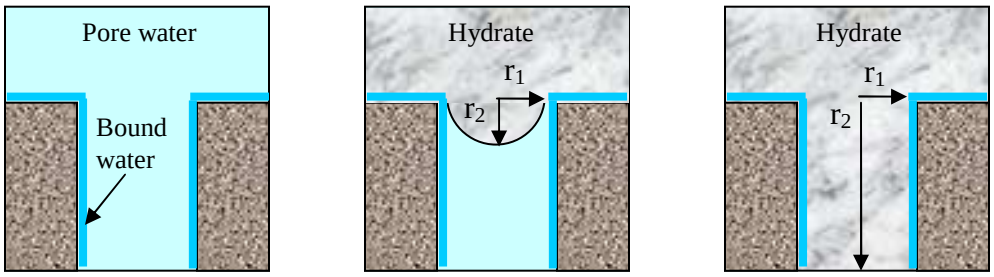

Figure3.11 Hydrate formation and dissociation in a pore (After Anderson et al., 2003)

On the other hand, the equilibrium temperature depression ΔT_{pore} [K] due to the curved interface between hydrate and fluid in saturated condition can be estimated by

combining Kelvin's and Clapeyron's equations (Clennell et al. 1999; Everett 1961; Jallut et al. 1992):

$$\Delta T_{pore} = \frac{\kappa \gamma_{hl} T_{bulk} \cos\theta}{\rho_{hydrate} \Delta H_{hydrate}} \tag{3.12}$$

where κ [nm^{-1}] is the interface curvature, T_{bulk} [K] is the equilibrium temperature in the bulk phase, γ_{hl} [mJ m^{-2}] is the hydrate-liquid interfacial tension, θ represents the contact angle between hydrate and the pore wall (θ =0° assuming unfrozen liquid layer at the pore wall), $\Delta H_{hydrate}$ [kJ mol^{-1}] is the heat of hydrate dissociation, and $\rho_{hydrate}$ [kg m^{-3}] is the hydrate mass density. If solid-liquid interface is hemispherical, κ =2/r (e.g. during formation), while if the interface is cylindrical, κ =1/r (e.g. during dissociation), where r [nm] is the pore radius (Figure 3.11, Clennell et al.1999 and Jallut et al. 1992). The material parameters for THF hydrates are: the heat of dissociation $\Delta H_{hydrate}$ =98kJ/mol, hydration number N=17 (Leaist et al. 1982), hydrate-liquid interfacial tension γ_{hl} = 31mJ m^{-2}, and mass density $\rho_{hydrate}$=970 kg m^{-3}. The average separation r (=1/κ) between platy particles can be estimated from the specific surface S_a and the liquid content w:

$$r = \frac{w}{S_a \rho_l} \tag{3.13}$$

where ρ_l is the mass density of liquid ρ_l=1009 kg m^{-3} for 20% THF+0.91 molal salt solution. The estimated pore size for the KC151 specimen ranges from 2 to 5 nm. Then, the Kelvin- Clapeyron equation (Equation 3.12) predicts a depression of ΔT≈ -15K (larger pores) to -36K (small pores) i.e. the equilibrium temperature T_{eq} ranges from T_{eq} =-10.5°C to -31.5°C.

The hydrate formation gradually invades from larger pores to smaller pores, so there is a gradual depression in equilibrium temperature. The measured equilibrium

temperature ranges from T_{eq} =1°C to -20°C in KC151 specimen (Figure3.8). This range overlaps the equilibrium temperature for both salt and pore size effects. However, the estimated depression estimated due to pore size effect is larger than experimentally measured values. This is probably due to underestimation of pore size. The pore size estimation in Equation 3.13 assumes that particles are dispersed and aligned parallel to each other, and pore size can be underestimated when flocculated structures are present.

3.5 CONCLUSIONS

The thermal signature of nucleation process is characterized by the induction time, the degree of supercooling, and the equilibrium temperature depression.

- The initiation of nucleation presents stochastic characteristics. The factors that affect nucleation follow.

- Mechanical impact facilitates the initiation of nucleation and reduces the induction time when the strain rate exceeds a threshold level. Vibration does not affect the equilibrium temperature and does not prevent the stochastic nature of nucleation (yet it reduces its randomness).

- Salts do not affect the induction time considerably. However, salts depress the equilibrium temperature during phase transformation as the water activity is lowered, and ion exclusion leads to diffusion limited nucleation.

- Nucleation is favored in the presence of mineral surfaces.

- The character of mineral surfaces affects the induction time but it does not change the equilibrium temperature during phase transformation.

- Mineralogy and surface roughness are the most important particle characteristics to prompt the initiation of nucleation on mineral surfaces. Particle size plays a secondary role.

- Pore size causes a significant depression in equilibrium temperature in fine grained sediments.

- Hydrate formation gradually invades the porous network, starting at large pores and advancing into the small ones. Therefore, the equilibrium temperature is gradually depressed during hydrate formation in sediments.

CHAPTER IV.

MECHANICAL AND ELECTROMAGNETIC PROPERTIES OF HYDRATE-BEARING SEDIMENTS

4.1 INTRODUCTION

Natural gas hydrates consist of a hydrogen-bonded water lattice and guest gas molecules. The stability of gas hydrate depends on temperature, pressure, salinity, and other factors such as sediment characteristics. Difficulties in sampling and maintaining recovered natural samples at in situ temperatures and fluid pressures hinders the study of natural gas hydrate-bearing sediments. On the other hand, the interpretation of data obtained in hydrate-bearing formations during borehole logging or an exploration geophysical survey requires reliable calibrations with reference physical properties. These can be obtained from synthetic laboratory samples with well-characterized lithology, hydrate saturation, and confining pressures. Although numerous laboratory studies have used sediments containing synthetic gas hydrates to investigate mechanical, thermal, and electromagnetic properties of both pure crystals and hydrate-bearing sediments (Cameron et al. 1990; Ebinuma et al. 2005; Priest et al. 2005a; Priest et al. 2005b; Santamarina et al. 2005; Waite et al. 2002; Winters et al. 2005; Yun et al. 2006), the controlled synthesis of methane hydrate in sediments is limited by the low solubility of methane in water and the prolonged time required to form hydrate from aqueous phase methane, which is the way that gas hydrate probably forms in deep sediments (Buffett

and Zatsepina 2000; Hyndman and Spence 1992)

The purpose of this study is to generate an unprecedented database of geophysical parameters for hydrate-bearing sediments with emphasis on electrical and small-strain mechanical properties. THF is selected as the hydrate former for this study because of its complete miscibility with water and its capacity to form hydrate from the aqueous phase. A detailed discussion on the advantages and the disadvantages of using THF as hydrate former is presented in Chapter 2. The experiments with high fluid pressure cell were performed by Dr. Franco Francisca and added in this section to support other data.

4.2 THEORETICAL BACKGROUND

Concepts relevant to the elastic and electromagnetic properties of hydrate bearing sediments are reviewed in this section.

4.2.1 Elastic Properties

The elastic properties of hydrate-bearing sediments are governed by the state of effective stress, void ratio, and hydrate saturation. Bulk modulus B [Pa], constrained modulus M [Pa], and shear modulus G [Pa] in small-strain regime are related to wave propagation velocities as follows.

$$V_P = \sqrt{\frac{M}{\rho}} = \sqrt{\frac{B + \frac{4}{3}G}{\rho}} \tag{4.1}$$

$$V_S = \sqrt{\frac{G}{\rho}} \tag{4.2}$$

$$\frac{V_P}{V_S} = \sqrt{\frac{M}{G}} = \sqrt{\frac{2(1-\nu)}{1-2\nu}} \tag{4.3}$$

where ρ [kg·m^{-3}] is mass density of the medium.

The shear modulus and the bulk modulus increase when gas hydrates form in sediments, and thus P- and S-wave velocities increase (Berge et al. 1999; Pearson et al. 1986; Stoll 1974; Stoll and Bryan 1979; Stoll et al. 1971; Wittebolle and Sego 1985; Yun et al. 2005). Also, hydrate-bearing sediments can convey higher frequency wave components (Wittebolle and Sego 1985). Published P- and S-wave velocities in pure gas hydrates measured in the laboratory are tabulated in Table 4.1; published values measured in the laboratory synthesized hydrate-bearing sediments are summarized in Table 4.2. Variations in velocities reflect specimen preparation methods as well as factors listed above.

Several methods have been suggested to model the acoustic velocities of hydrate-bearing sediments. Wyllie's time average equation can be used to relate velocity, porosity, and hydrate saturation (Bangs et al. 1993; Korenaga et al. 1997; Lee and Collett 2001; Lee et al. 1996; Wood et al. 1994; Wyllie et al. 1958). Effective media models provide a rock physics based approach to relate velocity and can be generalized for high porosity media or hydrate-bearing sediments (Digby 1981; Dvorkin et al. 1994; Ecker et al. 1998; Helgerud et al. 1999; Jakobsen et al. 2000; Walton 1987). Rock-physics models that take into account the pore-scale internal structure of hydrate-bearing sediments can be categorized into cementation model, pore filling model, structure builder model, and combination. In the cementation model, hydrates form at grain contact or envelope the surfaces of grains and even a small amount of relatively soft cement at contacts increases stiffness dramatically (Dvorkin et al. 1994; Guerin et al. 1999). In the pore filling model,

Table 4.1 Wave velocities in pure gas hydrates measured in the laboratory.

Guest molecules	Specimen conditions	Measurement Method	V_p (m/s)	V_s (m/s)	References
Propane	Compacted Slurry	Pulse transmission	2400	NA	(Stoll and Bryan 1979)
Methane	Single crystal	Brillouin spectroscopy	3369	NA	(Kiefte et al. 1985)
Hydrogen Sulfide	Single crystal	Brillouin spectroscopy	3355	NA	(Kiefte et al. 1985)
Sulfur Dioxide	Single crystal	Brillouin spectroscopy	3144	NA	(Kiefte et al. 1985)
Xenon	Single crystal	Brillouin spectroscopy	2910	NA	(Kiefte et al. 1985)
Propane	Single crystal	Brillouin spectroscopy	3698	NA	(Kiefte et al. 1985)
Tetrahydrofuran	Single crystal	Brillouin spectroscopy	3665	1890	(Kiefte et al. 1985)
Freon-11	Single crystal	Brillouin spectroscopy	3459	NA	(Kiefte et al. 1985)
Sulfur Hexafulouride	Single crystal	Brillouin spectroscopy	3390	NA	(Kiefte et al. 1985)
Propane	Propane hydrate and ice	Pulse Transmission	2050 ~3250	1675	(Pandit and King 1983)
Tetrahydrofuran	Bulk hydrate	Pulse-echo overlap	3510 ~3580	1610 ~1660	(Bathe et al. 1984)
Freon-11	Freon-11 gas hydrate and ice	Pulse Transmission	2500	NA	(Berge et al. 1999)
Methane	Compacted polycrystalline hydrates	Pulse Transmission	3800	1950	(Helgerud et al. 2003b)
Methane-Ethane			3840	1990	

Table 4.2 Wave velocities in laboratory synthesized hydrate-bearing sediments

Gas	Sediment	Specimen conditions	Measurement Method	V_p (m/s)	V_s (m/s)	Reference
Methane	Ottawa 20/30 D_{50}= 0.7mm	Percolate methane to saturated sediment Applied σ´ is not specified	Pulse Transmission	2000		(Stoll et al. 1971)
Methane	Ottawa 20/30 D_{50}= 0.7mm	Inject gas to sea-water saturated sediment Applied σ´ is not specified	Pulse Transmission	2690		(Stoll 1974)
Propane	Ottawa 20/30 D_{50}=0.7mm	Mixed sand, water, and liquid propane n= 0.4	Ultra sonic pulse-transmission	2260		(Stoll and Bryan 1979)
Tetrahydrofuran	Berea sandstone	Submerged dried sample cores in THF-water mixture σ´ = 0 kPa	Ultra sonic pulse-transmission	4500		(Pearson et al. 1986)
Freon-12	Sand	Inject R12 to saturated sediment σ_o = 200 kPa	Piezo-Ceramic Transducer (Bender Element)	3550		(Wittebolle and Sego 1985)
Freon-11	Sand	Inject R11 to saturated sediment n=0.4, σ´ = 0 kPa	Pulse Transmission	3810	2200	(Berge et al. 1999)
Methane	Sand	Ice seed method Partially saturated σ´ = 590 kPa S_{hyd} = 0.4	Resonant Column	2826	1535	(Priest et al. 2005; Priest et al. 2006)
Methane	Sand	Ice seed method Partially saturated σ´ = 230~270 kPa S_{hyd} = 0.2~0.7	Piezo electric transducer	3080~ 4000		(Winters et al. 2005)
Tetrahydrofuran	Sand D_{50} = 120μm	Mixed sand, water, and liquid THF n=0.4, no confinement S_{hyd} = 1.0	Piezo-Ceramic Transducer (Bender Element)	3800	1600	(Yun et al. 2005)
Methane	Sand	Flushing methane dissolved water Applied σ´ is not specified S_{hyd} = 1.0	Ultrasonic P-wave transducer	4653		(Spangenberg and Kulenkampff 2005)

hydrate formation in pore spaces affects only bulk modulus until hydrate crystals interconnect soil particles, thereafter, the structure builder model takes over (Ecker et al. 1998; Hyndman and Spence 1992; Lee 2002).

4.2.2 Electromagnetic Properties

External electric field causes charge displacement and polarization in the media and the resulting current is out of phase with the applied electric field. The relative permittivity κ^*, the complex permittivity ε^* normalized by the permittivity of vacuum ε_o ($=8.854\times10^{-12}$F·m^{-1}), captures these phenomena and is expressed as follows.

$$\kappa^* = \frac{\varepsilon^*}{\varepsilon_o} = \kappa' - i\kappa'' \tag{4.4}$$

The real permittivity κ' is a measure of polarization, and the imaginary permittivity κ'' measures electric losses due to polarization and conduction. The effective AC conductivity σ_{el} [S·m^{-1}] can be computed as follows.

$$\sigma_{el} = \kappa'' \varepsilon_o \omega \tag{4.5}$$

where ω [sec^{-1}] is the angular frequency.

The real permittivity κ' of soil-water mixtures in the microwave frequency range is dominated by the orientational polarization of unfrozen free water molecules and thus by the volume fraction of water. On the other hand, the electrical conductivity σ_{el} of fluid-saturated sediments is determined by the porosity n of the sediments, the unfrozen pore volume, and the pore fluid conductivity (i.e., ionic concentration and mobility in the pore fluid).

Electromagnetic waves have been used in monitoring phase transformation in the laboratory study of hydrates (Devarakonda et al. 1999; Jakobsen and Folgero 1997;

Jakobsen et al. 1996; Pearson et al. 1986): when water is cooled, the number of hydrogen bonds increases, molecules form clusters, the guest molecules enter the water cluster, and hydrate forms. Extensive hydrogen bonds in water molecules reduce the water-molecule polarizability and ionic concentration and/or mobility in water significantly during hydrate formation (Devarakonda et al. 1999). Ions are either excluded from or trapped in the hydrate lattices during hydrate formation. Consequently, the real permittivity and the electric conductivity are good indicators of hydrate formation.

4.3 EXPERIMENTAL STUDY

The experimental study is conducted in zero-lateral strain cells, instrumented to measure the electrical properties, small-strain stiffness, and zero lateral strain compressibility of hydrate-bearing sediments. The parametric study includes the sediment type, effective stress states, and the volume fraction of hydrates in pores S_{hyd}.

4.3.1 Test Devices

Two different sediment cells were designed and built to study hydrate bearing sediments under zero lateral strain conditions. The cells are illustrated in Figure 4.1. The maximum vertical effective stress for both cells is 3 MPa, and the high fluid pressure cell can sustain 20 MPa of fluid pressure.

The dimensions of the low pressure cell are: OD=113mm, ID=100mm, and H=80mm. The low fluid pressure cell contains sensors to record the complex permittivity κ^*, S-wave velocity V_S, volume change ε_{vol}, and temperature T (Figure 4.1a). The cell

design permits all measurements to be conducted at steady state (constant temperature) as well as during formation and dissociation of synthetic hydrate (changing temperature). A K-type thermocouple mounted through the top cap of the cell is used to monitor the specimen temperature with precision of 0.1ºC. Volume change is determined from the instantaneous vertical position of the top cap using a linear variable displacement transducer (LVDT) with precision of 2.5×10^{-6} m. Piezocrystal bender elements are used for S-wave measurements (Lee and Santamarina 2005). The frequency content varies from 5 kHz to 70 kHz, depending on the sediment stiffness, which in turn reflects effective stress and/or hydrate saturation. The source is housed in the bottom plate and connected to a signal generator, while the receiver bender element is mounted in the top cap and connected to a filter/amplifier. Both the signal generator and the filter/amplifier are connected to a digital storage oscilloscope. The bottom plate also houses the dielectric permittivity probe, which is connected to a computer-controlled network analyzer that measures the complex permittivity κ^* spectrum between 200 MHz and 1.3 GHz. The cell, the loading frame, and peripheral electronics are placed in a cold room, where the temperature is controlled with a 0.01^{o}C precision.

The high fluid pressure cell (OD=100mm, ID=60mm, and H=241mm) was developed for methane hydrates and applied to this study with THF hydrates to ensure saturation for proper P-wave velocity measurements in these soft sediments (Figure 4.1b). Furthermore, data duplication between the two cells provides information related to the robustness of measured values. Pinducers (Valey Fisher, VP1093) for P-wave measurements and bender elements for S-wave measurements are installed in the bottom plate and the top cap of the cell. The frequency content varies from 5 kHz to 1MHz for

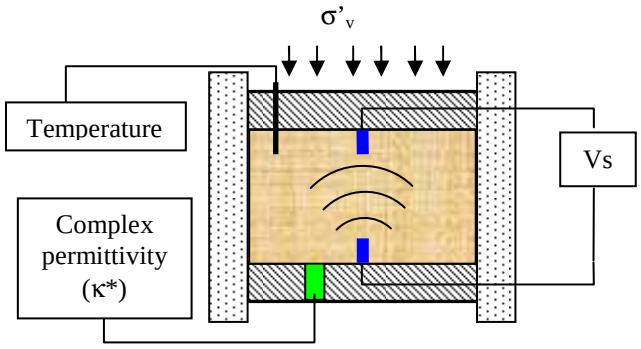

(a) Low pressure oedometer cell (ε_h=0)

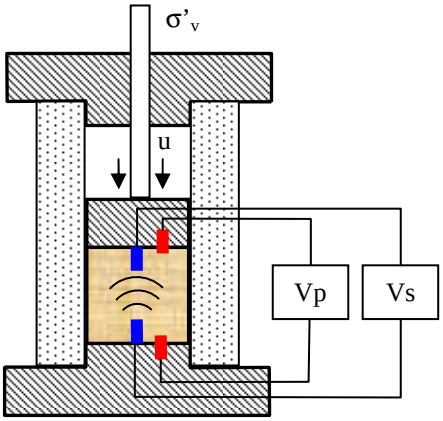

(b) High pressure oedometer cell (ε_h=0)

Figure 4.1 Experimental devices. (a) Low pressure oedometer cell (Specimen height: 4~5 cm; diameter: 10cm) (b) High pressure oedometer cell (Specimen height: 4~5 cm; diameter: 6cm)

Table 4.3. SEM pictures and characteristics of tested soils.

Sand -F110	Precipitated silt
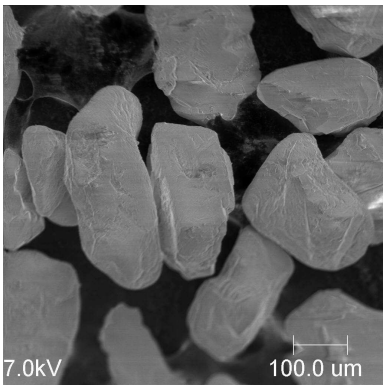	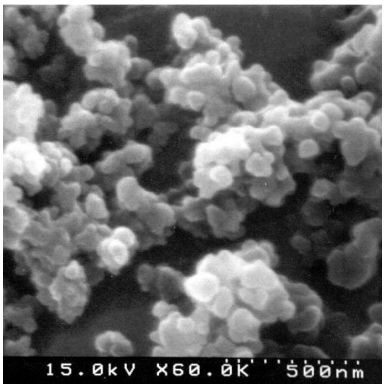
D_{50} = 120µm G_s = 2.65 S_a = 0.019m^2/g e_{max} / e_{min} = 0.848 / 0.535 Sphericity = 0.7 Roundness = 0.7	D_{50} = 20µm G_s = 2.2 S_a = 5-7m^2/g by methylene blue method, 120 m^2/g by N_2 absorption Sphericity = 0.9 Roundness = 0.7
Crushed silt	**Kaolinite**
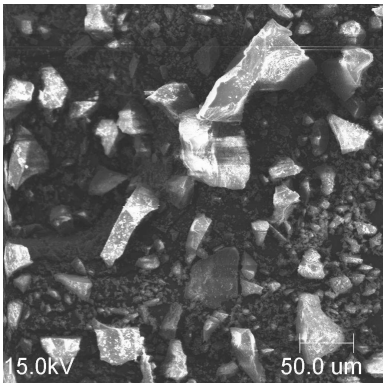	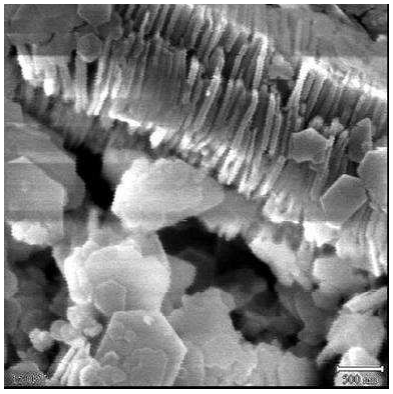
D_{50} = 20µm G_s = 2.65 S_a = 0.113 m^2/g e_{max} / e_{min} = 1.51 / 0.67 Sphericity = 0.9 Roundness = 0.1	D_{50} = 1.1µm G_s = 2.6 S_a = 36-37m^2/g by methylene blue method Sphericity = 0.7 Roundness = 0.1

Data sources: (Guimaraes 2002; Klein 1999; Parks 1990; Santamarina and Cho 2001)
SEM pictures: Courtesy of Angelica Palomino (2003)

pinducers and from 5 kHz to 70 kHz for bender elements depending on the sediment stiffness. The output signals are amplified with a multi-channel filter amplifier and logged with a digital storage oscilloscope operating at a sampling rate at least ten times higher than the frequency band of the measurements. The cell is submerged in to the chamber of which temperature is changed between 20°C and -10°C by circulating coolant from a cooler.

4.3.2 Materials

Soils: Sand, crushed silt, precipitated silt, and kaolinite clay are selected for this study to cover a wide range of particle size, specific surface, and particle shapes (Table 4.3). The selected quartz sand consists of uniform round particles and has low specific surface. The crushed silica flour silt has angular particle shape and low specific surface. The precipitated silica flour silt consists of an aggregation of smaller particles with inter-particle porous networks, so its specific surface is much larger than those for similar sized solid silt particles. Kaolinite has the smallest particle size among the tested sediments.

Tetrahydrofuran (THF, C_4H_8O): THF is a clear, colorless, low-viscosity liquid with an ether-like odor, high volatility, a low freezing point (-108.5^{o}C), and high miscibility with water. It forms structure II hydrate at a composition of 1:17 molar ratio, which corresponds to a volume fraction of 21.0% THF and 79.0% water. With this optimal solution, 100% of the pore fluid is converted into hydrate, and 50% of the pore fluid is converted into hydrate when the pore fluid consists of 10.5% THF and 89.5% water (excess water remains after hydrate formation) or 60.5% THF and 39.5% water (excess

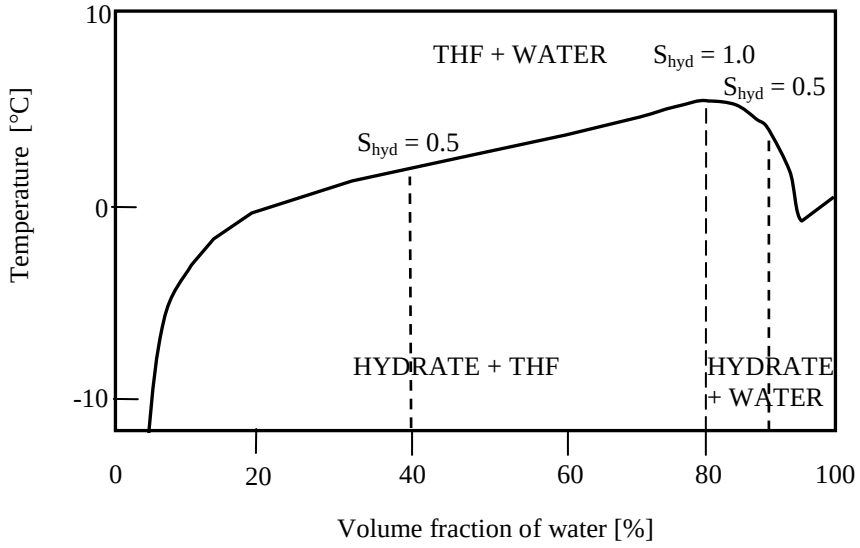

Figure 4.2 THF hydrate formation – Phase diagram for different THF-water volume fraction at atmospheric pressure (Data obtained from Makino et al. (2005)).

Table 4.4 Fluid compositions for experiments

	Fluid composition (by volume)		S_{hyd} after phase transformation
	THF [%]	Water [%]	
Deionized water	0	100	0.0 (Phase: water)
10 % THF solution	10.5	89.5	0.5 (Phase: hydrate + water)
20 % THF solution	21.0	79.0	1.0 (Phase: hydrate)
60 % THF solution	60.5	39.5	0.5 (Phase: hydrate + THF)

THF remains after hydrate formation). Details are tabulated in Table 4.4, and Figure 4.2 shows the phase diagram for THF and water mixtures.

4.3.3 Specimen Preparation

Specimens with S_{hyd}=0, 0.5, and 1.0 are prepared by thoroughly saturating soils with the pre-mixed THF and water solution. Mixture preparation lasts a few minutes to minimize selective evaporation of THF (The vapor pressure of THF is 160 mmHg.while that of pure water is 24 mmHg). Specimens are prepared under a ventilation hood. The S_{hyd} = 0.5 specimens for the high fluid pressure cell were prepared with 60% THF solution to avoid ice formation during rapid phase transformation under T=-10°C. The S_{hyd} = 0.5 specimens for the low pressure cell were prepared with 10% THF solution to properly capture the evolution of electric properties; therefore, these specimens require slow and moderate cooling in the cold room to prevent ice formation.

4.3.4 Test Procedures - Measurements

The vertical effective stress σ_v' was applied in four loading steps: 0.01, 0.1, 0.5, and 1.2 MPa in the low fluid pressure cell and 0.04, 0.5, 1, and 2 MPa in the high fluid pressure cell. The test sequence follows: (1) The external load is applied to the specimen without hydrates; (2) the specimen is completely consolidated; (3) the specimen temperature is lowered to induce hydrate formation; (4) the temperature is subsequently increased to provoke hydrate dissociation; and (5) a new load is applied. These steps are repeated until the maximum load is reached. After the final loading step, the frozen specimen is unloaded to simulate core extraction in the field.

The temperature ranges and cooling methods vary according to experiments. The temperature ranges from 20°C to -10°C for both specimens with 20% and 60% THF solution pore fluid in high pressure cell, and temperature is controlled by circulating coolant in the cooling chamber where the cell is submerged. The temperature changes from 10°C to -10°C for specimens with 20% THF solution pore fluid in low pressure cell, and temperature is controlled by putting dry ice at the cell wall at constant cold room temperature (10°C). The specimen temperature ranges from 10°C to -5°C, and the temperature is controlled by changing cold room temperature 1°C per 30 minutes.

4.4 RESULTS

4.4.1 Volume Change (Low Pressure Cell)

Figure 4.3 shows the void ratio at the end of consolidation for each loading step in the low fluid pressure cell tests, during both loading (without hydrates) and unloading (with hydrates). The compression index C_c describes the slope of the normal consolidation line in e-log σ_v' plot, while the swelling index C_s is the slope during unloading. Values of C_c and C_s are summarized in Table 4.5. Overall, C_c increases as the specific surface of sediments increases and as hydrate saturation S_{hyd} increases except for clay. Sand and crushed silt specimens have stable fabrics under quasi-static loading and exhibit relatively low C_c values. On the other hand, in precipitated silt and clay specimens, the void ratio decrease significantly during loading, resulting in high C_c values. Also, as S_{hyd} increase, the degree of freezing/thawing induced consolidation increases resulting in higher C_c.

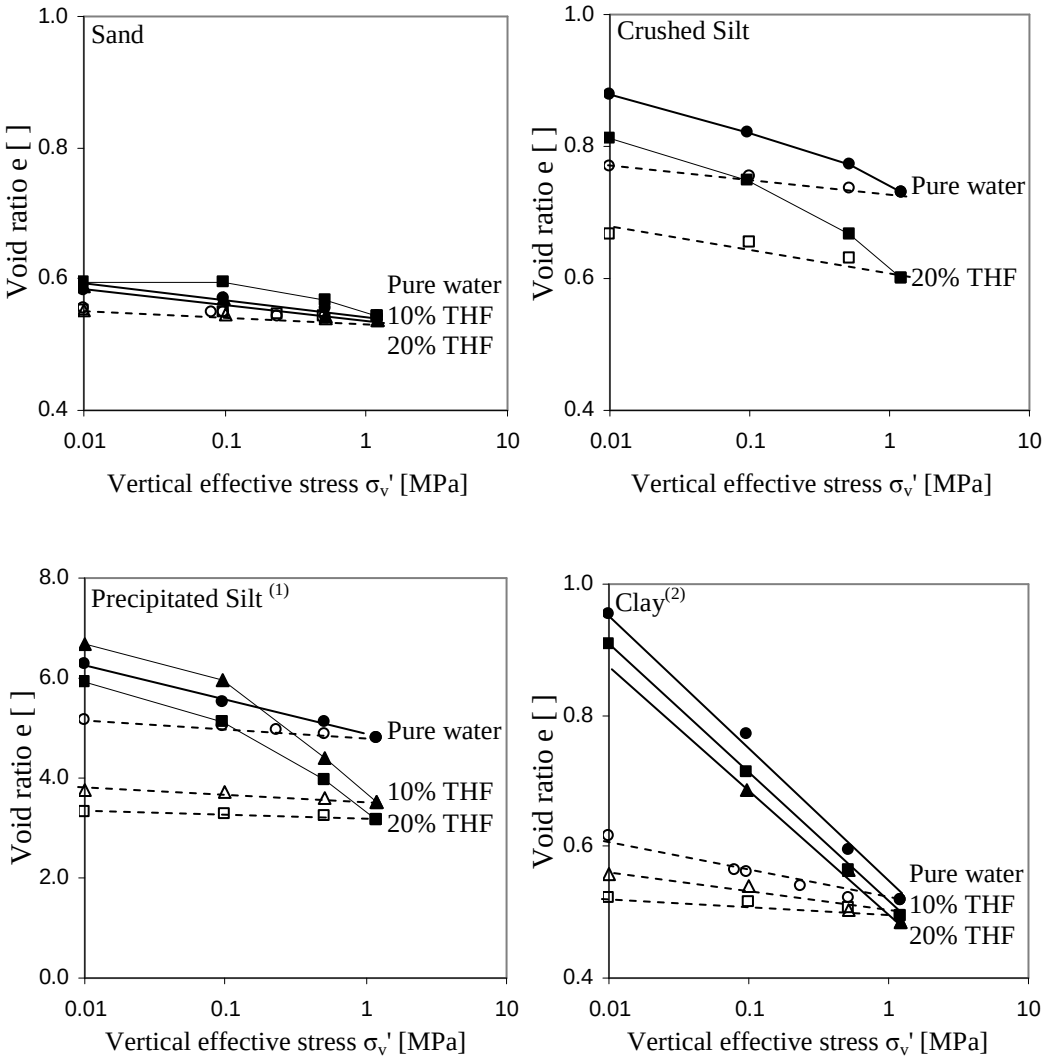

Figure 4.3 Void ratios versus effective stresses - Four sediments and three pore fluids. The pore fluid composition is indicated for each dataset. Load is applied at a temperature above phase transformation, i.e. to the specimen without hydrates. Specimens are unloaded at a temperature below phase transformation, i.e. with hydrates. Note: (1) Precipitated silt is plotted in a wider range of void ratio. (2) For the 50% hydrate specimen, material loss occurred during the third (0.5 MPa) and the fourth (1.2 MPa) loading steps. For the 100% hydrate specimen, material loss occurred during the fourth (1.2MPa) loading step. Circles indicate pure water pore fluid specimen, triangles indicate 10% THF pore fluid specimen, and rectangles indicate 20% THF pore fluid specimen. Solid symbols with solid lines are loading path, and hollow symbols with dotted lines are unloading path.

The volume change during unloading shows that C_s increases as the specific surface of sediments increases. In sediments with high specific surfaces, C_s decreases as hydrate saturation S_{hyd} increases, indicating that hydrates in pores reinforces the tensile strength of specimen that resist tension induced by depressurization.

Table 4.5. Summary of C_c and C_r

	S_{hyd}=		S_{hyd} increases →			S_{hyd} increases →		
			0.0	0.5	1.0	0.0	0.5	1.0
			Cc			Cs		
			C_c increases →			C_s decreases →		
Specific surface increases ↓	Sand	C_c and C_s increase ↓	0.02	0.03	0.04	0.01	0.01	0.01
	Crushed silt		0.08	-	0.12	0.03	-	0.03
	Clay		0.21	0.20	0.20	0.05	0.04	0.02
	Precipitated silt		0.70	1.60	2.10	0.14	0.12	0.05

4.4.2 P- and S-wave Velocities

Typical examples of S- and P-wave signals for the clay specimens with S_{hyd}=1.0 are shown in Figure 4.4 and 4.5. Before hydrate formation, the first arrival time decreases as the vertical effective stress increases, indicating that the P- and S-wave velocities are dependent on the effective stress, which plays a critical role in controlling the stiffness of uncemented sediments (Santamarina et al. 2001). On the other hand, the arrival times in hydrate-bearing sediments are nearly independent on the vertical effective stress. The frequency components in wavelets also change before and after hydrate formation.

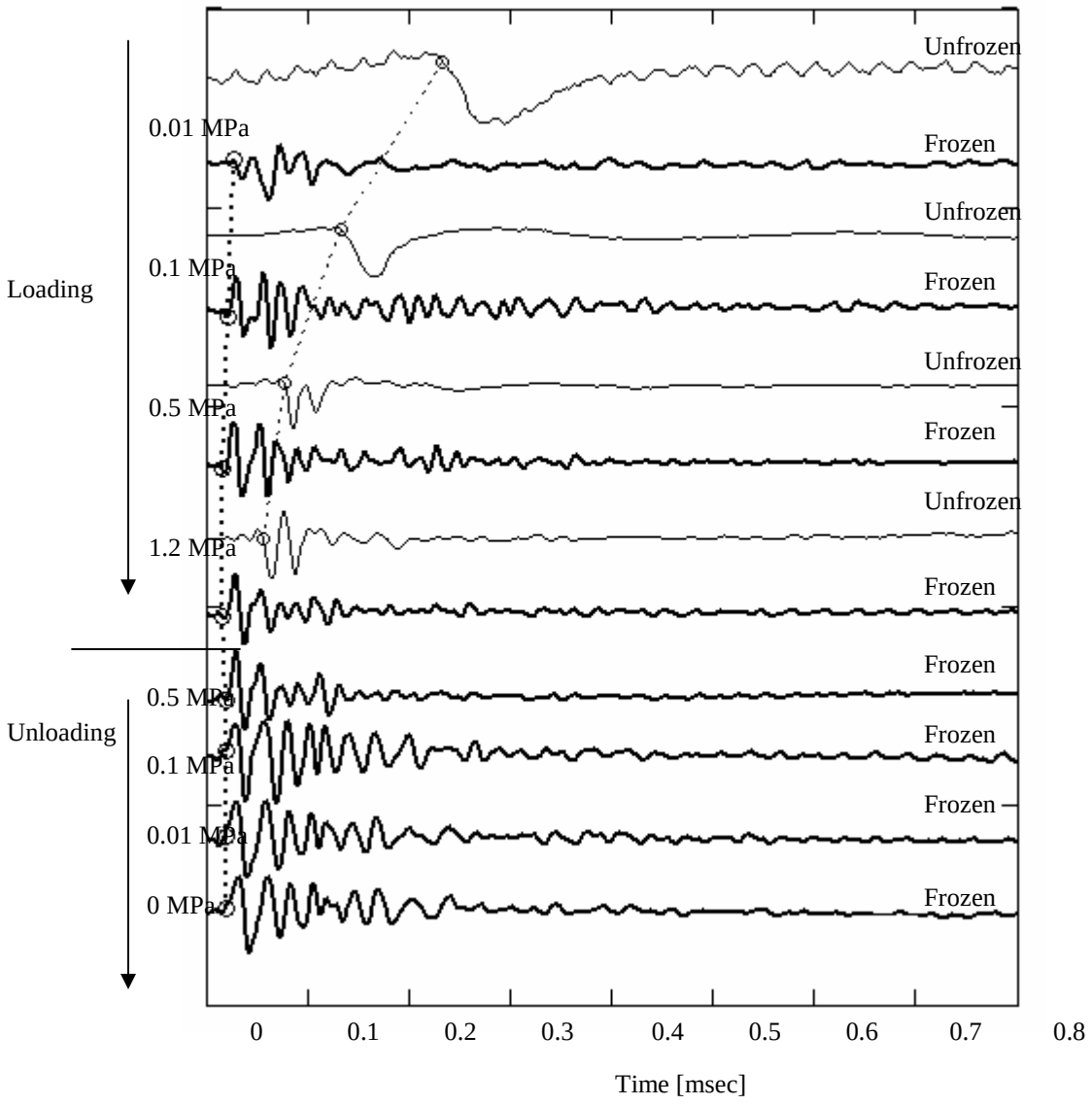

Figure 4.4 Evolution of shear wave signals for clay specimen with 20% THF solution as pore fluid in low fluid pressure cell (i.e. S_{hyd} = 1.0 after hydrate formation)

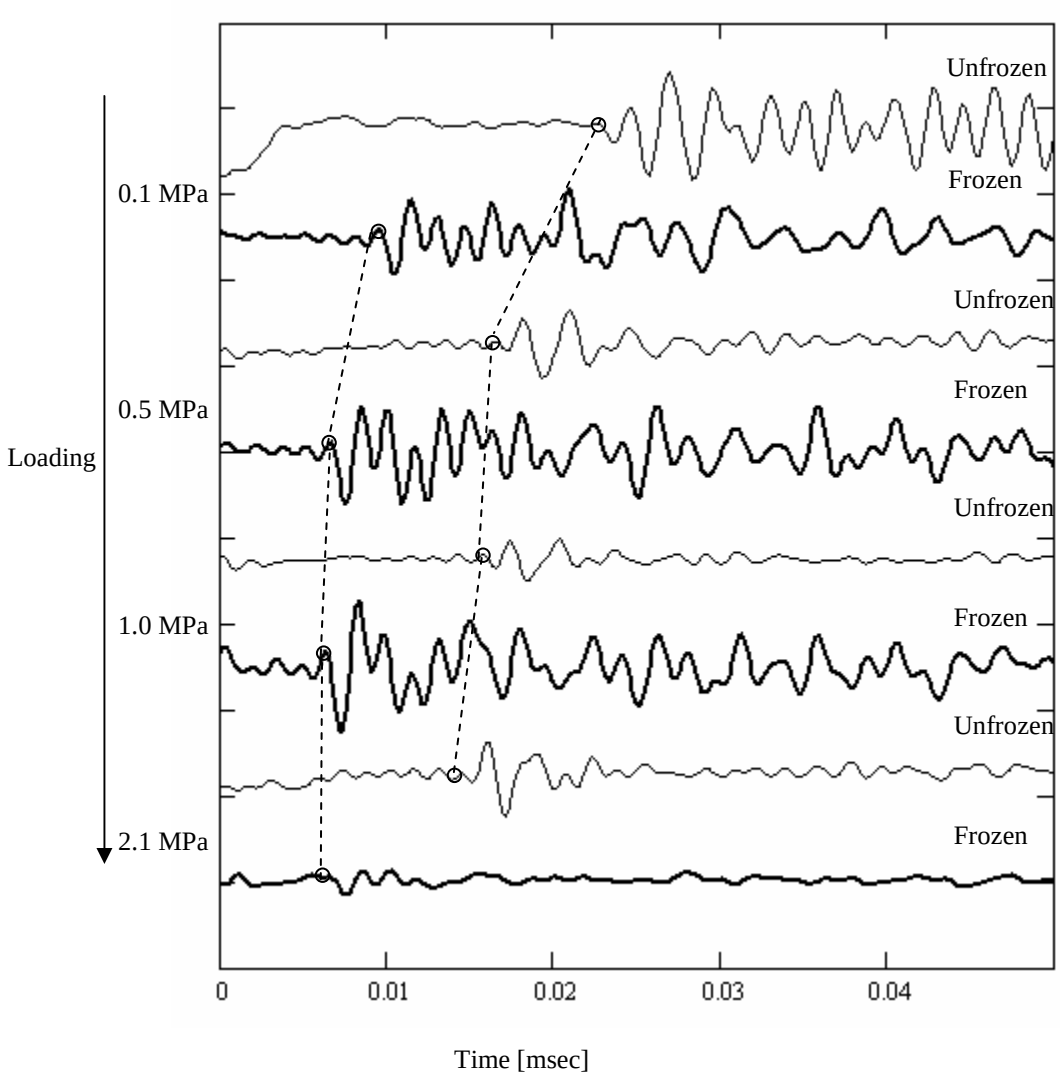

Figure 4.5 Evolution of P-wave signals for clay with 20% THF solution as pore fluid in high fluid pressure cell during loading and hydrate formation.

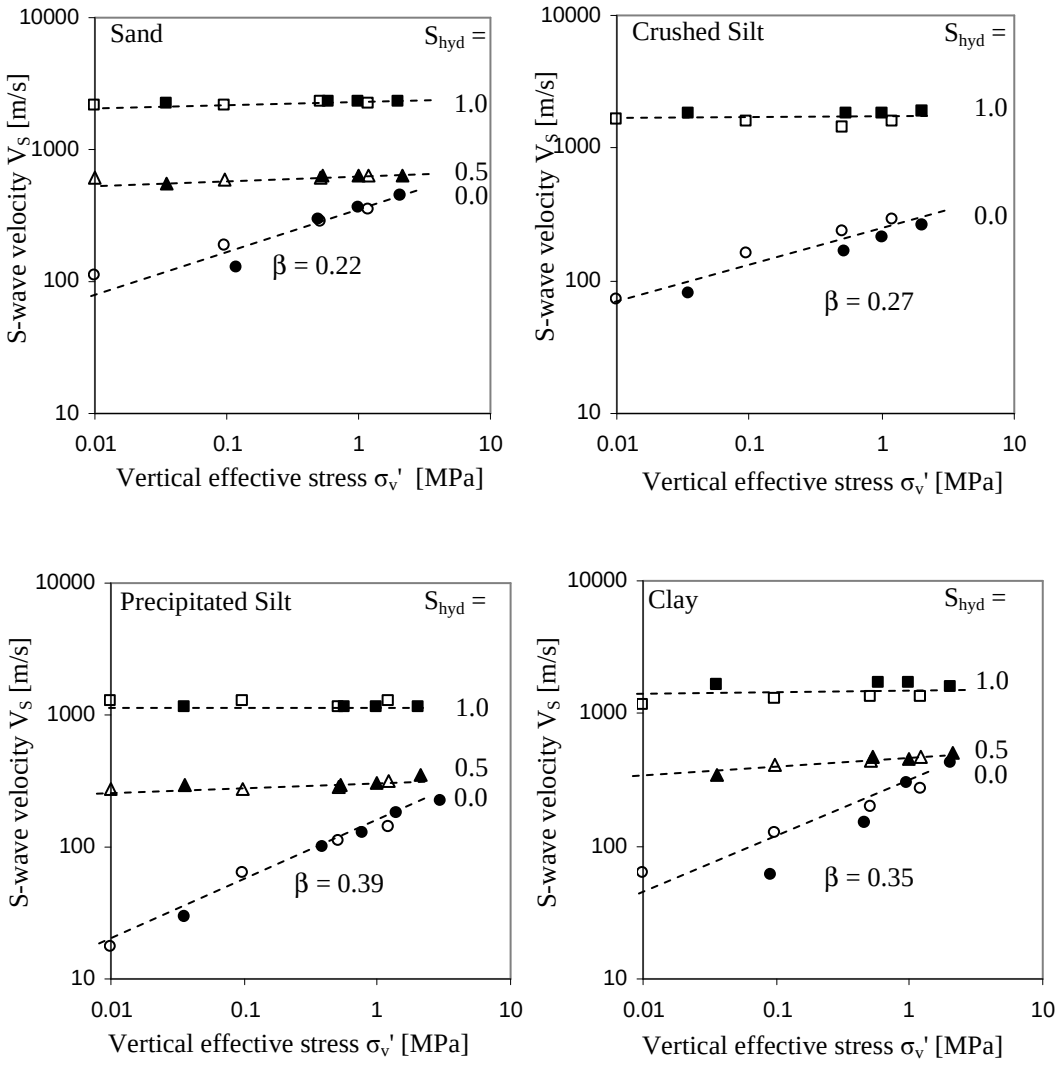

Figure 4.6 S-wave velocity versus vertical effective stress for different hydrate concentration in the pore space S_{hyd}. Circles indicate pure water pore fluid specimen, triangles indicate 10% THF pore fluid specimen, and rectangles indicate 20% THF pore fluid specimen. (Filled symbols: high pressure oedometer cell, open symbols: regular oedometer cell)

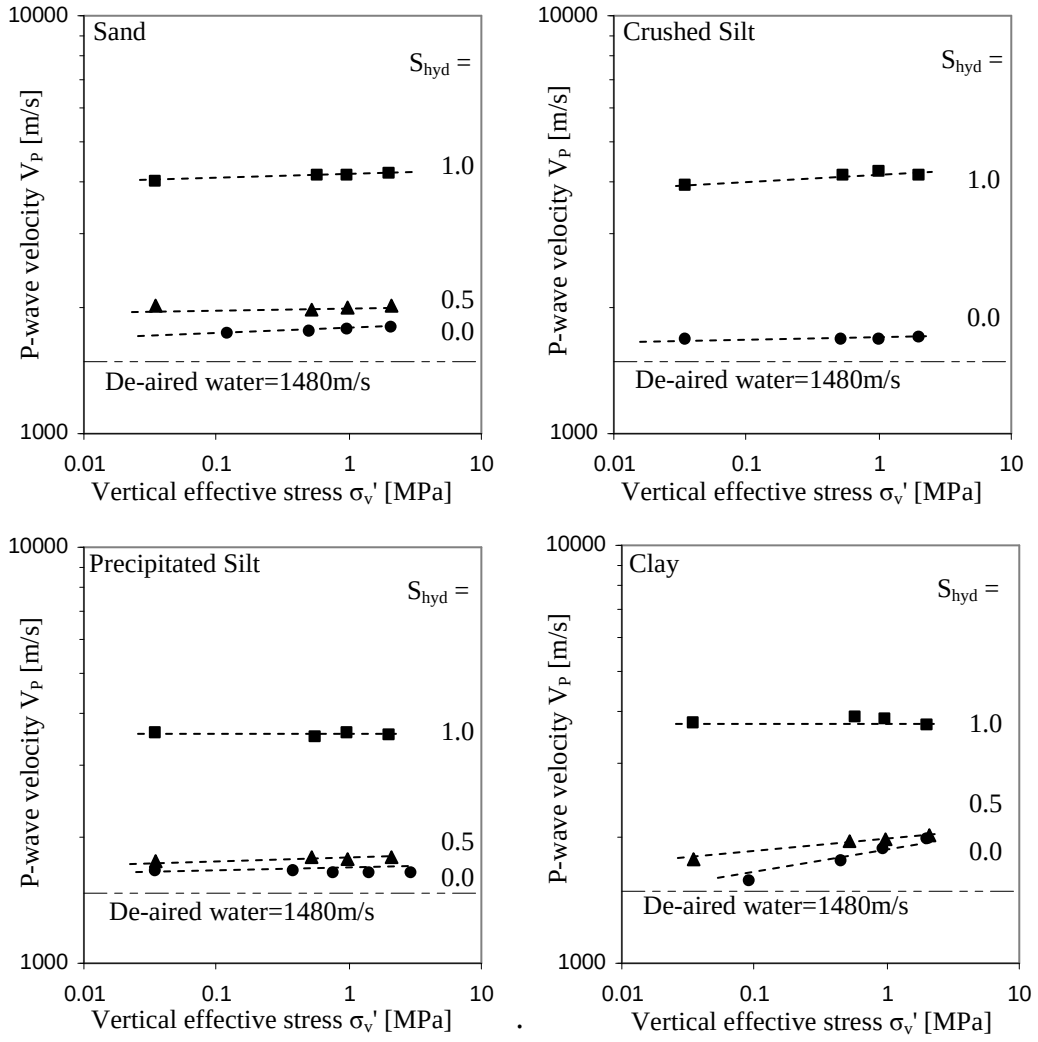

Figure 4.7 P-wave velocity versus vertical effective stress for different hydrate concentration in the pore space S_{hyd} (high fluid pressure cell). Circles indicate pure water pore fluid specimen, triangles indicate 10% THF pore fluid specimen, and rectangles indicate 20% THF pore fluid specimen.

The summary plots in Figure 4.6 shows S-wave velocities gathered using the two test devices (low and high fluid pressure cells) by two different operators. Figure 4.7 shows complementary P-wave velocity (data available only for the high pressure cell). Several observation can be made from these figures:

- The shear stiffness of soils without hydrates (S_{hyd} =0.0) increases with effective stress, i.e., Hertzian-type behavior. The slope β of the $\log V_S$-$\log \sigma_v'$ indicates the nature of contact behavior and fabric changes: stiffer contacts and more stable fabrics exhibits lower β values.
- The changes in P-wave velocity along with the vertical effective stress are small (Figure 4.7). In all cases, measured P-wave velocities are above 1480 m/s, which is the P-wave velocity for de-aired water.
- The S-wave velocity of hydrate-bearing specimens is much higher than that of non hydrate-bearing specimens. The influence of effective stress on S-wave velocity decreases as S_{hyd} increases, and the slope β becomes near zero for S_{hyd} = 1.0.
- Both P- and S-wave velocities exhibit a large increase after hydrate formation in specimens with S_{hyd} = 1.0.

4.4.3 Permittivity and Electrical Conductivity

The spectral response of deionized water, pure THF, THF solutions, and THF hydrates are shown in Figure 4.8. The real permittivity κ′ of water and THF solutions decreases with frequency, and the electrical conductivity σ_{el} increases with frequency due to the orientational polarization of water. On the other hand, the premittivity and

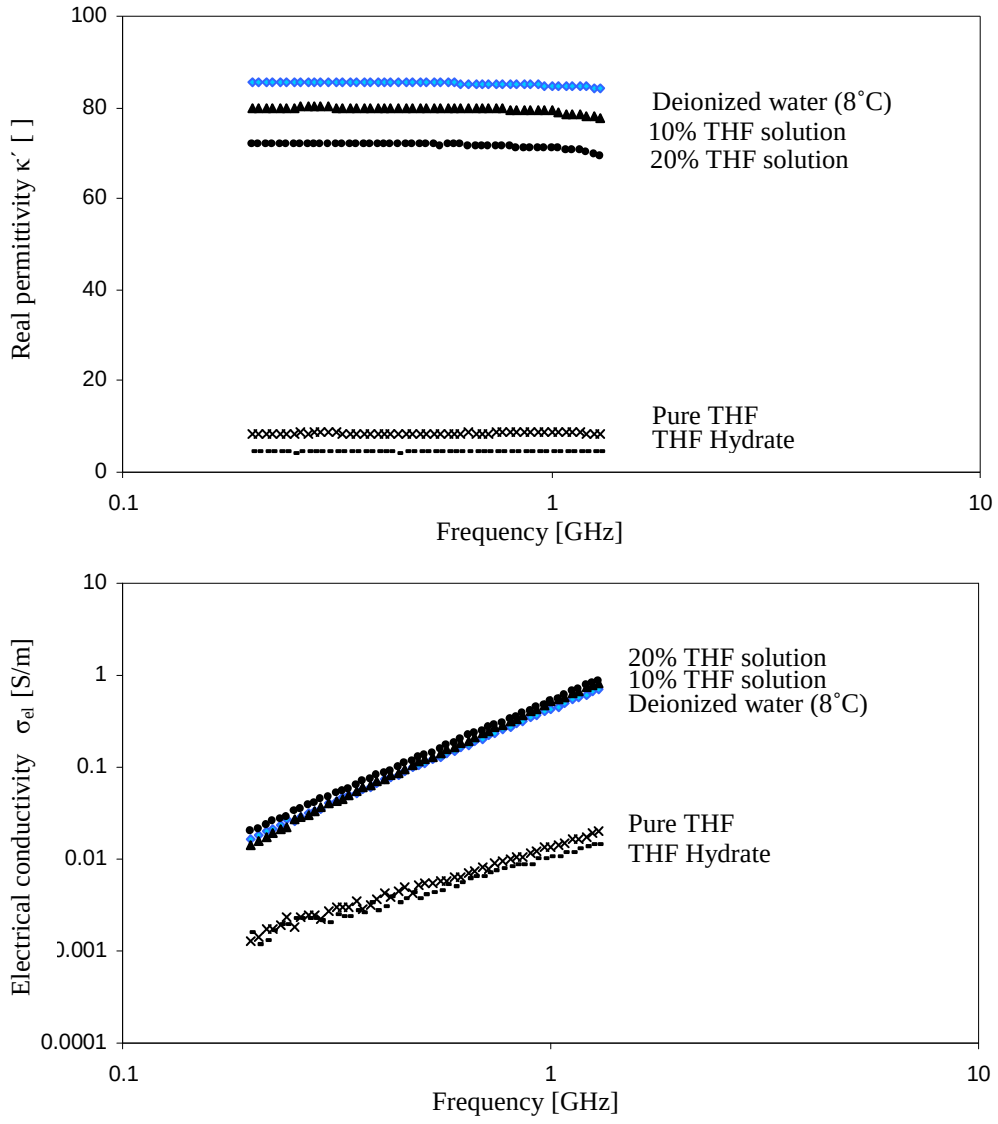

Figure 4.8 Spectral response of water, THF, THF solution, and THF hydate.

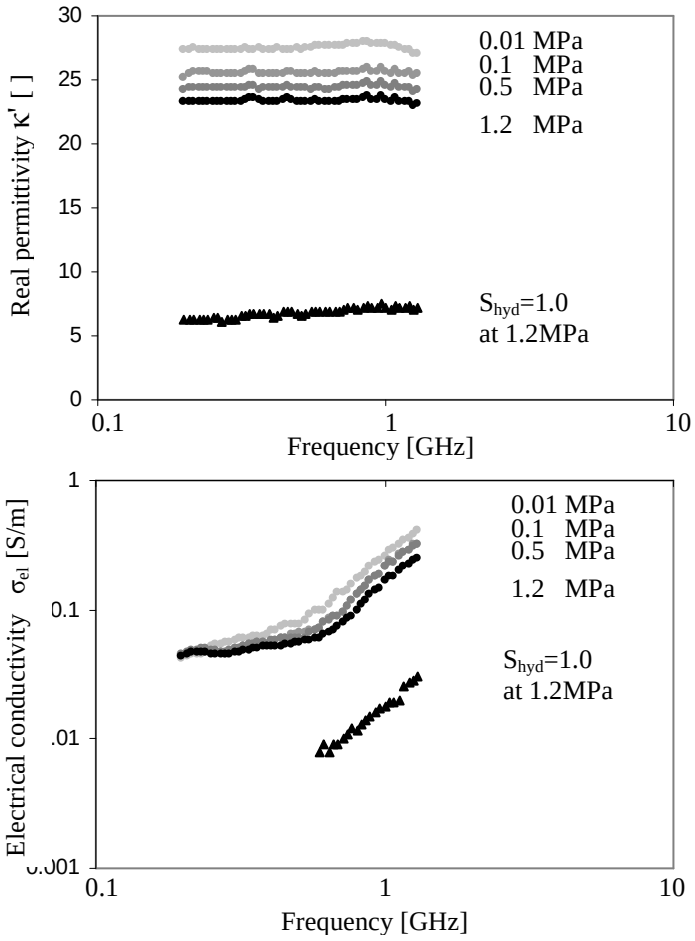

Figure 4.9 Evolution of permittivity spectrum during consolidation of clay specimen with 20% THF solution as pore fluid (T = 10°C, S_{hyd} = 0.0).

conductivity of THF and THF hydrate are very low due to low polarizability and more or less constant with frequency.

Typical spectral permittivity plots gathered from the clay specimen without hydrates at different effective stress levels and with hydrates at 1.2 MPa are shown in Figure 4.9. As the effective stress increases, κ' and σ_{el} decrease due to the decrease in the volume fraction of free water. A pronounced decrease in polarizability and conductivity occurs upon hydrate formation.

The real permittivity κ' and the electrical conductivity σ_{el} measured at 1GHz for all specimens are plotted against the vertical effective stress in Figures 4.10 and 4.11. The following observations can be made:

- *S_{hyd}=0.0 specimens*: As the vertical effective stress increases, the real permittivity and the electrical conductivity decrease due to the reduction in void ratio, i.e. the volume fraction of water.
- *S_{hyd}=0.5 specimens*: The real permittivity and the electrical conductivity values are lower than those for S_{hyd}=0.0 specimens since hydrates occupy 50% of the pore volume.
- *S_{hyd}=1.0 specimens*: The real permittivity is in the range of non-polarizable materials, and the electrical conductivity has fallen to undetectable, near-null values. In contrast to S_{hyd}=0.0 specimens, the real permittivity of S_{hyd}=1.0 specimens slightly increases as the vertical effective stress increases and the void ratio decreases. This is probably due to the increase in the volume fraction of unfrozen bounded water as the pore volume decreases while the amount of bounded water on particle surface remains constant.

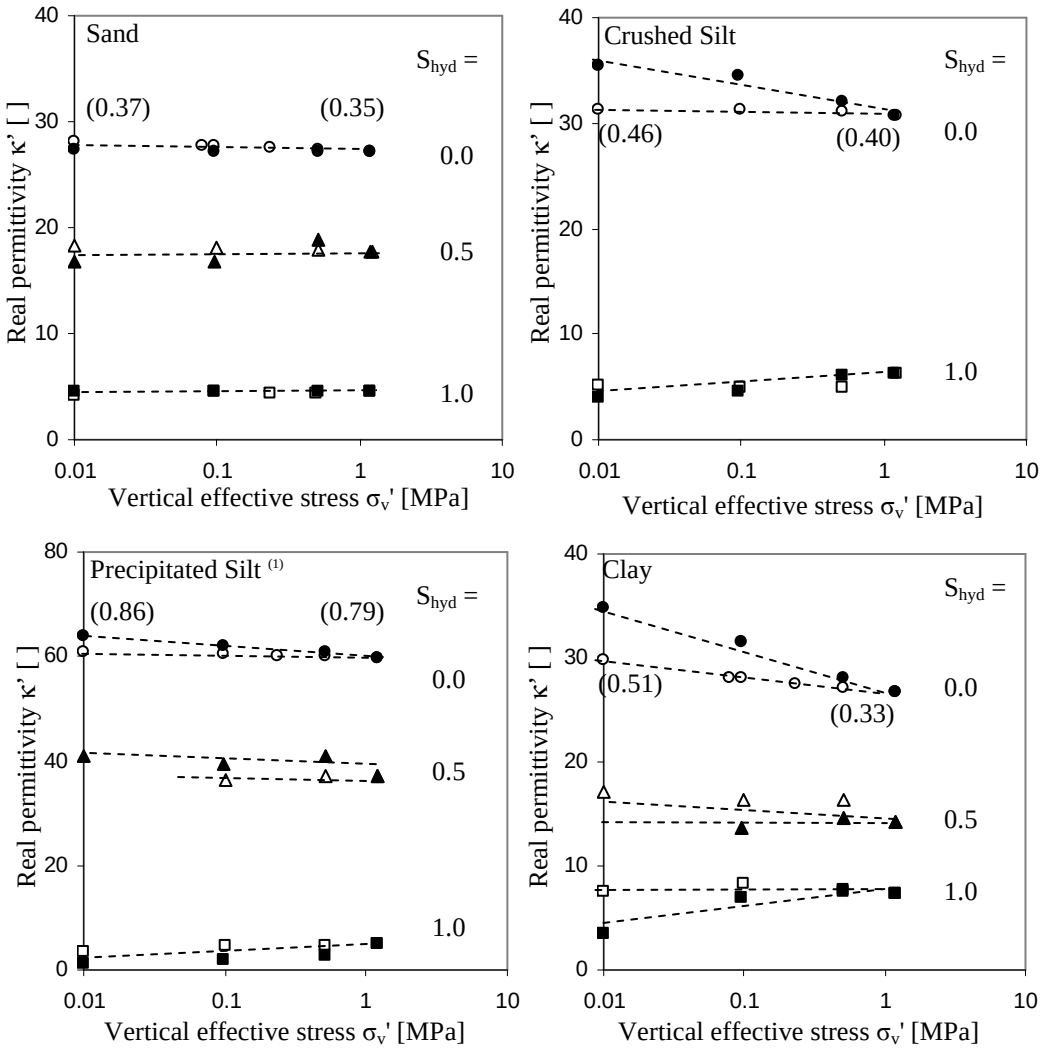

Figure 4.10 Real permittivity (at 1.0 GHz) versus vertical effective stress for different hydrate concentrations S_{hyd} in the pore space (Low fluid pressure cell). Black dots indicate loading, white dots indicate unloading, and numbers in parenthesis indicate mean porosity. Circles indicate pure water pore fluid specimen, triangles indicate 10% THF pore fluid specimen, and rectangles indicate 20% THF pore fluid specimen.
Note: (1) Precipitated silt is plotted in a wider void ratio range.

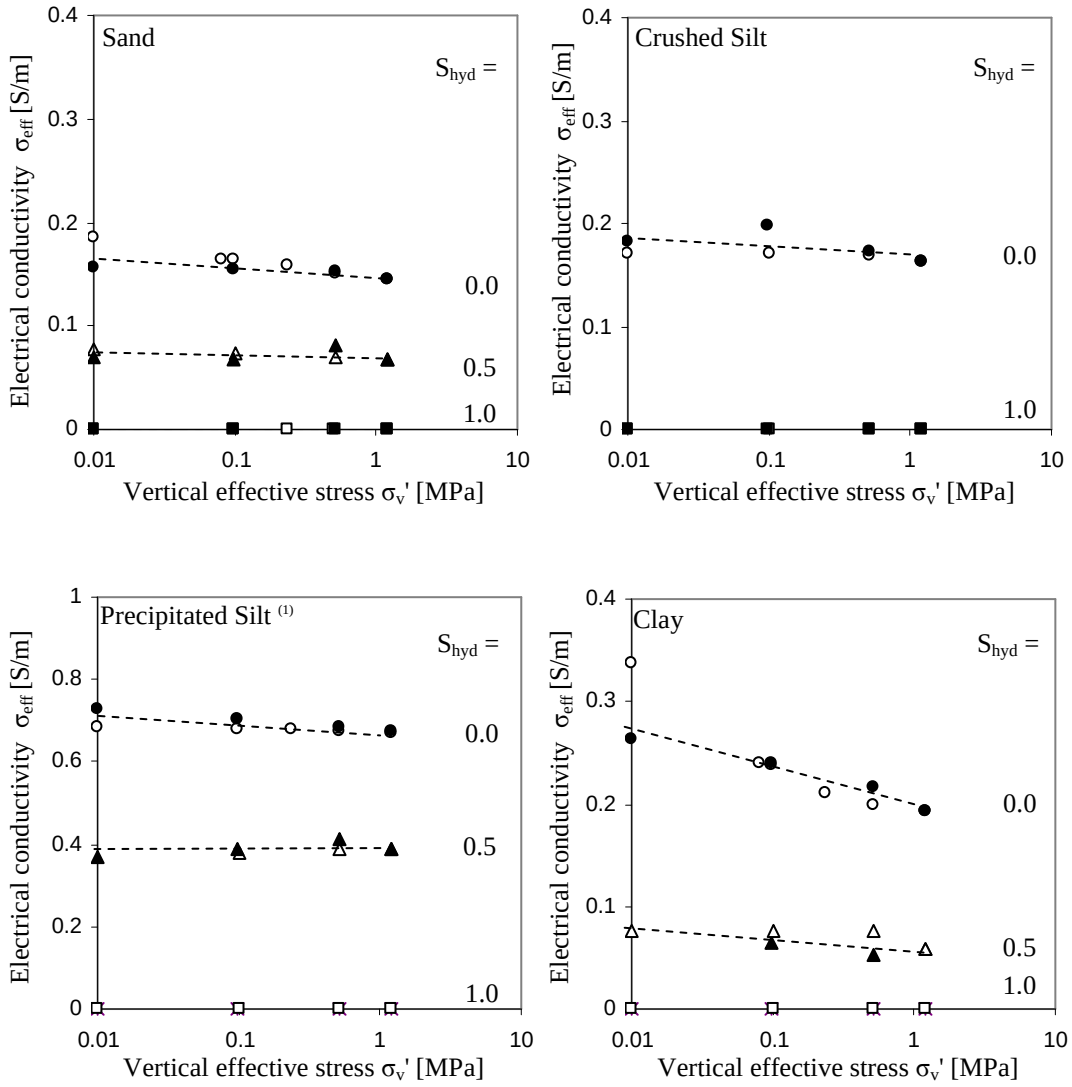

Figure 4.11 Effective conductivity (at 1.0 GHz) versus vertical effective stress for different hydrate concentrations S_{hyd} in the pore space (low fluid pressure cell). Black dots indicate loading, white dots indicate unloading, and numbers in parenthesis indicate mean porosity. Circles indicate pure water pore fluid specimen, triangles indicate 10% THF pore fluid specimen, and rectangles indicate 20% THF pore fluid specimen.
Note: (1) Precipitated silt is plotted in a wider void ratio range.

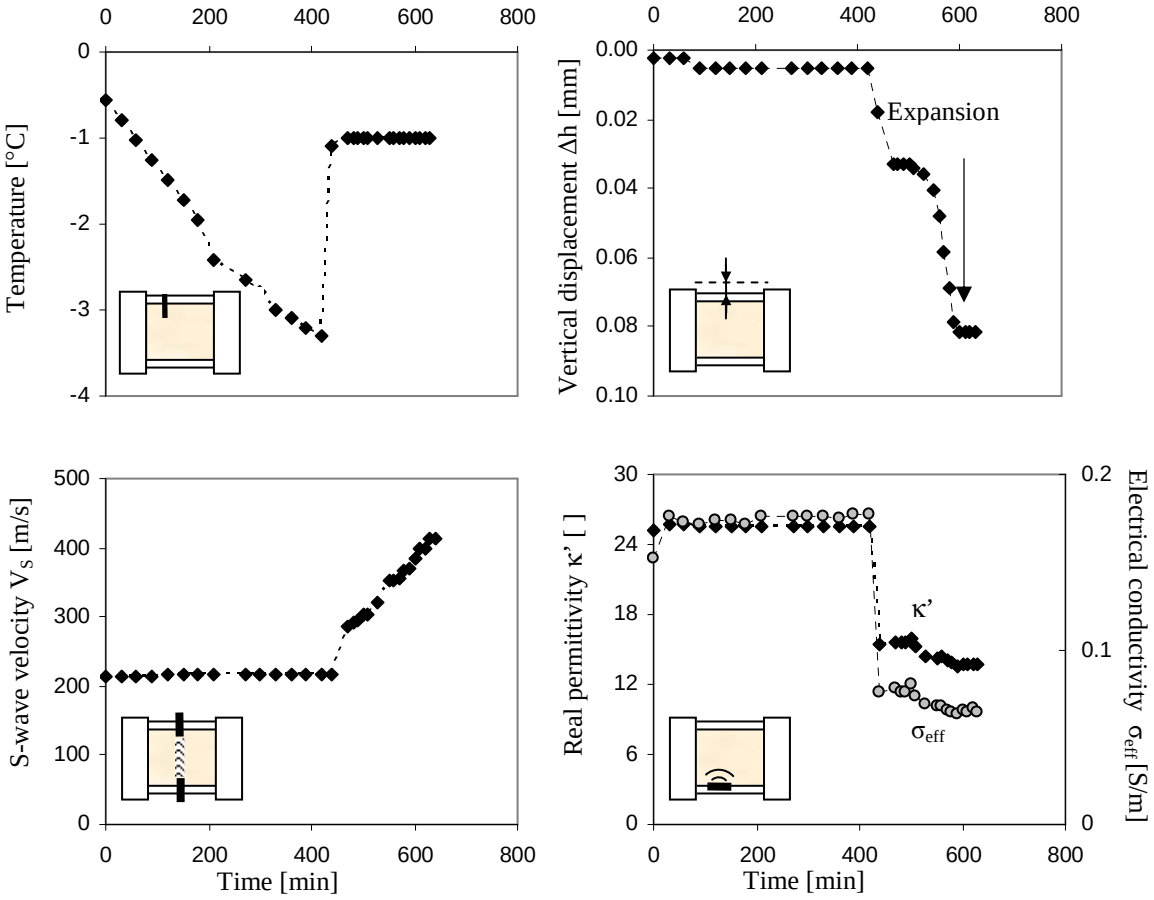

Figure 4.12 Phase transformation in a clay specimen with 10% THF solution (Vertical effective stress = 0.5 MPa). Volume change and S-wave velocity are global measurements across the specimen, and temperature and permittivity are local measurements.

4.4.4 Phase Transformation

Temperature T, vertical deformation Δh, S-wave velocity V_S, and complex permittivity (κ′ and σ_{el}) are monitored during the phase transformation. Figure 4.12 shows the evolution these parameters in S_{hyd} = 0.5 specimen. The cold room temperature is lowered to -4˚C, and hydrates start to form after 420 minutes. The temperature of the specimen decreases until it reaches -3.5˚C, which corresponds to 8˚C of supercooling, and then increases abruptly, indicating the initiation of exothermic hydrate formation. The vertical displacement increases gradually producing ε_{vol}=0.0008. The S-wave velocity starts to increase 20 minutes after the initiation of hydrate formation and continues to increase until it reaches 640 m/s. On the other hand, the electrical parameters σ_{eff} and κ' decrease instantly from 25.51 S/m to 15.41 S/m for σ_{el} and from 0.18 to 0.08 for κ′. These differences in response time of measurements are related to locality of each measurement: the complex permittivity is a local measurement at the bottom of the specimen, while the S-wave velocity represents the average change along the specimen height.

4.5 ANALYSES AND DISCUSSION

4.5.1 Volume Change due to Hydrate Formation/Dissociation Cycle

Soils deform when subjected to an increased effective stress until they reach a new stable configuration at a lower void ratio. This equilibrium is altered during hydrate formation and dissociation. Figure 4.13 shows data for four cycles of loading, hydrate

formation, and hydrate dissociation for clay specimens with 10% and 20% THF pore fluid solutions.

THF hydrate formation induces volume expansion by S_{hyd}·7.4% of original pore volume, when the volume expansion is calculated with the densities of pore fluid and THF hydrate. This volume expansion can cause a pore pressure increase and/or alter skeletal equilibrium when S_{hyd} is high and porosity is low. Therefore, either contraction or expansion may occur during formation. On the other hand, contraction is always observed upon dissociation. The dissociation-associated contraction is greater than possible formation related expansion, so the net volume change during a formation/dissociation cycle is always contraction. The degree of contraction during a formation/dissociation cycle increases as specific surface increase, as S_{hyd} increases, and as the effective vertical stress decreases.

Published data with frozen soils (i.e. 100% pore space becomes frozen) show that the void ratio after a formation/dissociation cycle is independent of the previous stress history, so the consolidation properties change after every formation/dissociation cycle (Nixon and Morgenstern 1973). For this reason, C_C are different for S_{hyd}=0.0, 0.5, and 1.0 specimens even when the specimens consists of identical sediments (Table 4.5)

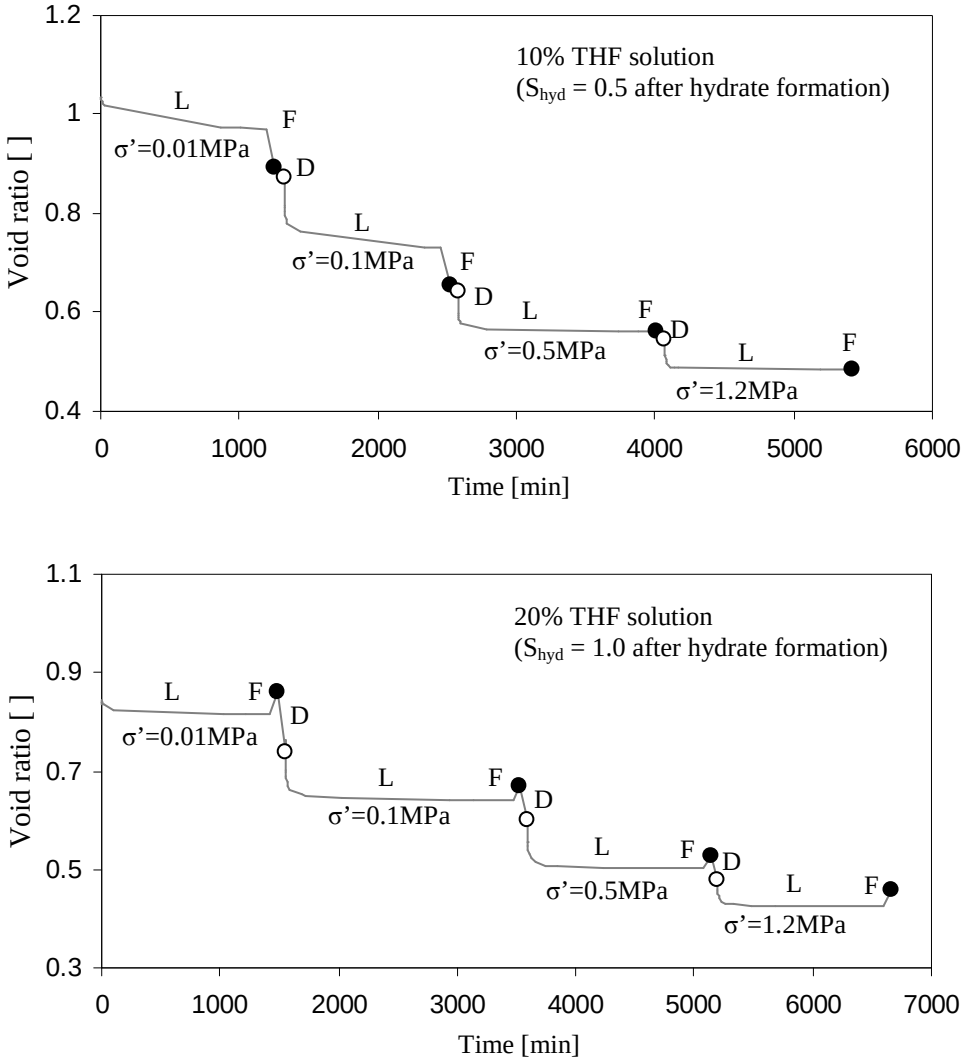

Figure 4.13 Volume changes in clay specimens induced by loading (L), hydrate formation (F), and dissociation (D)

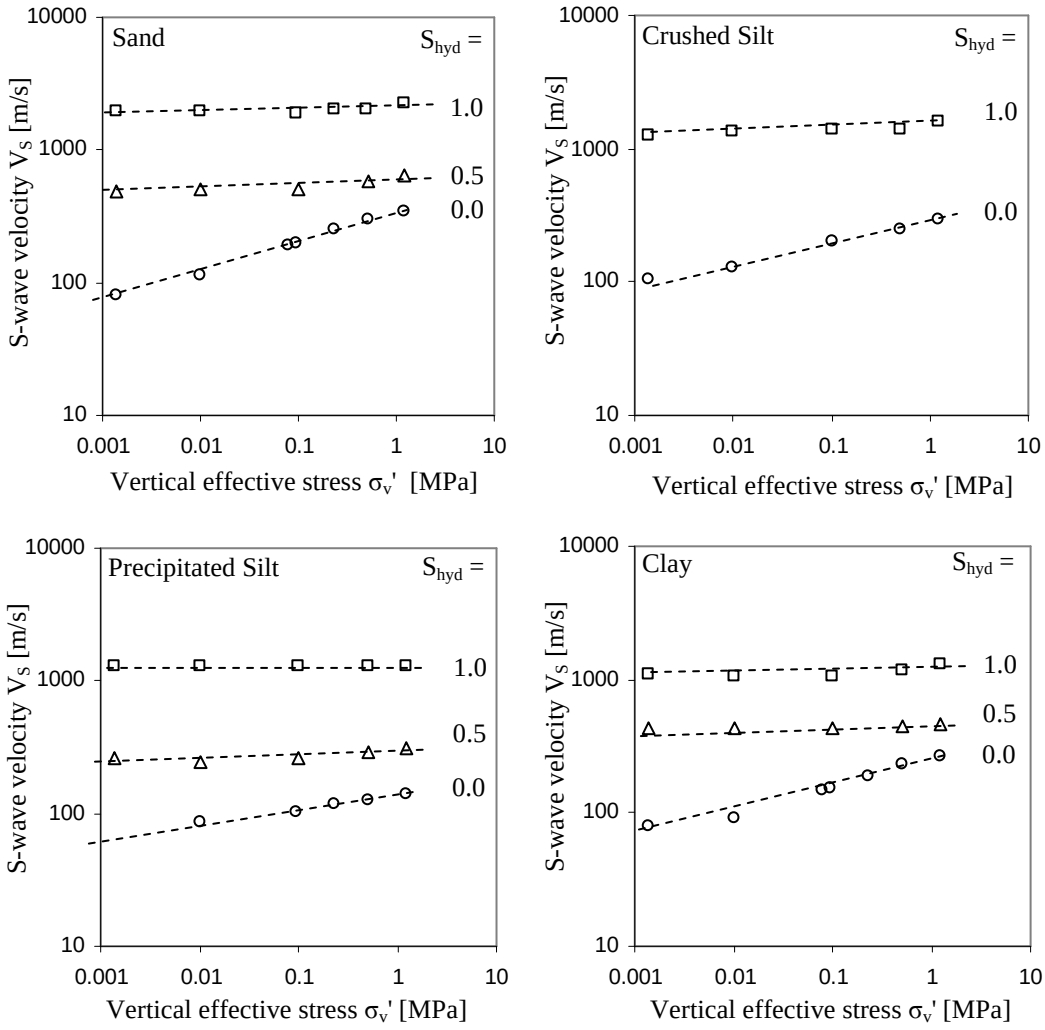

Figure 4.14 Shear wave velocity versus vertical effective stress for different hydrate concentration in the pore space S_{hyd} during unloading. Circles indicate pure water pore fluid specimen, triangles indicate 10% THF pore fluid specimen, and rectangles indicate 20% THF pore fluid specimen.

4.5.2 Sampling Effect

S-wave velocity (small strain mechanical property) evolution during unloading clearly indicates that the small strain stiffness evolution along the depressurization is significantly governed by S_{hyd} (Figure 4.14). The swelling index C_s (large stain mechanical property) of high specific surface material is also markedly decreased by S_{hyd} (Figure 4.3 and Table 4.5). These results indicate that hydrate in pores can bind soil particles and resist the tension associated to decompression during sampling or excavation. The equilibrium conditions of methane hydrate should be considered for field applications.

Therefore, the probability of sampling hydrate-bearing sediments without disturbing the original sediment fabric increases at low in-situ vertical effective stress, in low specific surface sediments, and with higher hydrate concentration. It is anticipated that the specimen should be restored to the in-situ effective stress as soon as possible to prevent pressure induced dissociation and diffusion. Clearly, these observations presume that pore fluid pressure and temperature conditions are maintained within the stability field.

4.5.3 P- and S-wave Velocity vs Hydrate Saturation

P-wave velocity data gathered in the high pressure cell are plotted against S-wave velocity in Figure 4.15. The concave trend indicates that the V_P increases at a lower rate than the V_S when S_{hyd} is lower. The bulk modulus can be estimated from V_P and V_S with Equation (4.1) and (4.2), and the estimated bulk modulus is plotted with parallel, series, and Hashin-Shtrikman bounds in Figure 4.16. The results show that hydrates do not

increase the bulk modulus significantly until hydrates fill most of the porosity. Experimental results approach the lower bounds (series type structure) for low S_{hyd} and the upper bound (parallel type structure for high S_{hyd}.

The P- and S-wave velocities according to S_{hyd} are plotted in Figure 4.17 together with data from literatures and modeled lines. Effective elastic moduli for cementation models are calculated using the cementation theory in (Dvorkin et al. 1994), and Modified Hashin-Strikman lower bound (Dvorkin and Nur 1996) is used for pore filling model. Parameters used for modeling are $K_{hydrate}$=5.6GPa, K_{grain}=36GPa, K_{fluid}=2.0GPa, $G_{hydrate}$=2.4GPa, and G_{grain}=45GPa. The wave velocity trends are either concave or convex, and these differences are caused by the different hydrate synthesis methods (Lee et al. 2007). For example, in specimens synthesized by percolating gas in unsaturated sediments, hydrate tends to form near contacts and particle surfaces, inducing significant increase in small-strain stiffness with relatively small amount of hydrates. On the other hand, small-strain stiffness does not increase significantly until $S_{hyd} \approx 0.5$ in specimens synthesized with flushing methane dissolved water since hydrates tends to grow into pore spaces. Data in this study exhibit characteristics similar to those of specimens synthesized by flushing methane dissolved water implying that the nucleation and growth of THF hydrate are similar to those of methane hydrate synthesized from dissolved methane.

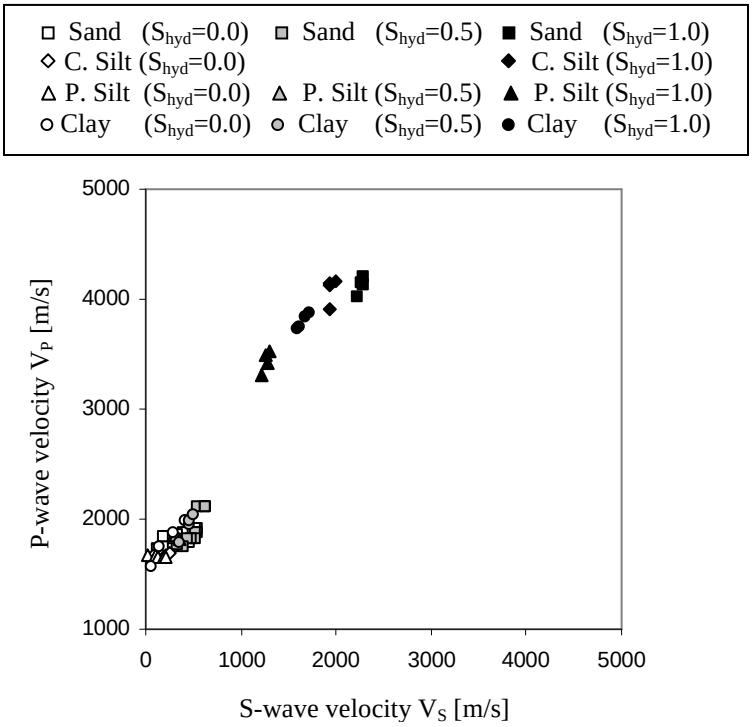

Figure 4.15 P-wave velocity against S-wave velocity

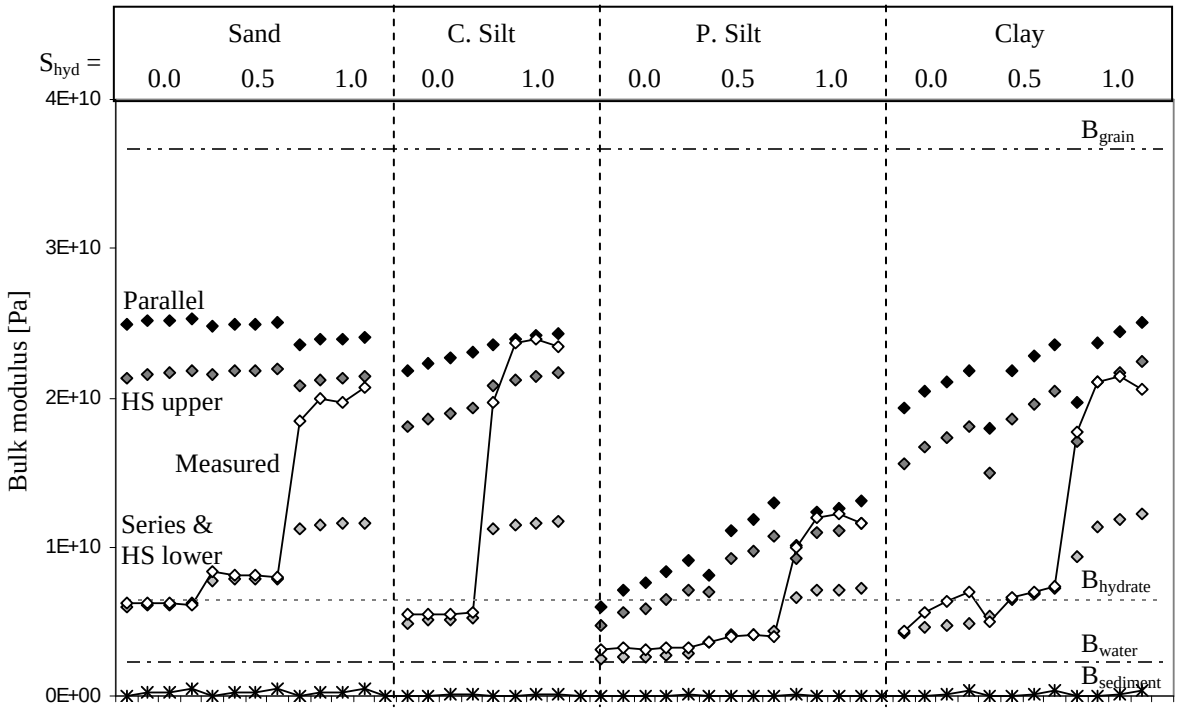

Figure 4.16 Parallel, series, and Hashin-Shtrikman bounds for bulk modulus

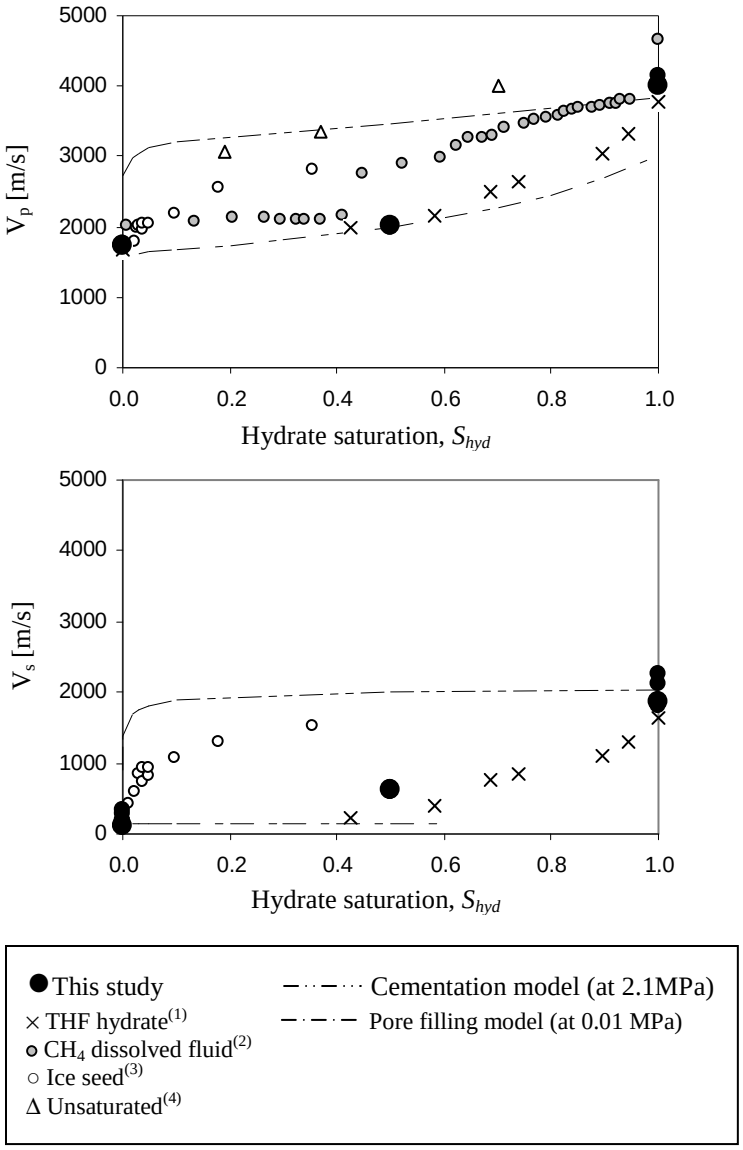

Figure 4.17 P- and S-wave velocities in sand specimens according to hydrate saturation. (1) Yun et al. 2005 (2) Spangenberg, E., and Kulenkampff, J. 2005 (3) Priest et al. 2005 (4) Winters et al. 2005. See Table 4.2 for detailed experiment conditions.

4.5.4 Fluid-filled Porosity

Experimental data confirm that effective stress, porosity, and hydrate saturation are the main factors that govern the mechanical properties of hydrate-bearing sediments. Since both hydrates and minerals are solid phase, the porosity and the hydrate saturation can be expressed with fluid-filed porosity n_{fl} as following.

$$n_{fl} = \frac{V_{fluid}}{V_{hydrate} + V_{soil} + V_{fluid}} \tag{4.7}$$

Fluid-filled porosity should exhibit strong correlation with geophysical measurements, considering the distinct electrical and mechanical properties of fluids and solids, and the correlations are explored as follows.

P-wave and S-wave: Figure 4.18 shows P- and S-wave velocity data for all soils, stress levels, and hydrate concentrations. Elastic wave velocities show a slight increasing trend along n_{fl}, but they are not distinct since the influence of stress conditions and soil type obscured the effect from n_{fl}.

Permittivity: Real permittivity values at 1 GHz for all soil types, stress levels and hydrate concentrations are plotted against water-filled porosity instead of fluid-filled porosity since the contribution of THF to orientational polarization is as low as that of soil particles (Figure 4.19). The real permittivity in microwave frequency is a robust tool to assess the volume fraction of water since it is not affected by ionic concentration or soil structure. The single trend that well fits all data in Figure 4.19 also confirms the robustness. The equation for the trend line is as following.

$$\kappa' = 13.3\times(V_w/V_t)^2+56.8\times(V_w/V_t)+5.4 \tag{4.8}$$

Conductivity: The normalized conductivity σ_{el}/σ_{fl} for all sediments is plotted as a function of the fluid-filled porosity in Figure 4.20. The best fitting trend is in power form, which is

analogous to the simplest and most extensively used formula, Archie´s law. The scattering of data is due to the different tortuosity of pores according to different soil type. Abnormally high conductivity is obtained in precipitated silt, indicating significant surface conduction due to high specific surface.

4.5.5 Hydrate Saturation Estimation with Electrical Conductivity

The conductivity of porous sediments can be obtained by Archie's equation (Archie 1942),

$$\sigma_{el} = a\sigma_{fl} n^{m}, \tag{4.9}$$

where σ_{fl} is the pore fluid conductivity, and a and m are fitting coefficients. The exponent m is related to the sediment structures such as the degree of cementation and geologic age of the formation, and usually more cementation and tortuosity produces higher m values (Jahrling and Tait 1996; Sen et al. 1981; Wong et al. 1984). The values of a and m coefficients from literature are tabulated at Table 4.6.

Figure 4.21 shows the relation between electrical conductivity and porosity at the end of the consolidation for all loading stages and for 10% THF solution specimens (becomes S_{hyd}=0.5 specimens after hydrate formation). Power Archie-type equations are fitted to the electrical conductivity data and used to estimate the fluid-filled porosity. The hydrate saturation is estimated from the measured electrical conductivity in S_{hyd}=0.5 specimen to assess the performance. The estimated values become more accurate when the data used in model fitting cover wider range of porosity as in clay specimen. The change in m exponent induced by change in tortuosity after hydrate formation also can be an error source. For example, the m exponent in the sand specimen increased after

hydrate formation implying that sand specimens gain tortuosity, and m exponent in the precipitated silt specimen decreased implying that tortuosity is reduced after hydrate formation.

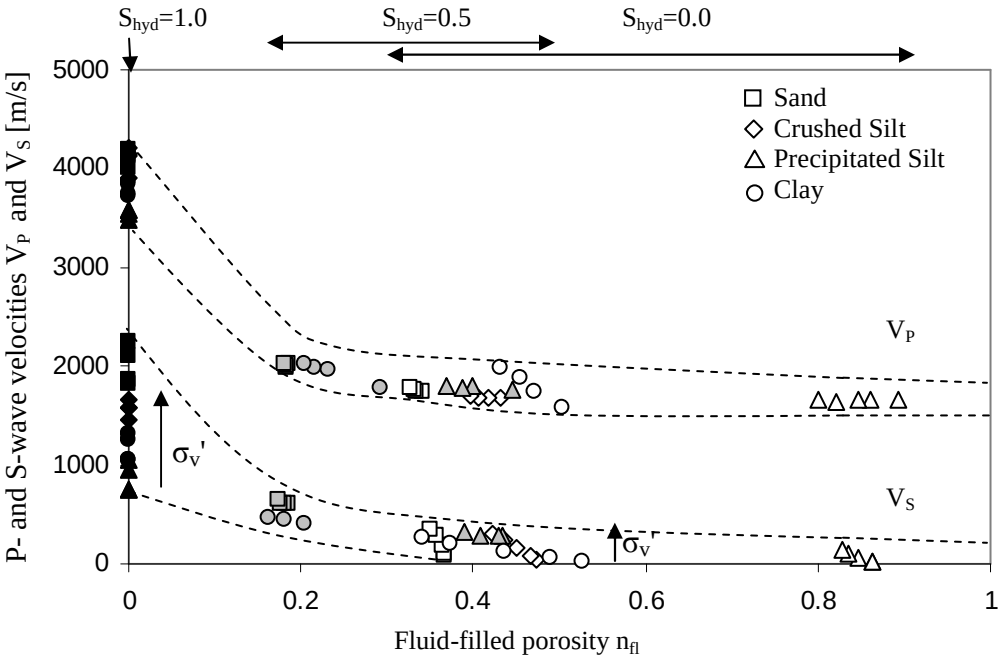

Figure 4.18 P- and S-wave velocities as a function of fluid filled porosity n_{fl}. Circles indicate pure water pore fluid specimen, triangles indicate 10% THF pore fluid specimen, and rectangles indicate 20% THF pore fluid specimen. (Black: S_{hyd}=1.0, gray: S_{hyd}=0.5, and white: S_{hyd}=0.0)

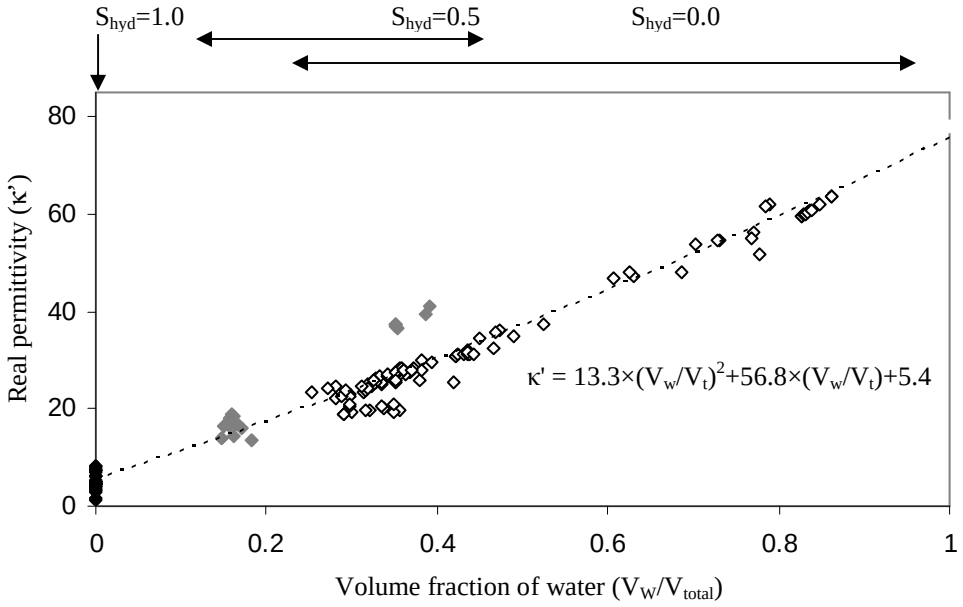

Figure 4.19 Empirical relationship between real permittivity (at 1.0 GHz) and volume fraction of water (Black: S_{hyd}=1.0, gray: S_{hyd}=0.5, and white: S_{hyd}=0.0)

.

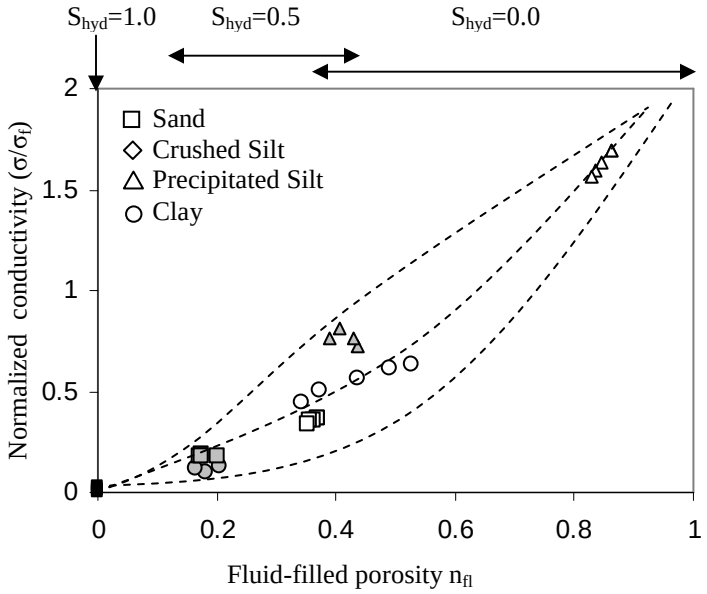

Figure 4.20 Electrical conductivity normalized by the conductivity of the pore fluid as a function of fluid filled porosity n_{fl} Circles indicate pure water pore fluid specimen, triangles indicate 10% THF pore fluid specimen, and rectangles indicate 20% THF pore fluid specimen. (Black: S_{hyd} = 1.0, gray: S_{hyd} = 0.5, and white: S_{hyd} = 0.0)

Table 4.6 Coefficients a and m of Archie's law used in literature

m	a	location	Description	Reference
2.7	0.90	Blake Ridge, USA	Deep sea sediment drift deposit, Mud and silt	(Paull 1996)
2.56	1.05	Blake Ridge, USA	Deep sea sediment drift deposit, Mud and silt	(Collet and Ladd 1999)
2.15	0.62	Mackenzie Delta, Canada	Non-gas-hydrate-bearing sediments	(Jin et al. 2002)
1.92	0.81	Mackenzie Delta, Canada	Gas-hydrate-bearing sediments	(Jin et al. 2002)
1.5	1.00	Lab test	Fonatinebleau sand (D_{50}=0.2mm) with porosity of 0.43	(Jahrling and Tait 1996)
1.72	1.00	Lab test	Fonatinebleau sand (D_{50}=0.2mm) with porosity of 0.43 with voids patially filled with ice crystals	(Jahrling and Tait 1996)

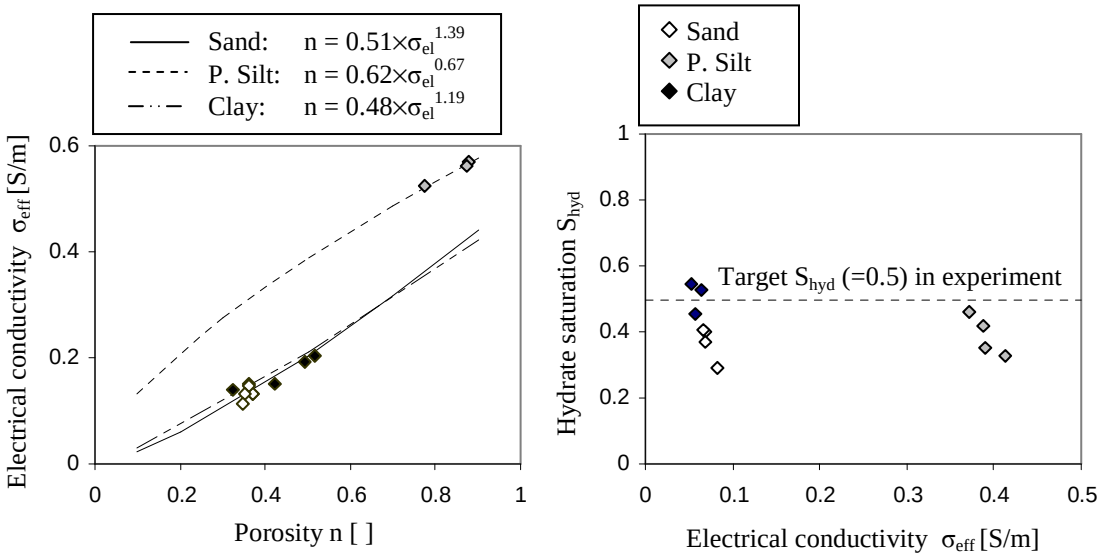

Figure 4.21 Hydrate saturation estimation with electrical conductivity data for S_{hyd}=0.5 specimens.

4.6 CONCLUSIONS

The formation of hydrates in the pore space of sediments alters the elastic and electromagnetic properties of soil-fluid mixtures. The measurement of the elastic and electromagnetic properties of sediments enables the quantification of the amount of hydrates in sediments and tracking of the formation process of hydrates in sediments.

- The S-wave velocity is mainly determined by the coordination number and the contact area between particles. The formation of hydrates reinforces the shear modulus by increasing internal coordination and enlarging contacts. There is a relatively low increase in shear modulus until the hydrate concentration exceeds ~40%; thereafter, the presence of hydrates has a decisive impact on skeletal coordination and stiffness.
- The P-wave velocity increases as hydrates form due to the increase in the bulk modulus of the mixture and shear modulus of the skeleton.
- Dielectric permittivity in the microwave frequency range is a good indicator of the volume fraction of free water in the sediment. The formation of hydrates reduces the volume fraction of free water in mixtures.
- Electrical conductivity is a measure of ionic mobility and concentration in the pore fluid, and the fluid volume fraction in the mixture. Hydrate formation causes ion exclusion and conductivity does not correlate linearly with the volume fraction of hydrates formed. Formation history, such as the time of reaction as compared to the time of diffusion must be considered in data interpretation

CHAPTER V.

MECHANICAL AND ELECTROMAGNETIC PROPERTIES OF NORTHERN GULF OF MEXICO SEDIMENTS WITH AND WITHOUT HYDRATES

5.1 INTRODUCTION

The impact of ice on the physical properties of host sediments has long been a subject of intense research in the geotechnical literature, but only in recent years has there been a major focus on understanding the properties of sediments containing another frozen substance—gas hydrate (e.g., Francisca et al., 2005; Yun et al., 2006a, 2006b, 2007). Gas hydrate consists of a hydrogen-bonded water lattice surrounding guest gas molecules of low molecular weight. Methane is the most common guest molecule, but higher order hydrocarbons, hydrogen sulfide, and carbon dioxide also form gas hydrates under appropriate pressure and temperature conditions. Compared to ice, which persists only in permafrost regions, gas hydrates are far more widespread, occurring in both permafrost sediments to depths of ~1 km and deep marine sediments at water depths greater than ~300 m on the world's continental margins.

The scientific motivations for studying gas hydrates include their potential as an unconventional hydrocarbon resource, their possible role in global climate change, and/or their connection to seafloor geohazards such as slope failures. Laboratory studies that compare the geotechnical and geophysical properties of natural sediments both with and without gas hydrate can contribute to these larger themes in several ways. The resulting data can be used to calibrate changes in geophysical parameters with variations in gas

hydrate saturations for use in assessing resource potential, to provide insight into the impact of hydrate formation and dissociation on sediment properties for understanding the mechanical behavior of hydrate-bearing sediments, and to assess how coring and drilling of hydrate-bearing sediments affects their properties for evaluation of production technologies.

In this study, we report on the geophysical and geotechnical properties of natural sediments obtained during conventional coring in gas hydrate provinces in the northern Gulf of Mexico. The specimens are studied in both their undisturbed and remolded states and with and without synthetic hydrate. The results provide insight into processes accompanying the nucleation and growth of gas hydrate, new approaches to estimating hydrate-filled porosity using geophysical observables, and the impact of coring on hydrate-bearing sediments.

5.2 STUDY SITE

Specimens for this study were obtained during 2005 drilling by the ChevronTexaco Joint Industry Project (JIP) on Methane Hydrates at two sites in the Northern Gulf of Mexico (Figure 5.1). The northern Gulf of Mexico seaward of the shelf break is a complex passive margin setting characterized by a variable-thickness sedimentary section overlying deformed, allochthonous salt deposits. Salt dissolution and withdrawal have led to the formation of sediment-filled minibasins, which mostly occupy bathymetric lows, surrounded by ridges that are cored by salt and that form bathymetric highs (e.g., Diegel et al., 1995; Peel et al., 1995). Faults that accommodate the rising salt

play an important role in focusing fluid flow near the ridges at the edges of minibasins. Such faults often channel thermogenic gases upward toward the seafloor from deep hydrocarbon reservoirs (e.g., Sassen et al., 1999), leading to the formation of gas hydrates in the shallow subseafloor sediments and occasionally at the seafloor when appropriate pressure-temperature conditions are encountered by the ascending fluids. At some other high flux locations, biogenic gas hydrates prevail (Lorenson et al., 2005), forming either from biogenic gases created in situ in the sediments by microbial processes or through the migration of accumulated, older biogenic gas into the stability zone from elsewhere.

The two focus sites for the 2005 JIP drilling were Atwater Valley lease block 13 (AT13 at 28°N, 89.289°W and water depth of 1291m) and Keathley Canyon lease block 151 (KC151-3 at 26.823°N, 92.987°W and water depth of 1323m). Detailed descriptions of these sites are given elsewhere (e.g., GOMJIP, 2005). The Keathley Canyon site lies on a salt ridge at the edge of a mini-basin in a location at which a BSR has been imaged (e.g., Hutchinson et al., 2007). Drilling at the Atwater Valley site primarily focused on seafloor features identified before the cruise as possible gas hydrate mounds, but also included some reference sites. The AT13 sample analyzed in this paper was obtained at one of the reference sites. The KC and AT drilling sites were chosen to lie at approximately the same water depth since pressure represents an important control on gas hydrate stability. At the same time, the sites represent different endmembers in the spectrum from a low flux gas hydrate site characterized by a BSR (KC151) to high flux site with punctuated fluid flow at the gas hydrate mounds (AT13).

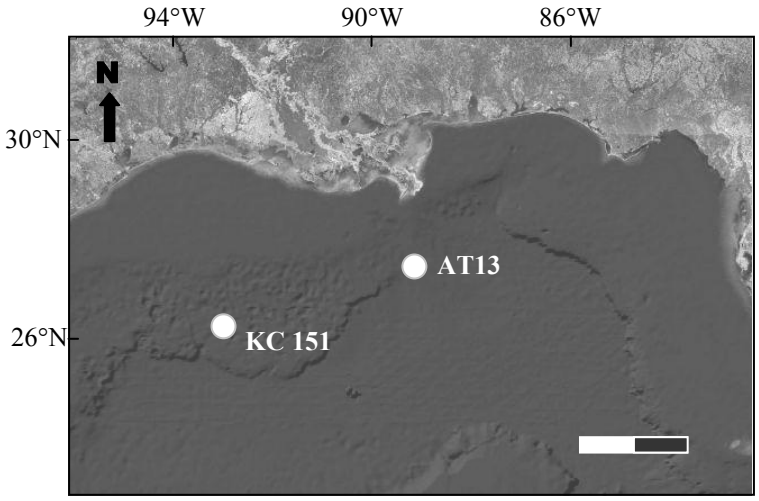

Figure 5.1. Locations at which cores used in this study were recovered during 2005 drilling in the northern Gulf of Mexico salt province.

5.3 SAMPLE DESCRIPTION

Geotechnical and physical properties results obtained on conventional (Yun et al., 2006a) and pressure cores (Yun et al., 2006b) recovered at the KC151 and AT13 sites have been previously documented. Data reported by Yun et al. (2006a) indicate that the specific surface S_a of the sediments at these sites varies from 62 m^2 g^{-1} to 143 m^2 g^{-1} in samples obtained from the uppermost ~150 m of sediments at AT13 and ~350 m at KC151. Such a high S_a suggests that the sediments are clay-dominated and likely indicates the presence of illite or/and montmorillonite. Based on the liquid limit LL (74.9 to 77.0 at AT13 and 51.2 to 66.6 at KC151) and the plastic limit PL (27.0 to 30.5 at AT13 and 20.7 to 22.7 at KC151), these sediments are classified as inorganic clays with

high plasticity, corresponding to designator CH in the Unified Soil Classification System (Yun et al., 2006a).

For this study, we used whole-round samples obtained at 0.65 m below seafloor (mbsf) at AT13 (core AT13-1H) and 275 mbsf at KC151 (core KC151-3-19H). Both specimens were retrieved using the Fugro hydraulic piston corer. Conventional cores acquired at depths closest to the depths of our specimens have S_a of 94.2 $m^2\ g^{-1}$ and 119.9 $m^2\ g^{-1}$ and water content of 123.9% and 36.1% for AT13 and KC151, respectively (Yun et al., 2006a). Reported pore fluid salinities at these depths are 3.5% by weight at AT13 and between 5.0% and 5.3% by weight at KC151 (M. Kastner, pers. comm., 2005). The samples we tested originally lay within the stability field for methane hydrate, but there is no evidence from either geophysical and geochemical data (GOMJIP, 2005) or textural analysis of the core material that the specimens may have contained gas hydrate in situ.

5.4 EXPERIMENTAL STUDY

This study was conducted using an instrumented oedometer cell to apply vertical effective stress to the sediment sample (7.62 cm high and 6.6 cm diameter) at zero-lateral strain. The cell contains sensors to record complex permittivity κ^*, S-wave velocity V_S, volume change ε_{vol}, and temperature T. The cell's design permits all measurements to be conducted at steady state (constant temperature) as well as during formation and dissociation of synthetic hydrate (changing temperature).

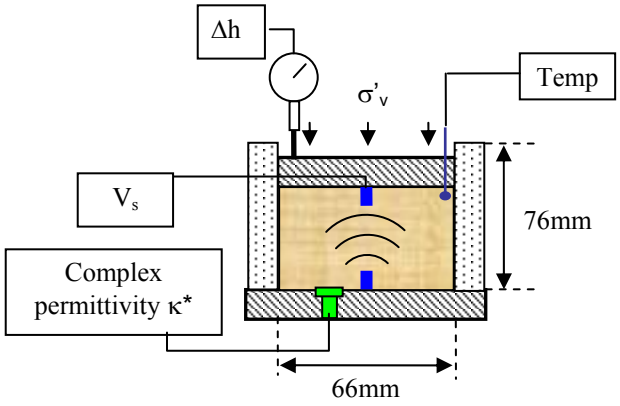

Figure 5.2. Schematic of oedometer cell, sensors, and peripheral electronics.

The temperature and complex permittivity sensors provide local measurements that average over only a small volume adjacent to the sensor. In contrast, the shear wave velocity represents a bulk, height-averaged value, primarily along the axis of the sample.

A K-type thermocouple mounted through the top endcap of the cell is used to monitor the specimen temperature with precision of 0.1ºC. Volume change is determined by tracking the instantaneous vertical position of the top cap using a linear variable displacement transducer (LVDT) with precision of 2.5×10^{-6} m.

Piezocrystal bender elements are used for S-wave measurements (Lee and Santamarina, 2005). The frequency content varies from 5 kHz to 70 kHz, depending on the sediment stiffness, which in turn reflects effective stress and/or hydrate saturation. The source is housed in the bottom plate and connected to a signal generator, while the receiver bender element is mounted in the top cap and connected to a filter/amplifier.

Both the signal generator and the filter/amplifier are connected to a storage oscilloscope that records data digitally.

The bottom plate houses the dielectric permittivity probe, which is connected to a computer-controlled network analyzer that measures the complex permittivity κ* between 200 MHz and 1.3 GHz. Complex relative permittivity is given by $\kappa^* = \kappa' + j\kappa''$, where κ' denotes the dielectric permittivity, j^2=-1, and the imaginary component κ'' includes both conduction and polarization losses, the latter being considered negligible. The electrical conductivity σ_{el} is given by $\kappa''\varepsilon_0\omega$, where ε_0 is the permittivity of free space (8.854×10^{-12} F m^{-1}), and ω denotes angular frequency.

5.4.1 Test Procedure

The oedometer cell, shown in Figure 5.2, is placed in a lever-type gravity loading frame to facilitate stable, longterm loading. The cell, the loading frame, and peripheral electronics are then placed in an environmental chamber at 4°C. The applied vertical effective stress σ_v' ranges from 0.01 to 1.2 MPa over 4 loading steps for the AT specimens and from 0.01 to 2.3 MPa over 5 loading steps for the KC specimens. This range of σ_v' covers not only the effective stress experienced by these specimens under in situ conditions, but also other stress conditions likely to prevail in shallow sediments of the northern Gulf of Mexico. The standard consolidation test procedure ASTM D2435 (ASTM, 2003) is followed during the tests for specimens without hydrates.

Specimens prepared for hydrate formation are subjected to additional steps: (1) Specimens are loaded at T=4°C without forming hydrates, with each loading step continuing until consolidation is complete; (2) the temperature is then reduced to induce

complete hydrate formation; (3) the temperature is subsequently increased to provoke dissociation of all hydrate; and (4) a new loading step is applied. After the final loading step, the frozen specimen is unloaded to simulate core extraction in the field.

THF is selected as hydrate former for this study because of its complete miscibility with water and its capacity to form hydrate from the aqueous phase, as methane hydrate probably forms over much of the thickness of the gas hydrate stability zone (e.g., Hyndman et al., 1992; Zatsepina and Buffett, 2003). A detailed discussion of advantages and disadvantages of using THF as hydrate former is presented in Lee et al. (2006). Over the range of conditions used for these experiments, the hydrate formation process appears to have a greater impact on mechanical properties than does the specific hydrate former (e.g., THF, methane; Yun et al., 2007).

5.4.2 Specimen Preparation

The AT and KC specimens were tested under three different conditions:

- Undisturbed without hydrates: A 5 cm-thick core slice was placed in the oedometer cell within its original plastic core liner to prevent additional disturbance.
- Remolded without hydrates: The specimen is dried in an oven, ground in a mortar, and mixed with deionized water to the water content before drying. Then, a NaCl solution (3% by weight for AT13 and 5% by weight for KC151) was added until the soil-solution mixture attained a saturated, paste-like consistency. This procedure is designed to destroy the soil structure while maintaining the pore fluid salt concentration close to the in situ conditions.

- Remolded with hydrates: Sediments were dried in an oven, ground with a mortar, and mixed with 20% THF solution to the water content before drying. Then, a 20% THF solution with the appropriate salt concentration was added until the mixture exhibited a saturated, paste-like behavior.

5.5 RESULTS

This section provides an overview of the results of the laboratory experiments. Data from the experiments are shown in Table 5.1.

5.5.1 Volume Change

Figure 5.3 shows the void ratio at the end of consolidation for each loading step for all six tests, during both loading and unloading. The initial void ratio for the undisturbed AT13 specimen was high (e_0=3.07), consistent with its shallow subseafloor depth. The preconsolidation pressure estimated from the overburden is ~2.5 kPa, so the loading imposed during this experiment is virgin loading. The compression index C_c describes the slope of the normal consolidation line on a plot of void ratio versus the logarithm of σ'_v, while the swelling index C_s or recompression index C_r refers to the slope of the unloading/reloading curves on the same type of plot. The AT13 sample has C_c = 0.9 and C_s = 0.1, which confirms that the specimen is normally consolidated in its undisturbed state.

In contrast, the initial void ratio for the undisturbed KC151 specimen was low (e_0=0.96) since it was buried at ~275 mbsf. The estimated preconsolidation pressure is

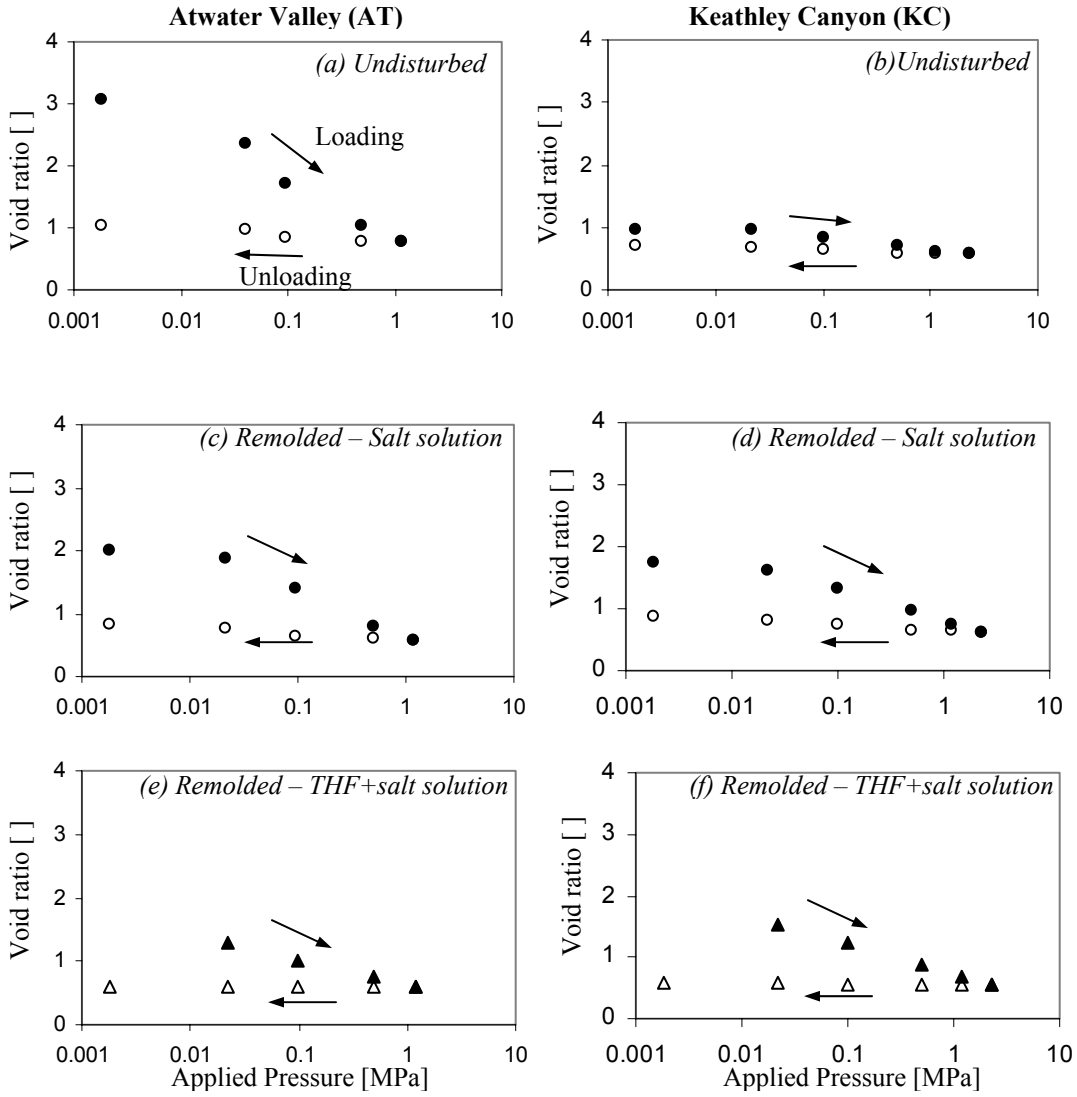

Figure 5.3. Void ratio evolution during loading and unloading. All loading stages were applied while pore fluid was in the liquid phase. Circles indicate specimens lacking hydrates, and triangle show specimens with hydrates.

~2.3 MPa, so the loads applied during this experiment were in the reloading branch. Consequently, the KC151 specimen was in the overconsolidated range (C_r = 0.15 and C_s = 0.05), and the measured volume changes were small in both loading and unloading.

Significant discussion of the consolidation state for the remolded samples is unnecessary. By their very nature, remolded samples are inherently normally consolidated (Figure 5.3).

5.5.2 S-wave Velocity

Figure 5.4a shows a selection of waveforms gathered at the end of each consolidation step and during phase transformation for the remolded KC151 specimen. The pattern of increasingly fast first arrivals indicates that the S-wave velocity is dependent on the effective stress, which plays a critical role in controlling the stiffness of uncemented sediments (Santamarina et al., 2001). However, Figure 5.4b highlights another effect, namely the impact of hydrate formation on the stiffness of hydrate-bearing sediments held at constant effective stress. Between 0.5 MPa and 2.3 MPa, the increase in S-wave velocity during hydrate formation at σ_v'=0.5 MPa is as great as the increase due to effective stress alone (Figure 5.4a).

These observations are further confirmed through analysis of the complete S-wave velocity data set shown in Figure 5.5. Following a Hertzian-type formulation, V_S can be related to the mean stress in the polarization plane through:

$$V_s = \alpha \left(\frac{\sigma_v' + K_0' \sigma_v'}{2 \quad kPa} \right)^{\beta}, \tag{5.1}$$

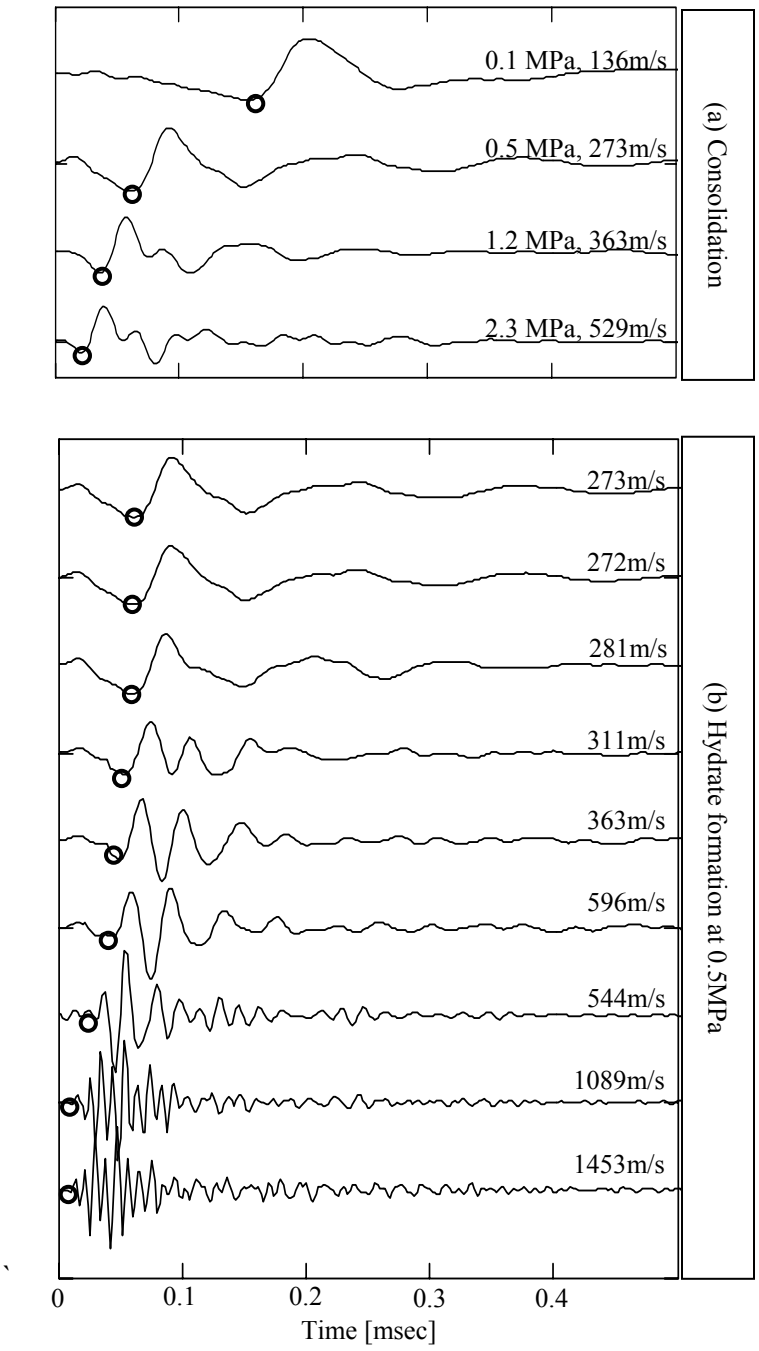

Figure 5.4. The evolution of S-wave signatures gathered for KC specimen with 20% THF-salt solution at the end of each loading step and during phase transformation at 0.5MPa. Dots on waveforms indicate first arrivals from which velocities were calculated.

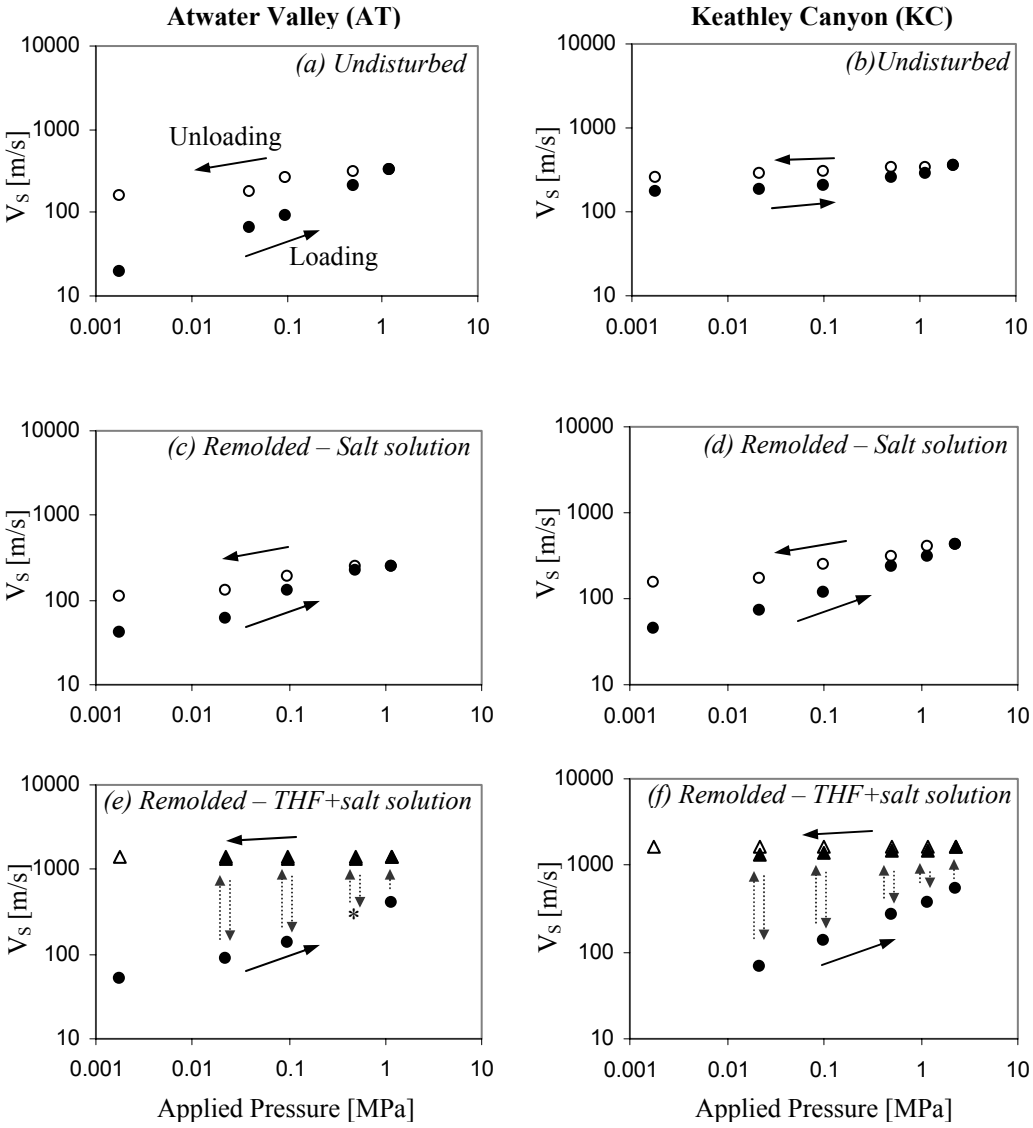

Figure 5.5. S-wave velocity evolution during loading and unloading. An asterisk indicates interpolated data. Circles denote specimens lacking hydrates, and triangle show specimens with hydrates.

where K_0' is the lateral earth pressure coefficient at zero-lateral strain, and α and β are experimentally determined coefficients. The constant α denotes V_S at σ_v'=1 kPa, and the exponent β is a measure of the sensitivity of V_S to the effective stress σ_v'.

The S-wave velocity in the undisturbed specimens without hydrates (Figure 5.5a and 5.5b) increases with the applied vertical effective stress σ_v' with an exponent of β=0.1 in the overconsolidated KC151 specimen. In the AT13 specimen, β=0.4 due to the significant change in the coordination number -the number of contacts per particle- during virgin loading. During vertical unloading, V_S decreases slightly in both specimens because high coordination and horizontal effective stress remain locked in.

The S-wave velocity of remolded specimens without hydrates (Figure 5.5c and 5.5d) increases with increasing vertical effective stress with exponent $\beta \cong 0.3$ for both the KC and AT specimens. This result reflects the fact that remolded specimens are inherently normally consolidated. During unloading, the S-wave velocity in specimens decreases slightly, similar to the case of undisturbed specimens.

The S-wave velocity of remolded specimens with hydrates (20% THF-salt pore fluid solution) increases markedly during each hydrate formation event (Figure 5.5e and 5.5f). Importantly, the S-wave velocity for the specimen with the nominal 100% hydrate-filled porosity is nearly independent of the state of stress. (Note: hydrate-filled porosity is herein defined as the volume of voids filled with hydrates normalized by the total volume of voids.)

After the completion of phase transformation at the final loading step (σ_v'=2.3 MPa), the frozen specimens were unloaded to σ_v'=0 Pa. Almost no decrease in V_S

occurred during unloading, indicating that no significant decementation/debonding occurred in these fine-grained specimens with high hydrate concentration.

5.5.3 Permittivity and Electrical Conductivity

The electrical conductivity σ_{el} of fluid-saturated sediments is governed by the fluid-filled porosity n of the sediments and the conductivity of the pore fluid (i.e., ionic concentration and mobility). Surface conduction effects can be neglected in marine sediments (Klein and Santamarina, 2003). On the other hand, the dielectric permittivity κ' of soil-water mixtures in the microwave frequency range is dominated by the orientational polarization of free water molecules factored by the volume fraction. These guidelines provide insight into the permittivity and conductivity spectra shown in Figure 5.6 for specimens at the end of each loading step and during phase transformation.

As the load increases or as the phase transformation proceeds, κ' decreases due to the decrease in the volume fraction of free water. At the same time, σ_{el} decreases due to the decrease in porosity and ionic mobility (local - measured at microwave frequencies). The decrease in κ' and the increase in σ_{el} with the increase in frequency are due to free water polarization in the microwave frequency range. These observations are further validated by the trends in permittivity and electrical conductivity data as a function of the vertical effective stress shown in Figures 5.7 and 5.8.

As the vertical effective stress increases in specimens lacking hydrate, the real permittivity and the electrical conductivity decrease due to the decrease in void ratio (Figure 5.3). Larger changes in the electrical properties imply larger changes in void

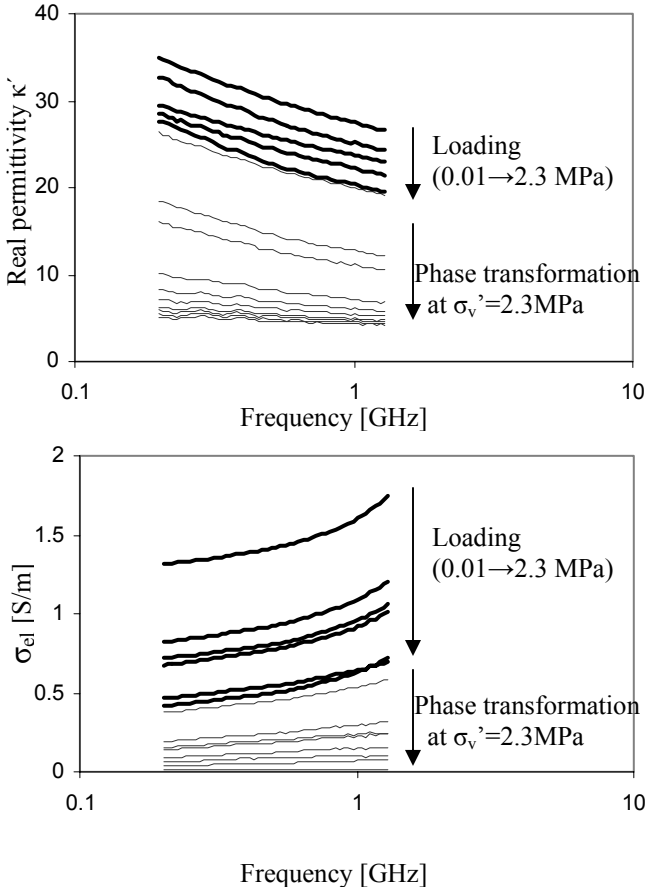

Figure 5.6. Real and imaginary permittivity spectra gathered for KC specimen with 20% THF-salt pore fluid at the end of each loading step (0.01, 0.1, 0.5, 1.2, and 2.3 MPa) and during phase transformation after the final loading step (2.3 MPa). Thick black lines indicate measurements in the specimen at the end of consolidation before hydrate formation, and thin gray lines indicate measurements in the specimen during hydrate formation after consolidation under 2.3 MPa. In each graph, the upper arrow indicates the direction of the increase in the vertical effective pressure, and lower arrow indicates the progress of hydrate formation.

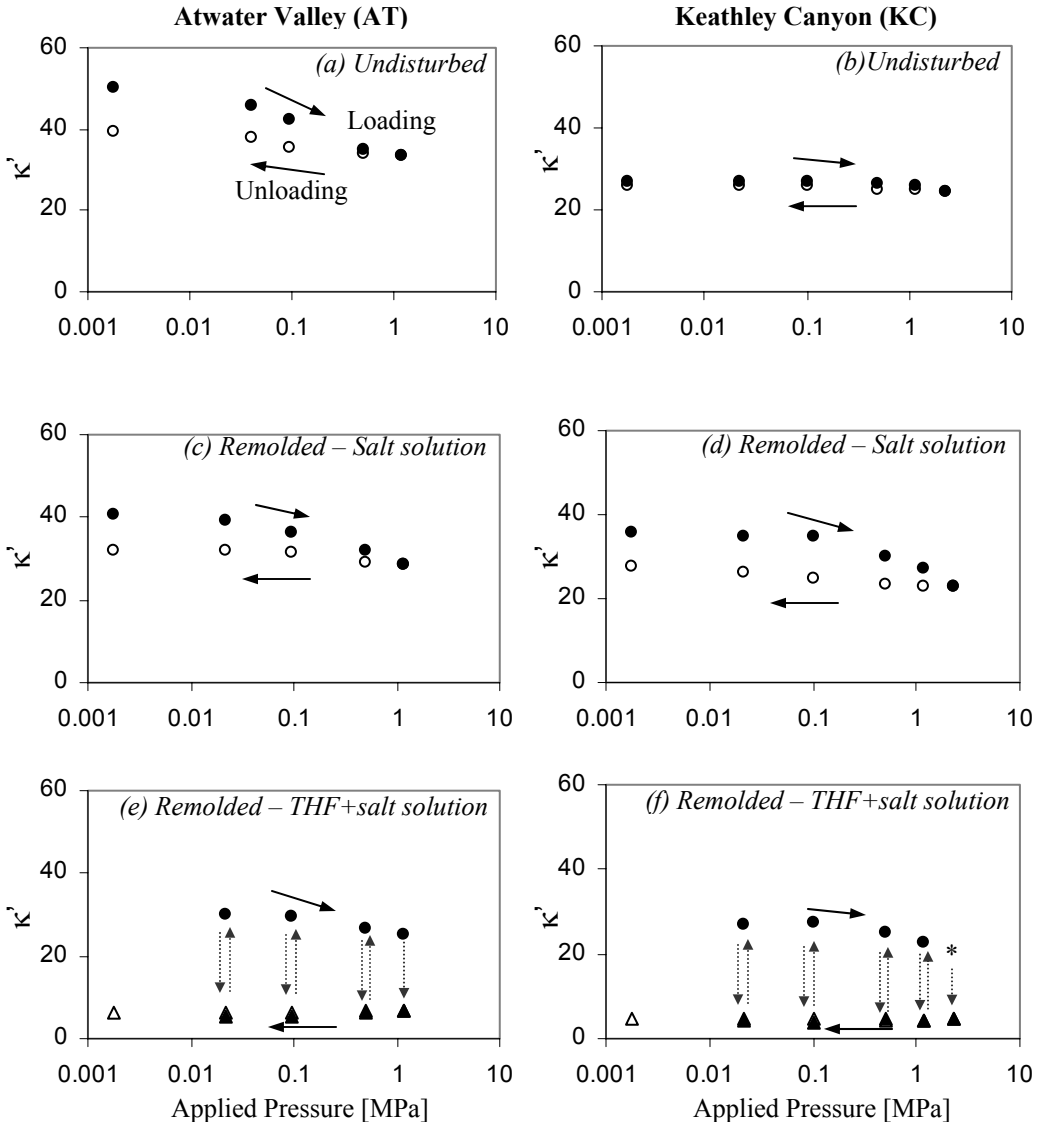

Figure 5.7. Real permittivity during loading, phase transformation, and unloading. Asterisk indicates interpolated missing data. Circles denote specimens lacking hydrates, and triangles indicate specimens with hydrates.

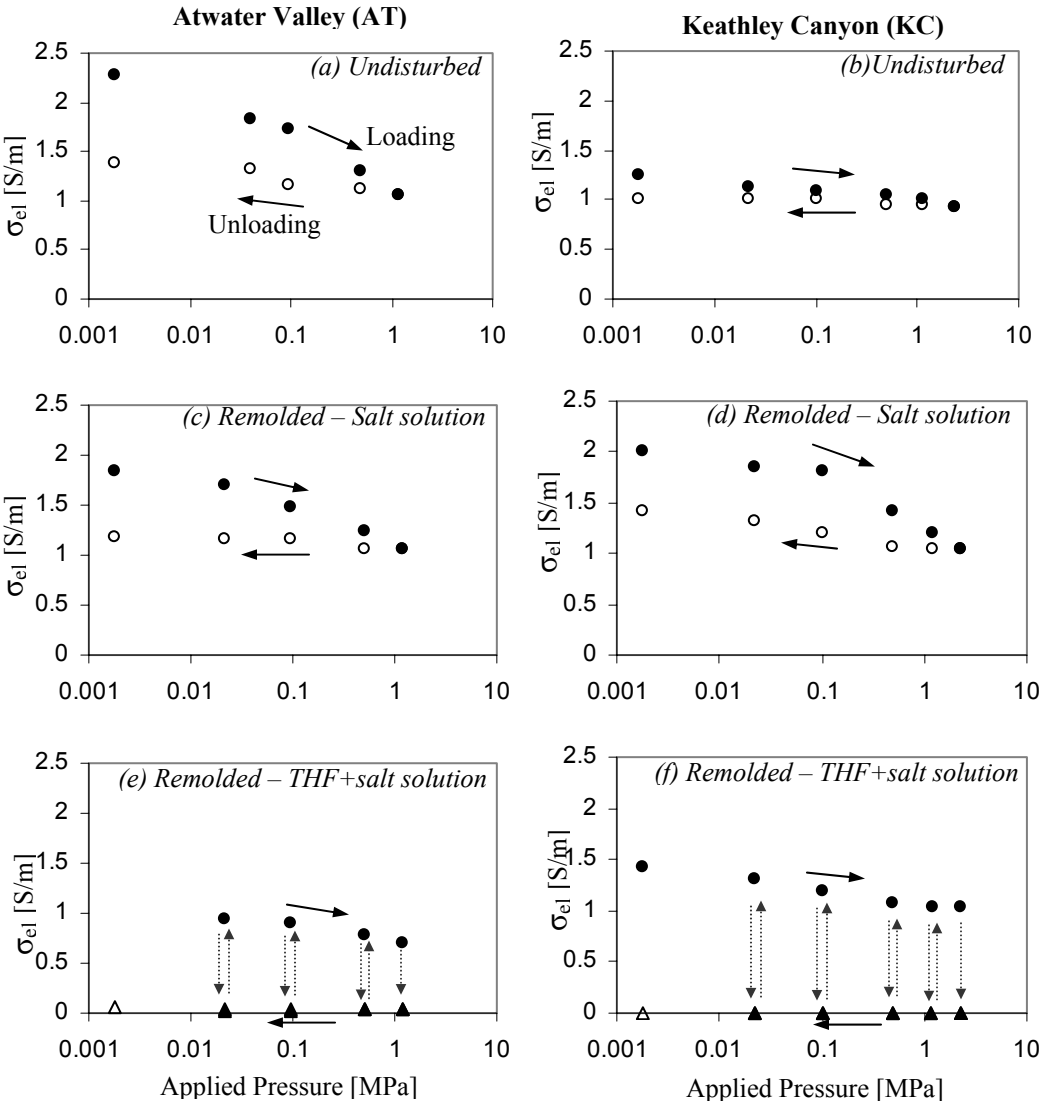

Figure 5.8. Electrical conductivity during loading, phase transformation, and unloading. Circles indicate specimens lacking hydrates, and triangle indicates specimens with hydrates.

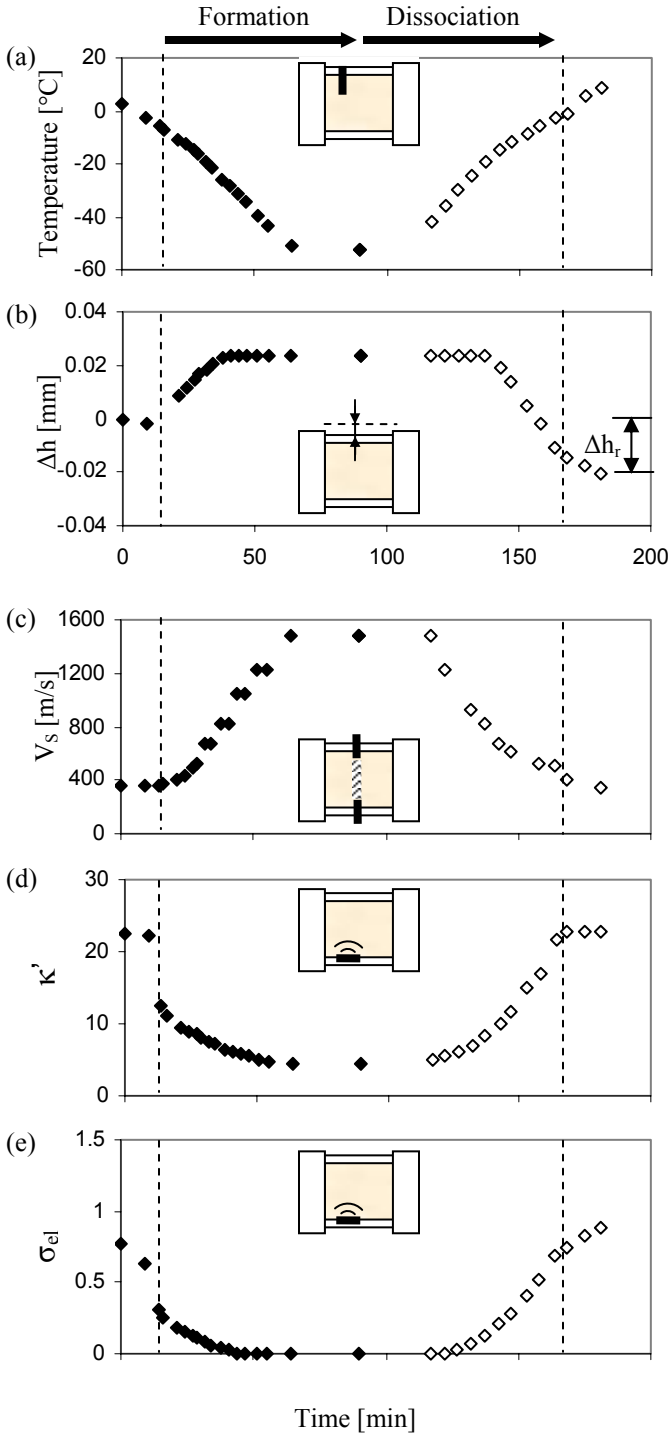

Figure 5.9. Phase transformation in KC specimen subjected to the vertical effective stress σ_v'= 1.2 MPa. Vertical displacement Δh and S-wave velocity V_S are global height-averaged measurements across the specimen. Temperature T, real permittivity κ', and electrical conductivity σ_{el} are local measurements. The schematic diagram in each graph illustrates the location of sensors. Dotted lines indicate the onset of hydrate formation and the end of hydrate dissociation.

ratio: The soft undisturbed AT13 specimen experiences a more pronounced drop in κ' and σ_{el} than the stiff undisturbed KC151 specimen.

Hydrate formation causes a pronounced decrease in permittivity, down to the range of non-polarizable materials (Table 5.1). At the same time, electrical conductivity drops to undetectable, near-null values (Figures 7e, 7f, 8e, and 8f). In contrast to sediments lacking hydrate, the real permittivity of hydrate-bearing sediments slightly increases as the vertical effective stress increases and the void ratio decreases (Figures 7e and 7f). Two factors may contribute to this phenomenon. First, the fraction of unfrozen bounded water in a pore volume increases as free water drains and the porosity decreases under the higher vertical effective stress. Second, clay minerals, which make up a significant fraction of these specimens, have higher permittivity than THF hydrate.

5.5.4 Phase Transformation

Figure 5.9 shows a data set gathered for the KC specimen while subjected to σ'_v = 1.2 MPa. The temperature of the cell was gradually lowered to -52°C by placing ground dry ice against the thick stainless steel cell wall. Although the geophysical signatures clearly indicate hydrate formation, no exothermic event was detected in the temperature data. This is not surprising in light of the extremely low temperature attained during cooling, a temperature far within the stability field for THF hydrate at the range of pressures tested here. During hydrate formation, the S-wave velocity increased from 360 m s^{-1} to 1480 m s^{-1}, permittivity decreased from 23 to 5, and electrical conductivity decreased to undetectably low values (Table 5.1). Hysteresis between freezing and thawing was evident in all geophysical measurements when data were plotted versus

temperature. We also detected volume expansion of ε_{vol}=0.01 during hydrate formation. Such volume expansion alters equilibrium conditions at grain contacts and fundamentally perturbs the soil skeleton. During hydrate dissociation, we observed a corresponding residual settlement Δh_r induced by the perturbation of soil skeleton during volume expansion.

5.6 ANALYSES AND DISCUSSION

The initial porosity (related to C_c) and the stiffness (related to V_S) of sediments are controlled by their loading history, grain size distribution, and specific surface, which in turn control the mean pore size. Following consolidation, the lower void ratio attained by the AT and KC specimens with THF solution in the pore space is a consequence of the lower pore fluid polarizability. This leads to thin double layer thickness and densification due to residual settlement after the end of the dissociation cycle.

The most important features in the S-wave velocity data are the stress-dependent stiffness in normally consolidated specimens without hydrates, the less stress-dependent stiffness in overly consolidated specimens, and the stress-independent stiffness in specimens with 100% hydrate saturation. We have previously made the same observations of S-wave velocities independent of stress in studies of synthetic sediment specimens with 100% THF hydrate in pore space (Santamarina et al., 2004).

The real permittivity in the microwave range is confirmed as a good indicator of volumetric free water content, capturing volume reduction of free water during consolidation and reduced water polarizability during hydrate formation. The electrical

conductivity follows similar trends, but its response is governed by ionic concentration and ionic mobility.

5.6.1 Core Sampling Effects on Hydrate-bearing Sediment Properties

The void ratio and S-wave velocity of sediments with 100% hydrate saturation show minimal change during unloading from σ_v' =1.2 and 2.3 MPa to σ_v' =0 MPa, indicating that the THF hydrate in pores can bind soil particles and resist the tension induced by the compressive force trapped in the granular skeleton (the equilibrium conditions of methane hydrate should be considered for field applications). Force equilibrium requires a minimum hydrate concentration in pore space S_{hyd} to resist the tension; for an unconsolidated (i.e., uncemented) sediment with porosity n

$$S_{hyd} \cdot n \geq \frac{\sigma'_{C\_skeleton}}{\sigma_{T\_hydrate}} \tag{5.2}$$

where $\sigma'_{C\_skeleton}$ represents the compressive forces trapped in the granular skeleton (per unit area), and $\sigma_{T\_hydrate}$ denotes the tensile strength that the hydrate may resist for a short period of time. Our results and analysis demonstrate that the probability of sampling hydrate-bearing sediment without disturbing the original sediment fabric increases as the in-situ vertical effective stress is lower, the porosity is higher, the hydrate concentration is higher, and the specimen is stored for a shorter period between retrieval and laboratory measurement. (Clearly, these observations presume that pore fluid pressure and temperature conditions are maintained within the stability field).

5.6.2 Impact of Hydrate Formation on Geophysical Parameters

The gradual increase in V_S observed during hydrate formation (Figure 5.9) indicates that hydrates do not form instantaneously throughout the specimen. Due to placement of the source and receiver, the measured V_S data represent a height-averaged value, and the pattern of the increase in V_S during hydrate formation may in part reflect a non-homogeneous thermal field and the existence of a propagating freezing front. However, there are also gradual decreases in κ' and σ_{el}, and both of these parameters average only over a small volume adjacent to the sensor. Thus, these gradual changes in local κ' and σ_{el} reflect gradual, rather than instantaneous, hydrate formation in pores. By gradually depressing the temperature of hydrate formation, two coexisting pore-scale phenomena can cause such changes in properties during hydrate formation: (1) Ion exclusion causes an increase in the ionic concentration of the remaining pore fluid in a closed system; and (2) gradually smaller pores remain unfrozen during hydrate formation due to pore size effects. Both effects contribute to the gradual magnification of the equilibrium temperature depression and are analyzed next.

5.6.2.1 Ionic concentration effect

The equilibrium temperature depression due to salt concentration can be estimated from the Hammerschmidt equation (Sloan, 1998). The activity of water a_w is related to the equilibrium temperature of gas-hydrate phase transformation with salts T_s [K] and without salts T_w [K] by:

$$\ln a_w = \frac{\Delta H}{NR}\left[\frac{1}{T_w} - \frac{1}{T_s}\right], \tag{5.3}$$

where ΔH is the heat of dissociation of THF hydrate (98 kJ mol^{-1}; Leaist et al., 1982), N is the hydrate number (17 for THF hydrate), and R denotes the universal gas constant (8.31 J K^{-1} mol^{-1}). The freezing temperature of water with salts T_{fs} [K] and without salts T_f [273.15 K] have a similar relationship with the activity of water:

$$\ln a_w = \frac{\Delta H^{fus}}{R}\left[\frac{1}{T_f} - \frac{1}{T_{fs}}\right], \tag{5.4}$$

where ΔH_{fus} [6008 J mol^{-1}] is the heat of fusion of ice. Combining these two equations leads to the equation for the equilibrium temperature of gas-hydrate phase transformation in an electrolyte:

$$\left[\frac{1}{T_W} - \frac{1}{T_S}\right] = \frac{\Delta H^{fus} N}{\Delta H}\left[\frac{1}{T_f} - \frac{1}{T_{fs}}\right] \quad . \tag{5.5}$$

The estimated equilibrium temperature is 2.2°C for AT specimen with 0.53 molal of initial salt concentration in the pore fluid, and 0.9°C for KC specimen with 0.91 molal of initial salt concentration in the pore fluid. However, the equilibrium temperature drops to -16.6°C for a salt-saturated (molality of 6) pore fluid.

5.6.2.2 Pore size effect

The presence of pores affects hydrate nucleation and growth. The size of hydrate nucleation embryos is restricted by sediment pore size, which leads to supercooling during hydrate formation, and the curved hydrate-water interface also depresses the equilibrium temperature for freezing in porous media (Everett, 1961). In addition, hydrate growth is affected by capillary pressure (Clennell et al., 1999; Mullin, 2001). The equilibrium temperature depression ΔT_{pore} [K] can be estimated with the Kelvin and

the Clapeyron equations for a cylindrical pore with radius r [nm] (Anderson et al., 2003; Clennell et al., 1999):

$$\Delta T_{pore} = \frac{2\gamma_{sl} T_{bulk} \cos\theta}{\rho \Delta H r}, \tag{5.6}$$

where T_{bulk} [K] is the equilibrium temperature in bulk phase, γ_{sl} denotes the interfacial tension between hydrate and liquid (31mJ m^{-2} for THF hydrate and water), θ represents the contact angle between hydrate and the pore wall (θ =0° assuming unfrozen liquid layer at the pore wall), and ρ=970 kg m^{-3} is the mass density of THF hydrate. The average separation r between platy particles can be estimated for application (5.6) from the specific surface S_a and the water content w:

$$r = \frac{w}{S_a \rho_w}, \tag{5.7}$$

where ρ_w is the mass density of pore fluid, here taken as ρ_w=1009 kg m^{-3} for 20% THF-salt solution. The estimated pore size ranges from 2 to 5 nm for KC specimen. The corresponding calculated temperature depression for pores of this size is -15K to -36K.

5.6.3 Estimation of Fluid-filled and Hydrate-filled Porosity

The estimation of fluid-filled porosity from real permittivity and electrical conductivity data can be robust when adequate material models are available. Here, we use permittivity and conductivity data gathered at the end of each consolidation stage to examine the relationship between these measurements and fluid-filled porosity. The goal of this analysis is to explore the use of these data to assess hydrate concentration in pore space, under the assumption that pore space must be either filled with fluid or gas hydrate.

Figure 5.10 shows the relation between electrical measurements and porosity at the end of the consolidation for all loading stages and for all specimens. A power Archie-type equation is used to fit the electrical conductivity data (Archie, 1942):

$$n = 0.40\left(\frac{\sigma_{el}}{\sigma_f}\right)^{0.75} \quad , \tag{5.8}$$

where σ_{el} is the specimen conductivity and σ_f is the pore fluid conductivity.

A CRIM (Complex Refractive Index Method)-type model is adopted for the real permittivity data (Birchak et al., 1974):

$$n = \frac{\sqrt{\kappa'} - \sqrt{\kappa_s'}}{\sqrt{\kappa_w'} - \sqrt{\kappa_s'}} \quad , \tag{5.9}$$

where κ' is the specimen permittivity, κ_s' represents soil particle permittivity, and κ_w' denotes pore fluid permittivity. The real permittivity value is mostly governed by porosity and the hydrate saturation and barely affected by pore fluid salinity.

These material models can be used to estimate the porosity filled with free water during phase transformation at constant effective stress and thus the gas hydrate saturation in pores; in the case of conductivity data, computations must take into consideration ion exclusion and the changes in conductivity in the remaining fluid in closed systems. The evolution in hydrate saturation S_{hyd} during formation and dissociation is estimated from the measured permittivity and conductivity. Figure 5.11 shows the estimated S_{hyd} during the phase transformation of the KC specimen under different applied vertical effective stress. Comparable results were obtained in the Mackenzie Delta Mallik 5L-38 well using 1.1 GHz measurements (real permittivity 5-to-

20, electrical conductivity 0.1-to-0.5 S/m and inferred hydrate saturations S_{hyd}=0.2~0.95 - Sun and Goldberg, 2005).

When shear wave velocity is plotted versus hydrate-filled porosity inferred from electrical measurements, the data show that the increase in S-wave velocity during hydrate formation is delayed with respect to hydrate formation, consistent with hydrate formation on mineral surfaces and subsequent crystal growth towards the pore space (Yun et al, 2005).

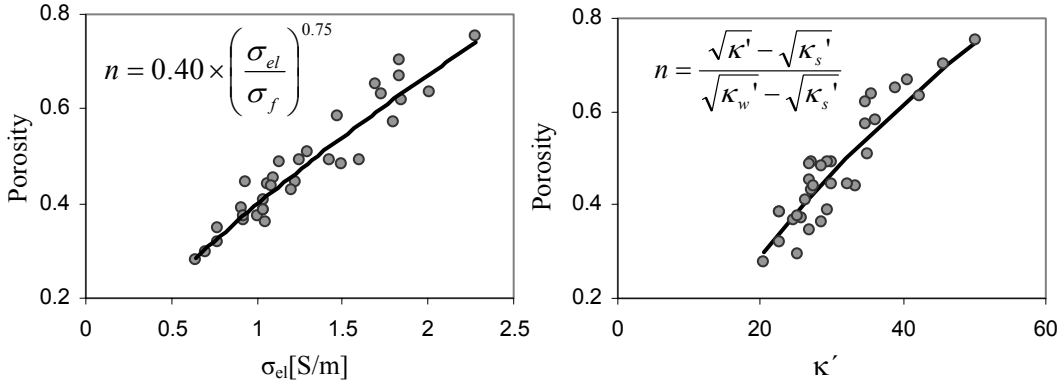

Figure 5.10. Porosity vs electrical conductivity σ_{el} (at 1GHz) and real permittivity κ′ (at 1GHz) from six experiments conducted in specimens lacking hydrate.

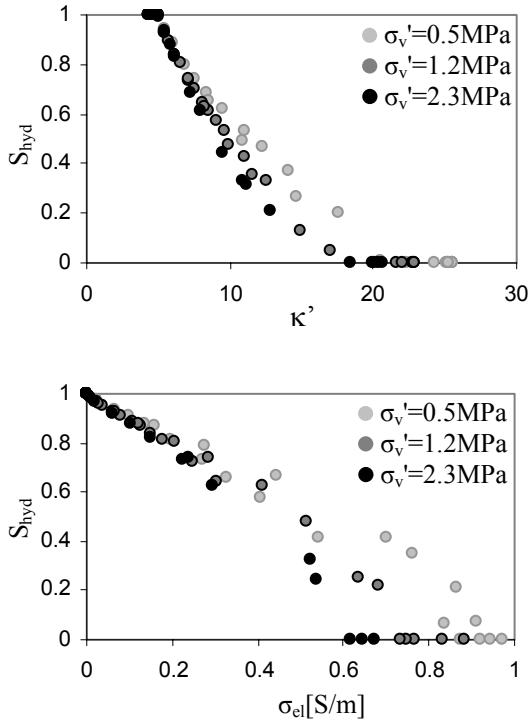

Figure 5.11. Hydrate saturation in the pore space S_{hyd} estimated from real permittivity κ' and electrical conductivity σ_{el} measured on the remolded KC specimen with synthetic hydrate.

5.7 CONCLUSIONS

Consolidation experiments on undisturbed and remolded natural sediments obtained during drilling in the northern Gulf of Mexico gas hydrates province and tested with and without synthetic hydrate reveal that:

- The high compression index of these Gulf of Mexico sediments in the normally consolidated range reflects their high plasticity.
- Effective stress controls the stiffness of uncemented, normally consolidated sediments lacking hydrates. The sensitivity to the state of stress is high (β= 0.3~0.4), consistent with the high specific surface and high plasticity of these sediments. In sediments with high hydrate concentration, the effect of hydrates overrides the effect of effective stress on stiffness ($\beta \approx 0$).
- Phase transformation monitoring reveals ion exclusion and an increase in ionic concentration in remaining pore fluids during hydrate formation, as previously documented in some field settings (e.g., Torres et al., 2004). This effect couples with a gradual decrease in unfrozen pore size to further depress the equilibrium temperature.
- No decementation or skeletal debonding is observed when the 100% hydrate-filled sediments are unloaded from effective vertical stresses ranging from 1.2 to 2.3 MPa. Therefore, such specimens should experience limited sampling effects due to skeletal unloading. We caution that care should be taken to reload such samples to the in-situ effective stress condition as soon as possible after retrieval. Our earlier work has demonstrated significant decementation and debonding at

50% hydrate saturation (Yun et al., 2007), and it is only at very high hydrate saturations, which are likely rare in most natural settings, that sampling effects are relatively minimal.

- Permittivity in the microwave frequency range provides a good measure of free water volume fraction, while electrical conductivity indicates the availability and mobility of ions. Taken together, these parameters are good indicators of the hydrate volume fraction. This method of estimating hydrate volume fraction can likely be adapted for use in field settings.

CHAPTER VI.

ELECTRICAL RESISTIVITY TOMOGRAPHY: PRELIMINARY STUDIES AND SYSTEM DESIGN

6.1 INTRODUCTION

Electrical measurements have been used for the in-situ characterization of natural gas hydrates (Edwards 1997; Riedel et al. 2006) and in laboratory studies (Hyndman et al. 1999; Zatsepina and Buffett 2001; Zatsepina and Buffett 2002).

Various tomographic systems are based on electrical measurements, such as electrical resistivity tomography ERT, electrical capacitance tomography ECT, and electrical impedance tomography EIT. Their main advantages are the implementation of non-destructive measurements, the fast data acquisition time, and relatively easy and inexpansive implementation in comparison to other tomographic systems such as X-ray tomography.

Electrical resistivity tomography determines the spatial distribution of electrical resistivity within a specimen from electrical measurements usually conducted with electrodes placed at the specimen boundaries. A current is injected between the source and sink electrodes by imposing an electrical potential difference between them, and potential differences among the remaining electrodes are measured by pairs (Note: all potential differences can be gathered with respect to the sink (or ground) electrode). This procedure is repeated by varying the source and sink electrode pairs until a

comprehensive dataset is obtained. The measured potentials are used to reconstruct the distribution of resistivity within the specimen using inversion algorithms. This chapter documents a series of studies conducted towards an optimal ERT system design for hydrate-bearing sediment study.

6.2 GEOMETRIC EFFECTS AND ELECTRODE POLARIZATION

6.2.1 Specimen Geometry and Electrode Location

Specimen geometry, electrode configuration, and the spatial distribution of resistivity determine the potential distribution and current density within the specimen. Consequently, the location of electrodes affects spatial resolution and signal-to-noise ratio (Booth and BasarabHorwath 1996). For example, (1) peripherally mounted electrodes have low resolution at the center (Seagar et al. 1986); (2) the addition of an electrode at the center improves the resolution within the central area (Lyon and Oakley 1992); (3) current injection between adjacent electrodes produces the best local resolution; and (4) current injection between opposite electrodes produces the best signal-to-noise ratio (Avis and Barber 1994).

Simple experiments and numerical simulations with two different specimen geometries and electrode configurations are designed to corroborate the effects of electrode location on the measured potential distribution. In the first configuration, tap water is used to fill a latex tube (D=8mm and L=250mm) to make a pseudo-1D current flow condition, and 10 electrodes are mounted along the tube (Figure 6.1a). The source (#1) and the sink (#10) electrodes are connected to an AC power supply (f = 1kHz and

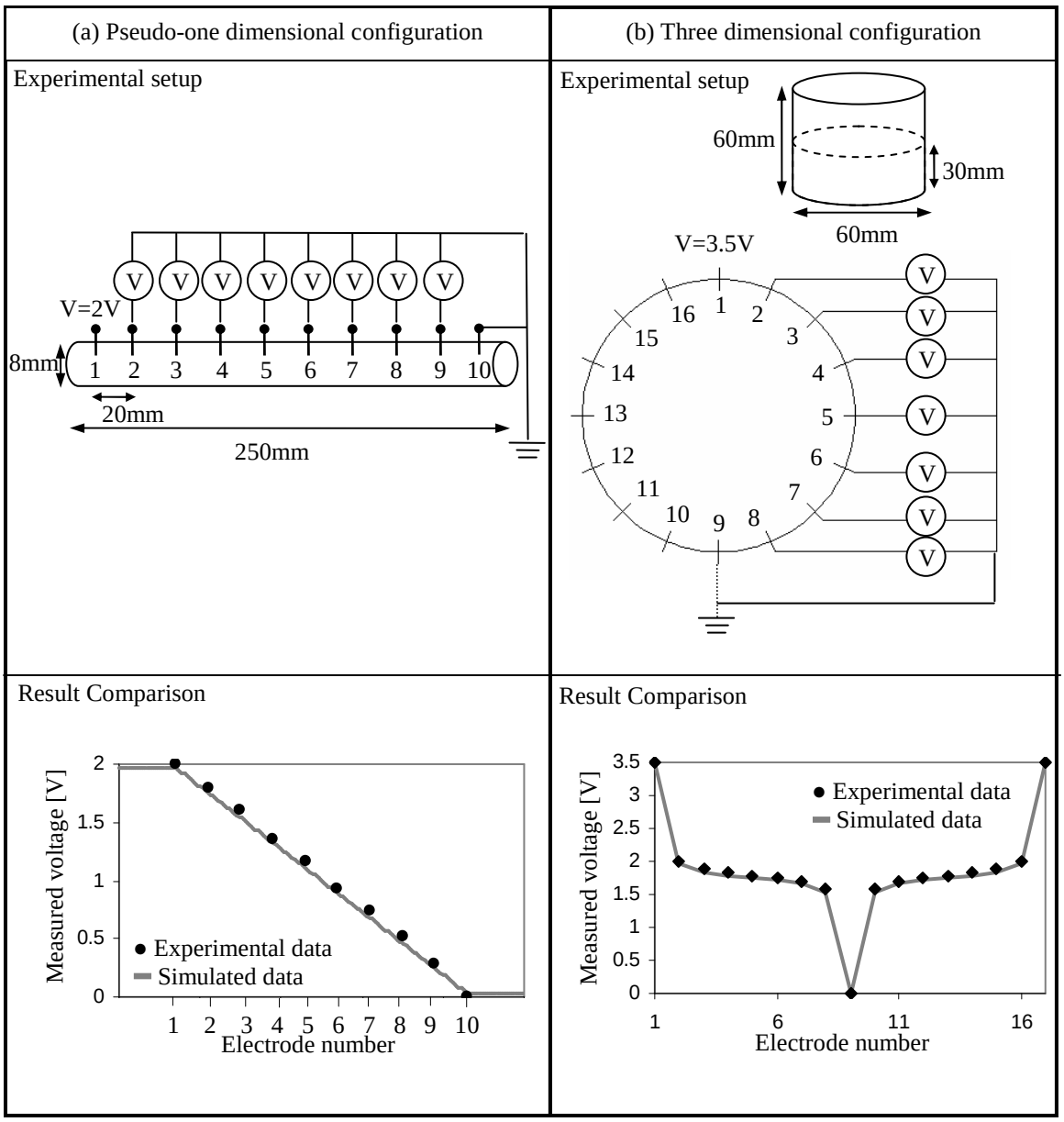

Figure 6.1 The effect of geometry of specimen and electrode location on the electrical potential distribution (Source frequency = 1kHz). (a) Pseudo-one dimensional configuration (b) Three dimensional configuration

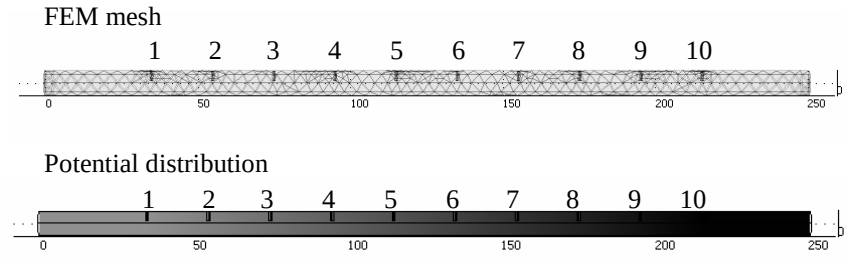

(a) Numerical simulation for pseudo-one dimensional current path

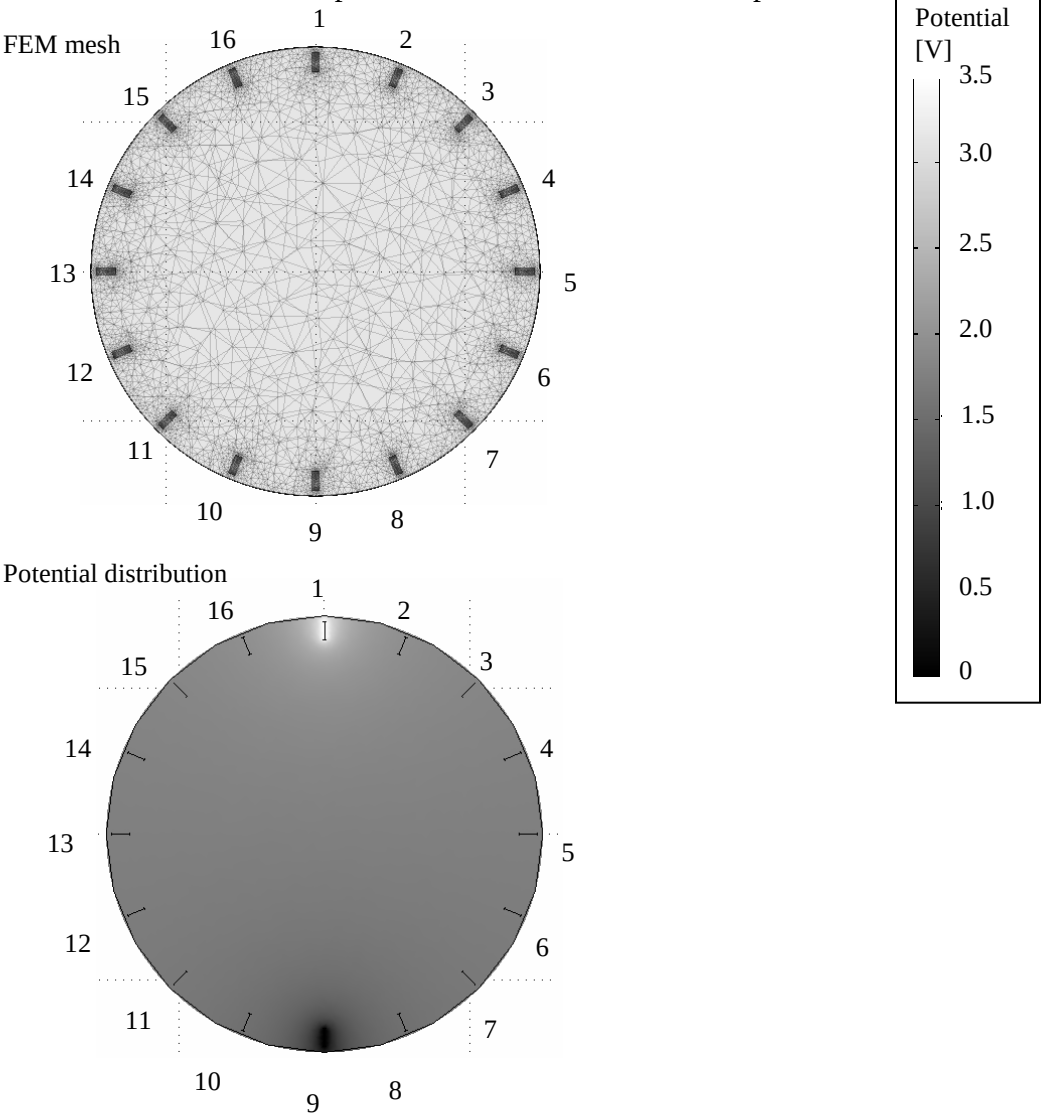

(b) Numerical simulation for three dimensional current path

Figure 6.2 Numerical simulation results for (a) pseudo-one dimensional current path configuration (b) three dimensional current path configuration

ΔV=2V); the potential at other electrodes are measured with respect to ground using an oscilloscope. The potential decreases linearly along the tube, indicating the evenly distributed equipotential lines (Figure 6.1a).

The second configuration consists of a short plastic cylinder filled with tap water (D=60mm and H=60mm, Figure 6.1b). A total of 16 electrodes is mounted around the perimeter of the cylinder. The opposite-electrode excitation scheme is used; the applied potential difference between the source (#1) and the sink (#9) electrodes is 3.5V at 1kHz. The results show significant potential change near source and sink electrodes, indicating a highly concentrated equipotential lines near the source and the sink electrodes.

A parallel numerical study is implemented using the commercial 3-D finite element code COMSOL Mulitiphysics. The numerical models reproduce the same geometries as the corresponding physical models in Figure 6.1. The outer boundaries are non conductive in both cases. The conductivity of stainless steel electrodes is set at 4×10^6 S/m, and the conductivity of the tap water is the measured value of 0.05 S/m. Figure 6.2 shows the detailed mesh near electrodes and potential distributions from simulations. Numerical simulation results are superimposed on experimental results at Figure 6.1. There is close agreement between experimental and numerical results. In conclusion, geometry effect have a predominant effect on the distribution of the potential near sink and source electrodes.

6.2.2 Electrode Polarization

The electrical current through electrodes, cables, and electronics involves the movement of electrons, whereas the current through electrolytes involves the movement

of ions. Therefore, electrode polarization i.e., the charge accumulation at electrode-specimen interfaces, takes place (Santamarina et al. 2001). Oxidation-reduction at the electrode-specimen interface reduces electrode polarization, so electrode effects increase with non-reactive electrodes. However, re-dox effects add complexity and uncertainty to the analysis of electrical measurements. Instead, electrode polarization effects can be minimized by increasing the operating frequency. The effect of frequency on electrode polarization is investigated using the 1D cell shown in Figure 6.1a and 3% NaCl solution (by weight). The potential difference between the source (#1) and the sink (#10) electrodes is 2V. The frequency is gradually increased from 1 Hz to 1 MHz. Figure 6.3 shows the evolution of the electrical potential measured between electrodes #4 and #10. These results show that strong electrode polarization effects take place at the frequencies below 100Hz. In particular, limited electrode effects and fast voltage measurement can be implemented using an operating frequency of 1kHz~10kHz.

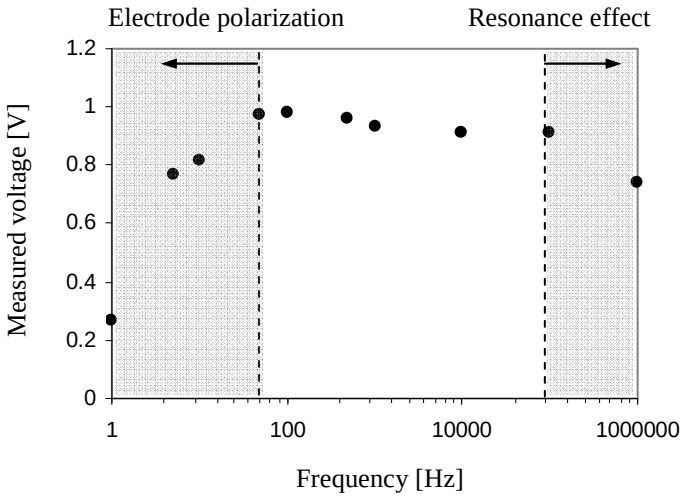

Figure 6.3 Electrode polarization effect: Potential difference between measured between electrodes 5 and 10 (sink electrode) as a function of the source signal frequency. The experimental setup is illustrated in Figure 6.1a.

6.3 ELECTRODE GEOMETRTY

The pronounced potential changes near the source and sink electrodes in 2D and 3D system (e.g., Figure 6.1b) leaves small potential changes between measurement electrodes, resulting in low sensitivity to anomaly and low signal to noise ratio (Pinheiro et al. 1998). The high potential gradient (and associated high current density) near small electrode may be reduced selecting wider electrodes (Wang et al. 2001).

6.3.1 Experimental Study on Electrode Size: Potential Drop Near Source and Sink

The cylindrical cell in Figure 6.1b is filled with tap water. The width W_{elec} and length L_{elec} of the source and sink electrodes are varied as follows: W_{elec}=1.1mm, 3.2mm, and 6.4mm; L_{elec}=1.1 mm, 30mm, and 60mm. Figure 6.4a and c show the electrical potential profiles measured around the perimeter of the cell, and Figure 6.4b and d show the potential at the measurement electrodes (#2 and #8) closest to the source (#1) and the sink (#9) to identify the maximum potential difference between measurement electrodes, which is a surrogate of signal-to noise ratio. Results clearly show that wider and longer electrodes reduce the potential change near source and sink electrodes, suggesting less current density near source and sink.

6.3.2 Numerical Study

Larger size electrodes reduce the spatial resolution in tomographic inversion (Wang et al. 2001). Ideally, the source and sink electrodes should be as large as possible, while the measuring electrodes should be as small as possible (Pinheiro et al. 1998).

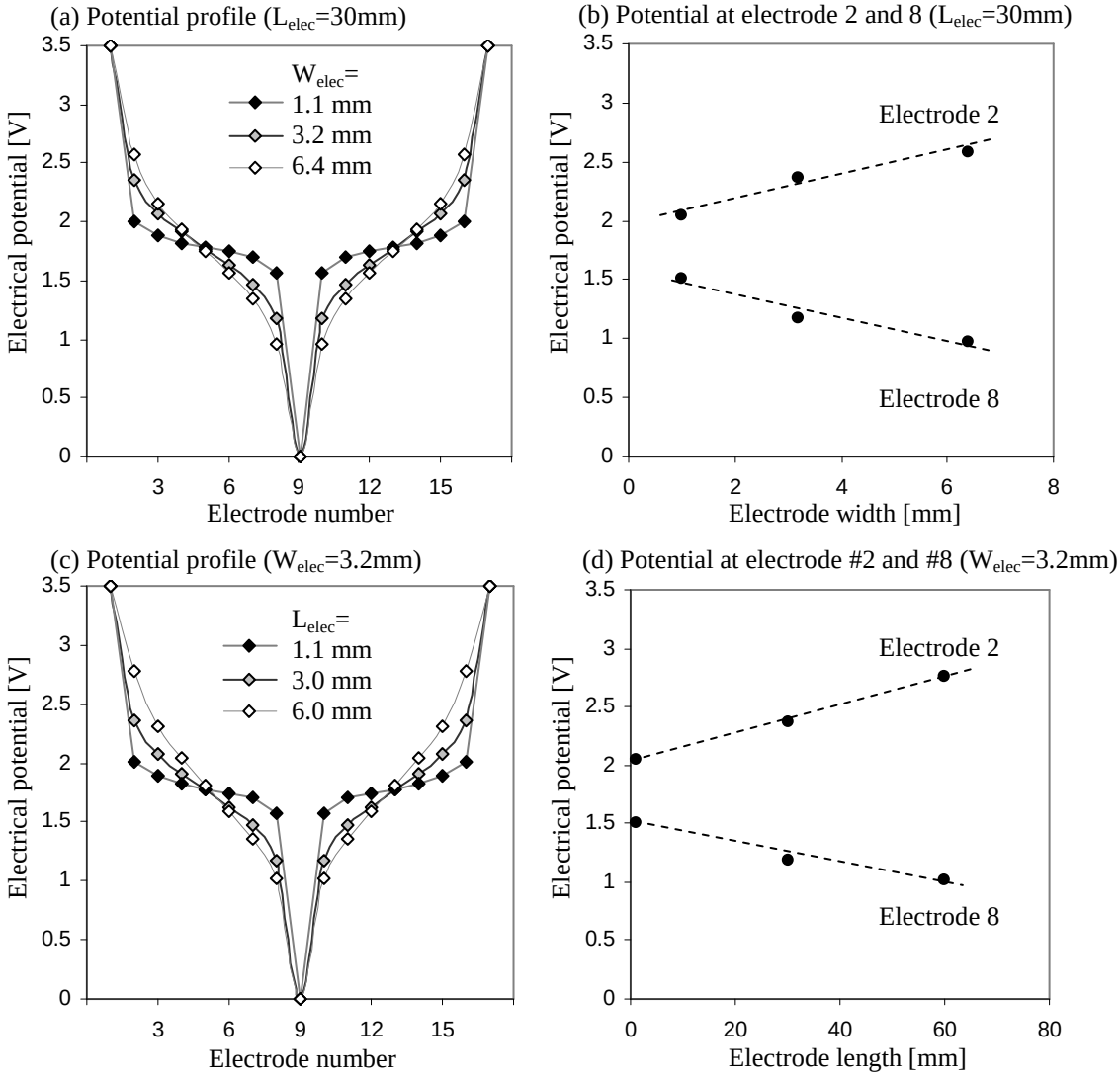

Figure 6.4 Experimental results on the effect of electrode width and length on the potential distribution. The cylindrical cell in Figure 6.1b is used with same source and sink conditions: (a) potential profile around the perimeter for electrode length L_{elec}=30mm and varying width, (b) potential at electrode #2 and #8 for electrode length L_{elec}=30mm and varying width, (c) potential profile around the perimeter for electrode width W_{elec}=3.2mm and varying length, and (d) potential at electrode #2 and #8 for electrode width W_{elec}=3.2mm and varying length. All potentials are measured with respect to the sink (#9) electrode, which is taken as ground.

However, electrodes are alternately used for source, sink, and measurement electrodes, so the size-related trade-offs should be properly considered in advance.

A series of numerical simulations is performed using COMSOL Multiphysics. The model geometry and boundary conditions are selected to match the condition for the high pressure cells used in this research for the study of hydrate-bearing sediments (Figure 6.5). The interface between the specimen and stainless steel cell includes an electrical insulation layer whereas the interfaces between specimen and end caps are electrically continuous as there is no insulation coating. The source electrode (#1) is set at a 3.5V, and the sink electrode 5 is set as ground. The conductivity values used in this numerical study are 0.5 S/m for the specimen and 4×10^{6} S/m for the cell and electrodes.

The general 3D mesh and all model characteristics are summarized in Figure 6.5a. The geometry of electrode and the inclusion and inclusion conductivity values are varied in the parametric study. Details and results follow.

6.3.2.1 Electrode Width and Shape: Near Electric Field.

Three different shapes of electrodes (cylindrical, half-cylindrical, and flat), four different electrode widths (W_{elec}=1.1mm, 3.2mm, 6.4mm, and 12.8mm) are simulated (fixed electrode length L_{elec}= 7mm, Figure 6.6). Other model conditions are described in Figure 6.5. Results are summarized in Figure 6.7. Regardless of the electrode shape, the voltage drop near source and sink electrodes decreases as the electrode width increases. A detail analysis of numerical results reveals that cylindrical and half-cylindrical electrodes produce better potential distribution near the source and the sink electrodes than flat electrodes. However, cylindrical electrodes are too intrusive, therefore half cylindrical and flat electrodes are considered for further analyses.

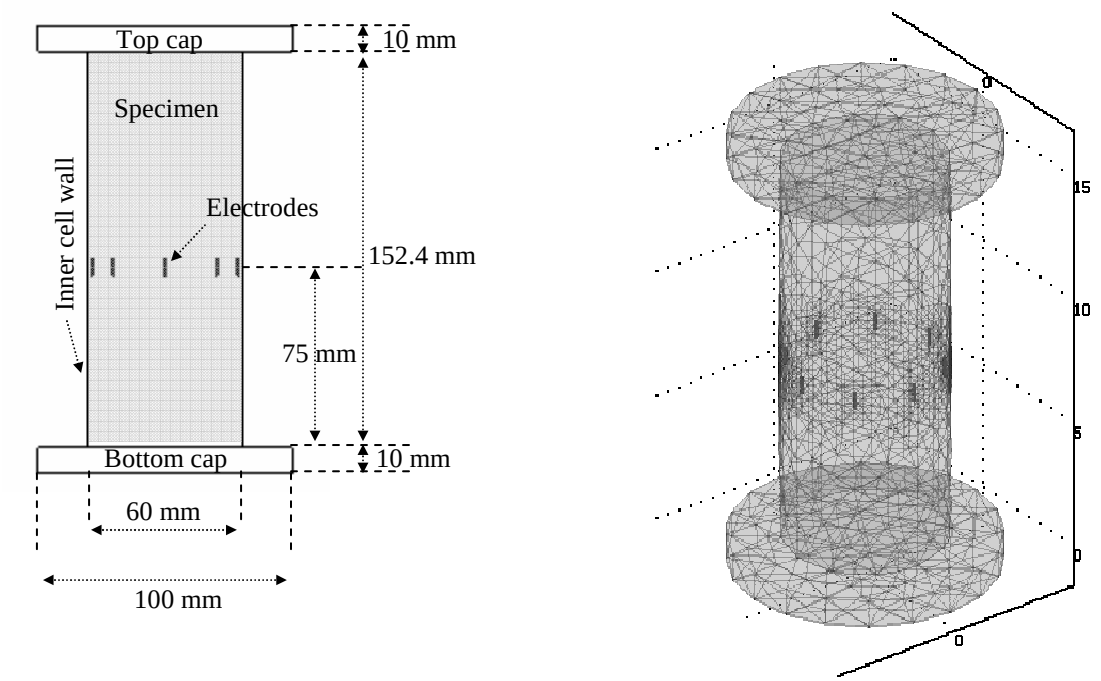

(a) Model geometry and FEM mesh

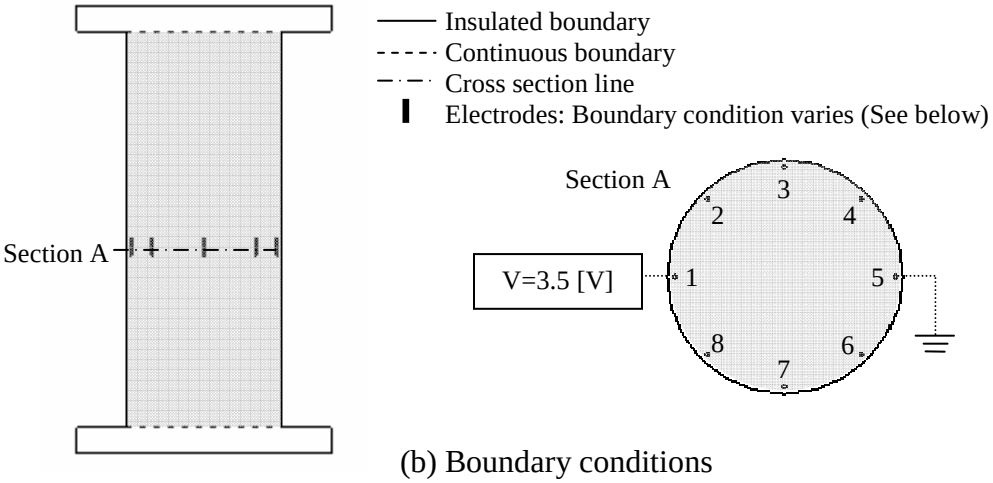

(b) Boundary conditions

(c) Model configuration summary

Parameters	Conductivity of specimen: 0.5 S/m
	Conductivity of stainless steel cell: 4×10^6 S/m
	Conductivity of electrodes: 4×10^6 S/m
Boundary conditions	Outer boundaries of the caps and the inner cell wall: Insulated
	Boundary between the specimen and caps: Continuous
	Measurement electrodes (2~4 and 6~8): Continuous boundary
	Source electrode (1): Electrical potential boundary (V=3.5[V])
	Sink electrode (5): Ground boundary

Figure 6.5 Model geometry, boundary conditions, and parameter values for numerical study. The electrode 1 is the source electrode (3.5V) and electrode 5 is the sink electrode (0.0V). (a) Model geometry and FEM mesh, (b) boundary conditions, and (c) model configuration summary

The effect of electrode width on anomaly detection is examined using four different locations for high and low conductivity inclusions (Figure 6.8). The diameter of the spherical inclusion is 12mm, and inclusion conductivities are 0.05S/m and 5.0S/m. Figures 6.9 and 6.10 show the potential change induced by either high of low conductivity inclusion for the half-cylindrical and flat electrodes. The following observations can be made from the results:

- A relatively large (D_{inc}/D_{cell}=0.2) and highly contrasting inclusion ($\sigma_{inc}/\sigma_{matrix}$=0.1 and 10) produce 1% $\Delta V/V_{in}$ as response to an inclusion at best.
- Electrodes are more sensitive to conductivity anomalies near the boundary than in the center regardless of electrode diameter and shape (similar results reported in (CohenBacrie et al. 1997; Dickin and Wang 1996; Pinheiro et al. 1998).
- The response is slightly higher for high conductivity inclusions ($\sigma_{inc}/\sigma_{matrix}$=10) than to low conductivity inclusions ($\sigma_{inc}/\sigma_{matrix}$=0.1).
- The response to different inclusion locations exhibits more unique patterns as electrodes become wider.
- Both half-cylindrical and flat electrodes show similar response patterns according to inclusion type and location but the sensitivity is higher with half-cylindrical electrodes. This is in part due to the shorter distance between inclusion and half-cylindrical electrodes

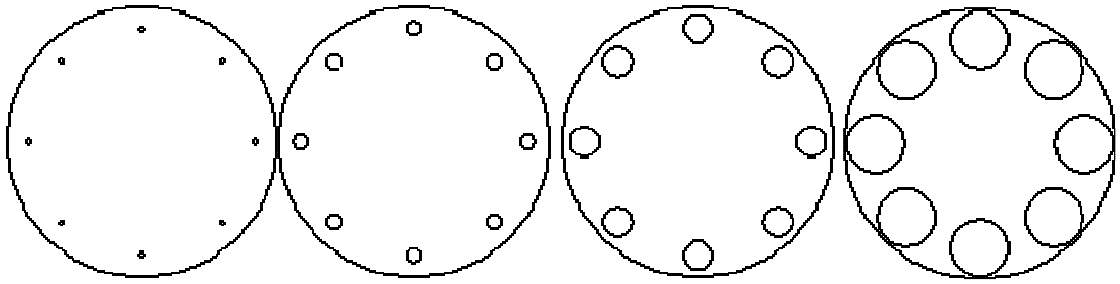

(a) Plan views for simulations with cylindrical.

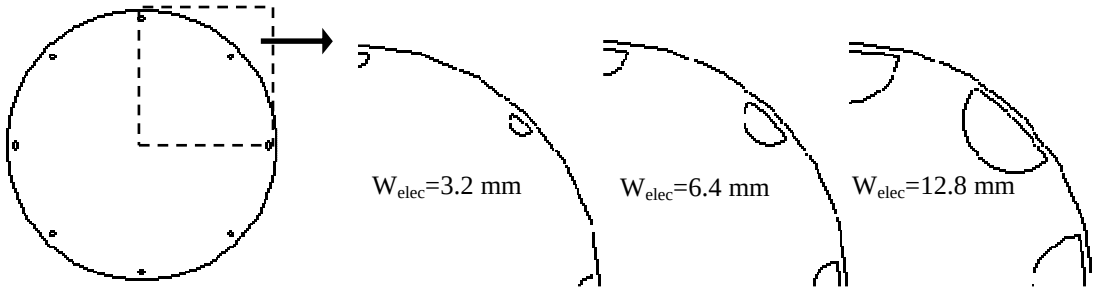

(b) Plan views for simulations with half-cylindrical electrodes

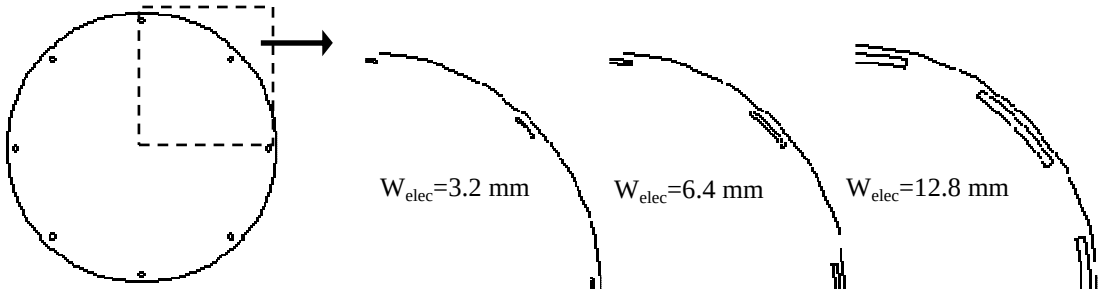

(c) Plan views for simulations with flat electrodes

Figure 6.6 Electrode width and shape effect – Electrode geometry for numerical simulation. Electrode width and shape vary and the electrode length is fixed at 7mm. Other model configurations are specified in Figure 6.5

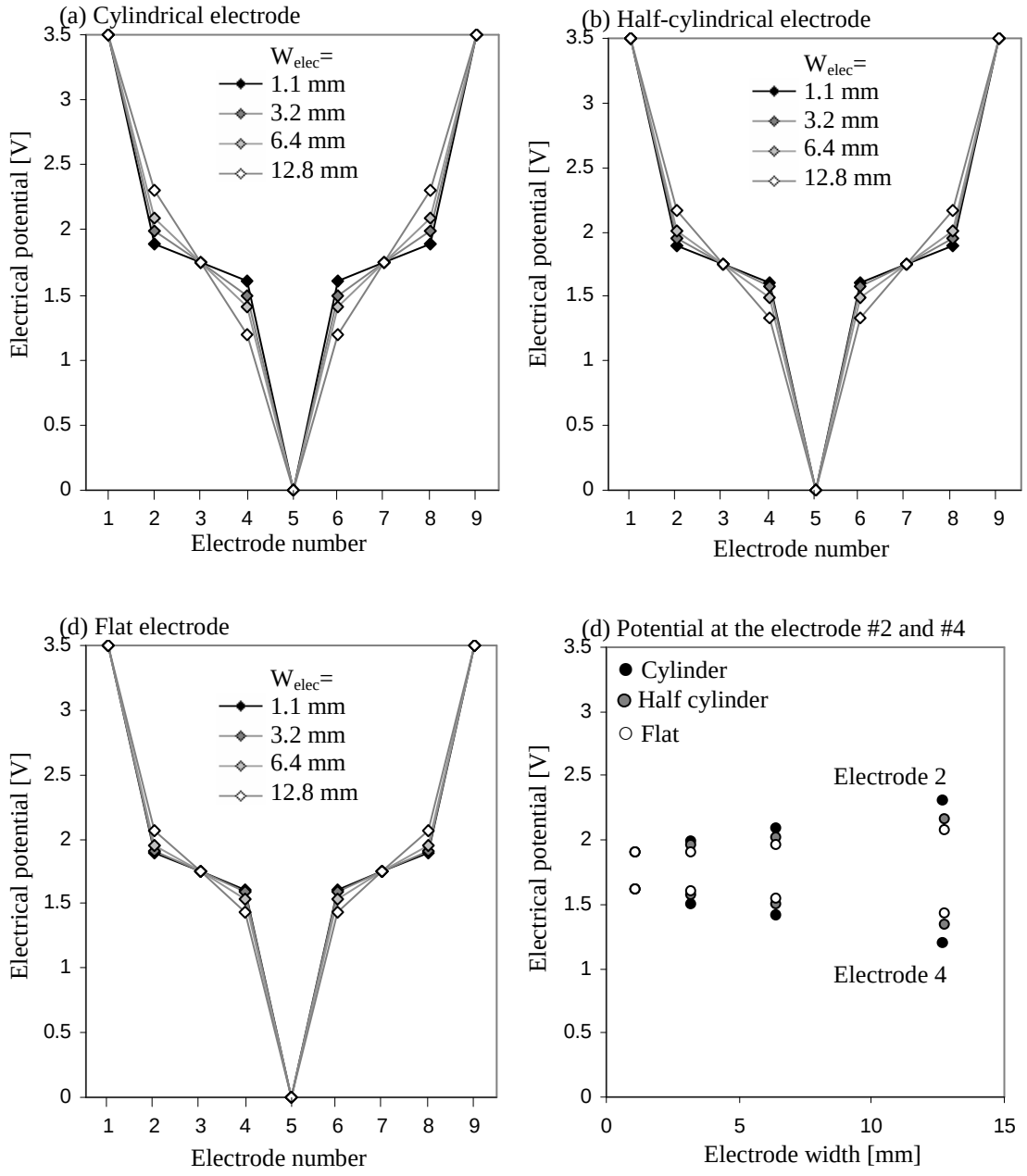

Figure 6.7 The electrode width and shape effect – The evolution of potential according to the electrode width and shape. The electrode length is 7mm. (a) Potential profile along cylindrical electrodes, (b) Potential profile along half cylindrical electrodes (c) Potential profile along flat electrodes, and (d) Potential at electrodes 2 and 4 against electrode width for all simulated shape and width.

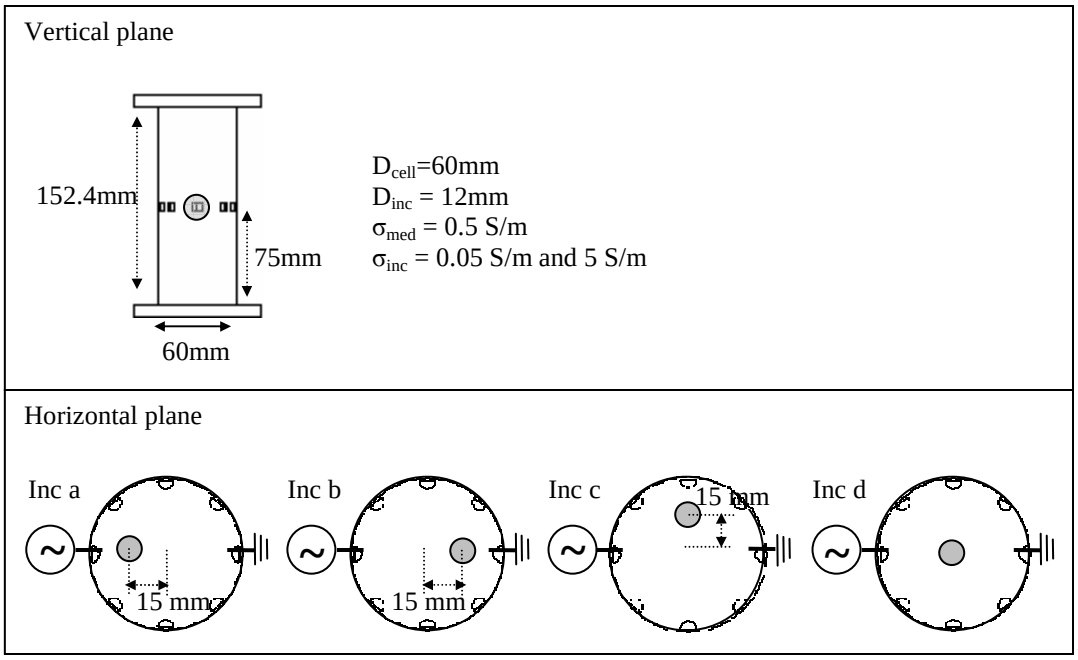

Figure 6.8 Electrode width and shape effect – Spherical inclusion specification for the sensitivity study (D_{inc} = 12mm, σ_{inc} = 0.05 S/m and 5 S/m).

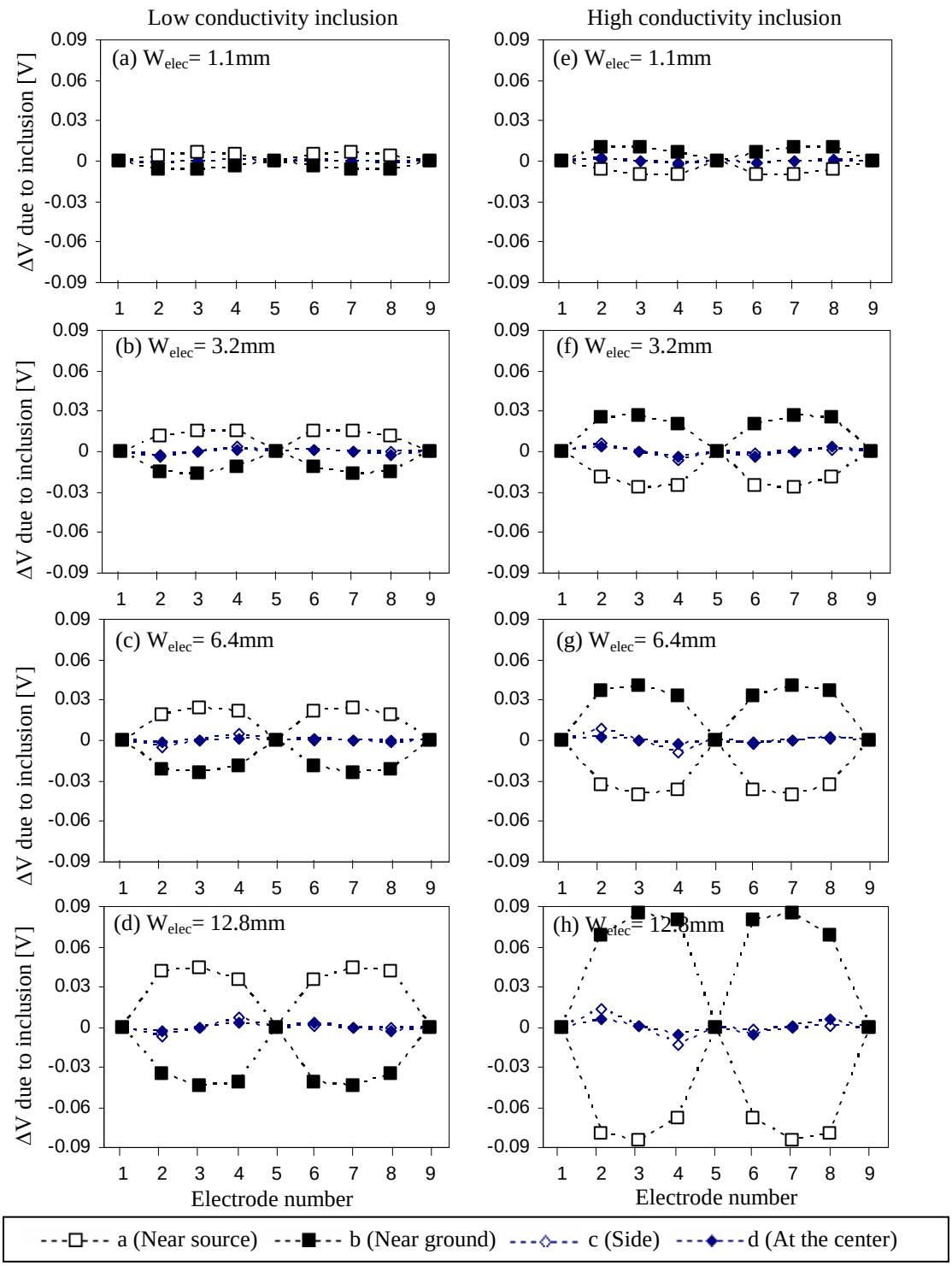

Figure 6.9 Half-cylindrical electrode-width effect - Sensitivity to the spherical inclusion (electrode length $L_{ele}c$= 7mm). Detailed inclusion specification is in Figure 6.8. (a)-(d): potential change induced by a low conductivity inclusion and (e)-(h): potential change induced by a high conductivity inclusion. Potentials for homogeneous cases can be found in Figure 6.7.

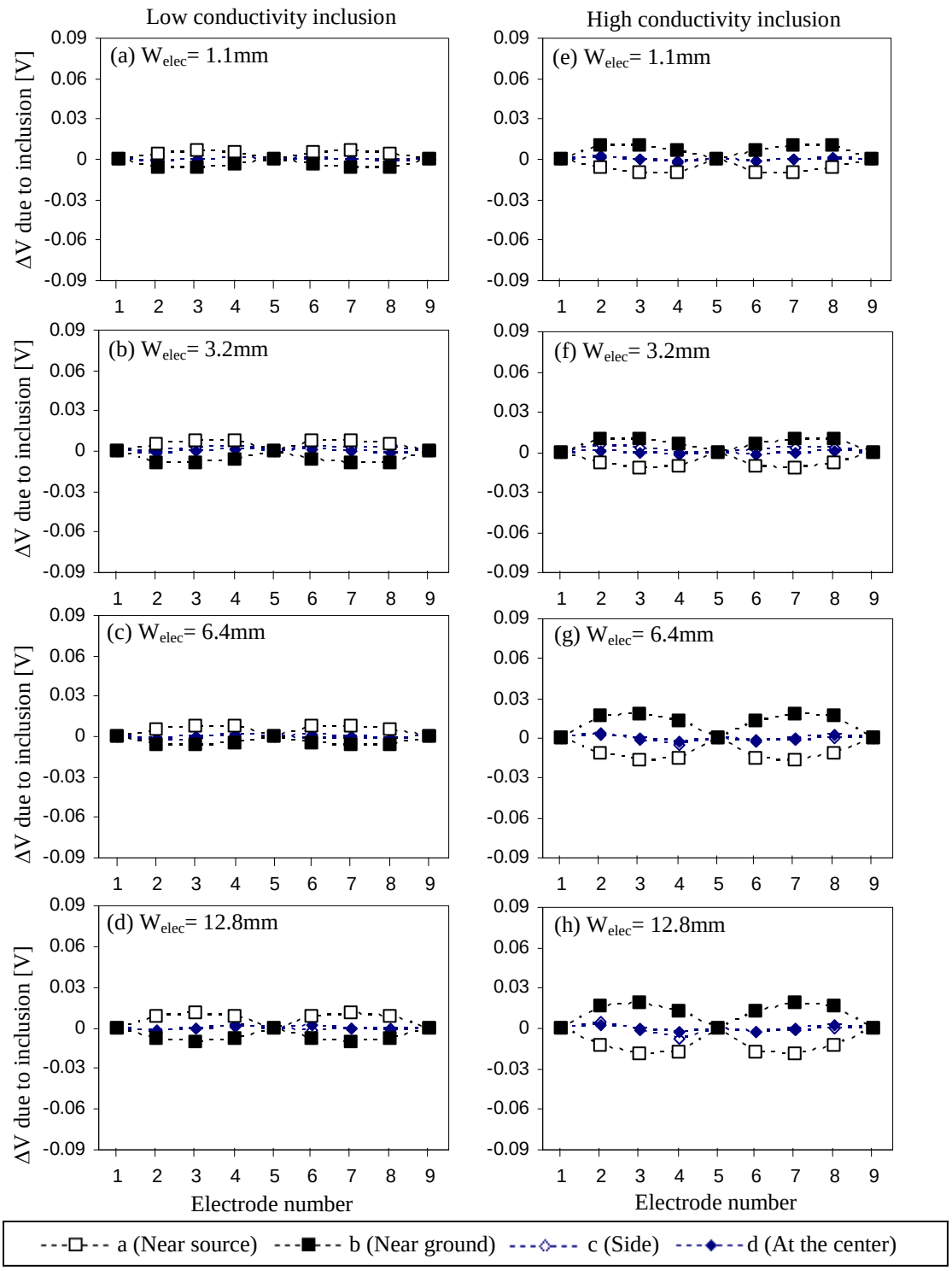

Figure 6.10 Flat electrode width effect- Sensitivity to the spherical inclusion (electrode length L_{elec}= 7mm). Detailed inclusion specification is in Figure 6.8. (a)-(d): potential change induced by a low conductivity inclusion and (e)-(h): potential change induced by a high conductivity inclusion. Potentials for homogeneous cases can be found in Figure 6.7.

In summary, half-cylindrical 12.8mm wide electrodes (W_{ele}/D_{cell}=0.21) provide the highest sensitivity to the presence of conductivity anomalies for the 60mm diameter cylindrical cell. However, considering the tomographic spatial resolution and the accommodation of 16 electrodes in the final configuration of the high pressure ERT cell, 6.4mm wide electrodes (W_{ele}/D_{cell}=0.11) are suggested for the optimal results.

6.3.2.2 Electrode Length.

Similarly to electrode width, electrode length is also expected to affect the sensitivity of measurements to the presence of conductivity anomalies and the ability of tomographic inversion to resolve spatial distribution of the conductivity. However, limited information is available in the literature. Published results suggest that the sensitivity to an inclusion varies with both electrode length and the inclusion size (Newell et al. 1998). Consequently, a numerical parametric study is conducted to explore these effects by varying the inclusion size and the length of electrodes. All model conditions except those for electrodes and inclusions are described in Figure 6.5. Simulations involve half-cylindrical 6.4mm wide electrodes with a varying length between 7mm and 50mm (Figure 6.11a) and spherical low conductivity inclusions with the size of either 12 mm or 24mm (σ_{inc}=0.05S/m, Figure 6.11b).

Figure 6.12a shows the potential at electrodes #2 and #4 which are the electrodes closest to source and sink electrodes for different electrode lengths: the potential difference between electrodes #2 and #4 increases as the electrode lengths increase until the difference reaches an asymptote at $L_{elec}\approx$40mm, ($L_{elec}/D_{cell}\approx$0.67) suggesting that the electric field approach a 2D rather than 3D condition. Figure 6.12b and c show the

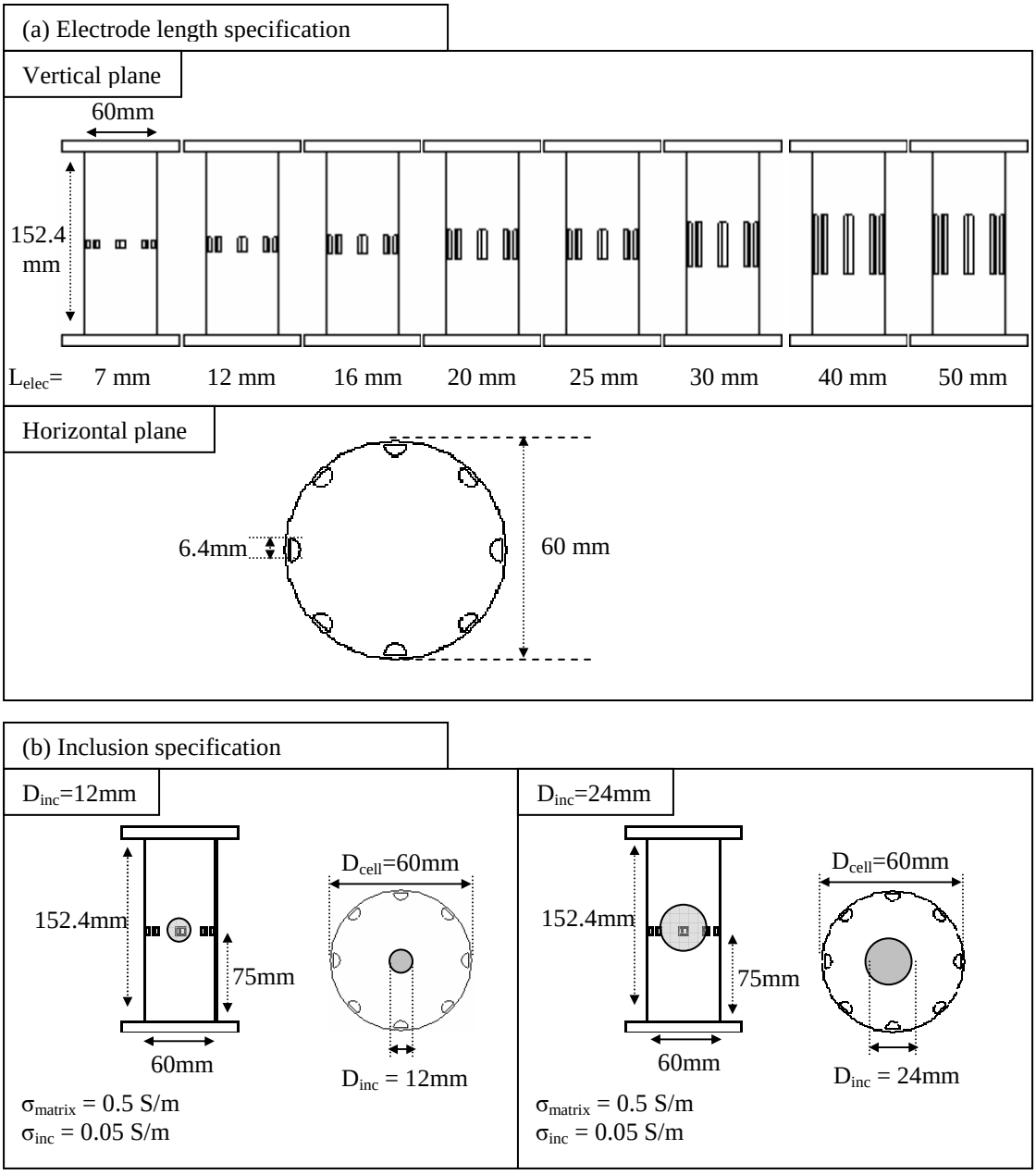

Figure 6.11 Electrode length effect-Electrode and spherical inclusion geometry for numerical simulation with half-cylindrical electrodes with W_{elec}=6.4 mm and varying length (σ_{matrix} = 0.5 S/m and σ_{inc} = 0.05 S/m). (a) Electrode length specification (b) Inclusion specification

.

(a) Homogenous specimen-Potential at electrode #2 and #4

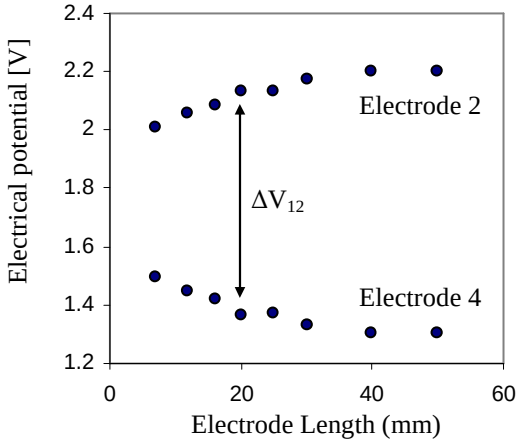

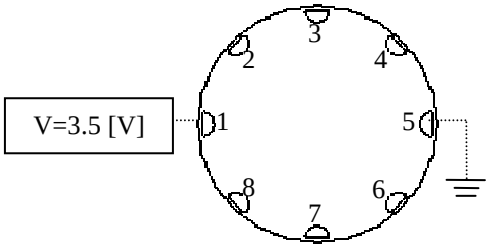

(b) Small inclusion (D_{inc}=12mm)-Potential change with respect to homogeneous medium

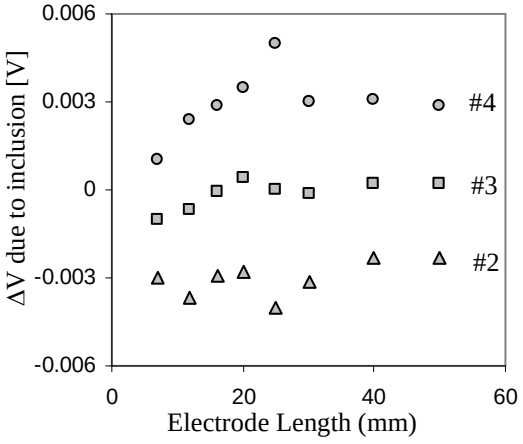

(c) Large inclusion (D_{inc}=24mm)-Potential change with respect to homogeneous medium

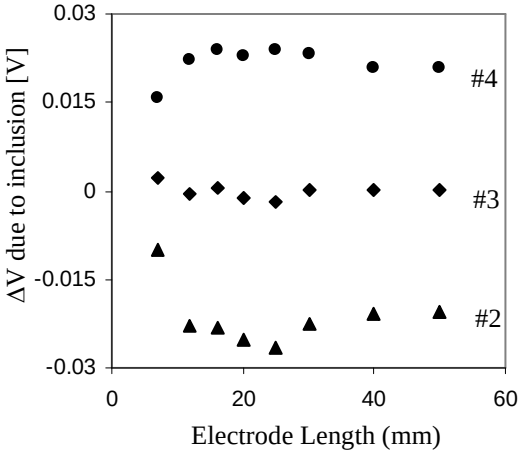

Figure 6.12 Electrode length effect - Potential distribution and sensitivity to a low conductivity spherical inclusion at the center of the cell. Model details are in Figures 6.5 and 6.11. (a) Potential at electrode #2 and #4 in homogeneous specimen. (b) Potential change induced by a small inclusion (D_{inc}=12mm) (c) Potential change induced by a large inclusion (D_{inc}=24mm)

potential changes at electrodes #2, #3, and #4 induced by low conductivity inclusions. Note the responses are only $\Delta V/V_{in} \approx 0.002$ in the case of the small size inclusion ($D_{inc}/D_{cell}=0.2$). Maximum sensitivity to the inclusion is observed when the electrode length is 25mm for both D_{inc}= 12mm and D_{inc}= 24 mm inclusions ($D_{inc}/D_{cell}=0.2$ and 0.4). However, trends are relatively stable relative to the electrode length for this geometry.

6.3.2.3 Additional Electrode at the Center.

Results in previous section (Figure 6.9 and 6.10) and simulation in the literature (Lyon and Oakley 1992; Seagar et al. 1986) show low sensitivity of ERT with perimeter electrodes to conductivity anomalies at the center. In order to examine whether an electrode at the center can improve the detection of anomalies, an ERT system with an electrode at the center of the specimen is simulated. The geometry, boundary conditions, and conductivity values are the same as those in previous simulations of the flat electrode ERT system (Figure 6.5 and 6.6c), except for the location of the newly-introduced central sink electrode. A cylindrical sink electrode (W_{elec}=3.2mm, L_{elec}=7mm) is placed at the center of the cell. The peripheral flat electrodes are W_{elec}=3.2mm wide and L_{elec}=7mm long (Figure 6.13a). The electrode #1 is the source electrode (V=3.5V) and the center electrode is the sink electrode. The sensitivity to inclusions is tested for a spherical inclusion (D_{inc}=12mm) of either low or high conductivity values (σ_{inc}=0.05S/m or 5S/m). The inclusion locations are depicted in Figure 6.13b.

Figure 6.14a shows the potential distribution around the peripheral electrodes, and Figure 6.14b and c shows the potential change at each electrode induced by either high of low conductivity inclusion. The sensitivity to off-center inclusions is similar to that of

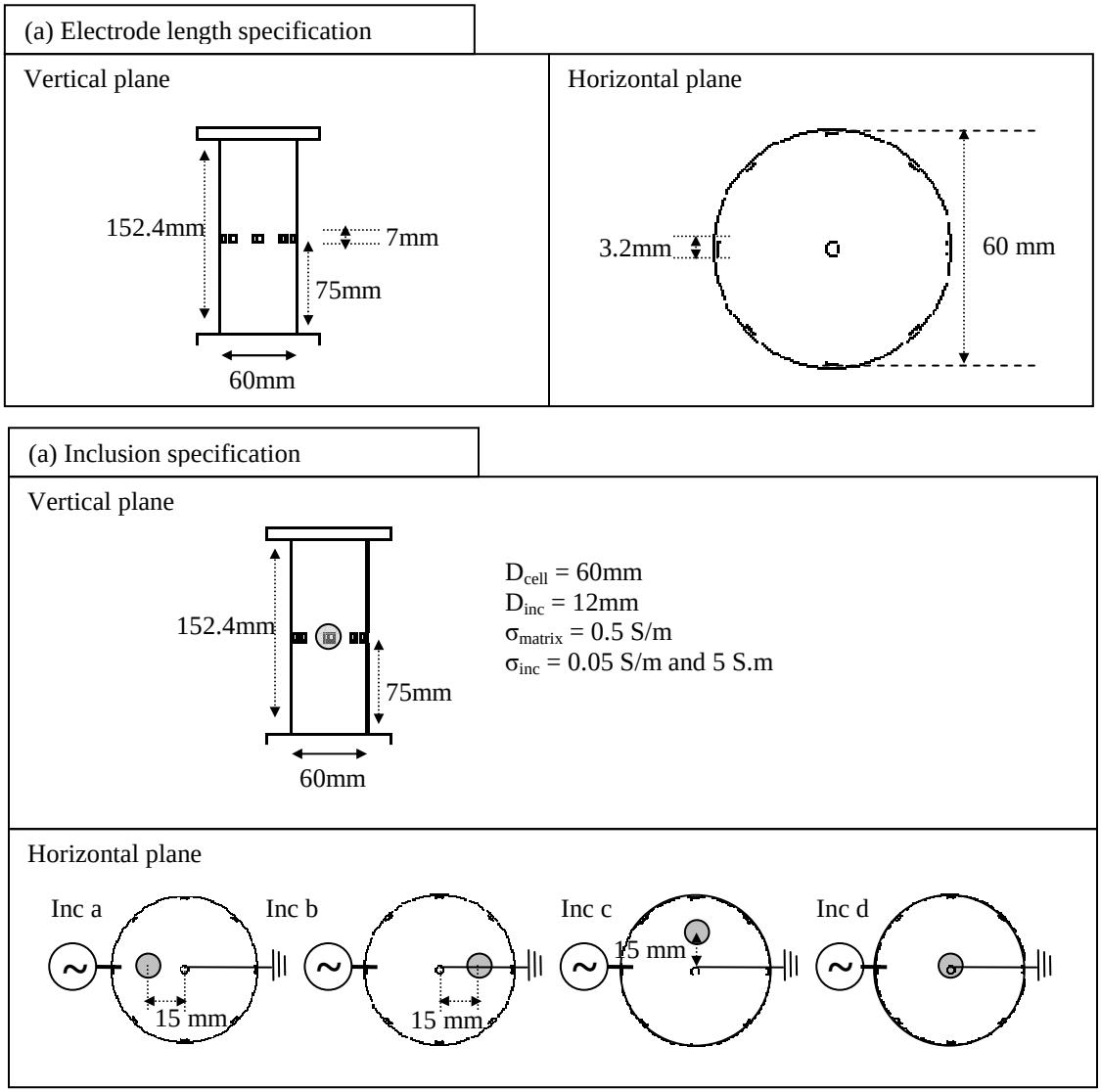

Figure 6.13 An additional electrode at the center-The electrode configurations and the spherical inclusion specifications. Detailed model condition is illustrated in Figure 6.5. (a) Electrode specification (b) Inclusion specification.

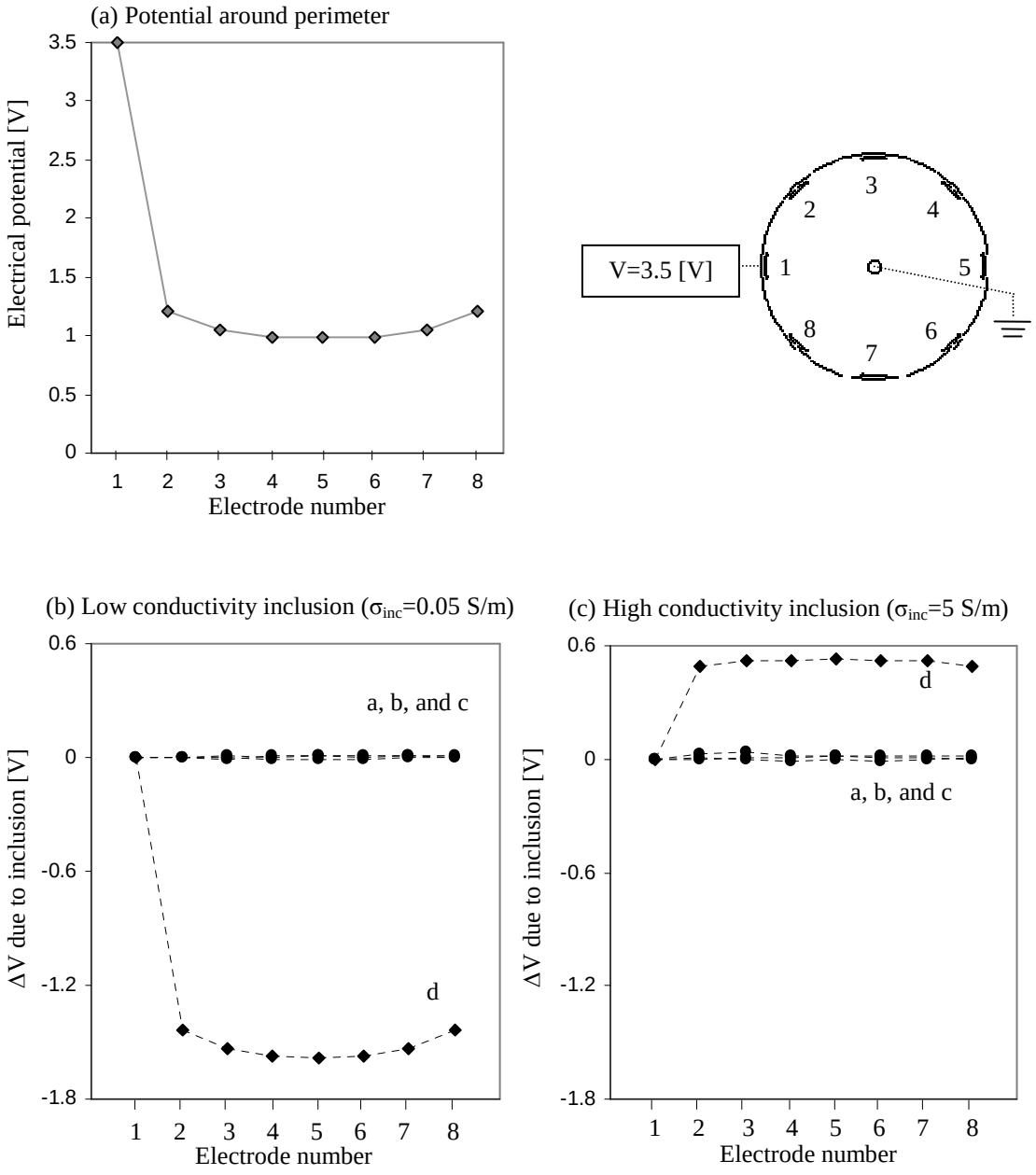

Figure 6.14 An additional electrode at the center-Electrical potential distribution and the sensitivity to inclusions. Model specifications are in Figure 6.5 and 6.13. (a) Potential along electrodes (b) Potential change induced by an low conductivity spherical inclusion inclusion (σ_{inc}=0.05S/m) (c) Potential change induced by high conductivity spherical inclusion (σ_{inc}=5.0S/m)

peripheral source and sink electrodes ERT system (0.01~0.02V for a 3.5V source input). However, the sensitivity to the center inclusion is dramatically improved, particularly in the case of a low conductivity anomaly.

6.4 ELECTRICAL INSULATION

The electrical insulation between the specimen and the stainless steel high pressure cell is crucial given the high conductivity of the cell material. In particular, while the cell wall can be electrically shielded, top and bottom caps cannot be perfectly shielded due to the inherent installation sequence and the presence of inlet and outlet ports for fluids and sensors. Therefore, the effect of partial shielding is numerically examined in this section. The basic model specifications correspond to those summarized in Figure 6.5. Boundary and inclusion conditions are specified in Figure 6.15. Half-cylindrical 6.4mm wide and 25mm high electrodes are used, and either low or high conductivity spherical inclusion (σ_{inc}=0.05S/m or 5S/m) with diameter of either 12mm or 24mm is tested.

Figure 6.16 shows the potential around the perimeter and the potential at electrode #2 and $4 for different insulation conditions. The electrical potential in the non-insulated cell is homogeneous at 1.7V, and no information can be gathered about the medium. Wall insulation only and all insulation (wall and end caps) show almost the same results (Figure 6.16). These observations apply to the case with inclusions as well (Figure 6.17). The results suggest that the presence of conductive boundaries between the specimen and either the top or the bottom plate does not hinder the performance of the ERT system in

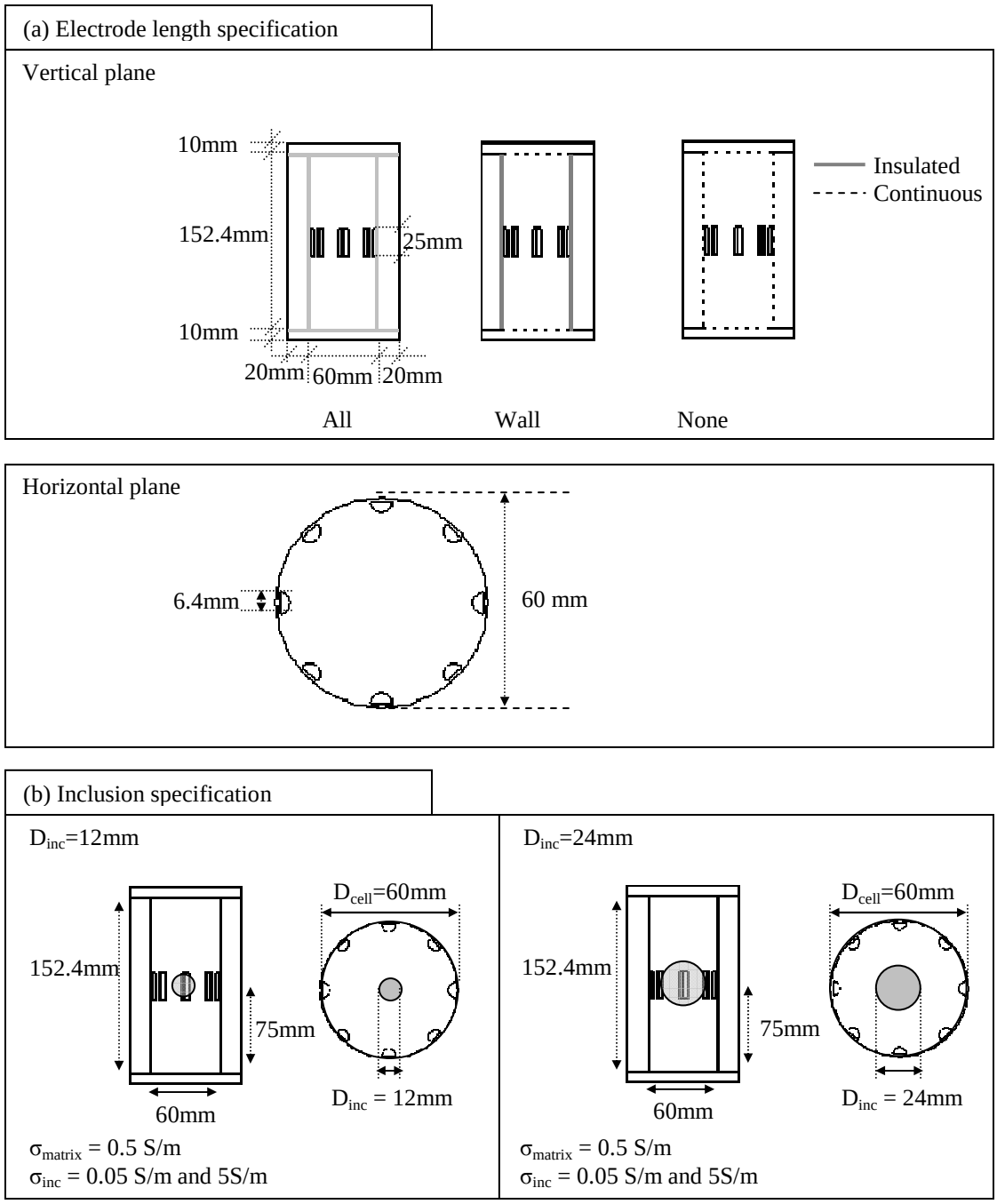

Figure 6.15 Electrical insulation - The boundary condition between the specimen and the cell and the inclusion condition. The specimen boundary condition varies from all insulated boundary to completely continuous boundary. The inclusion is at the center with varying size and conductivity. Detailed model specification is in Figure 6.5.

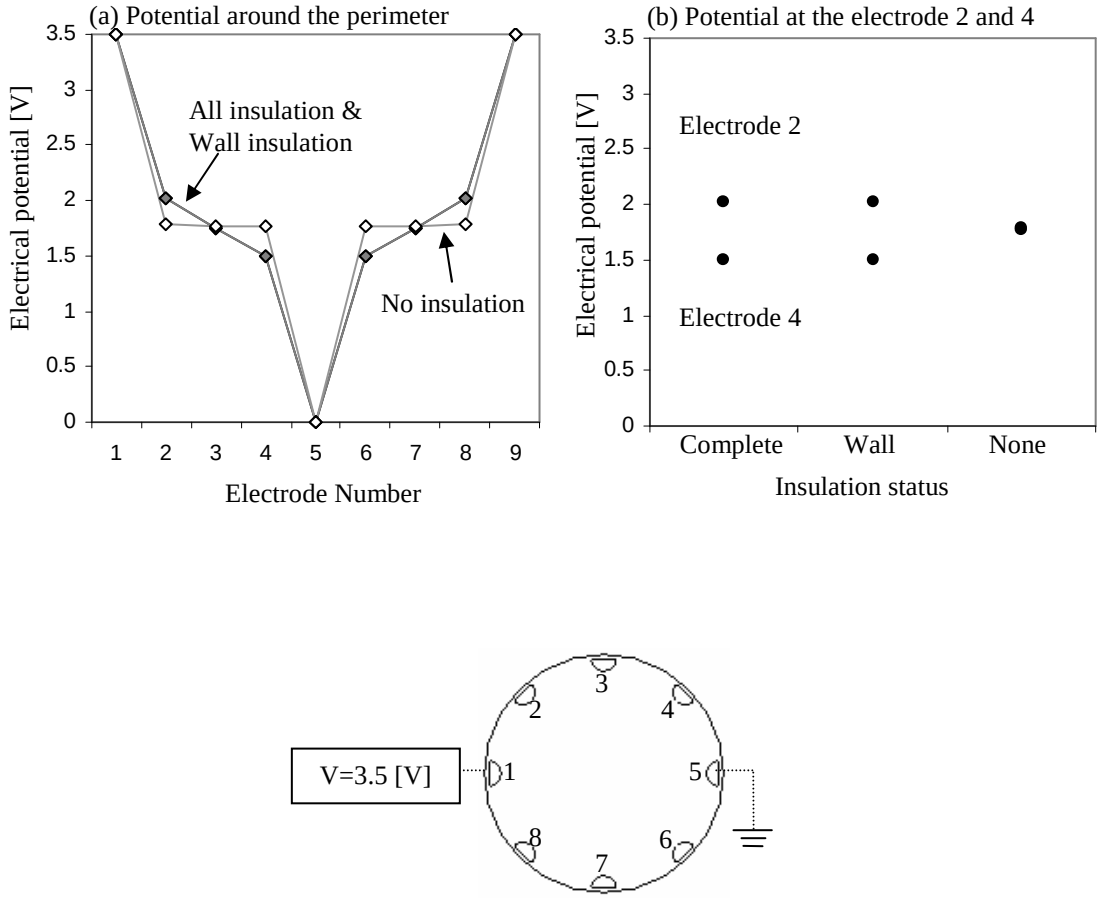

Figure 6.16 Electrical insulation - Electrical potential distribution along the perimeter of specimen in a completely insulated cell, a wall-insulated cell, and a non-insulated stainless steel cell. Model specification is Figure 6.5 and 6.15. (a) Potential profile along electrodes (b) Potential at the electrodes 2 and 4

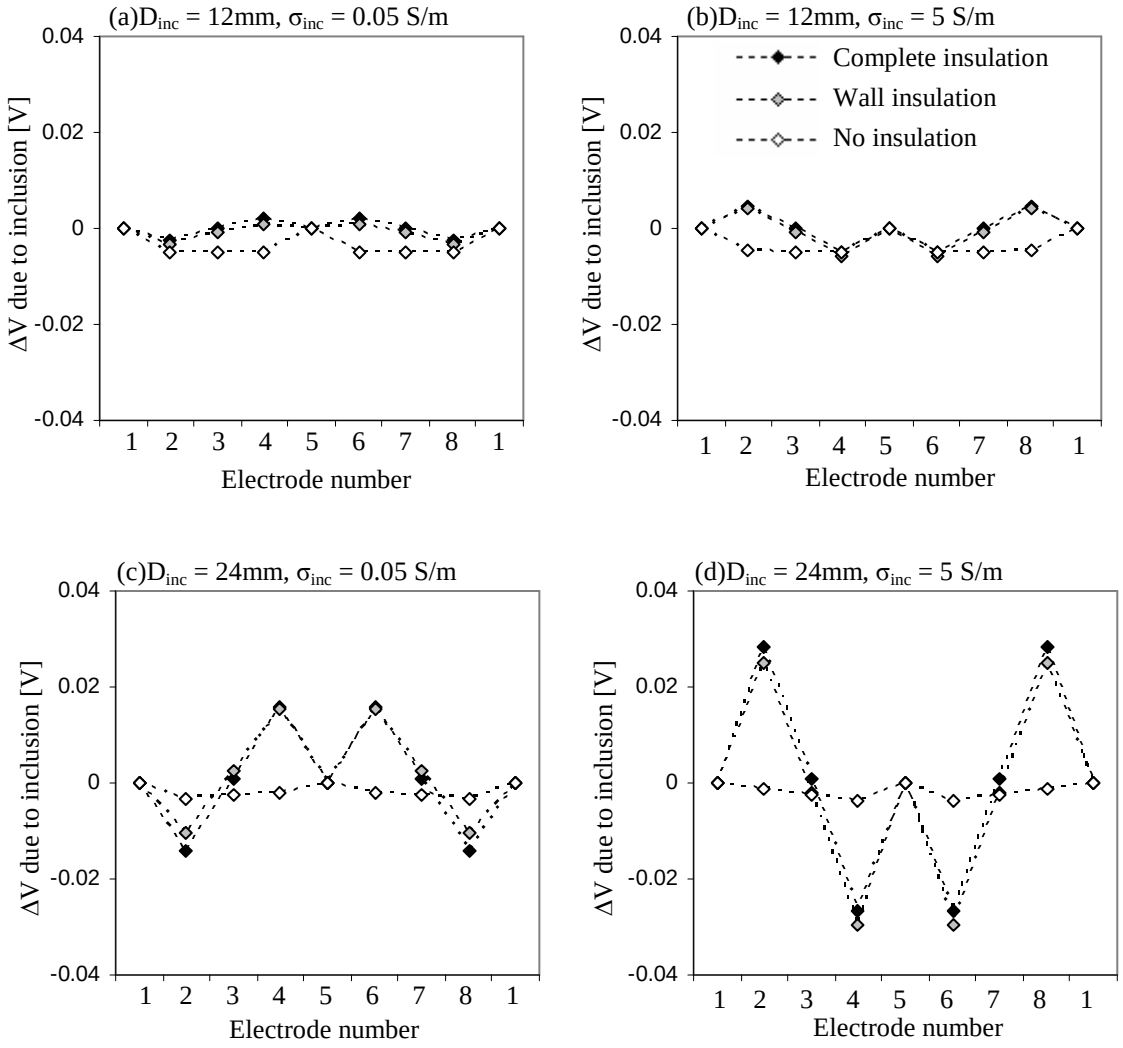

Figure 6.17 Electrical insulation - Sensitivity analyses for different insulation status. Model specifications are in Figure 6.5 and 6.15 (a)D_{inc} = 12mm, σ_{inc} = 0.05 S/m (b)D_{inc} = 12mm, σ_{inc} = 5 S/m (c)D_{inc} = 24mm, σ_{inc} = 0.05 S/m (d)D_{inc} = 24mm, σ_{inc} = 5 S/m

this cell configuration because most of the current flows in the plane of electrodes located at the center height.

6.5 SUMMARY

- Electrode polarization effect can be avoided if measurements are conducted in the kHz frequency range.

- The drop in electrical potential near source and sink electrodes and associated high current densities are due to geometric-Laplacian effects and can be reduced by using wider electrodes at the expense of lower spatial resolution. Therefore, the response to inclusions becomes stronger as the electrode width increases.

- Taking into consideration spatial resolution, electric field and shunting effects, optimal ERT results can be obtained when the electrode width is $W_{elec}/D_{cell} \cong 0.1$.

-Longer electrodes change the 3D current flow condition into a pseudo 2D case. The signal strength and the sensitivity to inclusions benefit from the longer length of electrodes but reaches an asymptote when $L_{elec}/D_{cell} \cong 0.7$ (for $D_{inc}/D_{cell}=0.2\sim0.4$).

- An electrode at the center of the cell dramatically improves the sensitivity to conductivity anomalies in the central region.

- End-cap insulation is not required in cylindrical cells with electrodes located at the mid-height of the cell if $H_{cell}/D_{cell} \geq 2.5$ and $L_{elec}/H_{cell} < 0.2$.

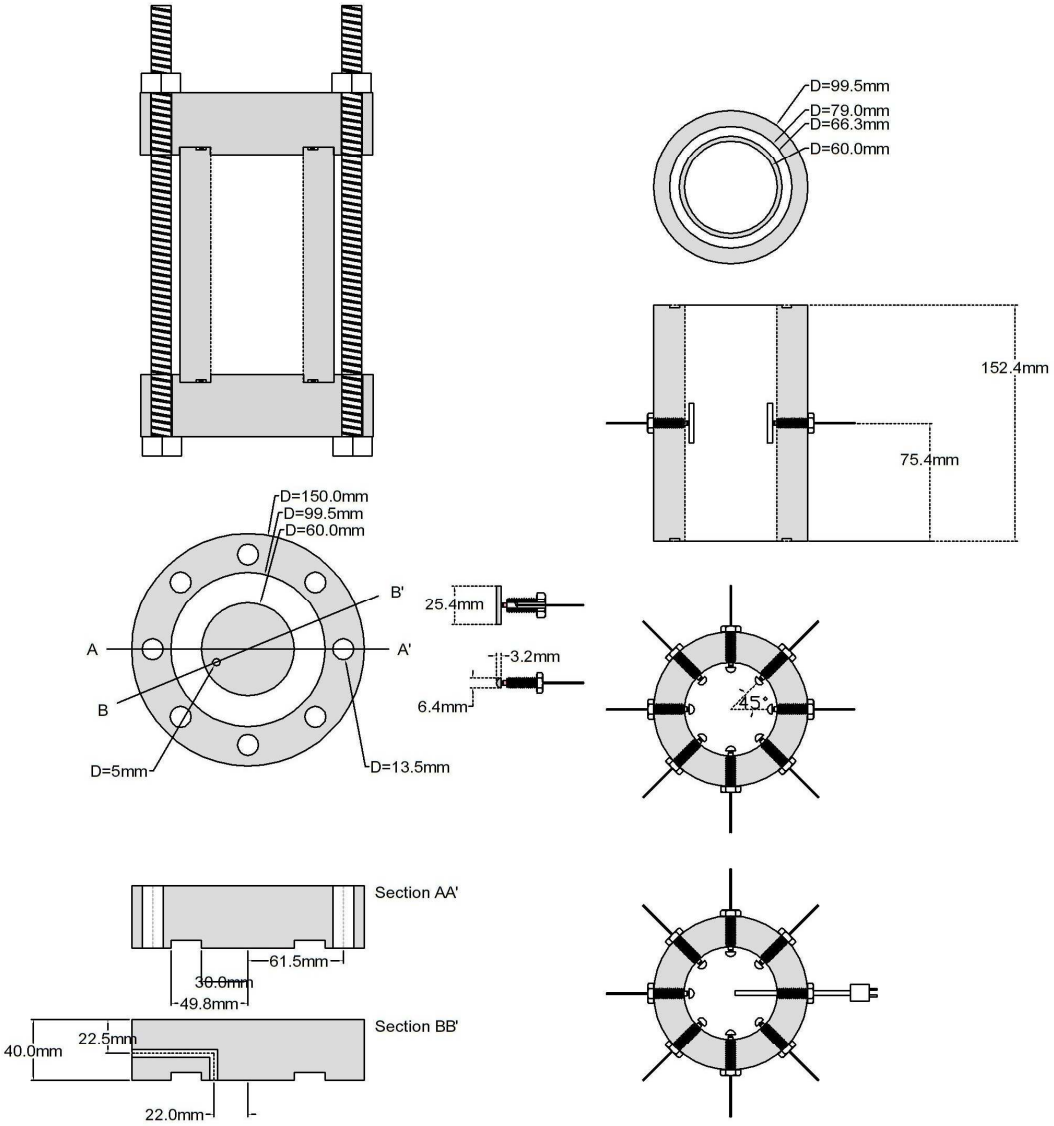

Figure 6.18 Specification of high pressure Electrical Resistivity Tomography cell for the study of hydrate-bearing sediments – Engineering drawings.

The high pressure ERT cell must satisfy the dimensionless geometrical ratios identified in this chapter for optimal performance (W_{elec}/D_{cell}=0.1 and L_{elec}/D_{cell}=0.7). Detailed specifications of the cell are shown in Figure 6.18. The cylindrical cell is 152mm high and 100mm wide with inner diameter of 60mm. The half-cylindrical, 20mm high, and 64mm wide electrodes are installed against the cell wall at mid height.

.

CHAPTER VII.

ERT DATA ANALYSIS AND PREPROCESSING

-CO_2 HYDRATE-BEARING SEDIMENTS-

7.1 INTRODUCTION

The electrical resistivity of hydrate-bearing sediments captures the combined effect of porosity, gas hydrate saturation, gas content, pore fluid composition, and temperature. Electrical measurements have been used to explore gas hydrate-bearing sediments through well logging and electromagnetic field surveys (Hyndman and Spence 1992; Weitemeyer et al. 2006) and in the laboratory studies (Buffett and Zatsepina 2000).

Continuous monitoring using electrical resistivity tomography can give insight into the spatial distribution and the fate of pore water, natural gas, hydrate, and ions in sediments during formation and dissociation processes. This information is crucial for seafloor stability analyses and gas production studies. This chapter documents a series of tomographic measurements and data analyses during CO_2 hydrate formation and dissociation in sediments.

7.2 BRIEF REVIEW OF FUNDAMENTAL CONCEPTS

7.2.1 Conductivity in Hydrate-bearing Sediments

The electrical resistivity, or its inverse conductivity, of hydrate-bearing sediments reflects the mobility and the concentration of ions. Therefore, ion exclusion, concentration change, and temperature change during hydrate formation will affect conductivity measurements.

The electrolyte conductivity $\sigma_{electrolyte}$ can be estimated as a function of the ionic concentration c_i [mol/m^3], the valence z_i, the molar conductivity Λ_i [Sm^2/mol], and the ionic mobility u_i of ith species,

$$\sigma_{electrolyte} = F\sum_i c_i z_i u_i = \sum_i c_i \Lambda_i \tag{7.1}$$

where F = 9.6485×10^{4}C/mol is Faraday's constant. The conductivity of electrolytes increases as temperature increases because of increased ion mobility (Keller and Frischknecht 1966).

$$\sigma_T = \sigma_{T_0}\left[1 + \alpha_T\left(T - T_0\right)\right] \tag{7.2}$$

where α_T is about 0.025 [°C^{-1}] for electrolytes.

Porosity n, water saturation S_w, and hydrate saturation S_{hyd} affect the conductivity of mixtures through changes in pore connectivity (low frequency) and in the volume fraction of the conducting phase. Therefore, conductivity increase as porosity and water saturation increase, and hydrate saturation decreases. Empirical equations relate the electrical conductivity of porous media to the volume fraction of electrolyte, where gas, hydrate and minerals are considered as insulators. In its simplest form,

$$\sigma = \sigma_w n^m \qquad \text{Pore fluid-sediment system} \tag{7.3}$$

$$\sigma = \sigma_w \left(nS_w\right)^m \qquad \text{Pore fluid-gas-sediment system} \qquad (7.4)$$

$$\sigma = \sigma_w \left[n\left(S_w - S_{hyd}\right)\right]^m \qquad \text{Pore fluid-gas-hydrate-sediment system} \qquad (7.5)$$

where σ_w is the pore fluid conductivity and m is a constant related to the pore structure (e.g. m=1.5 for spherical particle (Feng and Sen 1985)). The sensitivity to changes in porosity, hydrate saturation, and water saturation increases as the fluid conductivity increases (Rinaldi and Cuestas 2002).

In fine grained sediments, conduction along the particle surfaces can be significant (Santamarina et al. 2001). The contribution of surface conduction λ_{ddl} [S] can be taken into account as a function of the specific surface S_a [$m^2 \cdot g^{-1}$]

$$\sigma = \sigma_w \left[n\left(S_w - S_{hyd}\right)\right]^m + (1-n) \cdot \rho_p \cdot \lambda_{ddl} \cdot S_a \qquad (7.6)$$

where ρ_p is the particle density [$g \cdot cm^{-3}$], and is the

7.2.2 Inversion of Boundary measurements

The objective function is a measure of the fit between estimated and measured values, and other criteria imposed in the inversion. The simplest measure of error for the i^{th} measurement e_i is the difference between the i^{th} estimated value $y_i^{<est>}$ and the ith measured value $y_i^{<meas>}$ (Santamarina and Fratta 2005)

$$e_i = y_i^{<meas>} - y_i^{<est>} \qquad (7.7)$$

Alternative error definitions are summarized in Table 7.1. The log-difference is preferred when variables vary across more than one order of magnitude.

Errors for individual measurements are accumulated to compute a single measure of fit. Common error norms are shown in Table 7.1. The L_1 norm is the least sensitive to

Table 7.1 Error definitions and error norms

Error definitions	
Difference	$e_i = y_i^{<meas>} - y_i^{<est>}$
Log difference	$e_i = \log\left(y_i^{<meas>}\right) - \log\left(y_i^{<est>}\right)$
Proportional error	$e_i = \dfrac{y_i^{<meas>} - y_i^{<est>}}{y_i^{<sim>}}$
Standard error	$e_i = \dfrac{y_i^{<meas>} - y_i^{<est>}}{\sigma_i}$ σ_i : standard deviation for the ith measurement
Error norms	
Sum of absolute errors	$L_1 = \sum_i \lvert e_i \rvert$
Sum of squared errors	$L_2 = \left(\sum_i \lvert e_i \rvert \right)^{\frac{1}{2}} = \sqrt{e^T e}$
Maximum absolute errors	$L_\infty = \max\left(\lvert e_1 \rvert \cdots \lvert e_i \rvert \ldots \lvert e_M \rvert \right)$

outliers, whereas the L_∞ norm is the least sensitive to the distribution of information (Santamarina and Fratta 2005).

Linearization of the non-linear ERT problem: Non-linear problems can be linearized using the Jacobian Matrix $\underline{\underline{G}}$. The linearized forward ERT problem becomes (Stummer et al. 2004):

$$(\underline{d}^{obs} - \underline{d}^{ini}) = \underline{\underline{G}} \cdot (\underline{m}^{true} - \underline{m}^{ini}) \tag{7.8}$$

where $\underline{d} = \ln(\underline{V})$ and $\underline{m} = \ln(\underline{\rho})$. Model parameters are log transformed to facilitate convergence.

Solution by Matrix Inversion – Regularized Least Square Solution: The least square solution has been implemented in several ERT studies (Parks 1990; Stummer et al. 2004). The regularized least square solution is

$$\underline{m}^{est} = \underline{m}^{ini} + \left(\underline{\underline{G}}^T \underline{\underline{G}} + \lambda \cdot \underline{\underline{R}}^T \underline{\underline{R}}\right) \cdot \underline{\underline{G}}^T \left(\underline{d}^{obs} - \underline{d}^{ini}\right) \tag{7.9}$$

where λ is a nonnegative regularization coefficient and $\underline{\underline{R}}$ is the regularization matrix (Parks 1990; Santamarina and Fratta 2005).

Solution by Successive Forward Simulations: The trial-and-error solution by successive forward simulations consists of the following steps: (1) generate an estimate of solution $\underline{x}^{<est>}$, (2) compute $\underline{y}^{<est>}$ by forward simulation, (3) analyze the residual $\underline{y}^{<est>}$ - $\underline{y}^{<meas>}$, (4) update $\underline{x}^{<est>}$ based on residual analysis, and (5) repeat step 1 to 4 until a physically meaningful estimate is found with small enough residuals.

The number of unknowns can be reduced by recasting the forward problem with prior information. For example, when the shape of an anomaly can be assumed, the number of unknowns can be reduced from a large number pixel resistivity values to the

location, size and resistivity of the inclusion (d_{inc}, x_{inc}, y_{inc}, z_{inc}, and ρ_{inc}) and the resistivity of the matrix (ρ_{matrix}).

7.3 EXPERIMENTAL and NUMERICAL STUDY PROCEDURES

The experimental device used in this study is depicted in Figure 7.1. The gas pressure is regulated by the high pressure gas regulator attached to the gas cylinder(max. working pressure = 25MPa). Gas is injected through the top cap and drained through the bottom cap. The high pressure cell for tomographic studies is designed considering the effect of electrode configuration and electrical shielding on tomographic measurements discussed in Chapter 6. The cell body is constructed from stainless steel (SS316) to safely resist both high pressure and corrosion. The inner diameter of the cylindrical cell is 60mm and the height is 152.4mm.

Detailed dimensions and specifications are depicted in Figure 7.1b. Electrodes are connected to the ERT signal generator and data logger through the electric circuit box (The circuit diagram is shown in Appendix C). Sinusoidal wave with 3.5V amplitude and 1kHz frequency is used as the source signal.

Ottawa 20/30 sand (D_{50}=0.72mm, Roundness=0.9, and Sphericity=0.9) and Ottawa F110 sand (D_{50}=0.12mm, Roundness=0.7, and Sphericity=0.7) are used as sediments. Saturated specimens are prepared by the water pluviation method; when required, unsaturated specimens are obtained by gravity drainage after water pluviation. The specimen height is 10 cm, which is about two thirds of the cell height. The rest of the cell is filled with CO_2.

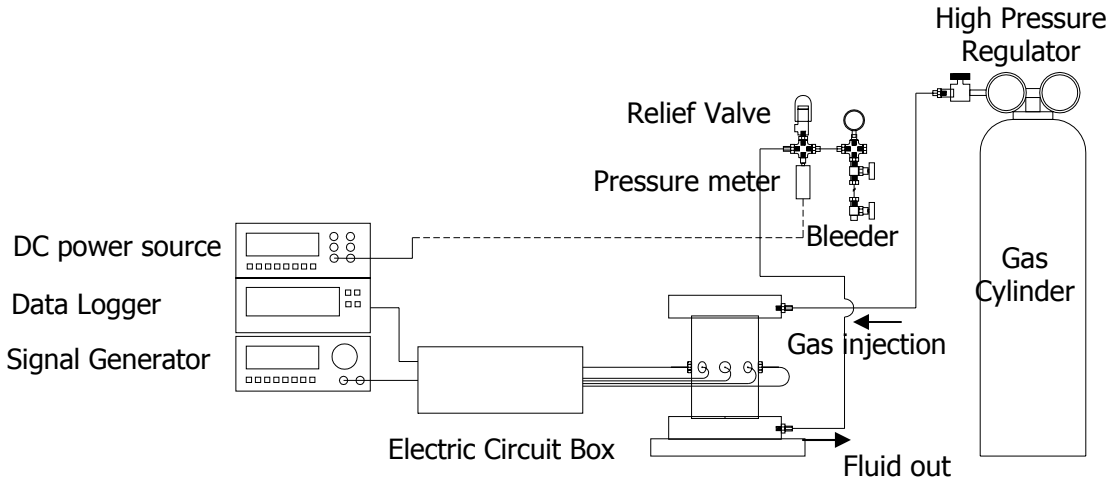

(a) Outline of high pressure ERT system for hydrate-bearing sediment study.

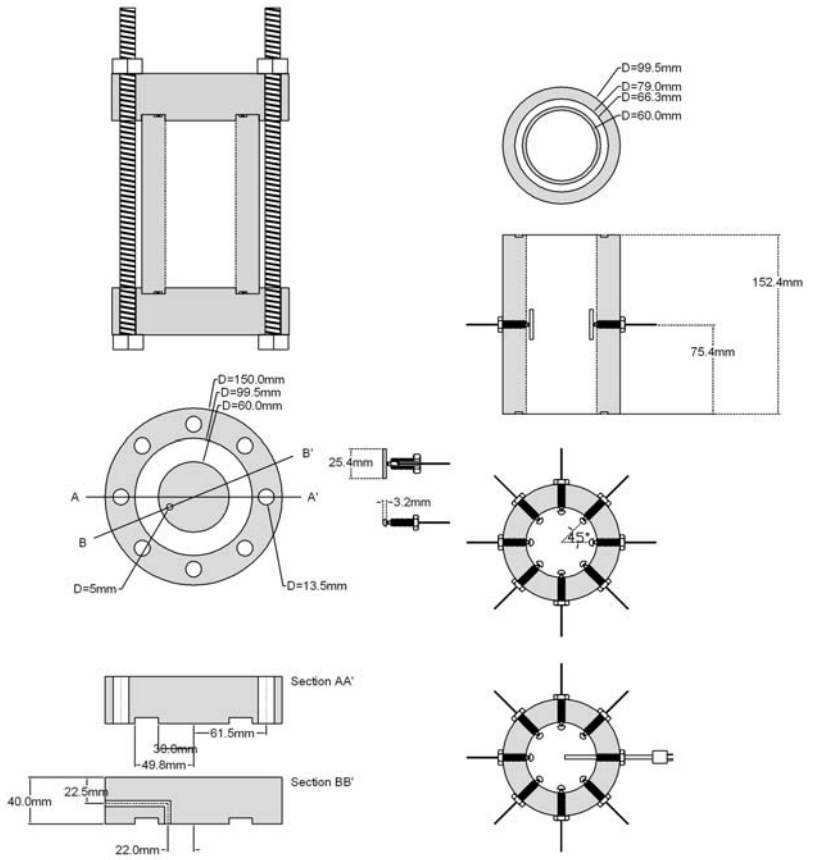

(b) The detailed specification of high pressure ERT cell and electrode

Figure 7.1 Devices: Schematic diagrams of experimental system and high pressure ERT cell for hydrate-bearing sediment studies: (a) Outline of high pressure ERT system for hydrate-bearing sediment study. (b) Detailed specification of the high pressure ERT cell and electrodes

Temperature, pressure, and ERT measurements start after the specimen is prepared. The cell is pressurized to 4.5 MPa and temperature is slowly lowered to 11°C, which is slightly above the equilibrium temperature of CO_2 hydrate at 4.5 MPa. When the specimen temperature reaches 11°C, the gas injection valve is closed, and the temperature is lowered to 3~5 °C to induce CO_2 hydrate formation. Finally, the temperature is raised to induce hydrate dissociation, and the cell is depressurized to conclude the test.

Numerical simulations are designed to determine shape factors for each excitation scheme, to explore various inclusion cases, and to analyze tomographic results. The commercial 3-D finite element code COMSOL Multiphysics is used for these simulations. The geometry, boundary conditions, and parameters for numerical simulations are illustrated in Figure 7.2. Electronically insulated parts are not included in the model. The interface between a specimen and either a measurement electrode or the bottom cap is electronically continuous. Boundary conditions for electrodes vary depending on their role as source (V=3.5V), sink (V=0V), or measurement electrodes. Conductivity values for the specimen vary according to simulations: the conductivity of stainless steel bottom caps and electrodes is 4×10^6 S/m.

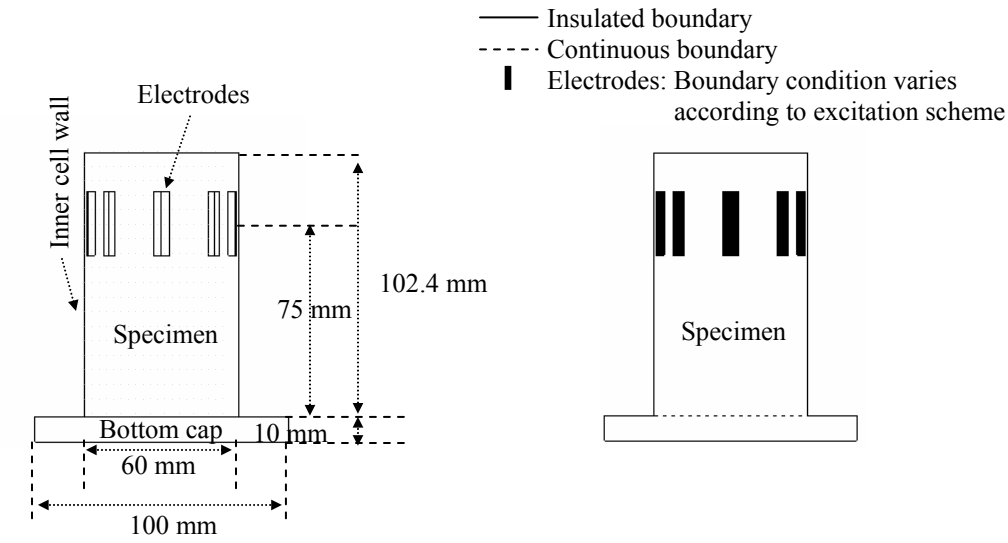

(a) Model geometry (b) Boundary conditions

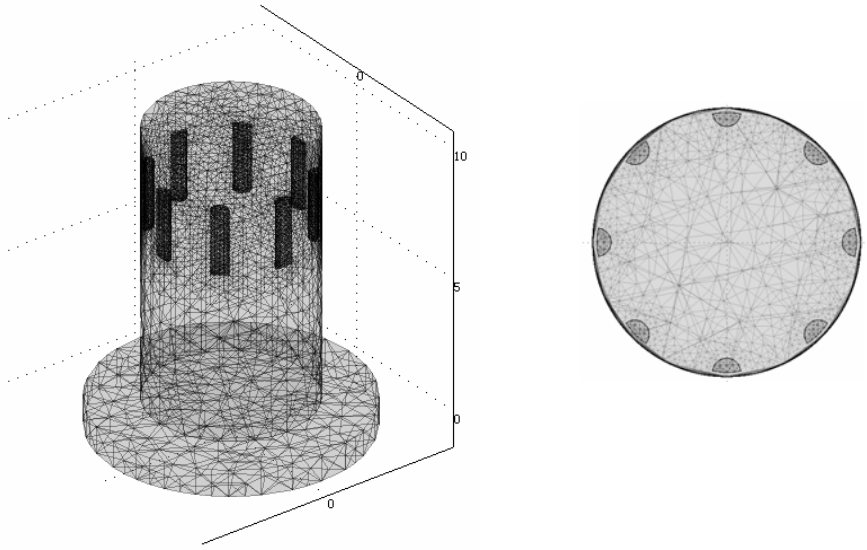

(c) FEM mesh for numerical simulation

Figure 7.2 Model geometry for numerical simulation studies (a) Model geometry. (b) Boundary conditions. (c) FEM mesh for numerical simulation

7.4 RESULTS

Several experimental and numerical studies were conducted to elucidate the effect of different components and variables on measured values during hydrate formation. These include shape factor for data analysis and the effects of CO_2 dissolution, temperature changes, and unsaturation.

7.4.1 Shape Factor

The electrical resistance R [Ω] of a medium with a homogeneous electrical resistivity ρ [Ωm] is a function of geometry:

$$R = \frac{V}{I} = \rho\beta \tag{7.10}$$

where β [m] is the shape factor. In the case of a cylindrical resistor of length l [m] and cross sectional area A [m^2], the shape factor is $\beta = l/A$.

The concept can be extended to the geometry of the ERT system. Then, shape factors allow us to relate resistance values R measured from the ERT system to average resistivity value ρ within the region affected by the measurement. Shape factors are numerically computed for excitation schemes that vary from opposite-electrode excitation to adjacent-electrode excitation as illustrated in Figure 7.3b. Model geometry and boundary conditions are described in previous section, and the specimen conductivity varies from 0.01 S/m to 1 S/m. Shape factors are plotted in Figure 7.3c: shape factors decrease as the distance between source and sink electrodes decreases because the current path shortens.

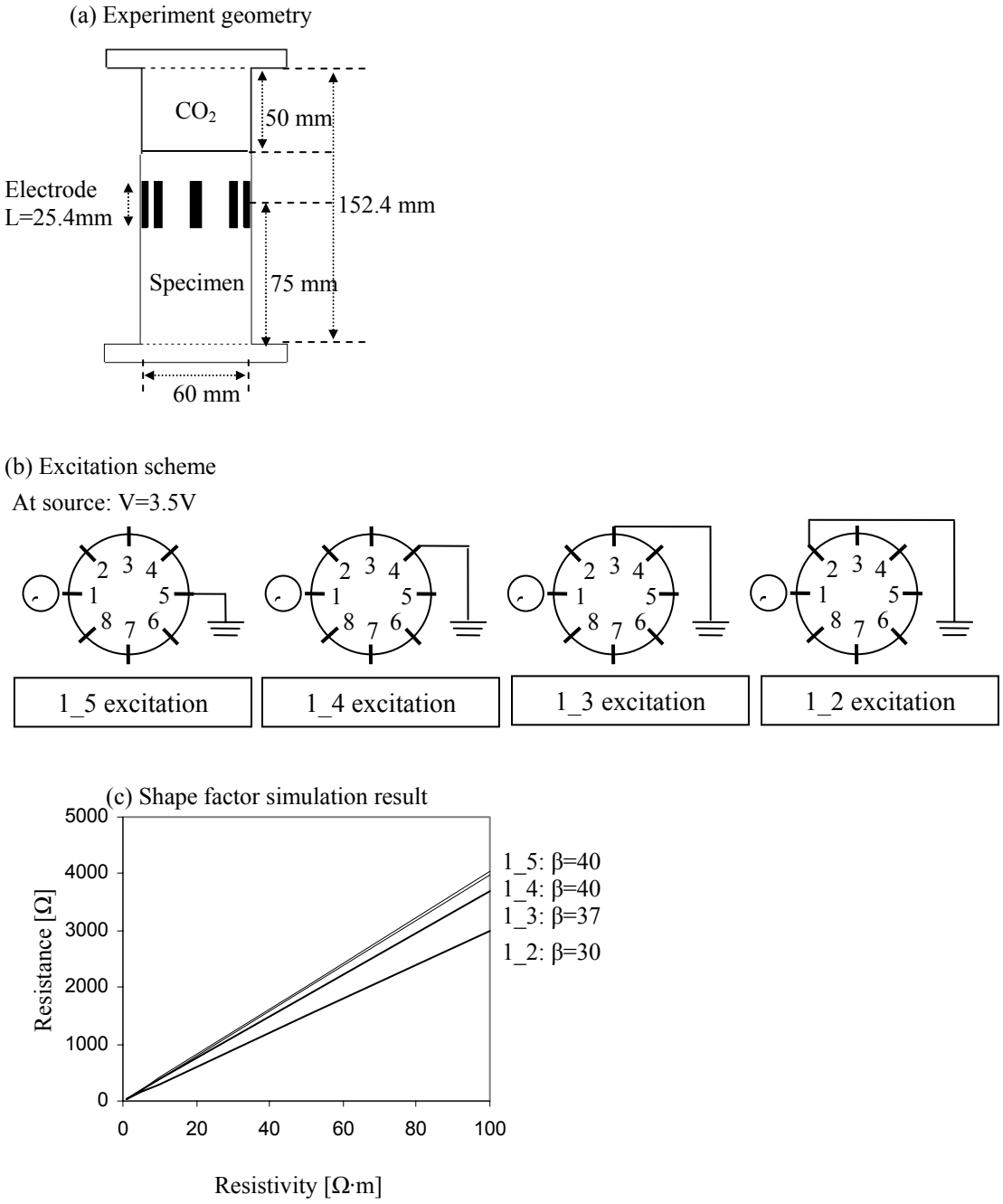

Figure 7.3 Shape factors for 6.4 mm wide and 25.4mm high electrodes for four different excitation schemes. Detailed model specification is in Figure 7.2. (a) Experiment geometry. (b) Excitation schemes. (c) Shape factors.

7.4.2 Ionization of Dissolved Carbon Dioxide

Dissolved CO_2 is in equilibrium with carbonic acid, which subsequently ionizes as follows

$$\begin{aligned} &CO_2(aq) + H_2O \leftrightarrow H_2CO_3(aq) \\ &H_2CO_3(aq) + H_2O \leftrightarrow H_3O^+(aq) + HCO_3^-(aq) \end{aligned} \tag{7.11}$$

Consequently, the conductivity of the pore water increases as CO_2 dissolves in water. The contribution of dissolved CO_2 to the pore water conductivity is verified by filling two thirds of the cell with tap water (Figure 7.4a) and pressurizing the cell with CO_2 to 4.2MPa at room temperature. A differential voltage of 3.5V (f=1kHz) is imposed using the opposite-electrode excitation scheme (electrodes #1 and #5), and the current and pressure are monitored during CO_2 dissolution. The resistivity is calculated with current and potential measurements and the shape factor for 1_5 excitation scheme in Figure 7.3c. Figure 7.4b and c show the evolution of the pressure and resistivity during the dissolution of CO_2 in water. The decrease in both pressure and resistivity indicates the gradual dissolution of CO_2 into water.

7.4.3 Temperature Effect

Temperature effects on pore fluid conductivity are corroborated using the water-filled ERT cell. A differential voltage of 3.5V (f=1kHz) is imposed using the opposite-electrode excitation scheme (electrodes #1 and #5), and the current and temperature are monitored while the temperature of water changes from 20°C to 5°C. Resistivity is calculated with current and potential measurements and the shape factor for 1_5 excitation scheme in Figure 7.3c. Figure 7.5 shows measured values and predicted values

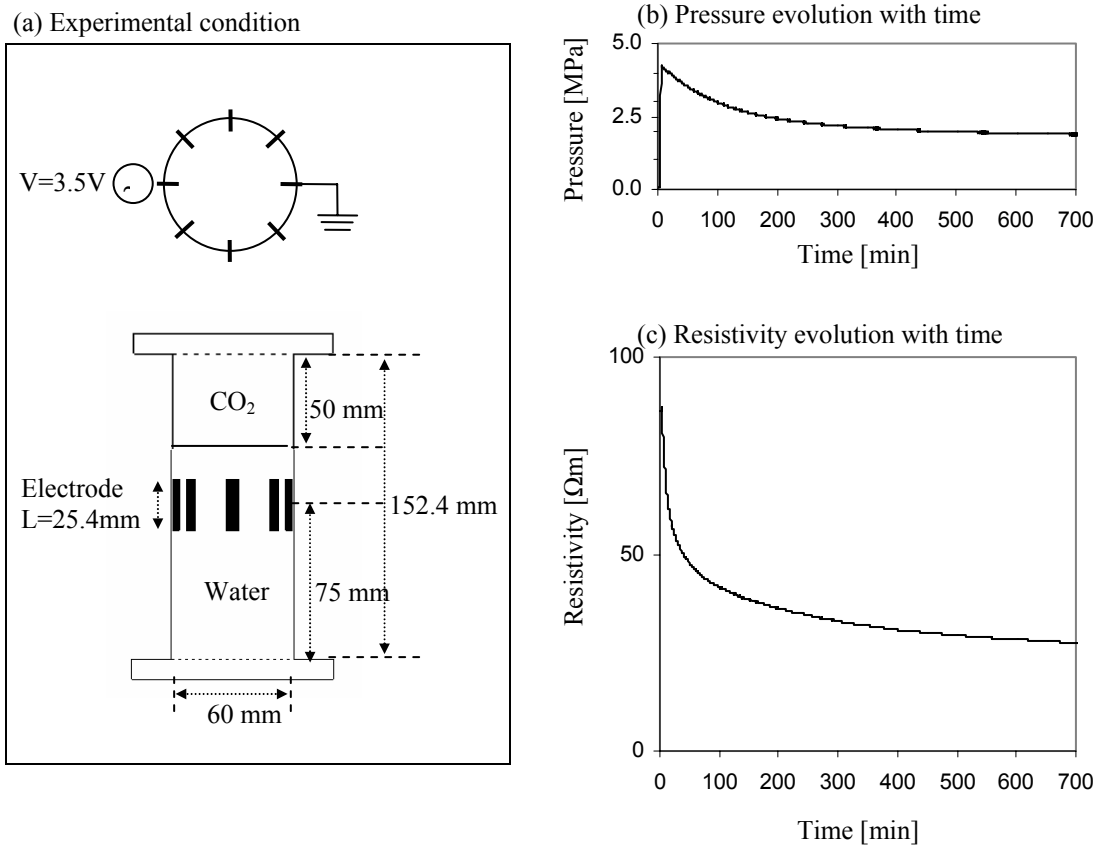

Figure 7.4 The effect of CO_2 dissolution in tap water on the evolution of resistivity at a room temperature. (a) Experimental conditions. (b) Pressure evolution with time. (c) Resistivity evolution with time.

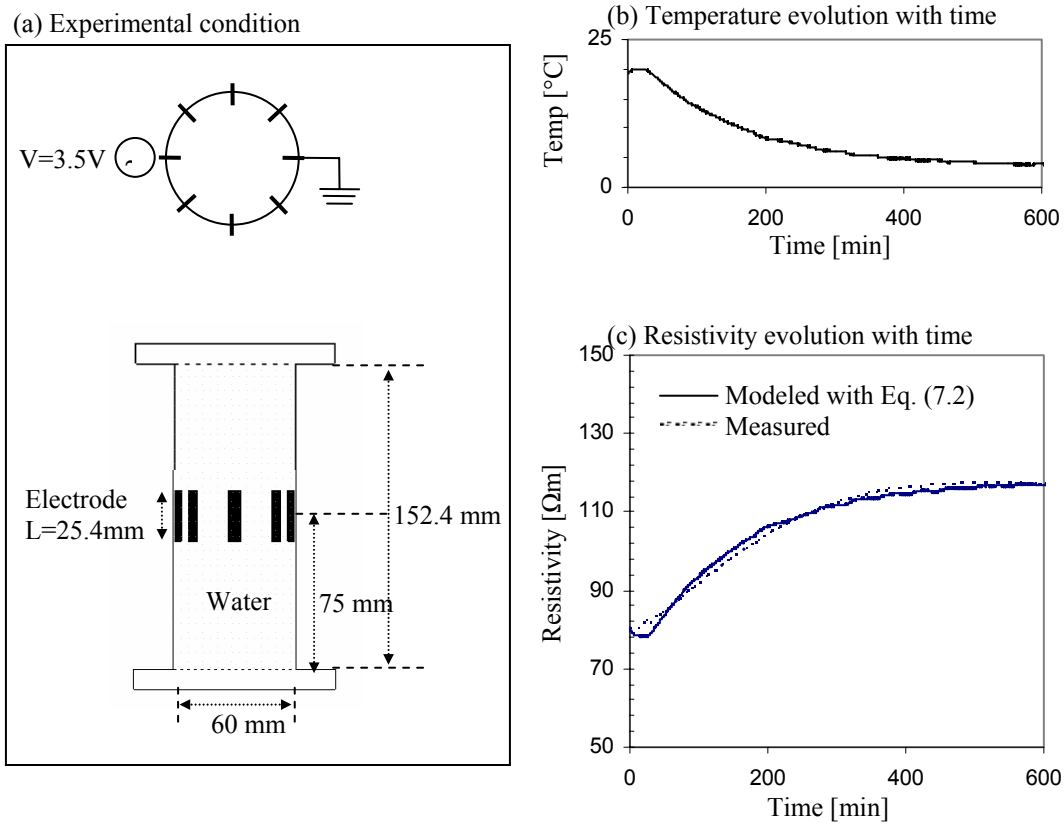

Figure 7.5 Temperature effects on the evolution of the tap water resistivity during cooling. (a) Experimental conditions. (b) Temperature evolution with time. (c) Resistivity evolution with time.

using Equation (7.2) and α=0.025. The resistivity increases due to reduced ionic mobility as the temperature decreases.

7.4.4 Change in Saturation

The resistivity of a soil-water mixture increases as the degree of saturation decreases due to the decrease in water content and pore water connectivity. Furthermore, drainage generates heterogeneity in the specimen, so the decrease in resistivity and corresponding potential changes depend on the spatial distribution of pore water. Ottawa 20/30 (D_{50}=0.72mm) sand and F110 (D_{50}=0.12mm) sand are used to explore changes in resistivity due to de-saturation (Figure 7.6). A differential voltage of 3.5V (f=1kHz) is imposed using the opposite-electrode excitation scheme (electrodes #1 and #5), and the current and temperature are monitored during drainages. The resistivity is calculated with current and potential measurements and the shape factor for 1_5 excitation scheme in Figure 7.3c.

Ottawa 20/30 sand: The measured electrical potential distribution along the periphery decreases from the source to the sink in the saturated specimen. The degree of saturation decreases significantly (S_w=0.48) upon drainage and the resistivity increases accordingly. The distribution of potential along the periphery deviates from the trend that corresponds to a homogeneous conductivity distribution, and currents flow along preferential paths. The resistivity estimated using 1_5 electrode excitation scheme decreases in time, suggesting fluid redistribution in the pore space.

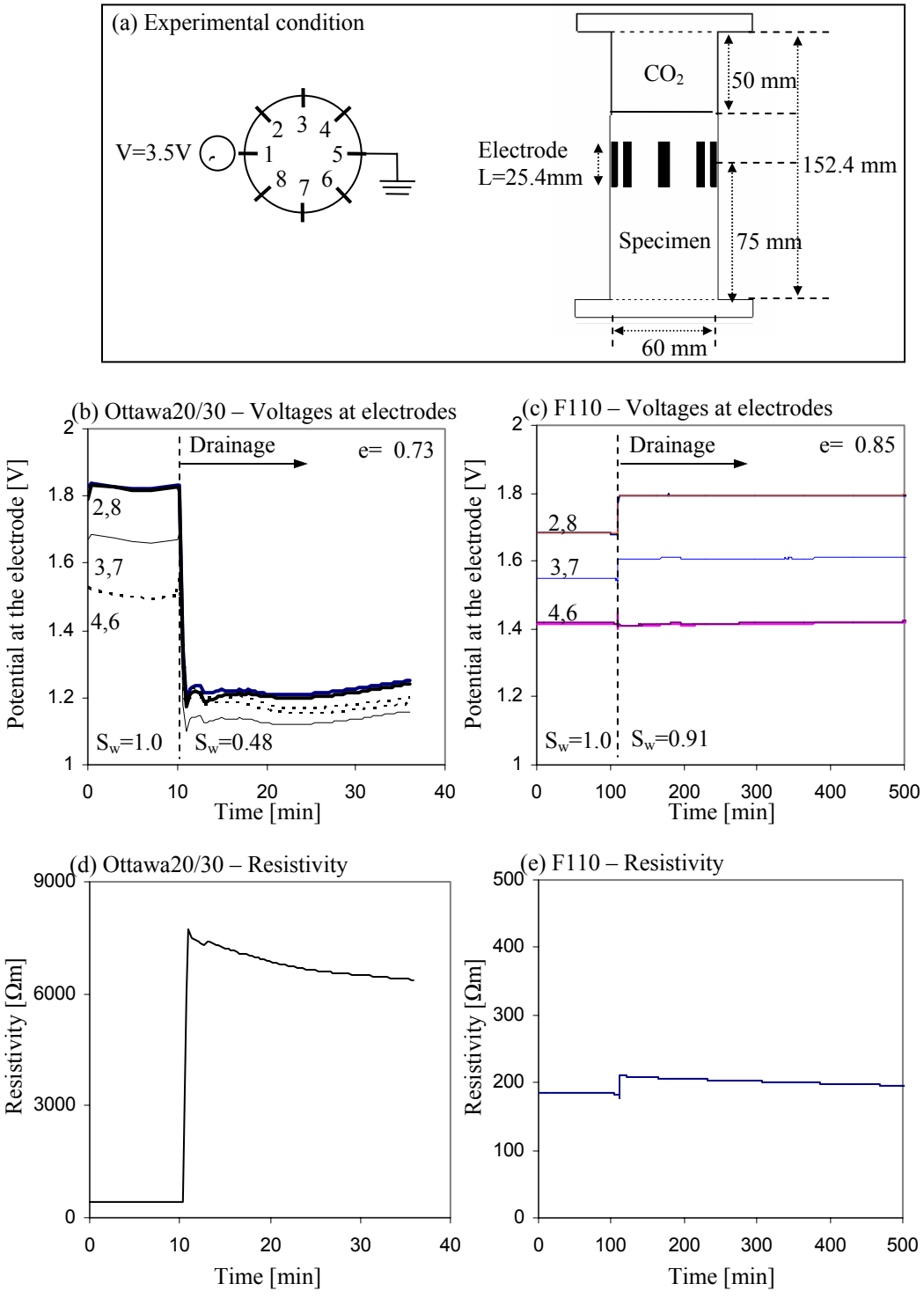

Figure 7.6 Water drainage. The evolution of electric potential at the electrodes and resistitivy during the transition from saturated condition to unsaturated conditions. (a) Experimental condition. (b) Ottawa20/30-Voltages at electrodes. (c) F110 – Voltages at electrodes. (d) Ottawa20/30 – Resistivity. (e) F110 – Resistivity.

Ottawa F110 sand: The degree of saturation decreases slightly (S_w=0.91) after drainage because a significant portion of the water is retained by capillarity in this finer sand. Hence, the resistivity increases slightly in comparison to the Ottawa 20/30 case.

7.4.5 CO_2 Hydrate Formation and Dissociation

Tests on CO_2 hydrate formation are performed using unsaturated 20/30 sand, unsaturated F110 sand, and saturated F110 sand. The specimens are pressurized to 4.5 MPa, and the temperature is lowered to 11°C (Note: starting temperatures vary according to specimens). This temperature and pressure condition (4.5MPa at 11°C) is maintained for 2 days in water saturated specimen to allow for CO_2 diffusion. Then, the gas valve is closed, and the temperature is lowered to 3°C to induce hydrate formation. Finally, the temperature is raised to induce dissociation. The cell is depressurized after full dissociation. A differential voltage of 3.5V (f=1kHz) is imposed using the opposite-electrode excitation scheme (electrodes #1 and #5), and the current and temperature are monitored. The mean resistivity is calculated using current and potential measurements and the shape factor for 1_5 excitation scheme in Figure 7.3c. Representative measurements are shown in Figures 7.7, 7.8, and 7.9. The evolution of measurements can be divided into three parts: (1) pressurization and cooling, (2) formation, and (3) dissociation. The three experiments exhibit some similarities as well as clear differences:

-Two concurrent effects define the resistivity signature during pressurization and cooling periods: ionic concentration increases due to CO2 dissolution and ionic mobility decreases due to the decrease in temperature.

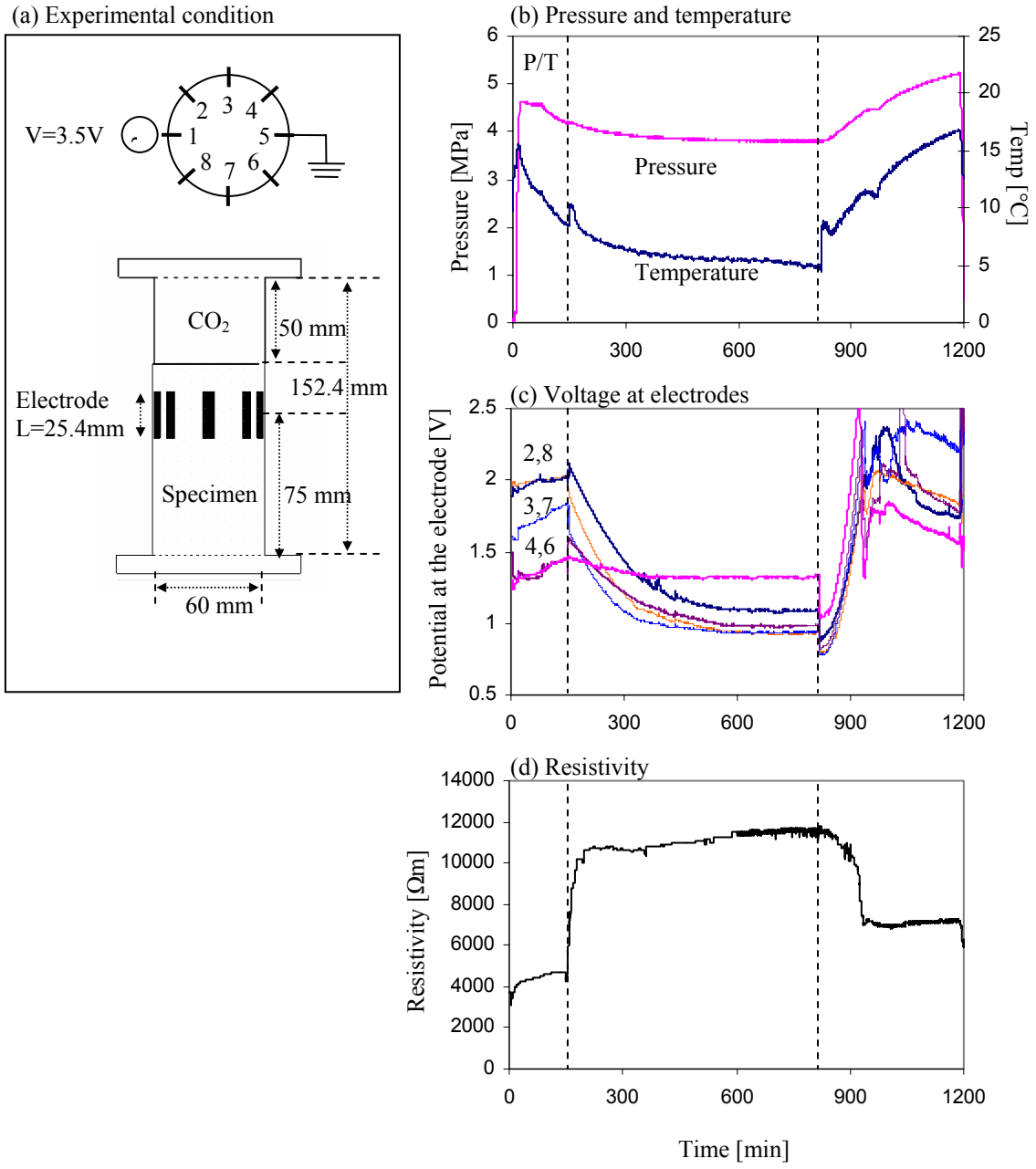

Figure 7.7 CO_2 hydrate formation and dissociation in unsaturated Ottawa 20/30 sand. The evolution of temperature, pressure, potentials at the electrodes, and resistivity during hydrate formation and dissociation. (a) Experimental condition. (b) Pressure and temperature. (c) Voltage at electrodes. (d) Resistivity.

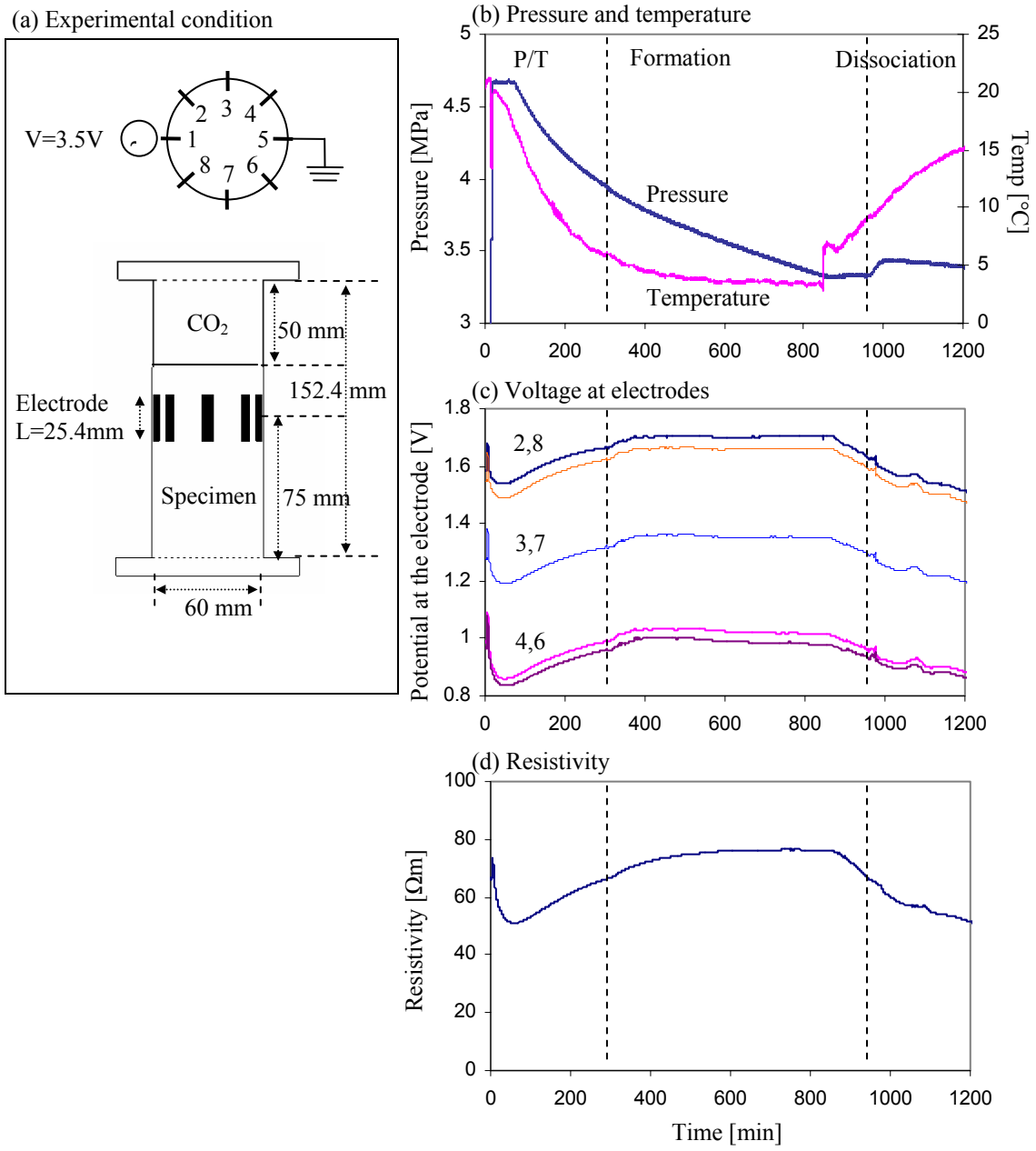

Figure 7.8 CO_2 hydrate formation in unsaturated F110 sand. The evolution of temperature, pressure, potentials at the electrodes, and resistivity during hydrate formation and dissociation. (a) Experimental condition (b) Pressure and temperature (c) Voltage at electrodes (d) Resistivity

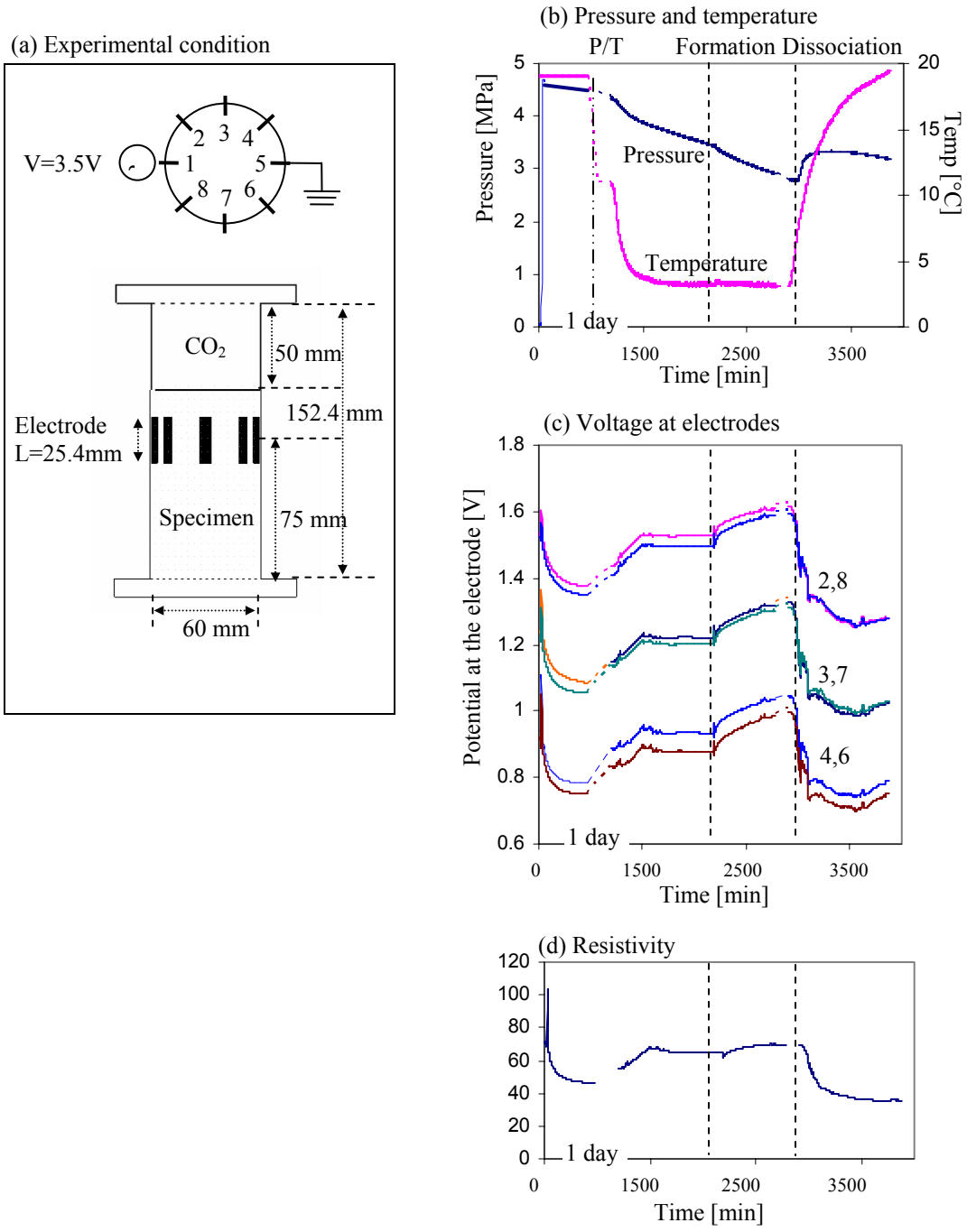

Figure 7.9 CO_2 hydrate formation in saturated F110 sand. The evolution of temperature, pressure, potentials at the electrodes, and resistivity during hydrate formation and dissociation. (a) Experimental condition (b) Pressure and temperature (c) Voltage at electrodes (d) Resistivity

-The resistivity increases further upon hydrate formation and decreases upon hydrate dissociation.

- The resistivity after dissociation is higher in Ottawa 20/30 specimen. This implies that gas nucleates and form bubbles that destabilize water menisci (water leaves the sediment) upon dissociation rather than dissolve back into the water. The higher pressure observed after dissociation also supports this hypothesis.

- The resistivity after dissociation is more or less the same as the initial resistivity in F110 specimens, implying no residual effects in either gas or water contents.

7.5. ANALYSES

7.5.1 Numerical Studies

The potential at electrodes changes according to the size and location of hydrate formation. Several low conductivity, hydrate-like inclusions are simulated to explore the potential response at electrodes. The basic model configuration is described in Figure 7.2. Electrode 1 is the source electrode (V=3.5V), and electrode 5 is the sink electrode. The inclusion specifications and conductivity values vary according to the cases. Each case represents different possible hydrate formation patterns in a wet sediment with hydrate forming gas at the top of the specimen. Results for the different cases are summarized in Figure 7.10. Due to symmetry, the potential at electrodes 2-and-8 and 4-and-6 are the same, and the potential at electrodes 3-and-7 is not shown since it is relatively insensitive to inclusions in 1_5 excitation scheme. The potential difference between electrode 2-and-4, V_{24}, or between 8-and-6, V_{86} is the gap between the corresponding electrode potentials.

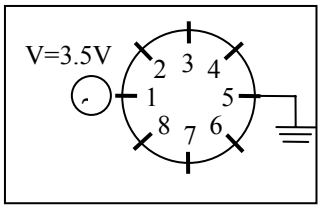
V=3.5V
1
2
3
4
5
6
7
8

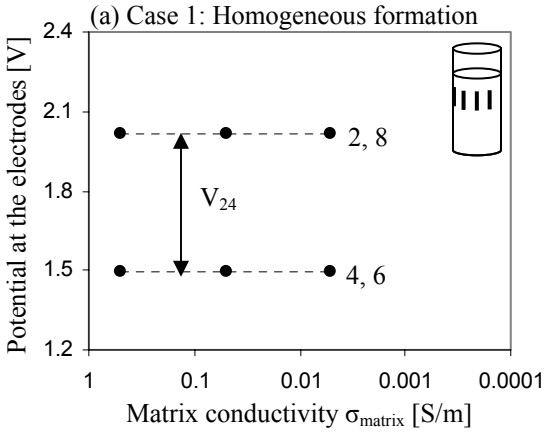
(a) Case 1: Homogeneous formation
Potential at the electrodes [V]
2.4
2.1
1.8
1.5
1.2
2, 8
4, 6
V_{24}
1
0.1
0.01
0.001
0.0001
Matrix conductivity σ_{matrix} [S/m]

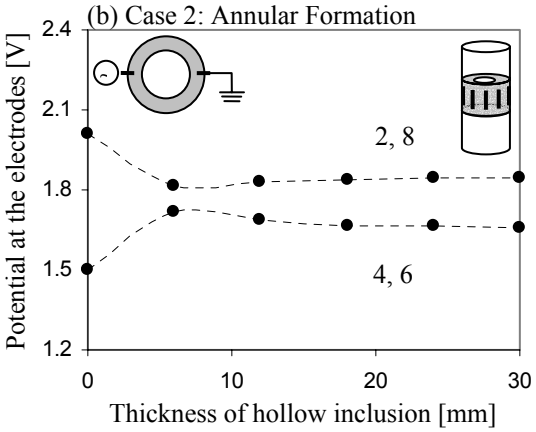
(b) Case 2: Annular Formation
Potential at the electrodes [V]
2.4
2.1
1.8
1.5
1.2
2, 8
4, 6
0
10
20
30
Thickness of hollow inclusion [mm]

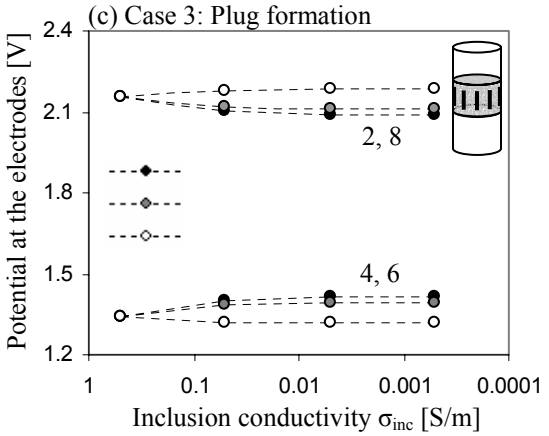
(c) Case 3: Plug formation
Potential at the electrodes [V]
2.4
2.1
1.8
1.5
1.2
2, 8
4, 6
1
0.1
0.01
0.001
0.0001
Inclusion conductivity σ_{inc} [S/m]

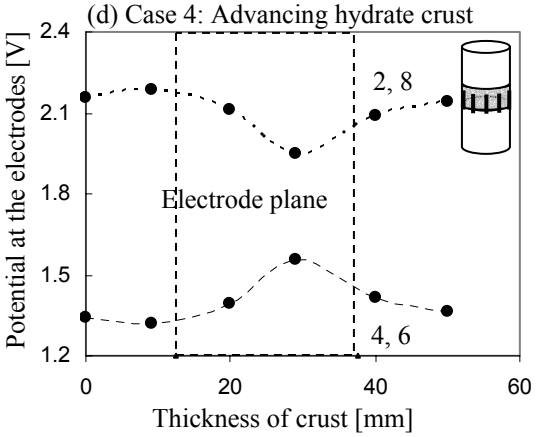
(d) Case 4: Advancing hydrate crust
Potential at the electrodes [V]
2.4
2.1
1.8
1.5
1.2
2, 8
Electrode plane
4, 6
0
20
40
60
Thickness of crust [mm]

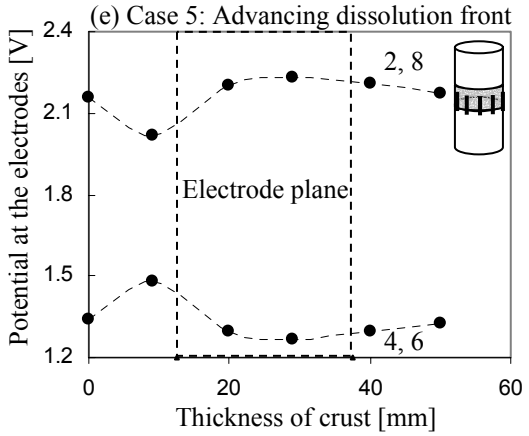
(e) Case 5: Advancing dissolution front
Potential at the electrodes [V]
2.4
2.1
1.8
1.5
1.2
2, 8
Electrode plane
4, 6
0
20
40
60
Thickness of crust [mm]

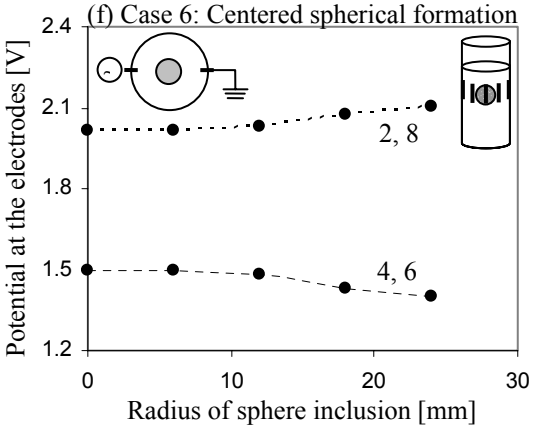
(f) Case 6: Centered spherical formation
Potential at the electrodes [V]
2.4
2.1
1.8
1.5
1.2
2, 8
4, 6
0
10
20
30
Radius of sphere inclusion [mm]

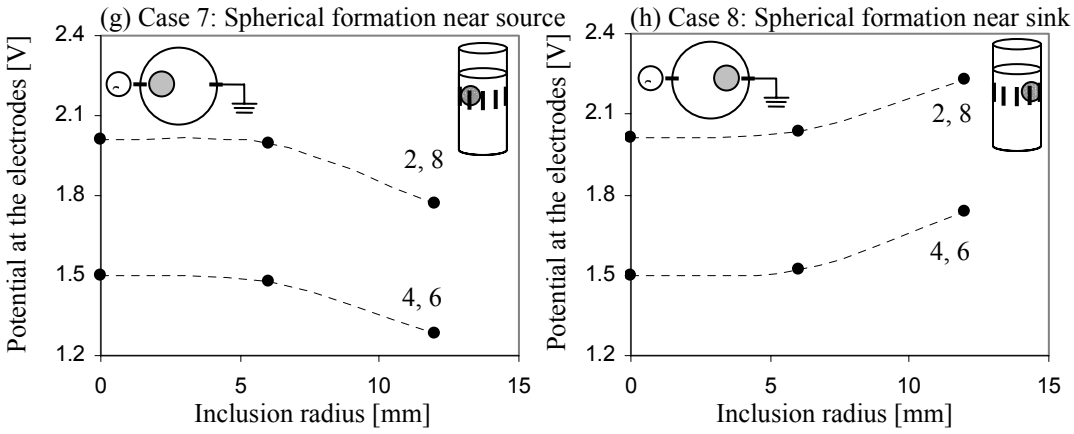

Figure 7.10. The variation of potential at the measurement electrodes induced by the geometry and the conductivity of inclusions and specimens. Basic model specification is illustrated in Figure 7.2. The conductivity of specimen σ_{matrix} is 0.5 S/m except for case 1. Gray area indicates an inclusion. (a) Case 1: Homogeneous specimen with σ_{matrix} decreasing from 0.5 S/m to 0.005 S/m, (b) Case 2: Annular inclusion thickening from the cell wall (σ_{inc}=0.05 S/m), (c) Case 3: Cylindrical inclusion (D: 60mm, H: 10,20, and 40mm) with varying inclusion conductivity σ_{inc}, (d) Case 4: Low conductivity front advancing from the top (σ_{inc}=0.005 S/m), (e) Case 5: High conductivity front advancing from the top (σ_{inc}=5.0 S/m), (f) Case 6: Spherical inclusion growing from the center (σ_{inc}=0.05 S/m), (g) Case 7: Spherically growing inclusion near source (σ_{inc}=0.05 S/m), (h) Case6: Spherically growing inclusion near sink(σ_{inc}=0.05 S/m)

Case 1 depicts the evolution of potential at the electrode when hydrate forms homogeneously and gradually throughout the specimen, and the assumed conductivity values decreases from 0.5S/m for the water-saturated homogeneous specimen to 0.005S/m for the hydrate-bearing sediments. The potentials at electrodes do not change and the input potential difference V_{1_5} is kept constant.

Case 2 illustrates hydrate formation starting at cell wall and advancing towards the center. The annular cylindrical inclusion is 40mm high and is located at the top of the specimen. The annular ring thickness varies from 5mm to 30mm (matrix conductivity: 0.5S/m; annular ring conductivity: 0.05S/m). The potential difference between electrodes

2 and 4 decreases with increasing ring thickness as most of the potential loss occurs near the source and sink electrodes due to high annular resistivity.

Case 3 represents hydrate formation and growth near the gas-sediment interface. The conductivity of the cylindrical plug (same diameter as the specimen) at the top of the specimen is decreased from 0.05S/m to 0.0005S/m, while the conductivity of the sediment is kept constant at 0.5 S/m. Three different plug thicknesses are simulated. If the plug is above the electrode plane (H=10mm), the potential difference between electrodes 2 and 4 becomes larger as the plug conductivity decreases due to higher current density and more uniform equipotential line distribution at the electrode plane. The opposite trend occurs as plug conductivity decreases when the cylindrical plug reaches the electrode plane (H=20 or 40mm) as some of the current within the electrode plane is deviated towards the lower region where the water-saturated sediment conductivity remains higher than the hydrate-bearing sediments.

Case 4 further explores the advancing hydrate crust, growing from the top of the specimen as the thickness increases from 10mm to 50mm (crust conductivity: 0.005S/m; matrix conductivity: 0.5S/m). The potential difference between electrodes 2 and 4 reaches a minimum as the hydrate crust invades the electrode plane and recovers to values corresponding to homogenous specimens as the dissolution front advances beyond the electrode plane.

Case 5 simulates the CO_2 dissolution front advancing downwards (i.e. high conductivity front). In this case, the dissolution front conductivity is 5S/m while the rest of the specimen is assumed to be 0.5S/m. The potential difference between electrodes 2 and 4 reaches a minimum before the dissolution front reaches the electrode plane and

recovers to values corresponding to homogenous specimens as the dissolution front advances beyond the electrode plane.

Case 6 depicts spherical hydrate formation taking place at the center of the specimen, within the electrode plane. The radius of the spherical inclusion varies from 5mm to 24mm (inclusion conductivity: 0.05S/m; matrix conductivity: 0.5S/m). The potential difference between electrodes 2 and 4 increases as the inclusion size increases. In this case, the low conductivity inclusion at the center drives the current towards the external donut shaped high-conductivity region at the electrode plane, which gradually approaches a pseudo 1D current flow.

Case 7 is for spherical hydrate formation near the source growing up to a12mm radius inclusion (inclusion conductivity: 0.05S/m; matrix conductivity: 0.5S/m). The potential decreases at all measurement electrodes, indicating local potential loss near the source due to the presence of the low conductivity inclusion.

Case 8 corresponds to a spherical hydrate formation near the sink electrode, growing up to a 12mm radius inclusion (inclusion conductivity: 0.05S/m; matrix conductivity: 0.5S/m). The potential increases at all measurement electrodes because the presence of the hydrate inclusion hinders current flow into the sink.

The results corresponding to cases 3, 4, and 5 highlight the complex interpretation of out-of electrode plane conditions.

7.5.2 Analyses of Experimental Results

Experimental results are compared to simulation results to identify hydrate formation patterns in experiments. While the potential difference between source and

ground electrodes is kept constant (at 3.5V) in the simulation, the applied potential in experiments tends to change according to changes in specimen conductivity. Therefore, the experimental results are adjusted accordingly for the changes in input potential to the specimen by multiplying measured values with the ratio of the initial applied potential over the instantaneous potential, V_t/V_0.

Figure 7.11 shows the evolution of corrected potentials in the unsaturated F110 sand (refer to Figure 7.8) and in the saturated F110 sand (refer to Figure 7.9). The following observations can be made:

- CO_2 dissolution period: The potential evolution resembles Case 5 (high conductivity crust advancing downward) in both saturated and unsaturated F110 specimen during CO2 dissolution.

- Hydrate formation period: The converging trend of potential in unsaturated specimen changed to diverging and slightly descending trend upon formation, implying that the hydrate started form somewhere between the center and the source (electrode #1 during monitoring). The potential increases implying that hydrate formed near the sink (electode #5 during monitoring) in the saturated F110 specimen.

- Hydrate dissociation period: The diverging trend in the unsaturated F110 specimen vanishes upon dissociation, and the potential remains more or less constant with some fluctuations probably due to bubble formation during dissociation. The potentials at the electrodes in the saturated F110 specimen decrease simultaneously with some fluctuation, suggesting a dissociation event near sink.

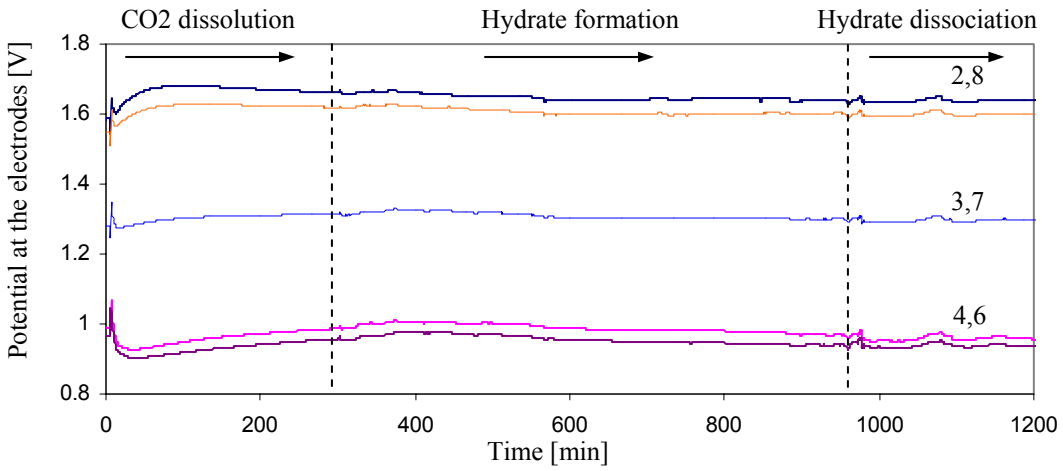

(a) Unsaturated F110 sand specimen

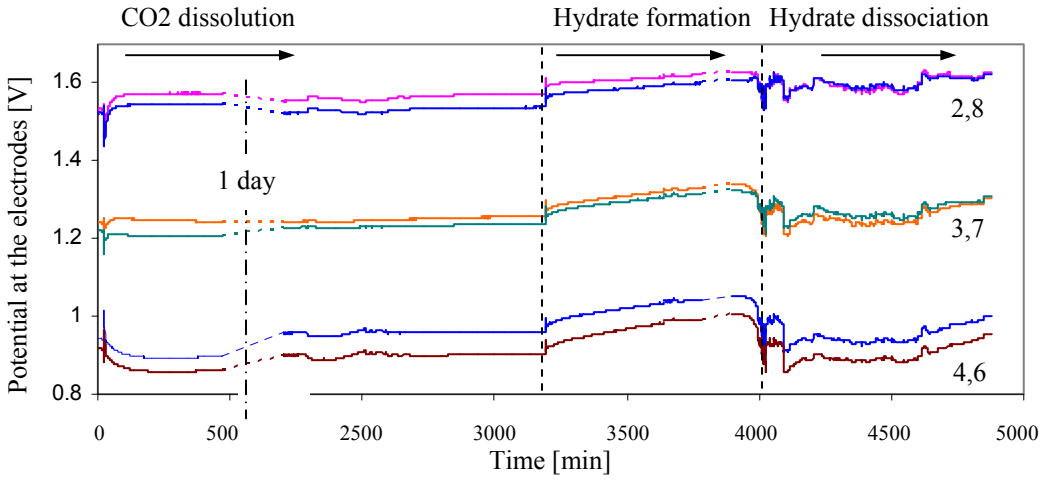

(b) Saturated F110 sand specimen

Figure 7.11 The potential evolution at measurement electrodes during CO2 dissolution, hydrate formation, and hydrate dissociation. The potential is corrected according to the change in the potential at specimens. (a) Unsaturated F110 sand specimen from Figure 7.8 (b) Saturated F110 sand specimen from Figure 7.9

7.5.3 Data Pre-processing

A simple yet robust data pre-processing algorithm is developed to estimate general lateral location of hydrates. The algorithm presumes that the conductivity measured from each excitation scheme reflects the conductivity of the area with higher current density. The flow chart for the pre-processing algorithm is presented in Figure 7.12.

A full set of tomography measurements is numerically simulated and processed with this algorithm to verify its performance. The inclusion location in the specimen is shown in Figure 7.13a. The basic model specifications are same as in Figure 7.2, and the lateral location of inclusion is in Figure 7.13a. The matrix conductivity is 5×10^{-4}S/m, and the inclusion conductivity is 5×10^{-6} S/m. The estimated conductivity values from the simulated tomography measurements are tabulated in Appendix C. Figure 7.13b, c, and d show the estimated values for homogenous case, heterogeneous case, and the differences between two cases. The result suggests that the algorithm can detect the location of low conductivity inclusion. However, the boundary of the inclusion is smoothed and the conductivity distribution is also averaged correspondingly.

Tomographic measurements are performed in the saturated F110 specimen (refer to Figure 7.9). Estimation results are shown in Figure 7.14. The initial conductivity is higher near electrode 5 (the sink electrode during monitoring), indicating that the specimen had higher porosity in that area before hydrate formation. The conductivity distribution becomes homogenized after hydrate formation. This observation also agrees with the case study comparison in previous section.

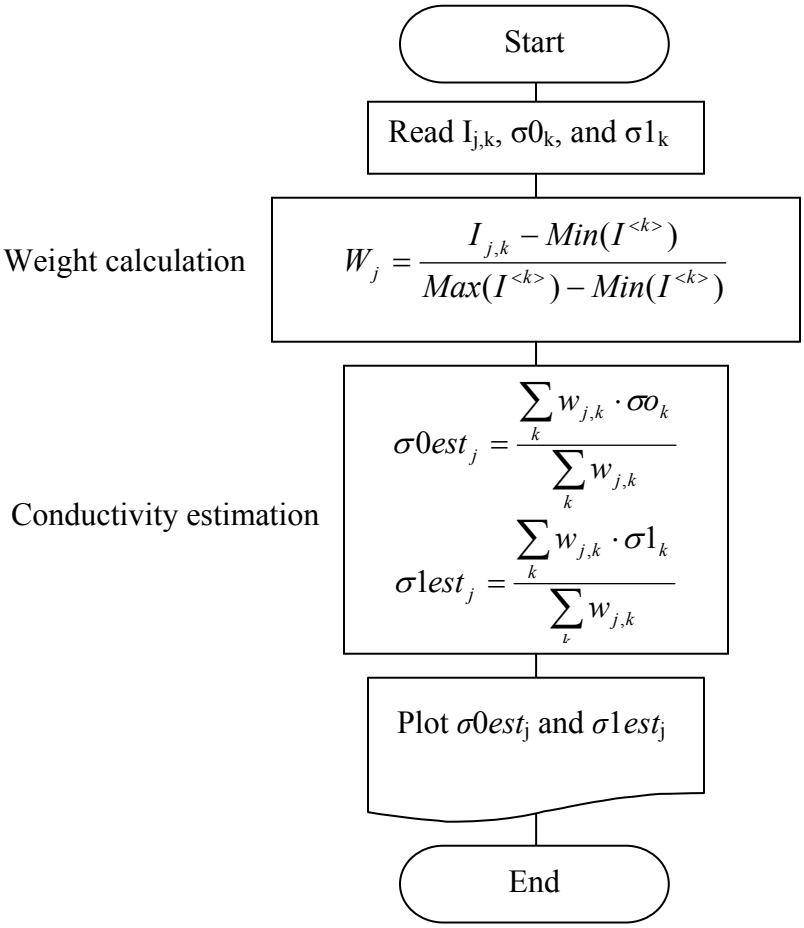

$I_{j,k}$: Current density for j^{th} pixel and k^{th} excitation
$\sigma 0_k$: Measured mean conductivity before hydrate formation for k^{th} excitation
$\sigma 1_k$: Measured conductivity after hydrate formation for k^{th} excitation
$\sigma 0est_j$: Estimated conductivity before hydrate formation for j^{th} pixel
$\sigma 1est_j$: Estimated conductivity after hydrate formation for j^{th} pixel

Figure 7.12 Algorithm for initial guess of conductivity distribution

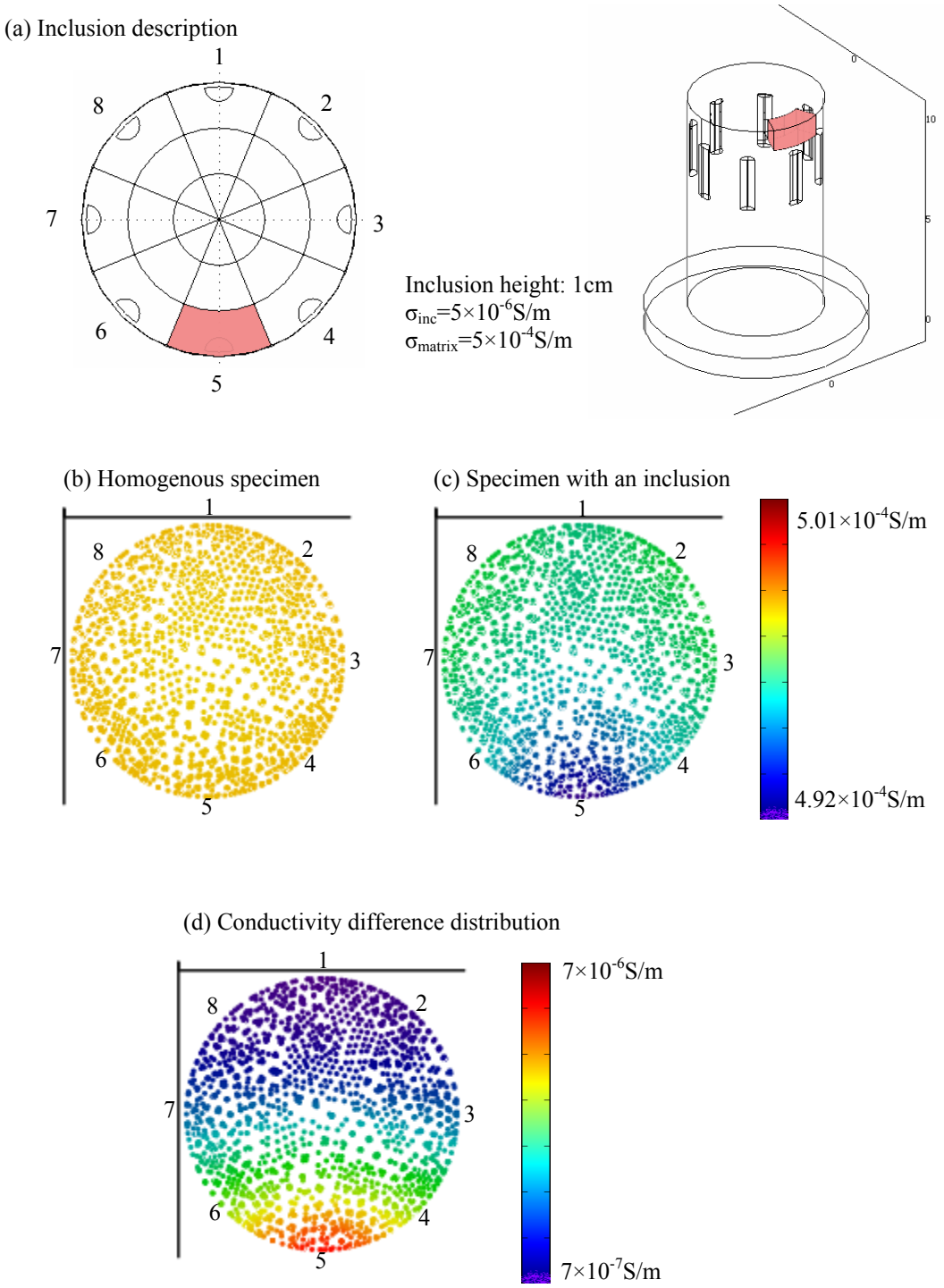

Figure 7.13 Data pre-processing Estimated conductivity distribution – inclusion near electrode #5. Simulated data. (a) Inclusion description. (b) Conductivity before hydrate formation. (c) Conductivity after hydrate formation. (d) Conductivity difference distribution.

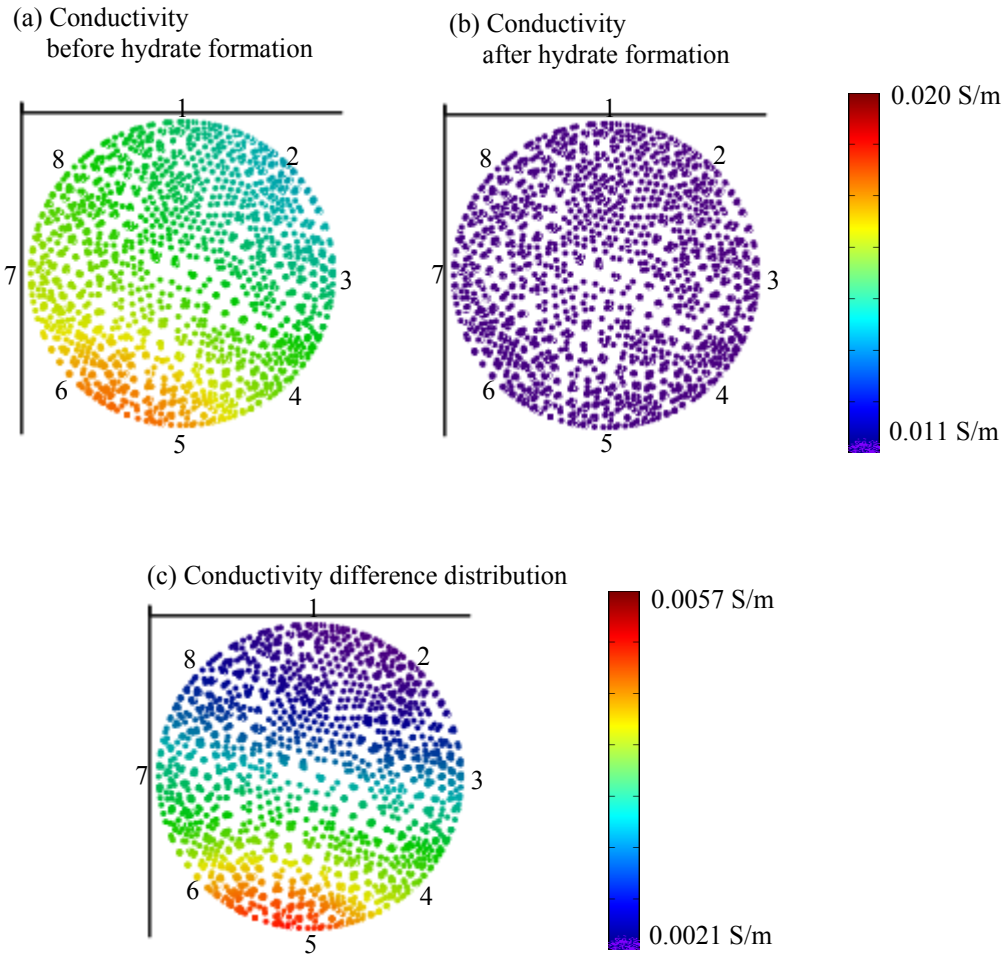

Figure 7.14 Data pre-processing. Estimated conductivity distribution from experimental data in Figure 7.9. (a) Conductivity before hydrate formation. (b) Conductivity after hydrate formation. (c) Conductivity difference distribution.

7.5.4 Inversion by Successive Forward Simulation

Tomographic measurements from the saturated specimen in Figure 7.9 are used for this parametric inversion study. A saturated specimen is selected since the initial condition tends to be more homogenous than unsaturated one. The potential evolution at electrodes during hydrate formation indicates that the hydrate formation occurred as an inclusion form which can be a good tomographic example.

The hydrate-bearing heterogeneity in homogeneous sediments can be represented parametrically instead of pixel-based representation. The cylindrical specimen with semi-cylindrical hydrate-bearing heterogeneity can be described with the location and the conductivity of homogeneous specimen and heterogeneity. The sum of squared errors is used for the error norm to be minimized. The matrix conductivity is set at 0.017S/m, which is the average measured conductivity in the specimen before hydrate formation.

Then, the inclusion is successively positioned at different locations, and the potential a electrodes is numerically predicted and compared to the measured potentials. The position is searched with initial emphasis on the plane of electrodes as depicted in Figure 7.15. After the approximate depth is determined, depth and inclusion conductivity is varied simultaneously. Error surface suggest that inclusion size and inclusion conductivity are in trade-off relationship. This inverse study shows that hydrate formed over a small region near electrode #5, and the inclusion conductivity is 5×10^{-3}S/m. The conductivity distribution determined from the parametric study is depicted in Figure 7.17.

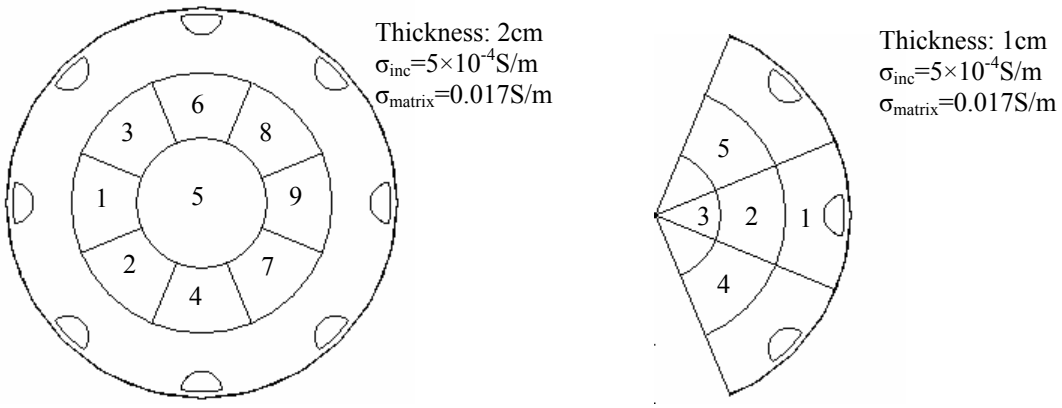

(a) Global inclusion position (b) Local inclusion position

Figure 7.15 Specifications for global and local inclusions. (a) Global inclusion position (b) Local inclusion position

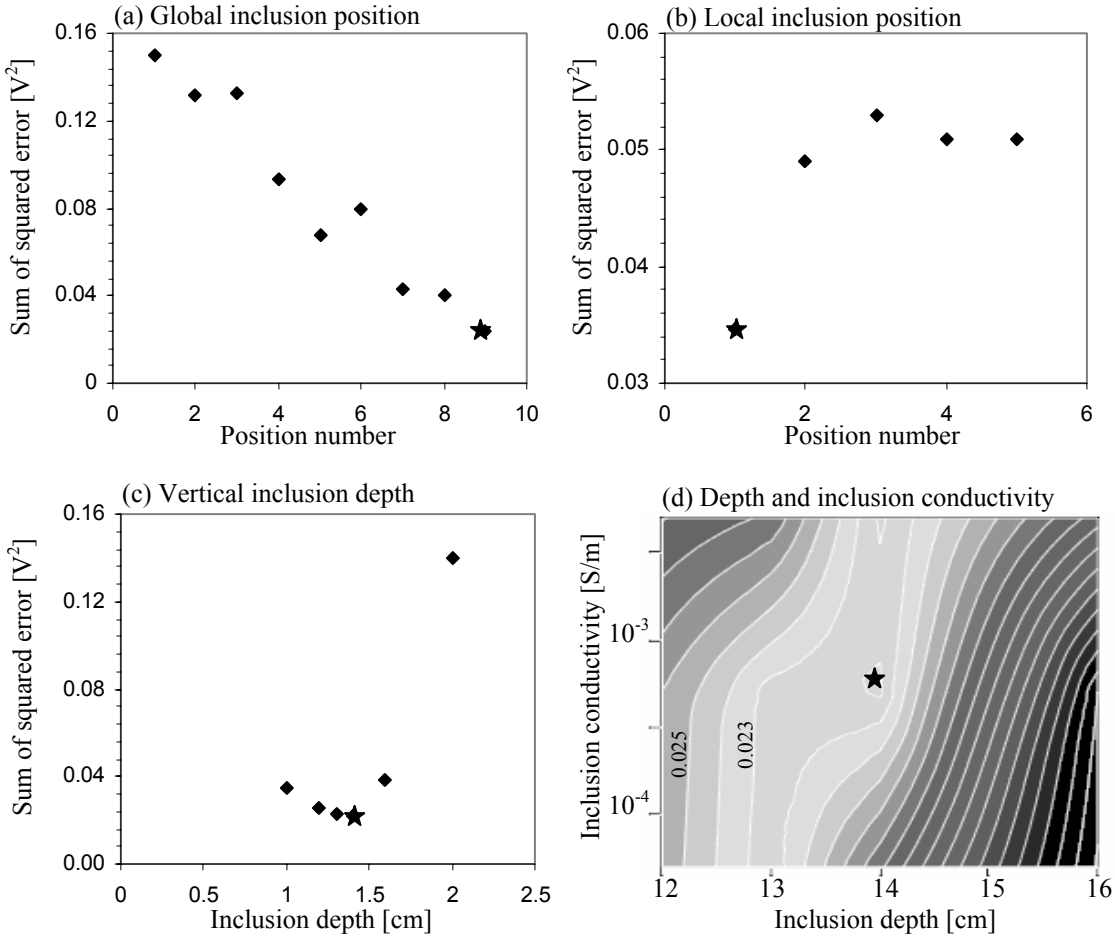

Figure 7.16 Inversion by successive forward simulations with experimental data from the case in Figure 7.9. Error norm distribution in parametric study with inclusion location, depth, and inclusion conductivity as parameters. Black star on each plot indicates the minimum of the error norm. (a) Global inclusion position. (b) Local inclusion position. (c) Vertical inclusion depth. (d) Depth and inclusion conductivity.

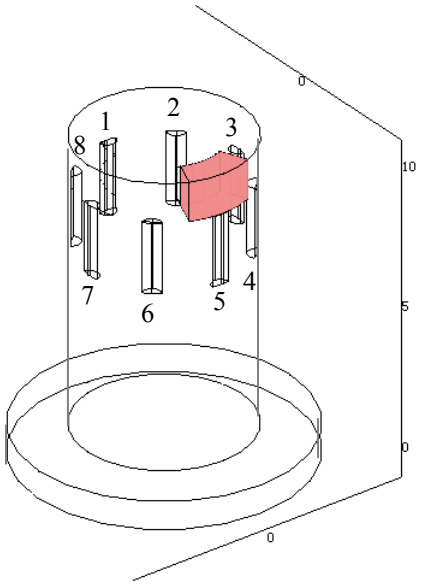

Figure 7.17 Result obtained by successive forward simulation based inversion for the experimental data corresponding to the case shown in Figure 7.9 Shaded region indicates hydrate bearing inclusion.

7.5.5 Tomographic Inversion

The tomographic measurements gathered with the saturated F110 specimen (refer to Figure 7.9) is inverted with regularized least square method using the pubic domain software EIDORS. This is an image reconstruction program based on Gauss-Newton method for electrical tomography to reduce ill-conditioning, a constrained two-dimensional conductivity difference distribution at the electrode plane (at height=75mm) is reconstructed. The reconstructed distribution of the conductivity differences between before and after hydrate formation shown in Figure 7.18 confirms that hydrates formed near electrode 5, similar to the results from data processing and the inversion by successive forward simulation.

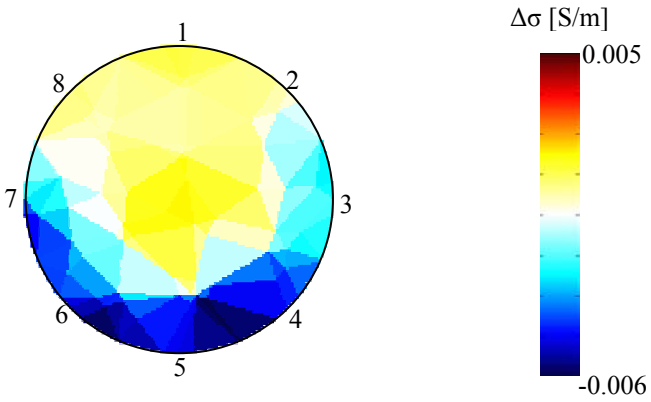

Figure 7.18 The 2D image reconstruction for Δσ [S/m] between before and after hydrate formation. Data corresponds to case shown in Figure 7.9

7.6 CONCLUSIONS

- The evolution of electrical conductivity during CO_2 hydrate formation and dissociation reflects the combined effects of concurrent changes that include ionization of dissolved CO_2, temperature-dependent ionic mobility, changes in the degree of saturation, ion exclusion, surface conduction, and porosity changes.

- Unsaturation is characterized by a fractal network near the air or liquid percolation thresholds. Electrical measurements are difficult to interpret near the percolation regime.

- Measurements during hydrate formation and dissociation require careful analysis to properly interpret signatures, in particular when out-of plane conductivity anomalies prevail.

- Data preprocessing plays a critical role towards obtaining robust solutions. The new algorithm developed to estimate conductivity distribution provides a smoothed global conductivity distribution.

- Inversion by successive forward simulations is robust and viable if seeking for well defined features such as lenses and nodules.

- The solution by matrix inversion requires constraining and regularization to reduce the effect of ill-conditioning.

- A three dimensional measurement configuration and three dimensional tomographic inversion are required for adequate process monitoring of advancing hydrate fronts.

CHAPTER VIII.

CONCLUSIONS

The goals of this research were to gain a fundamental understanding of hydrate bearing sediments, to address the effect of hydrate guest molecules, to investigate the evolution of nucleation in sediments, and to learn about the effects hydrates exert on the mechanical and electromagnetic properties of hydrate bearing sediments. Unprecedented experimental methods and devices were developed as part of this study. Experimental results were complemented with numerical simulations to facilitate the physical interpretation of measurements. The most important conclusions from this study follow.

THF as Hydrate Former:

- THF has permittivity as low as that of nonpolar molecules owing primarily to the large size of the molecule, despite a dipole moment close to that of water.
- The molecular size hinders THF from hydrating salts or mineral surfaces; therefore, the overall behavior of THF in sediments resembles that of a nonpolar fluid.
- THF forms weaker hydrogen bonds with water than the water molecules form with each other, meaning that THF has only limited impact on the hydrogen-bonded water network. The available data also indicate that the interfacial tension, a factor important in hydrate growth in pore space, between water and either THF or methane hydrate is similar.
- The laboratory formation history and ensuing pore-scale spatial distribution

likely have a more pronounced effect on the macroscale mechanical properties of hydrate-bearing sediments than differences between THF and methane hydrates themselves.

Nucleation in Sediments: The thermal signature of nucleation process is characterized by the induction time, supercooling at the inhibition of nucleation and equilibrium temperature depression.

- The initiation of nucleation presents stochastic characteristics. The factors that affect nucleation follow.

- Mechanical impact facilitates the initiation of nucleation and reduces the induction time when the strain rate exceeds a threshold level. Vibration does not affect the equilibrium temperature and does not prevent the stochastic nature of nucleation (yet it reduces its randomness).

- Salts do not affect the induction time considerably. However, salts depress the equilibrium temperature during phase transformation as the water activity is lowered down, and ion exclusion leads to diffusion limited nucleation.

- Nucleation is favored in the presence of mineral surfaces.

- The character of mineral surfaces affects the induction time but it does not change the equilibrium temperature during phase transformation.

- Mineralogy and surface roughness are the most important particle characteristics to prompt the initiation of nucleation on mineral surfaces. Particle size plays a secondary role.

- Pore size cause a significant depression in equilibrium temperature in fine grained sediments.

- Hydrate formation gradually invades the porous network, starting at large pores and advancing into the small ones. Therefore, the equilibrium temperature is gradually depressed during hydrate formation in sediments.

Mechanical and Electromagnetic Properties: The formation of hydrates in the pore space of sediments alters the elastic and electromagnetic properties of soil-fluid mixtures. The measurement of the elastic and electromagnetic properties of sediments enables the quantification of the amount of hydrates in sediments and tracking of the formation process of hydrates in sediments.

- The S-wave velocity is mainly determined by the coordination number and the contact area between particles. The formation of hydrates reinforces the shear modulus by increasing internal coordination and enlarging contacts. There is a relatively low increase in shear modulus until the hydrate concentration exceeds ~40%; thereafter, the presence of hydrates has a decisive impact on skeletal coordination and stiffness.

- The P-wave velocity increases as hydrates form due to the increase in the bulk modulus of the mixture and shear modulus of the skeleton.

- Dielectric permittivity in the microwave frequency range is a good indicator of the volume fraction of free water in the sediment. The formation of hydrates reduces the volume fraction of free water in mixtures.

- Electrical conductivity is a measure of ionic mobility and concentration in the pore fluid, and the fluid volume fraction in the mixture. Hydrate formation causes ion exclusion and conductivity does not correlate linearly with the volume

fraction of hydrates formed. Formation history, such as the time of reaction as compared to the time of diffusion must be considered in data interpretation

Mechanical and Electromagnetic Properties in GOM Sediments: Consolidation experiments on undisturbed and remolded natural sediments obtained during drilling in the northern Gulf of Mexico gas hydrates province and tested with and without synthetic hydrate reveal that:

- Effective stress controls the stiffness of uncemented, normally consolidated sediments lacking hydrates. The sensitivity to the state of stress is high, consistent with the high specific surface and high plasticity of these sediments. In sediments with high hydrate concentration, the effect of hydrates overrides the effect of effective stress on stiffness.

- Phase transformation monitoring reveals ion exclusion and an increase in ionic concentration in remaining pore fluids during hydrate formation. This effect couples with a gradual decrease in unfrozen pore size to further depress the equilibrium temperature.

- No decementation or skeletal debonding is observed when the 100% hydrate-filled sediments are unloaded from effective vertical stresses. Therefore, high hydrate content specimens should experience limited sampling effects due to skeletal unloading. Care should be taken to reload such samples to the in-situ effective stress condition as soon as possible after retrieval.

Electrical Resistivity Tomography:

- Electrode polarization effect can be avoided if measurements are conducted in the kHz frequency range.

- The drop in electrical potential near source and sink electrodes and associated high current densities are due to geometric-Laplacian effects and can be reduced by using wider electrodes at the expense of lower spatial resolution. Therefore, the response to inclusions becomes stronger as the electrode width increases.

- Taking into consideration spatial resolution, electric field and shunting effects, optimal ERT results can be obtained when the electrode width is $W_{elec}/D_{cell} \cong 0.1$.

-Longer electrodes change the 3D current flow condition into a pseudo 2D case. The signal strength and the sensitivity to inclusions benefit from the longer length of electrodes but reaches an asymptote when $L_{elec}/D_{cell} \cong 0.7$ (for $D_{inc}/D_{cell}=0.2\sim0.4$).

- End-cap insulation is not required in cylindrical cells with electrodes located at the mid-height of the cell if $H_{cell}/D_{cell} \geq 2.5$ and $L_{elec}/H_{cell} < 0.2$.

- The evolution of electrical conductivity during CO_2 hydrate formation and dissociation reflects the combined affects of concurrent changes that include ionization of dissolved CO_2, temperature-dependent ionic mobility, changes in the degree of saturation, ion exclusion, surface conduction, and porosity changes.

- Unsaturation is characterized by a fractal network near the air or liquid percolation thresholds. Electrical measurements are difficult to interpret near percolation regime.

- Measurements during hydrate formation and dissociation require careful analysis to properly interpret signatures, in particular when out-of plane conductivity anomalies prevail.

- Data preprocessing plays a critical role towards obtaining robust solutions. The new algorithm developed to estimate conductivity distribution provides a smoothen global conductivity distribution.

- Inversion by successive forward simulations is robust and viable if seeking for well defined features such as lenses and nodules.

- The solution by matrix inversion requires constraining and regularization to reduce the effect of ill-conditioning.

- A three dimensional measurement configuration and three dimensional tomographic inversion are required for adequate process monitoring of advancing hydrate fronts.

APPENDIX A.

GAS HYDRATE SYNTHESIS METHOD IN LITERATURES

Method	Procedure	Specimen Condition	References	Comments
Bubbling methane gas into saturated sediment	Lower the cylinder to 910m water depth (T=277.4K) Fill the cylinder with seawater or seawater and sediments Bubble methane into cylinder from the bottom– methane hydrate was formed in a few seconds	Coarse sand Find grained mud No volume fraction specified	Brewer et al, 1998	Location: Monterey bay, CA Formation of hydrate at the top of the tube Reduced permeability in sediments prevents further injection
	Place slurry in the cell (gas interface presents in the cell) Evacuated the system for 30 min 2 times Pressurize with Methane (2~8MPa) Equilibrate initial temperature at 295~300K Slowly lower the temperature down to 272K	Bentonite & Polymer Water content 2900%	Cha et al., 1998	The cell was rocked to renew the interface
	Hydrate formation is detected by pressure drop – 1~2 days for reactions	1~2.3 volume %	Ouar et al, 1992	
	Place slurry in the cell (Gas interface presents in the cell) Flush with CO2 several times Pressurize with CO2 to 0.05~0.15 MPa above the estimate hydrate formation pressure Equilibrate system at target temperature (267~282K) Stirring start inside the cell with magnetic stirrer Increase pressure further to induce hydrate formation (1~3 MPa)	(CO2 gas) Montmorillonite & Polymer 20000% Water Content	Englezos and Hall, 1994	
	Place water in the cell (Gas interface presents in the cell) Equilibrate temperature at 3.5°C Bubble methane from the bottom by increasing pressure of methane injection – 2 hours for reactions	Pure hydrate – preliminary result	Phelps et al., 2001	SPS – Preliminary study Partial clogging in diffuser
	Place slurry in the cell (Gas interface presents in the cell) Pressurize with methane up to 3 MPa and equilibrate temperature at ~5°C – 12 hours Bubble methane from the bottom by increasing pressure of methane injection (up to ~ 5 MPa)	Bentonite 200mg/l	Riestenberg et al., 2003	SPS – Slurry experiment No description on reaction time

Methods	Procedures	Specimen conditions	References	Comments
Flushing methane into partially saturated sediment	Place specimen in the cell Equilibrate temperature at 273.5K Pressurize up to 6.8~13.6 MPa by injecting methane from the bottom- 2~14days for reactions (depend on sediment type)	Glass beads 100~5000 μm Saturation varies from 18~53%	(Kono et al. 2002)	- Unsaturated condition - Forcing the hydrate form at contact
	Prepare pore saturated porous material – 3 days Specimen is cooled to liquid nitrogen temperature and degassed Pressurize with methane to ~12 MPa (so that T/P condition is still within hydrate stable region after a full reaction) Subject several freeze-thaw cycles Set temperature 0.5K above ice melting point to initiate reaction – 3days for reaction	Porous Silica gel Pore radius 70A Particle size 200-425mesh Saturated pore volume, no free water	(Handa and Stupin 1992)	During the reaction, pressure increased periodically to maintain reaction rate
	Prepare pore saturated porous material – 1 day Place the specimen and degas the inside the cell Pressurize with methane such that upon completion of the reaction there is enough gas left over to stabilize hydrate Equilibrate temperature at experimental conditions – 3~5 days for reaction	Porous silica glass powder Mean particle diameter = 20μm	(Uchida et al. 1999)	
	Prepare partially saturated sand specimen and place in the cell Pressurize the with gas (CH_4: 8~9MPa; CO_2: 3.5~4MPa) Perform cooling/heating cycle (-263°C~293°C)	Natural quartz sand D_{50} = 0.32mm W_w = 14~18% Porosity 0.4~0.5	(Chuvilin et al. 2003)	
	1) Prepare saturated specimen Raise confining and pore pressure up to 12 MPa Apply consolidation stress σ_c' of 0.34 MPa 2) Prepare partially saturated specimen Raise confining and pore pressure up to 12 MPa Apply consolidation stress σ_c' of 0.2, 0.3, 4.8 MPa Methane is slowly percolated (making specimen unsaturated) Alternate injections from the bottom and the top for more homogeneous distribution Temperature is lowered	Sand (250 and 500 μm) Silt (10 μm)	(Winters et al. 2005)	

Methods	Procedures	Specimen conditions	References	Comments
Mixing granular ice and sediments and injecting methane	Place Ice seeds (or mixture of ice seeds and quartz sand) (250K) Pressurize with methane (250K, 25-30 MPa) Temperature is slowly raised to 290K for reaction – 8~12 hours Specimens are cooled to 250K for preservation	Ice seed 180~250 μm 40% porosity	Stern and Kirby, 1998, Durham et al, 2003, Circone et al., 2003	Homogeneous distribution of methane hydrate in sediment
		Quartz Sand D50 = N/A Gas-filled porosity 30~40% 0,33,67, and 100% solid volume of hydrate	Waite et al, 2002,	
		Oklahoma sand (125 μm)	(Durham et al. 2005)	
	Prepare specimen by ice and sand 140 mm × 70 mm cylindrical specimen is attached to resonant column (283.15K) Apply effective stress σ' of 250kPa (Wet condition, not frozen) Re-freeze specimen (263.15K) Inject methane up to 15MPa Raise temperature (283.15K) over 15 hours	Sand (100 μm)	(Priest et al. 2005)	Resonant column test

Method	Procedure	Sediment Sample Condition	References	Comments
Mixing hydrate grain and sediment	Synthesize polycrystalline hydrate with method suggested by (Stern et al. 1996) Hydrate/sediment mixture is placed inside a supporting soft-metal container Hydrostatically pressurized to a dense, mechanically competent material	Oklahoma sand (125 μm)	(Durham et al. 2005)	Triaxial test Confining pressure 50~100MPa Pore Pressure 1.6~1.5MPa
	Synthesize polycrystalline hydrate with method suggested by (Stern et al. 1996) Prepare mixture (sand + ice + hydrate) Compact massive sediment core (47.6mm diameter) in a piston cylinder apparatus	62% sand, 28% hydrate, and 10% ice by volume	(Spangenberg and Kulenkampff 2005)	
	Synthesize granular hydrate by mixing misted water with pure methane hydrate Prepare hydrate + sediment mixture and store under -80°C Lower the mold temperature to -30°C and fill the mold with prepared mixture Apply axial pressure of 12 MPa (1~2 hours) Raise the temperature to 3°C to eliminate ice (0.5 hour) Lower the temperature to -30°C (2~3 hours)	Core from Nankai Trough Core depth : 1152.75 m and 207.75 m from the sea floor	(Hyodo et al. 2005)	Triaxial test

Method	Procedure	Sediment Sample Condition	References	Comments
Formation from dissolved gas	Place specimen (gas interface presents in the cell) System evacuated and purge with methane from the top Lower the temperature (276.5K) Pressurized with methane from the top (more than 8MPa)	Activated carbon Pore diameter 1.9nm	(Liang et al. 2005)	
	Place specimen (gas interface presents in the cell) Pressurize with CO2 to dissolve CO2 in water – ~4 weeks for diffusion (3MPa) Lower the temperature slightly above freezing point of water with CO_2 – 2 days for reactions Cycle cooling and warming	(CO2 gas) Lane Mtn sand 0.4~0.6mm	(Buffett and Zatsepina 2000; Zatsepina and Buffett 2001)	
	Dry glass beads are placed in the cell 0.1M NaCl solution is sucked into system Circulate methane dissolved water using pump and regulation valve (Cell pressure: 17.4 MPa) Decrease temperature from 20°C to 13°C	Glass beads 750~500 μm Porosity: 0.38	(Spangenberg and Kulenkampff 2005)	After 55days, specimen became almost impermeable.

Method	Procedure	Sediment Sample Condition	References	Comments
Water spraying method	Evacuate the cell Charge water (or water and LMGS (Large molecules guest substance)) Cool the system to 275K Pressurize with methane to 2.9 ~ 3.7 MPa (varies according to type of LMGS) Spraying water into chamber by circulating water with plunger pump (90cm^3/min)		(Ohmura et al. 2002; Tsuji et al. 2005; Tsuji et al. 2004)	
Using micro bubbles	Place 1% THF-water solution Several temperature above freezing temperature tested Xenon is supplied with an atmospheric pressure as micro bubbles		(Takahashi et al. 2003)	Xenon was used as guest gas 1% of THF is added in water to promote nucleation
Use of surfactant to enhance solubility of methane	Place water-surfactant solution by pumping Displace part of water with methane by injecting methane Lower the temperature to 275~278K Pressurize with methane from the top (~3.6 MPa) - ~ 5 hours for reactions	N/A	Zhong and Rogers, 2000	Differs formation mechanism by changing interfacial tensions
	Place specimen (gas interface presents in the cell) Air is purged with methane Pressurize with methane to 2.2MPa Lower the temperature (274K) – ~ 5 hours for reactions	Ottawa sand Bentonite Kaolinite	Woods, 2004	

APPENDIX B.

EXPERIMENTAL DATA TABLE FOR CHAPTER IV

Low fluid pressure cell – Sand specimen

S_{hyd}	Status	σ' [MPa]	e	Vs [m/s]	σ_{el}[S/m]	κ´
0%	Loading	0.00	0.58	86	0.16	27.34
		0.01	0.58	110	0.16	27.35
		0.10	0.57	188	0.15	27.26
		0.51	0.56	281	0.15	27.24
		1.21	0.54	346	0.15	27.20
	Unloading	1.21	0.54	346	0.15	27.20
		0.51	0.54	296	0.15	27.38
		0.24	0.54	251	0.16	27.57
		0.10	0.55	200	0.16	27.70
		0.08	0.55	190	0.16	27.78
		0.01	0.55	113	0.19	28.17
		0.00	0.56	81	0.19	28.31
50%	Loading	0.00	0.59	95	0.13	25.24
		0.01	0.59	140	0.13	25.27
		0.10	0.57	226	0.15	26.38
		0.51	0.55	394	0.13	25.18
		1.21	0.53	390	0.11	23.44
	Loading (after formation)	0.00	0.59	-	-	-
		0.01	0.59	609	0.07	16.70
		0.10	0.57	602	0.07	16.85
		0.51	0.54	605	0.08	18.84
		1.21	0.54	638	0.07	17.78
	Loading (after dissociation)	0.00		-	-	-
		0.01	0.59	132	0.15	26.50
		0.10	0.57	214	0.13	25.42
		0.51	0.54	313	0.12	23.71
		1.21		-	-	-
	Unloading	1.21	0.54	638	0.07	17.78
		0.51	0.54	583	0.07	17.87
		0.10	0.54	502	0.07	18.02
		0.01	0.55	505	0.08	18.27
		0.00	0.56	493	0.08	18.28
100%	Loading	0.00	0.60	-	0.18	22.79
		0.01	0.60	148	0.17	22.75
		0.10	0.59	220	0.15	20.51
		0.51	0.57	471	0.12	18.76
		1.21	0.54	564	0.17	22.34
	Loading (after formation)	0.00	0.60	-	-	-
		0.01	0.60	1864	0.00	4.46
		0.10	0.59	1822	0.00	4.45
		0.51	0.57	2115	0.00	4.44
		1.21	0.54	2252	0.00	4.44
	Loading (after dissociation)	0.00		-	-	-
		0.01	0.60	122	0.15	20.88
		0.10	0.57	199	0.12	18.85
		0.51	0.57	423	0.17	22.74
		1.21		-	-	-
	Unloading	1.20	0.54	2252	0.00	4.44
		0.50	0.54	2064	0.00	4.39
		0.24	0.55	2070	0.00	4.39
		0.10	0.55	1780	0.00	4.47
		0.01	0.55	1667	0.00	4.24
		0.00	0.55	1567	0.00	3.99

Low fluid pressure cell – Crushed silt specimen

S_{hyd}	Status	σ' [MPa]	e	Vs [m/s]	σ_{el}[S/m]	κ´
0%	Loading	0.00	0.90	45	0.19	35.96
		0.01	0.88	73	0.18	35.54
		0.10	0.82	162	0.20	34.47
		0.51	0.77	238	0.17	32.01
		1.21	0.73	294	0.16	30.77
	Unloading	1.21	0.73	294	0.16	30.77
		0.51	0.74	246	0.17	31.04
		0.10	0.76	205	0.17	31.22
		0.01	0.77	129	0.17	31.29
		0.00	0.78	105	0.17	31.31
		0.00	0.90	45	0.19	35.96
		0.01	0.88	73	0.18	35.54
100%	Loading	0.00	0.81	16	0.11	19.78
		0.01	0.77	53	0.11	19.46
		0.10	0.73	142	0.12	20.27
		0.51	0.67	219	0.11	19.70
		1.21	0.60	306	0.11	19.38
	Loading (after formation)	0.00	-			
		0.01	0.81	1665	0.00	4.03
		0.10	0.75	1569	0.00	4.61
		0.51	0.67	1451	0.00	6.15
		1.21	0.60	1577	0.00	6.16
	Loading (after dissociation)	0.00	-			
		0.01	0.78	63	0.12	21.00
		0.10	0.72	142	0.12	20.35
		0.51	0.66	229	0.11	19.57
		1.21				
	Unloading	1.21	0.60	1577	0.00	6.16
		0.51	0.63	1395	0.00	4.89
		0.10	0.65	1405	0.00	4.95
		0.01	0.67	1331	0.00	5.04
		0.00	0.67	1261	0.00	5.16

Low fluid pressure cell – Precipitated silt

S_{hyd}	Status	σ' [MPa]	e	Vs [m/s]	σ_{el}[S/m]	κ´
0%	Loading	0.00	6.29	15	0.73	63.60
		0.01	6.29	17	0.73	63.80
		0.10	5.52	64	0.70	62.20
		0.51	5.10	111	0.68	60.77
		1.21	4.80	141	0.67	59.73
	Unloading	1.21	4.80	141	0.67	59.72
		0.51	4.88	127	0.67	59.97
		0.24	4.95	116	0.68	60.11
		0.10	5.03	104	0.68	60.37
		0.01	5.14	85	0.68	60.79
		0.00		-	0.69	60.79
50%	Loading	0.00	7.07	-	0.57	61.84
		0.01	6.76	25	0.56	61.46
		0.10	5.89	66	0.52	56.30
		0.51	4.33	124	0.51	54.80
		1.21	3.47	145	0.52	53.94
	Loading (after formation)	0.00	-	-	-	-
		0.01	6.66	276	0.37	40.98
		0.10	5.97	278	0.39	39.41
		0.51	4.40	284	0.41	40.89
		1.21	3.53	316	0.39	37.22
	Loading (after dissociation)	0.00	-	-	-	-
		0.01	6.40	42	0.44	51.85
		0.10	5.77	73	0.52	54.97
		0.51	4.25	123	0.50	54.48
		1.21				
	Unloading	1.21	3.53	316	0.39	37.22
		0.51	3.60	155	0.39	36.97
		0.10	3.71	180	0.38	36.41
		0.01	3.76	178		
		0.00	3.85	180		
100%	Loading	0.00	6.07	23	0.46	48.22
		0.01	5.68	15	0.25	31.63
		0.10	4.77	23	0.38	40.39
		0.51	3.71	91	0.44	47.39
		1.21	3.13	198	0.45	46.97
	Loading (after formation)	0.00	-	-	-	-
		0.01	5.91	743	0.00	1.09
		0.10	5.12	745	0.00	1.78
		0.51	3.94	957	0.00	2.85
		1.21	3.18	1050	0.00	4.86
	Loading (after dissociation)	0.00	-	-	-	-
		0.01	5.47	19	0.23	30.05
		0.10	4.60	22	0.39	43.19
		0.51	3.59	88	0.46	47.95
		1.21				
	Unloading	1.21	3.18	1050	0.00	4.86
		0.51	3.22	817	0.00	4.76
		0.10	3.28	665	0.00	4.52
		0.01	3.31	639	0.00	3.49
		0.00	3.38	666	0.00	3.39

Low fluid pressure cell – Clay

S_{hyd}	Status	σ' [MPa]	e	Vs [m/s]	σ_{el}[S/m]	κ´
0%	Loading	0.00	1.11	22	0.27	37.37
		0.01	0.96	63	0.26	34.84
		0.10	0.77	127	0.24	31.45
		0.51	0.59	196	0.22	28.13
		1.21	0.52	267	0.19	26.73
	Unloading	1.21	0.52	267	0.19	26.73
		0.51	0.52	234	0.20	27.07
		0.24	0.54	190	0.21	27.54
		0.10	0.56	152	0.24	28.05
		0.08	0.56	147	0.24	28.06
		0.01	0.62	92	0.34	29.80
		0.00	0.65	80	0.31	29.55
50%	Loading	0.00	1.08	74	0.21	32.31
		0.01	0.97	124	0.19	31.17
		0.10	0.73	240	0.15	25.94
		0.51	0.56	361	0.15	24.70
		1.21	0.48	386	0.14	23.74
	Loading (after formation)	0.00	-	-	-	-
		0.01	-	-	-	-
		0.10	0.69	413	0.06	13.74
		0.51	0.56	441	0.05	14.57
		1.21	0.49	464	0.06	14.15
	Loading (after dissociation)	0.00				
		0.01	0.87	149	0.14	25.30
		0.10	0.64	239	0.17	25.59
		0.51	0.55	369	0.14	24.32
		1.21				
	Unloading	1.21	0.49	464	0.06	14.15
		0.51	0.50	452	0.08	16.35
		0.10	0.54	439	0.08	16.38
		0.01	0.56	429	0.08	17.09
		0.00	0.61	426	0.06	16.20
100%	Loading	0.00	0.92	76	0.25	27.81
		0.01	0.86	109	0.26	27.76
		0.10	0.68	169	0.22	25.67
		0.51	0.54	250	0.21	24.53
		1.21	0.46	317	0.17	23.41
	Loading (after formation)	0.00		-	-	-
		0.01	0.91	1060	0.00	3.41
		0.10	0.71	1059	0.00	6.92
		0.51	0.56	1252	0.00	7.74
		1.21	0.49	1321	0.00	7.26
	Loading (after dissociation)	0.00				
		0.01	0.78	99	0.25	25.99
		0.10	0.64	175	0.22	24.63
		0.51	0.52	279	0.23	24.31
		1.21				
	Unloading	1.21	0.49	1321	0.00	7.26
		0.51	0.51	1174	0.00	7.46
		0.10	0.51	948	0.00	8.32
		0.01	0.52	954	0.00	7.44
		0.00	0.56	909	0.00	8.41

High fluid pressure cell - Sand

S_{hyd}	Status	σ' [MPa]	e	Vs [m/s]	Vp [m/s]
0%	Loading	0.00	0.54	-	
		0.12	0.52	127	1734
		0.50	0.50	299	1749
		0.99	0.50	364	1768
		2.09	0.49	454	1787
50%	Loading	0.00	0.62		
		0.04	0.60	187	1756
		0.53	0.58	329	1741
		0.99	0.57	368	1736
		2.12	0.57	435	1770
	Loading (after formation)	0.00	0.62		
		0.04	0.59	546	2023
		0.53	0.58	634	1990
		0.99	0.57	626	2000
		2.12	0.57	636	2023
100%	Loading	0.00	0.81		
		0.04	0.78	160	1779
		0.58	0.75	268	1785
		0.99	0.74	338	1815
		2.02	0.73	386	1813
	Loading (after formation)	0.00	0.90		
		0.04	0.79	2221	4018
		0.58	0.75	2279	4145
		0.99	0.74	2280	4127
		2.02	0.73	2291	4196

High fluid pressure cell – Crushed silt

S_{hyd}	Status	σ' [MPa]	e	Vs [m/s]	Vp [m/s]
0%	Loading	0.00	0.77	-	
		0.04	0.76	80	1680
		0.53	0.72	168	1681
		1.00	0.68	209	1680
		2.02	0.66	258	1693
100%	Loading	0.00	0.88		
		0.04	0.79	66	1529
		0.53	0.75	168	1573
		1.00	0.73	211	1590
		2.02	0.71	255	1609
	Loading (after formation)	0.00	0.88		
		0.04	0.81	1844	3906
		0.53	0.76	1857	4136
		1.01	0.74	1824	4213
		2.02	0.72	1892	4156

High fluid pressure cell – Precipitated silt

S_{hyd}	Status	σ' [MPa]	e	Vs [m/s]	Vp [m/s]
0%	Loading	0.00	9.36	15	
		0.04	8.39	29	1664
		0.39	6.14	100	1670
		0.78	5.49	127	1654
		1.41	4.61	179	1647
		2.97	4.00	219	1654
50%	Loading	0.00	9.36		
		0.04	8.29	12	1494
		0.53	3.98	77	1601
		0.99	3.45	104	1610
		2.12	2.81	156	1616
	Loading (after formation)	0.00	9.36		
		0.04	8.31	293	1761
		0.53	3.98	297	1799
		0.99	3.42	309	1778
		2.12	2.79	348	1794
100%	Loading	0.00	9.38		
		0.04	8.47	62	1676
		0.57	4.44	91	1591
		0.99	4.24	100	1584
		2.02	3.74	114	1572
	Loading (after formation)	0.00	9.38		
		0.04	8.47	1156	3591
		0.57	4.55	1134	3477
		0.99	4.35	1153	3585
		2.02	3.83	1132	3537

High fluid pressure cell - Clay

S_{hyd}	Status	σ' [MPa]	e	Vs [m/s]	Vp [m/s]
0%	Loading	0.00	1.16	35	
		0.09	1.02	62	1571
		0.46	0.89	149	1749
		0.95	0.83	297	1881
		2.05	0.76	429	1981
50%	Loading	0.00	1.84		
		0.04	1.42	104	1594
		0.53	0.85	244	1764
		0.99	0.76	312	1819
		2.12	0.69	422	1860
	Loading (after formation)	0.00	1.84		
		0.04	1.40	350	1783
		0.53	0.87	464	1954
		0.99	0.76	458	1984
		2.12	0.69	507	2031
100%	Loading	0.00	1.73		
		0.04	1.33	61	1637
		0.58	0.74	244	1728
		0.99	0.69	278	1748
		2.02	0.62	338	1782
	Loading (after formation)	0.00	1.73		
		0.04	1.34	1627	3748
		0.58	0.77	1714	3872
		0.99	0.70	1675	3844
		2.02	0.64	1599	3719

APPENDIX C.

ELECTRICAL CIRCUIT DIAGRAM FOR ELECTRICAL RESISTIVITY TOMOGRAPHY MEASUREMENT

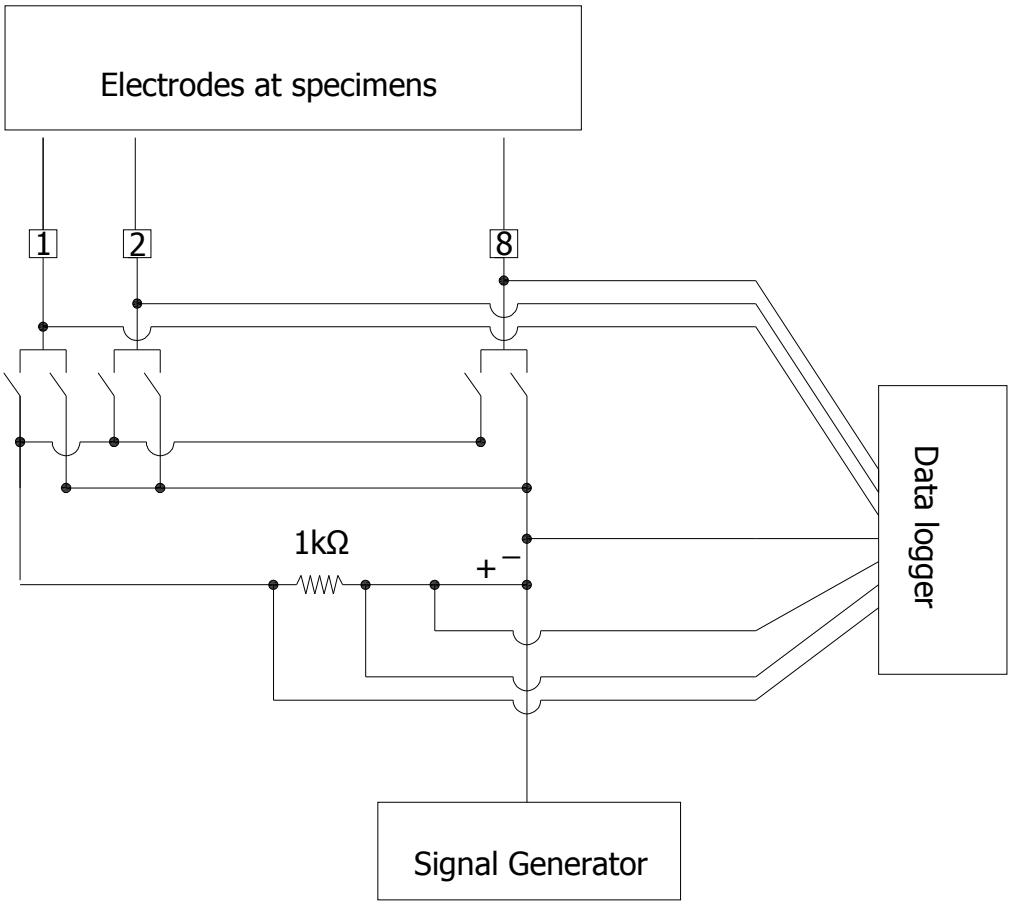
Electrodes at specimens
1
2
8
Data logger
1kΩ
+
−
Signal Generator

APPENDIX D.

THE CONDUCTIVITY VALUES USED IN TOMOGRAPHY DATA PRE-PROCESSING

The conductivity values from the numerically simulated tomography measurement

Source electrode	Sink electrode	σ before hydrate formation	σ after hydrate formation	Δσ
1	5	0.000498	0.000489	0.000009
2	6	0.000498	0.000496	0.000002
3	7	0.000498	0.000496	0.000002
4	8	0.000498	0.000496	0.000003
5	1	0.000498	0.000485	0.000013
6	2	0.000498	0.000496	0.000003
7	3	0.000498	0.000496	0.000002
8	4	0.000498	0.000496	0.000002
1	4	0.000500	0.000497	0.000003
2	5	0.000500	0.000491	0.000009
3	6	0.000500	0.000497	0.000003
4	7	0.000500	0.000497	0.000003
5	8	0.000500	0.000491	0.000009
6	1	0.000500	0.000497	0.000003
7	2	0.000500	0.000499	0.000001
8	3	0.000500	0.000499	0.000001
1	3	0.000500	0.000499	0.000001
2	4	0.000500	0.000497	0.000003
3	5	0.000500	0.000491	0.000009
4	6	0.000500	0.000497	0.000003
5	7	0.000500	0.000491	0.000009
6	8	0.000500	0.000497	0.000003
7	1	0.000500	0.000499	0.000001
8	2	0.000500	0.000499	0.000001
1	2	0.000500	0.0005	0.000000
2	3	0.000500	0.000499	0.000001
3	4	0.000500	0.000497	0.000003
4	5	0.000500	0.000493	0.000007
5	6	0.000500	0.000493	0.000007
6	7	0.000500	0.000497	0.000003
7	8	0.000500	0.000499	0.000001
8	1	0.000500	0.0005	0.000001

The conductivity values from the tomography measurement in the saturated F110 sand specimen from Figure 7.9

Source electrode	Sink electrode	σ before hydrate formation	σ after hydrate formation	Δσ
1	5	0.01823	0.01436	0.00387
2	6	0.01488	0.01200	0.00288
3	7	0.01645	0.01313	0.00332
4	8	0.01755	0.01397	0.00358
5	1	0.01826	0.01435	0.00390
6	2	0.01493	0.01207	0.00285
7	3	0.01648	0.01315	0.00333
8	4	0.01756	0.01399	0.00357
1	4	0.01700	0.01360	0.00340
2	5	0.01508	0.01196	0.00313
3	6	0.01719	0.01311	0.00408
4	7	0.01734	0.01344	0.00389
5	8	0.01892	0.01471	0.00421
6	1	0.01787	0.01434	0.00354
7	2	0.01439	0.01208	0.00231
8	3	0.01667	0.01365	0.00302
1	3	0.01613	0.01326	0.00287
2	4	0.01401	0.01123	0.00278
3	5	0.01723	0.01282	0.00441
4	6	0.01824	0.01335	0.00489
5	7	0.01868	0.01406	0.00462
6	8	0.01835	0.01452	0.00383
7	1	0.01714	0.01433	0.00281
8	2	0.01428	0.01233	0.00195
1	2	0.01336	0.01149	0.00187
2	3	0.01305	0.01070	0.00236
3	4	0.01580	0.01172	0.00407
4	5	0.01807	0.01271	0.00537
5	6	0.02069	0.01420	0.00649
6	7	0.01795	0.01362	0.00433
7	8	0.01790	0.01459	0.00332
8	1	0.01731	0.01489	0.00242

REFERENCES

Anderson, R., Llamedo, M., Tohidi, B., and Burgass, R. W. (2003). "Experimental measurement of methane and carbon dioxide clathrate hydrate equilibria in mesoporous silica." *Journal of Physical Chemistry B*, 107(15), 3507-3514.

Archie, G. E. (1942). "The electrical resistivity log as an aid in determining some reservoir characteristics." *Transactions of the American Institute of Mining and Metallurgical Engineers*, 146, 54-61.

Atkins, P. W. (1978). *Physical Chemistry*, W.H. Freeman and Company, San Francisco.

Avis, N. J., and Barber, D. C. (1994). "Image-Reconstruction Using Non-Adjacent Drive Configurations." *Physiological Measurement*, 15, A153-a160.

Bangs, N. L. B., Sawyer, D. S., and Golovchenko, X. (1993). "Free Gas at the Base of the Gas Hydrate Zone in the Vicinity of the Chile Triple Junction." *Geology*, 21(10), 905-908.

Bathe, M., Vagle, S., Saunders, G. A., and Lambson, E. F. (1984). "Ultrasonic Wave Velocities in the Structure-Ii Clathrate Hydrate Thf.17H2O." *Journal of Materials Science Letters*, 3(10), 904-906.

Berecz, E., and Balla-Achs, M. (1983). *Gas Hydrates*, Elesevier, New York.

Berge, L. I., Jacobsen, K. A., and Solstad, A. (1999). "Measured acoustic wave velocities of R11 (CCl3F) hydrate samples with and without sand as a function of hydrate concentration." *Journal of Geophysical Research-Solid Earth*, 104(B7), 15415-15424.

Bishnoi, P. R., and Natarajan, V. (1996). "Formation and decomposition of gas hydrates." *Fluid Phase Equilibria*, 117(1-2), 168-177.

Blackwell, V. R. (1998). "Formation Processes of Clathrate Hydrates of Carbon Dioxide and Methane," PhD., California Institute of Technology.

Bondarev, E. A., Groisman, A. G., and Savvin, A. Z. "Porous medium effect on phase equilibrium of tetrahydrofuran hydrate." *Second International Conference on Natural Gas Hydrates*, Toulouse, France.

Booth, M. J., and BasarabHorwath, I. (1996). "Comparing electrode configurations for electrical impedance tomography." *Electronics Letters*, 32(7), 648-649.

Buffett, B. A., and Zatsepina, O. Y. (2000). "Formation of gas hydrate from dissolved gas in natural porous media." *Marine Geology*, 164(1-2), 69-77.

Cameron, I., Handa, Y. P., and Baker, T. H. W. (1990). "Compressive strength and creep-behavior of hydrate-consolidated sand." *Canadian Geotechnical Journal*, 27(2), 255-258.

Carey, F. A. (1987). *Organic Chemistry*, McGraw-Hill, New York.

Cha, S. B., Ouar, H., Wildeman, T. R., and Sloan, E. D. (1988). "A 3Rd-Surface Effect on Hydrate Formation." *Journal of Physical Chemistry*, 92(23), 6492-6494.

Cho, G. C., and Santamarina, J. C. (2001). "Unsaturated particulate materials - Particle-level studies." *Journal of Geotechnical and Geoenvironmental Engineering*, 127(1), 84-96.

Chuvilin, E. M., Ebinuma, T., Kamata, Y., Uchida, T., Takeya, S., Nagao, J., and Narita, H. (2003). "Effects of temperature cycling on the phase transition of water in gas-saturated sediments." *Canadian Journal of Physics*, 81(1-2), 343-350.

Circone, S., Stern, L. A., Kirby, S. H., Durham, W. B., Chakoumakos, B. C., Rawn, C. J., Rondinone, A. J., and Ishii, Y. (2003). "CO2 hydrate: Synthesis, composition, structure, dissociation behavior, and a comparison to structure I CH4 hydrate." *Journal of Physical Chemistry B*, 107(23), 5529-5539.

Clennell, B. M., Hovland, M., Booth, J. S., Henry, P., and Winters, W. J. (1999). "Formation of natural gas hydrates in marine sediments 1. Conceptual model of gas hydrate growth conditioned by host sediment properties." *Journal of Geophysical Research-Solid Earth*, 104(B10), 22985-23003.

CohenBacrie, C., Goussard, Y., and Guardo, R. (1997). "Regularized reconstruction in electrical impedance tomography using a variance uniformization constraint." *Ieee Transactions on Medical Imaging*, 16(5), 562-571.

Collet, T. S., and Ladd, J. "Detection of gas hydrate with downhole logs and assessment of gas hydrate concentrations (saturations) and gas volumes on the Blake Ridge with electrical resitivity log data." *The Ocean Drilling Program, Scientific Results, 164*, College Station, TX, 179-191.

Davidson, D. W., Obrien, R. N., Saville, P., and Visaisouk, S. (1986). "Optical refraction by clathrate hydrates." *Journal of the Optical Society of America B-Optical Physics*, 3(6), 864-866.

deMartin, B. J. (2001). "Laboratory measurements of the thermal conductivity and thermal diffusivity of methane hydrate at simulated in situ conditions," MS Thesis, Georgia Institute of Technology.

Devarakonda, S., Groysman, A., and Myerson, A. S. (1999). "THF-water hydrate crystallization: an experimental investigation." *Journal of Crystal Growth*, 204(4), 525-538.

Dick, J., and Servio, P. "Effect of the Water Soluble Protein Bovine Serum Albumin on the Nucleation Time of Methane Hydrate Formation." *The Fifth International Conference on Gas Hydrates*, Trondheim, Norway.

Dickens, G. R., and Quinby-Hunt, M. S. (1997). "Methane hydrate stability in pore water." *Journal of Geophysical Research*, 102(B1), 773-783.

Dickin, F., and Wang, M. S. (1996). "Electrical resistance tomography for process applications." *Measurement Science & Technology*, 7(3), 247-260.

Digby, P. J. (1981). "The Effective Elastic-Moduli of Porous Granular Rocks." *Journal of Applied Mechanics-Transactions of the Asme*, 48(4), 803-808.

Doyle, E.H., S.R. Dallimore, R.A. Fine, A.M. Nur, M.E.Q. Pilson, W.S. Reeburgh, E.D. Sloan Jr., A.M. Tréhu, J. Bintz, J. Merrill, and N. Caputo (2004), *Charting the*

Future of Methane Hydrate Research in the United States. National Academies Press, Washington D.C., 192 pp.

Durham, W. B., Stern, L. A., Kirby, S. H., and Circone, S. "Rheological comparisons and structural imaging of sI and sII endmember gas hydrates and hydrate/sediment aggregates." *Fifth International Conference on Gas Hydrates*, Trondheim, Norway.

Dvorkin, J., and Nur, A. (1996). "Elasticity of high-porosity sandstones: Theory for two North Sea data sets." *Geophysics*, 61(5), 1363-1370.

Dvorkin, J., Nur, A., and Yin, H. Z. (1994). "Effective Properties of Cemented Granular-Materials." *Mechanics of Materials*, 18(4), 351-366.

Dyadin, Y. A., Larionov, E. G., Manakov, A. Y., and Zhurko, F. V. (1999). "Double clathrate hydrate of tetrahydrofuran and xenon at pressures up to 15 kBar." *Mendeleev Communications*(2), 80-81.

Ebinuma, T., Kamata, Y., Minagawa, H., Nagao, J., Narita, H., and Ohmura, R. "Mechanical properties of sandy sediment containing methane hydrate." *Fifth International Conference on Gas Hydrates*, Trondheim, Norway.

Ecker, C., Dvorkin, J., and Nur, A. (1998). "Sediments with gas hydrates: Internal structure from seismic AVO." *Geophysics*, 63(5), 1659-1669.

Edwards, G. R., Evans, L. F., and Zipper, A. F. (1970). "2-Dimensional Phase Changes in Water Adsorbed on Ice-Nucleating Substrates." *Transactions of the Faraday Society*, 66(565P), 220-&.

Edwards, R. N. (1997). "On the resource evaluation of marine gas hydrate deposits using sea-floor transient electric dipole-dipole methods." *Geophysics*, 62(1), 63-74.

Englezos, P., and Hall, S. (1994). "Phase-Equilibrium Data on Carbon-Dioxide Hydrate in the Presence of Electrolytes, Water-Soluble Polymers and Montmorillonite." *Canadian Journal of Chemical Engineering*, 72(5), 887-893.

Evans, L. F. (1967). "Selective Nucleation of High-Pressure Ices." *Journal of Applied Physics*, 38(12), 4930-&.

Everett, D. H. (1961). "Thermodynamics of Frost Damage to Porous Solids." *Transactions of the Faraday Society*, 57(9), 1541-&.

Feng, S. H., and Sen, P. N. (1985). "Geometrical Model of Conductive and Dielectric-Properties of Partially Saturated Rocks." *Journal of Applied Physics*, 58(8), 3236-3243.

Fisher, J. C., Hollomon, J. H., and Turnbull, D. (1949). "Rate of Nucleation of Solid Particles in a Subcooled Liquid." *Science*, 109(2825), 168-169.

Fletcher, N. H. (1958). "Size Effect in Heterogeneous Nucleation." *Journal of Chemical Physics*, 29(3), 572-576.

Fletcher, N. H. (1959). "Entropy Effect in Ice Crystal Nucleation." *Journal of Chemical Physics*, 30(6), 1476-1482.

Fletcher, N. H. (1960). "Nucleation and growth of ice crystals upon crystallization substrates." *Austrian Journal of Physics*, 13, 408-418.

Fletcher, N. H. (1969). "Active Sites and Ice Crystal Nucleation." *Journal of the Atmospheric Sciences*, 26(6), 1266-&.

Florusse, L. J., Peters, C. J., Schoonman, J., Hester, K. C., Koh, C. A., Dec, S. F., Marsh, K. N., and Sloan, E. D. (2004). "Stable low-pressure hydrogen clusters stored in a binary clathrate hydrate." *Science*, 306(5695), 469-471.

Francisca, F., Yun, T.-S., Ruppel, C., Santamarina, J. C. (2005). "Geophysical and geotechnical properties of near-seafloor sediments in the northern Gulf of Mexico gas hydrate province" *Earth and Planetary Science Letters*, v 237, n 3-4, Sep 15, p 924-939

Fukasawa, T., Tominaga, Y., and Wakisaka, A. (2004). "Molecular association in binary mixtures of tert-butyl alcohol-water and tetrahydrofuran-heavy water studied by mass spectrometry of clusters from liquid droplets." *Journal of Physical Chemistry A*, 108(1), 59-63.

Gagnon, R. E., Kiefte, H., Clouter, M. J., and Whalley, E. (1987). "Elastic-constants of Ice-Ih, up to 2.8 Kbar, by Brillouin spectroscopy." *Journal De Physique*, 48(C-1), 23-28.

Galashev, A. E., Chukanov, V. N., Novruzov, A. N., and Novruzova, O. A. (2006). "Molecular-dynamic calculation of spectral characteristics of absorption of infrared radiation by $(H_2O)(j)$ and $(CH_4)(i)(H_2O)(n)$ clusters." *High Temperature*, 44(3), 364-372.

Guerin, G., Goldberg, D., and Meltser, A. (1999). "Characterization of in situ elastic properties of gas hydrate-bearing sediments on the Blake Ridge." *Journal of Geophysical Research-Solid Earth*, 104(B8), 17781-17795.

Guimaraes, M. (2002). "Crushed stone fines and ion removal from clay slurries-fundamental studies " PhD, Georgia Institute of Technology, Atlanta.

Handa, Y. P. (1986). "Compositions, enthalpies of dissociations, and heat capacities in the range 85 to 270K for clathrate hydrates of methane, ethane, and propane, and enthalpy of dissociation of isobutene hydrate as determined by a heat-flow calorimeter." *Journal of Chemical Thermodynamics*, 18, 915-921.

Handa, Y. P. (1990). "Effect of hydrostatic-pressure and salinity on the stability of gas hydrates." *Journal of Physical Chemistry*, 94(6), 2652-2657.

Handa, Y. P., Hawkin, R. E., and Murray, J. J. (1984). "Calibration and testing of Tian-Calvet heat-flow calorimeter: Enthalpies of fusion and heat capacities for ice and tetrahydrofuran hydate in the range 85 to 270 K." *Journal of Chemical Thermodynamics*, 16, 623-632.

Handa, Y. P., and Stupin, D. (1992). "Thermodynamic properties and dissociation characteristics of methane and propane hydrates in 70-angstrom-radius silica-gel pores." *Journal of Physical Chemistry*, 96(21), 8599-8603.

Handa, Y. P., Zakrzewski, M., and Fairbridge, C. (1992). "Effect of Restricted Geometries on the Structure and Thermodynamic Properties of Ice." *Journal of Physical Chemistry*, 96(21), 8594-8599.

Helgerud, M. B., Dvorkin, J., Nur, A., Sakai, A., and Collett, T. (1999). "Elastic-wave velocity in marine sediments with gas hydrates: Effective medium modeling." *Geophysical Research Letters*, 26(13), 2021-2024.

Helgerud, M. B., Waite, W. F., Kirby, S. H., and Nur, A. (2003a). "Measured temperature and pressure dependence of compressional (V-p) and shear (V-s) wave speeds in compacted, polycrystalline ice Ih." *Canadian Journal of Physics*, 81(1-2), 81-87.

Helgerud, M. B., Waite, W. F., Kirby, S. H., and Nur, A. (2003b). "Measured temperature and pressure dependence of V-p and V-s in compacted, polycrystalline sI methane and sII methane-ethane hydrate." *Canadian Journal of Physics*, 81(1-2), 47-53.

Hobbs, P. V. (1974). *Ice Physics*, Clarendon, Oxford.

Hyndman, R. D., and Spence, G. D. (1992). "A Seismic Study of Methane Hydrate Marine Bottom Simulating Reflectors." *Journal of Geophysical Research-Solid Earth*, 97(B5), 6683-6698.

Hyndman, R. D., Yuan, T., and Moran, K. (1999). "The concentration of deep sea gas hydrates from downhole electrical resistivity logs and laboratory data." *Earth and Planetary Science Letters*, 172(1-2), 167-177.

Hyodo, M., Nakata, Y., Yoshimoto, N., and Ebinuma, T. (2005). "Basic research on the mechanical behavior of methane hydrate-sediments mixture." *Soils and Foundations*, 45(1), 75-85.

Institute, B. S. (1990). "Methods of testing soils for civil engineering purpose." British Standards 1377-2, British Standard Institute, London, England.

Jager, M. D., de Deugd, R. M., Peters, C. J., Arons, J. D., and Sloan, E. D. (1999). "Experimental determination and modeling of structure II hydrates in mixtures of methane plus water plus 1,4-dioxane." *Fluid Phase Equilibria*, 165(2), 209-223.

Jahrling, K., and Tait, S. (1996). "Measurements of the evolution of porosity in a mushy layer." *Journal of Crystal Growth*, 167(1-2), 285-291.

Jakobsen, M., Hudson, J. A., Minshull, T. A., and Singh, S. C. (2000). "Elastic properties of hydrate-bearing sediments using effective medium theory." *Journal of Geophysical Research-Solid Earth*, 105(B1), 561-577.

Jakobsen, T., and Folgero, K. (1997). "Dielectric measurements of gas hydrate formation in water-in-oil emulsions using open-ended coaxial probes." *Measurement Science & Technology*, 8(9), 1006-1015.

Jakobsen, T., Sjoblom, J., and Ruoff, P. (1996). "Kinetics of gas hydrate formation in w/o-emulsions The model system trichlorofluoromethane/water/non-ionic surfactant studied by means of dielectric spectroscopy." *Colloids and Surfaces a-Physicochemical and Engineering Aspects*, 112(1), 73-84.

Jallut, C., Lenoir, J., Bardot, C., and Eyraud, C. (1992). "Thermoporometry - Modeling and Simulation of a Mesoporous Solid." *Journal of Membrane Science*, 68(3), 271-282.

Jin, Y. K., Lee, M. W., and Collett, T. S. (2002). "Relationship of gas hydrate concentration to porosity and reflection amplitude in a research well, Mackenzie Delta, Canada." *Marine and Petroleum Geology*, 19(4), 407-415.

Kashchiev, D., and Firoozabadi, A. (2002). "Nucleation of gas hydrates." *Journal of Crystal Growth*, 243(3-4), 476-489.

Keller, G. V., and Frischknecht, F. C. (1966). *Electrical methods in geophysical prospecting*, Pergamon Press New York.

Khokhar, A. A., Gudmundsson, J. S., and Sloan, E. D. (1998). "Gas storage in structure H hydrates." *Fluid Phase Equilibria*, 151, 383-392.

Kiefte, H., Clouter, M. J., and Gagnon, R. E. (1985). "Determination of acoustic velocities of clathrate hydrates by Brillouin spectroscopy." *Journal of Physical Chemistry*, 89(14), 3103-3108.

Klein, K. (1999). "Electromagnetic properties of high specific surface minerals " PhD, Georgia Institute of Technology, Atlanta.

Klein, K., and Santamarina, J. C. (2003). " Electrical Conductivity In Soils: Underlying Phenomena." *Journal of Environmental Engineering Geophysics*, 8(4), 263-273.

Kono, H. O., Narasimhan, S., Song, F., and Smith, D. H. (2002). "Synthesis of methane gas hydrate in porous sediments and its dissociation by depressurizing." *Powder Technology*, 122(2-3), 239-246.

Korenaga, J., Holbrook, W. S., Singh, S. C., and Minshull, T. A. (1997). "Natural gas hydrates on the southeast US margin: Constraints from full waveform and travel time inversions of wide-angle seismic data." *Journal of Geophysical Research-Solid Earth*, 102(B7), 15345-15365.

Leaist, D. G., Murray, J. J., Post, M. L., and Davidson, D. W. (1982). "Enthalpies of decomposition and heat-capacities of ethylene-oxide and tetrahydrofuran hydrates." *Journal of Physical Chemistry*, 86(21), 4175-4178.

Lee, J., Yun, T., Santamarina, J. C., and Ruppel, C. (2007). "Observations related to tetrahydrofuran and methane hydrates for laboratory studies of hydrate-bearing sediments." *Geochemistry, Geophysics, and Geosystem*, 8(Q06003), doi:10.1029/2006GC001531.

Lee, J. S., and Santamarina, J. C. (2005). "Bender elements: Performance and signal interpretation." *Journal of Geotechnical and Geoenvironmental Engineering*, 131(9), 1063-1070.

Lee, M. W. (2002). "Biot-Gassmann Thoery for velocities of gas hydrates-bearing sediments." *Geophysics*, 67(6), 1711-1719

Lee, M. W., and Collett, T. S. (2001). "Elastic properties of gas hydrate-bearing sediments." *Geophysics*, 66(3), 763-771.

Lee, M. W., Hutchinson, D. R., Collett, T. S., and Dillon, W. P. (1996). "Seismic velocities for hydrate-bearing sediments using weighted equation." *Journal of Geophysical Research-Solid Earth*, 101(B9), 20347-20358.

Liang, M. Y., Chen, G. J., Sun, C. Y., Yan, L. J., Liu, J., and Ma, Q. L. (2005). "Experimental and modeling study on decomposition kinetics of methane hydrates in different media." *Journal of Physical Chemistry B*, 109(40), 19034-19041.

Lide, D. R. (2003). "CRC handbook of chemistry and physics." CRC Press, Cleveland, Ohio, 2576.

Lin, W., Chen, G. J., Sun, C. Y., Guo, X. Q., Wu, Z. K., Liang, M. Y., Chen, L. T., and Yang, L. Y. (2004). "Effect of surfactant on the formation and dissociation kinetic behavior of methane hydrate." *Chemical Engineering Science*, 59(21), 4449-4455.

Luck, W. A. P. (1973). "Chapter 4. Infrared Studies of Hydrogen Bonding in Pure Liquids and Solutions." Water in crystalline hydrates: Aqueous Solutions of Simple Nonelectrolytes, F. Franks, ed., Plenum Press, New York, 684.

Lyon, G. M., and Oakley, J. P. "Simulation Study of Sensitivity in Stirred Vessel Electrical Impedance Tomography." *Proceedings of a Workshop on Tomographic Techniques for Process Design and Operation*, Manchester, Engl, 137.

Makino, T., Sugahara, T., and Ohgaki, K. (2005). "Stability boundaries of tetrahydrofuran plus water system." *Journal of Chemical and Engineering Data*, 50(6), 2058-2060.

Masui, A., Haneda, H., Ogata, Y., and Aoki, K. "Effects of Methane Hydrate Formation on Shear Strength of Synthetic Methane Hydrate Sediments." *The fifteenth (2005) International Offshore and Polar Engineering* Seoul, Korea.

Milkov, A. V., and Sassen, R. (2003). "Preliminary assessment of resources and economic potential of individual gas hydrate accumulations in the Gulf of Mexico continental slope." *Marine and Petroleum Geology*, 20(2), 111-128.

Mires, H. A., and Issac, F. (1906). "Refractive indices of crystallizing solution." *Journal of the Chemical Society*, 89, 413-454.

Mitchell, J. K., and Soga, K. (2005). *Fundamentals of Soil Behavior*, Wiley, New York.

Moon, C., Taylor, P. C., and Rodger, P. M. (2003). "Clathrate nucleation and inhibition from a molecular perspective." *Canadian Journal of Physics*, 81(1-2), 451-457.

Mullin, J. W. (2001). *Crystallization*, Butterworth-Heinemann, London.

Natarajan, V., Bishnoi, P. R., and Kalogerakis, N. (1994). "Induction Phenomena in Gas Hydrate Nucleation." *Chemical Engineering Science*, 49(13), 2075-2087.

Newell, J. C., Peng, Y., Edic, P. M., Blue, R. S., Jain, H., and Newell, R. T. (1998). "Effect of electrode size on impedance images of two- and three-dimensional objects." *Ieee Transactions on Biomedical Engineering*, 45(4), 531-534.

Nishinaga, T., Yamazaki, D., Stahr, H., Wakamiya, A., and Komatsu, K. (2003). "Synthesis, structure, and dynamic behavior of cyclopentadienyl-lithium, -sodium,

and -potassium annelated with bicyclo[2.2.2]octene units: A systematic study on site exchange of alkali metals on a cyclopentadienyl ring in tetrahydrofuran." *Journal of the American Chemical Society*, 125(24), 7324-7335.

Nixon, J. F., and Morgenstern, N. R. (1973). "The Residual Stress in Thawing Soils." *Canadian Geotechnical Journal*, 10(4), 571-580.

Ohmura, R., Kashiwazaki, S., Shiota, S., Tsuji, H., and Mori, Y. H. (2002). "Structure-I and structure-H hydrate formation using water spraying." *Energy & Fuels*, 16(5), 1141-1147.

Ohmura, R., Shigetomi, T., and Mori, Y. H. (2002). "Bending tests on clathrate hydrate single crystals." *Philosophical Magazine a-Physics of Condensed Matter Structure Defects and Mechanical Properties*, 82(9), 1725-1740.

Ohtake, M., Yamamoto, Y., Kawamura, T., Wakisaka, A., de Souza, W. F., and de Freitas, A. M. V. (2005). "Clustering structure of aqueous solution of kinetic inhibitor of gas hydrates." *Journal of Physical Chemistry B*, 109(35), 16879-16885.

Ostergaard, K. K., Anderson, R., Llamedo, M., and Tohidi, B. (2002). "Hydrate phase equilibria in porous media: effect of pore size and salinity." *Terra Nova*, 14(5), 307-312.

Ouar, H., Cha, S. B., Wildeman, T. R., and Sloan, E. D. (1992). "The formation of natural gas hydrates in water-based drilling." *Fluids.Trans.IchemE.A*, 70, 48-54.

Palomino, A. M. (2003). "Fabric Formation and Control in Fine-grained materials," Ph.D, Georgia Institute of Techonology, Atlanta, GA.

Palomino, A. M., and Santamarina, J. C. (2005). "Fabric map for kaolinite: Effects of pH and ionic concentration on behavior." *Clays and Clay Minerals*, 53(3), 211-223.

Pandit, B. I., and King, M. S. (1983). "Elastic wave velocities of propane gas hydrates." Natural gas hydrates: properties, occurrence and recovery, J. L. Cox, ed., Butterworth, Boston, 125.

Park, S. K., and Van, G. P. (1991). "Inversion of Pole-Pole Data for 3-D Resistivity Structure beneath Arrays of Electrodes." *Geophysics*, 56(7), 951-960.

Parks, G. A. (1990). "Surface-Energy and Adsorption at Mineral-Water Interfaces - an Introduction." *Reviews in Mineralogy*, 23, 133-175.

Paull, C. K., Matsumoto, R., Wallace, P.J., and Leg 164 Scientific Party. (1996).

Pearson, C., Murphy, J., and Hermes, R. (1986). "Acoustic and Resistivity Measurements on Rock Samples Containing Tetrahydrofuran Hydrates - Laboratory Analogs to Natural-Gas Hydrate Deposits." *Journal of Geophysical Research-Solid Earth and Planets*, 91(B14), 14132-14138.

Petrenko, V. F., and Whitworth, R. W. (1999). *Physics of Ice*, Clarendon, Oxford.

Pinheiro, P. A. T., Loh, W. W., and Dickin, F. J. (1998). "Optimal sized electrodes for electrical resistance tomography." *Electronics Letters*, 34(1), 69-70.

Pound, G. M., Madonna, L. A., and Peake, S. L. (1953). "Critical Supercooling of Pure Water Droplets by a New Microscopic Technique." *Journal of Colloid Science*, 8(2), 187-193.

Priest, J., Best, A., Clayton, C., and Watson, E. "Seismic properties of methane gas hydrate-bearing sand." *Fifth International Conference on Gas Hydrates*, Trondheim, Norway.

Priest, J. A., Best, A. I., and Clayton, C. R. I. (2005b). "A laboratory investigation into the seismic velocities of methane gas hydrate-bearing sand." *Journal of Geophysical Research-Solid Earth*, 110(B04102), doi:10.1029/2004JB003259.

Priest, J. A., Best, A. I., and Clayton, C. R. I. (2006). "Attenuation of seismic waves in methane gas hydrate-bearing sand." *Geophysical Journal International*, 164(1), 149-159.

Riedel, M., Long, P. E., and Collett, T. S. (2006). "Estimates of in situ gas hydrate concentration from resistivity monitoring of gas hydrate bearing sediments during temperature equilibration." *Marine Geology*, 227(3-4), 215-225.

Riestenberg, D., West, O., Lee, S., McCallum, S., and Phelps, T. J. (2003). "Sediment surface effects on methane hydrate formation and dissociation." *Marine Geology*, 198(1-2), 181-190.

Rinaldi, V. A., and Cuestas, G. A. (2002). "Ohmic conductivity of a compacted silty clay." *Journal of Geotechnical and Geoenvironmental Engineering*, 128(10), 824-835.

Roberts, P., and Hallett, J. (1968). "A Laboratory Study of Ice Nucleating Properties of Some Mineral Particulates." *Quarterly Journal of the Royal Meteorological Society*, 94(399), 25-&.

Ross, R. G., Aderson, P., and Backstorm, G. (1981). "Unusual PT dependence of thermal conductivity for a clarthrate hydrate." *Nature*, 290, 322-323.

Rowan, M. G., Jackson, M. P. A., and Trudgill, B. D. (1999). "Salt-related fault families and fault welds in the northern Gulf of Mexico." *Aapg Bulletin-American Association of Petroleum Geologists*, 83(9), 1454-1484.

Rueff, R. M., and Sloan, E. D. (1985). "Effect of granular sediment on some thermal properties of tetrahydrofuran hydrate." *Industrial & Engineering Chemistry, Process Design and Development*, 24(3), 882-885.

Santamarina, J. C., and Cho, G. C. (2001). "Determination of critical state parameters in sandy soils - Simple procedure." *Geotechnical Testing Journal*, 24(2), 185-192.

Santamarina, J. C., and Fratta, D. (2005). *Discrete Signals and Inverse Problems*, John Wiley & Sons Ltd., Chichester.

Santamarina, J. C., Klein, K. A., and Fam, M. A. (2001). *Soils and Waves*, J. Wiley & Sons, New York.

Santamarina, J. C., Klein, K. A., Wang, Y. H., and Prencke, E. (2002). "Specific surface: determination and relevance." *Canadian Geotechnical Journal*, 39(1), 233-241.

Santamarina, J. C., Yun, T. S., Lee, J. Y., Martin, A., Francisca, F., and Ruppel, C. "Mechanical, thermal and electromagnetic properties of hydrate-bearing clay, silt, and sand at various confining pressure." *American Geophysical Union*, San Francisco, CA. U.S.A.

Sassen, R., Joye, S., Sweet, S. T., DeFreitas, D. A., Milkov, A. V., and MacDonald, I. R. (1999). "Thermogenic gas hydrates and hydrocarbon gases in complex chemosynthetic communities, Gulf of Mexico continental slope." *Organic Geochemistry*, 30(7), 485-497.

Seagar, A. D., Barber, D. C., and Brown, B. H. (1986). "Theoretical Limits to Sensitivity and Resolution in Impedance Imaging." *Clinical Physics and Physiological Measurement*, 8 supplA, 13-31.

Sen, P. N., Scala, C., and Cohen, M. H. (1981). "A Self-Similar Model for Sedimentary-Rocks with Application to the Dielectric-Constant of Fused Glass-Beads." *Geophysics*, 46(5), 781-795.

Shi, W. X., Wang, B. L., and Li, X. T. (2005). "A measurement method of ice layer thickness based on resistance-capacitance circuit for closed loop external melt ice storage tank." *Applied Thermal Engineering*, 25(11-12), 1697-1707.

Skovborg, P., Ng, H. J., Rasmussen, P., and Mohn, U. (1993). "Measurement of Induction Times for the Formation of Methane and Ethane Gas Hydrates." *Chemical Engineering Science*, 48(3), 445-453.

Sloan, E. D. (1998). *Clathrate Hydrates of Natural Gases*, Marcel Dekker, NewYork.

Smallwood, I. M. (1996). *Handbook of organic solvent properties*, Halsted Press, London.

Spangenberg, E., and Kulenkampff, J. (2005) "Physical properties of gas hydrate bearing sediments." *Fifth International Conference on Gas Hydrates*, Trondheim, Norway.

Stangret, J., and Gampe, T. (2005). "Hydration of tetrahydrofuran derived from FTIR spectroscopy." *Journal of Molecular Structure*, 734(1-3), 183-190.

Stern, L. A., Kirby, S. H., and Durham, W. B. (1996). "Peculiarities of methane clathrate hydrate formation and solid-state deformation, including possible superheating of water ice." *Science*, 273(5283), 1843-1848.

Stoll, R. D. (1974). "Effects of gas hydrates in sediments." Natural gases in marine sediments, I. R. Kaplan, ed.

Stoll, R. D., and Bryan, G. M. (1979). "Physical-Properties of Sediments Containing Gas Hydrates." *Journal of Geophysical Research*, 84(Nb4), 1629-1634.

Stoll, R. D., Ewing, J., and Bryan, G. M. (1971). "Anomalous Wave Velocities in Sediments Containing Gas Hydrates." *Journal of Geophysical Research*, 76(8), 2090-&.

Stummer, P., Maurer, H., and Green, A. G. (2004). "Experimental design: Electrical resistivity data sets that provide optimum subsurface information." *Geophysics*, 69(1), 120-139.

Tajima, H., Yamasaki, A., and Kiyono, F. "Continous Gas Hydrate Formation Process by Static Mixing of Fluids." *The Fifth International Conference on Gas Hydrates*, Trondheim, Norway.

Takahashi, M., Kawamura, T., Yamamoto, Y., Ohnari, H., Himuro, S., and Shakutsui, H. (2003). "Effect of shrinking microbubble on gas hydrate formation." *Journal of Physical Chemistry B*, 107(10), 2171-2173.

Tsuji, H., Kobayashi, T., Ohmura, R., and Mori, Y. H. (2005). "Hydrate formation by water spraying in a methane plus ethane plus propane gas mixture: An attempt at promoting hydrate formation utilizing large-molecule guest substances for structure-h hydrates." *Energy & Fuels*, 19(3), 869-876.

Tsuji, H., Ohmura, R., and Mori, Y. H. (2004). "Forming structure-H hydrates using water spraying in methane gas: Effects of chemical species of large-molecule guest substances." *Energy & Fuels*, 18(2), 418-424.

Turnbull, D., and Fisher, J. C. (1949). "Rate of Nucleation in Condensed Systems." *Journal of Chemical Physics*, 17(1), 71-73.

Turnbull, D., and Vonnegut, B. (1952). "Nucleation catalysis. ." *Ind. Engr. Chem.*, 44, 1292-1298.

Uchida, T., Ebinuma, T., and Ishizaki, T. (1999). "Dissociation condition measurements of methane hydrate in confined small pores of porous glass." *Journal of Physical Chemistry B*, 103(18), 3659-3662.

Uchida, T., Ebinuma, T., Takeya, S., Nagao, J., and Narita, H. (2002). "Effects of pore sizes on dissociation temperatures and pressures of methane, carbon dioxide, and propane hydrates in porous media." *Journal of Physical Chemistry B*, 106(4), 820-826.

Upstill, C. E., and Evans, R. (1977). "Surface-tension and density profile of simple liquids." *Journal of Physics C-Solid State Physics*, 10(15), 2791-2799.

Valiullin, R., and Furo, I. (2002). "The morphology of coexisting liquid and frozen phases in porous materials as revealed by exchange of nuclear spin magnetization followed by H-1 nuclear magnetic resonance." *Journal of Chemical Physics*, 117(5), 2307-2316.

Vysniauskas, A., and Bishnoi, P. R. (1983). "A Kinetic-Study of Methane Hydrate Formation." *Chemical Engineering Science*, 38(7), 1061-1072.

Waite, W. F., deMartin, B. J., Kirby, S. H., Pinkston, J., and Ruppel, C. D. (2002). "Thermal conductivity measurements in porous mixtures of methane hydrate and quartz sand." *Geophysical Research Letters*, 29(24), -.

Waite, W. F., Winters, W. J., and Mason, D. H. (2004). "Methane hydrate formation in partially water-saturated Ottawa sand." *American Mineralogist*, 89(8-9), 1202-1207.

Walton, K. (1987). "The Effective Elastic-Moduli of a Random Packing of Spheres." *Journal of the Mechanics and Physics of Solids*, 35(2), 213-226.

Wang, H. X., Wang, C., and Yin, W. L. (2001). "Optimum design of the structure of the electrode for a medical EIT system." *Measurement Science & Technology*, 12(8), 1020-1023.

Weimer, P., Rowan, M. G., McBride, B. C., and Kligfield, R. (1998). "Evaluating the petroleum systems of the northern deep Gulf of Mexico through integrated basin analysis: An overview." *Aapg Bulletin*, 82(5), 865-877.

Weitemeyer, K. A., Constable, S. C., Key, K. W., and Behrens, J. P. (2006). "First results from a marine controlled-source electromagnetic survey to detect gas hydrates offshore Oregon." *Geophysical Research Letters*, 33(3), -.

White, M. A., MacLaren, D. C., Marriott, R. A., and Zhan, B. Z. (2003). "Thermodynamic stability of clathrate hydrates relative to their separate chemical components." *Canadian Journal of Physics*, 81(1-2), 175-182.

Wilder, J. W., Seshadri, K., and Smith, D. H. (2001). "Modeling hydrate formation in media with broad pore size distributions." *Langmuir*, 17(21), 6729-6735.

Winters, W. J., Gilbert, L. Y., Mason, D. H., Pecher, I. A., and Waite, W. F. "Effect of grain size and pore pressure on acoustic and strength behavior of sediments containing methane gas hydrate." *Fifth International Conference on Gas Hydrates*, Trondheim, Norway.

Wittebolle, R. J., and Sego, D. C. " A laboratory facility for testing sediments containing gas hydrates." *Fourth International Offshore Mechanics and Arctic Engineering Symposium*, New York, 52–58.

Wong, P., Koplik, J., and Tomanic, J. P. (1984). "Conductivity and Permeability of Rocks." *Physical Review B*, 30(11), 6606-6614.

Wood, W. T., Stoffa, P. L., and Shipley, T. H. (1994). "Quantitative Detection of Methane Hydrate through High-Resolution Seismic Velocity Analysis." *Journal of Geophysical Research-Solid Earth*, 99(B5), 9681-9695.

Wyllie, M. R. J., Gregory, A. R., and Gardner, G. H. F. (1958). "An experimental investigation of factors affecting elastic wave velocities in porous media." *Geophysics*, 23, 459–493.

Yoshida, K., Tsuchihashi, N., Ibuki, K., and Ueno, M. (2005). "NMR and viscosity B coefficients for spherical nonelectrolytes in nonaqueous solvents." *Journal of Molecular Liquids*, 119(1-3), 67-75.

Young, S. W. (1911). "Mechanical stimulus to crystallization in supercooled liquids." *Journal of the American Chemical Society*, 33, 148-162.

Young, S. W., and Cross, R. J. (1911). "The mechanical stimulus to crystallization. II." *Journal of the American Chemical Society*, 33, 1375-1388.

Young, S. W., and Van Sicklen, W. J. (1913). "The mechanical stimulus to crystallization." *Journal of the American Chemical Society*, 35, 1067-1078.

Yun, T. S. (2005). "Mechanical and thermal study of hydrate-bearing sediments," PhD thesis, Georgia Institute of Techonology.

Yun, T. S., Francisca, F. M., Santamarina, J. C., and Ruppel, C. (2005). "Compressional and shear wave velocities in uncemented sediment containing gas hydrate." *Geophysical Research Letters*, 32(10), L10609 (doi: 10.1029/2005GL022607).

Yun, T. S., Narsilio, G. A., and Santamarina, J. C. (2006). "Physical Characterization of Core Samples Recovered from Gulf of Mexico." *Marine and Petroleum Geology*, 23, 893-900.

Yun, T. S., Santamarina, J. C., and Ruppel, C. (2007). "Mechanical properties and rheology of sand, silt, and clay containing synthetic hydrate " *Journal of Geophysical Research*, 112, B04106, doi: 10.1029/2006JB004484.

Zakrzewski, M., and Handa, Y. P. (1993). "Thermodynamic properties of ice and of tetrahydrofuran hydrate in confined geometries." *Journal of Chemical Thermodynamics*, 25(5), 631-637.

Zatsepina, O. Y., and Buffett, B. A. (2001). "Experimental study of the stability of CO2-hydrate in a porous medium." *Fluid Phase Equilibria*, 192(1-2), 85-102.

Zatsepina, O. Y., and Buffett, B. A. (2002). "Nucleation of CO2-hydrate in a porous medium." *Fluid Phase Equilibria*, 200(2), 263-275.

Zhong, Y., and Rogers, R. E. (2000). "Surfactant effects on gas hydrate formation." *Chemical Engineering Science*, 55(19), 4175-4187.